Visible to Near-Infrared Kinetic Inductance Detectors
Energy-Resolving Single Photon Detectors

Kouwenhoven, K.

DOI
10.4233/uuid:9cc06b76-63b6-46f4-a5eb-0a965b562c2e

Publication date
2024

Document Version
Final published version

Citation (APA)
Kouwenhoven, K. (2024). *Visible to Near-Infrared Kinetic Inductance Detectors: Energy-Resolving Single Photon Detectors*. [Dissertation (TU Delft), Delft University of Technology]. https://doi.org/10.4233/uuid:9cc06b76-63b6-46f4-a5eb-0a965b562c2e

Visible to Near-Infrared Kinetic Inductance Detectors

Energy-Resolving Single Photon Detectors

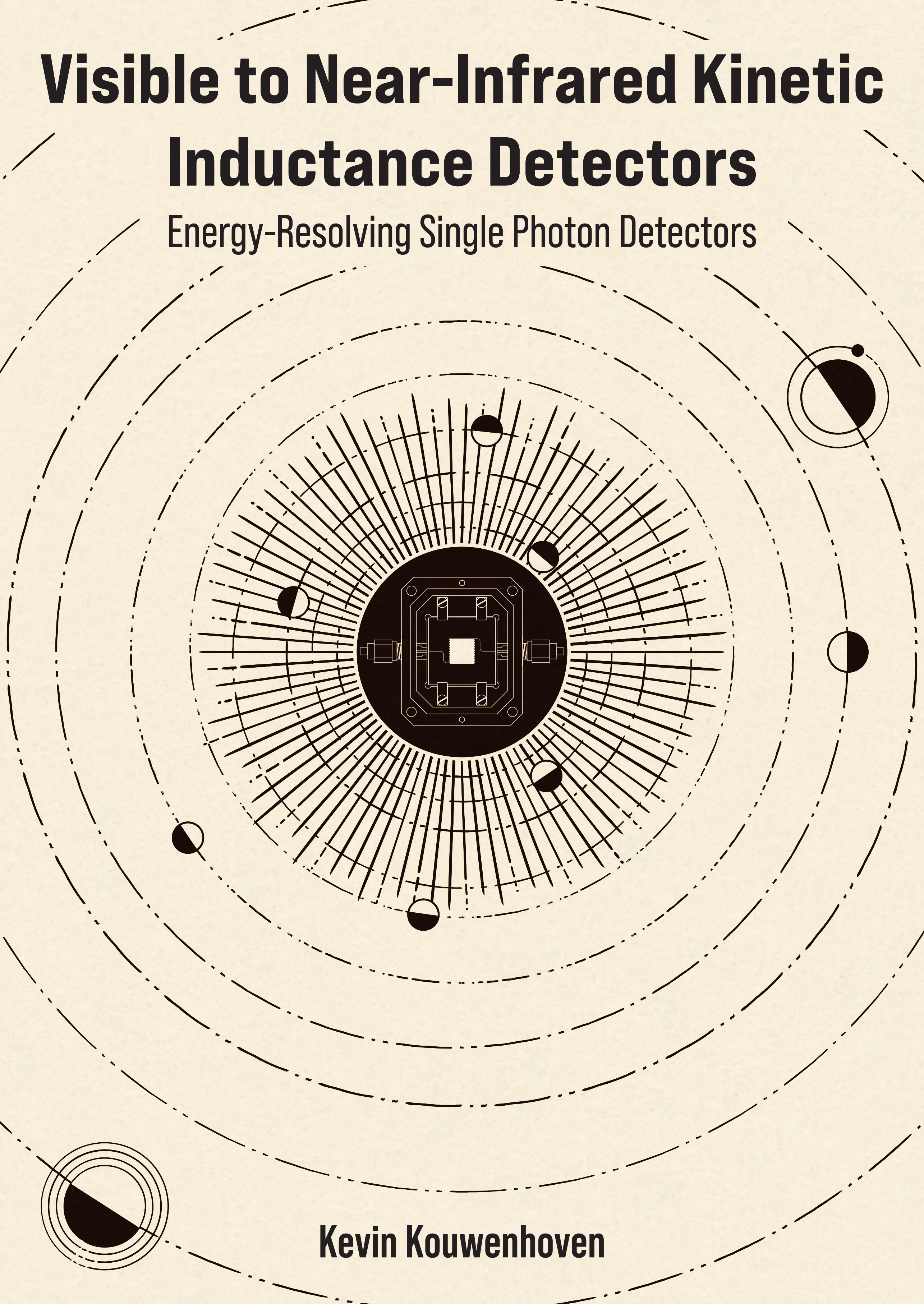

Kevin Kouwenhoven

Visible to Near-Infrared Kinetic Inductance Detectors

Energy-Resolving Single Photon Detectors

Visible to Near-Infrared Kinetic Inductance Detectors

Energy-Resolving Single Photon Detectors

Dissertation

for the purpose of obtaining the degree of doctor
at Delft University of Technology
by the authority of the Rector Magnificus prof. dr. ir. T. H. J. J. van der Hagen
chair of the board for doctorates,
to be defended publicly on Wednesday 8 January at 10:00 o'clock

by

Kevin KOUWENHOVEN

Master of Science in Electrical Engineering,
Delft University of Technology, the Netherlands
Born in Leiderdorp, Netherlands.

This dissertation has been approved by the promotors.

Composition of the doctoral committee:

Rector Magnificus	Chairman
Prof. dr. ir. J. J. A. Baselmans	Delft University of Technology/Netherlands Institute for Space Research (SRON), promotor
Dr. ir. P. J. de Visser	Delft University of Technology/Netherlands Institute for Space Research (SRON), copromotor
Independent members:	
Dr. M. Alonso Del Pino	Delft University of Technology
Prof. dr. ir. R. Barends	Jülich Research Center/RWTH Aachen University, Germany
Prof. dr. B. R. Brandl	Leiden University/Delft University of Technology
Prof. dr. B. A. Mazin	UC Santa Barbara, USA
Prof. dr. G. A. Steele	Delft University of Technology

Printed by: Ipskamp Drukkers B.V. – The Netherlands
Cover design by: K. Kouwenhoven

An electronic version of this dissertation is available at http://repository.tudelft.nl/
ISBN 978-94-6384-703-2

Na de volgende bocht...

Wiro Pieterse

Contents

Chapter 1

Introduction: Through alien eyes

Since the Kepler space telescope launch in 2009, there has been a massive acceleration of the number of detected exoplanets-planets that orbit stars other than our sun. To date, several hundred of these planets have been identified as Earth-like or "rocky" and lie in their star's habitable zone. This "Goldilocks" zone is the region where the temperature on the planet is just right for liquid water and to support life as we know it. One of the major astronomical goals of the coming decade is to determine what type of planets are out there in the universe. Are any of those planets like our own Earth? Do any of these planets host biological life? If so, are they single-cell organisms or more complex lifeforms? Ultimately, we aim to answer the question: "Are we alone in the universe?"

Most exoplanets are detected indirectly, often by observing the brief dimming of a star's light when a planet transits in front of it. However, to learn more about these small habitable exoplanets, we need to observe the light they reflect or emit directly. The challenge is that these planets can be up to a billion times dimmer than their host star, so without specialized equipment, these planets hide in the glare of their host star. If you manage to build a telescope with enough contrast—so that it can separate the planet from the starlight—you need an extremely sensitive detector to measure the faint light signal from the planet. A concept of such a telescope was the Habitable Exoplanets Observatory (HabEx), of which a concept drawing is given in Fig. 1.1.

Currently, two big missions aim to directly image Earth-like exoplanets: The Habitable Worlds Observatory (HWO) and the Large Interferometer for Exoplanets (LIFE). The light detected by these telescopes can be used for atmosphere spectroscopy, where we look for the fingerprints of biological life in a planet's atmosphere. To introduce this concept and the detector requirements it imposes, let's first consider a detector we are all intimately familiar with: the human eye.

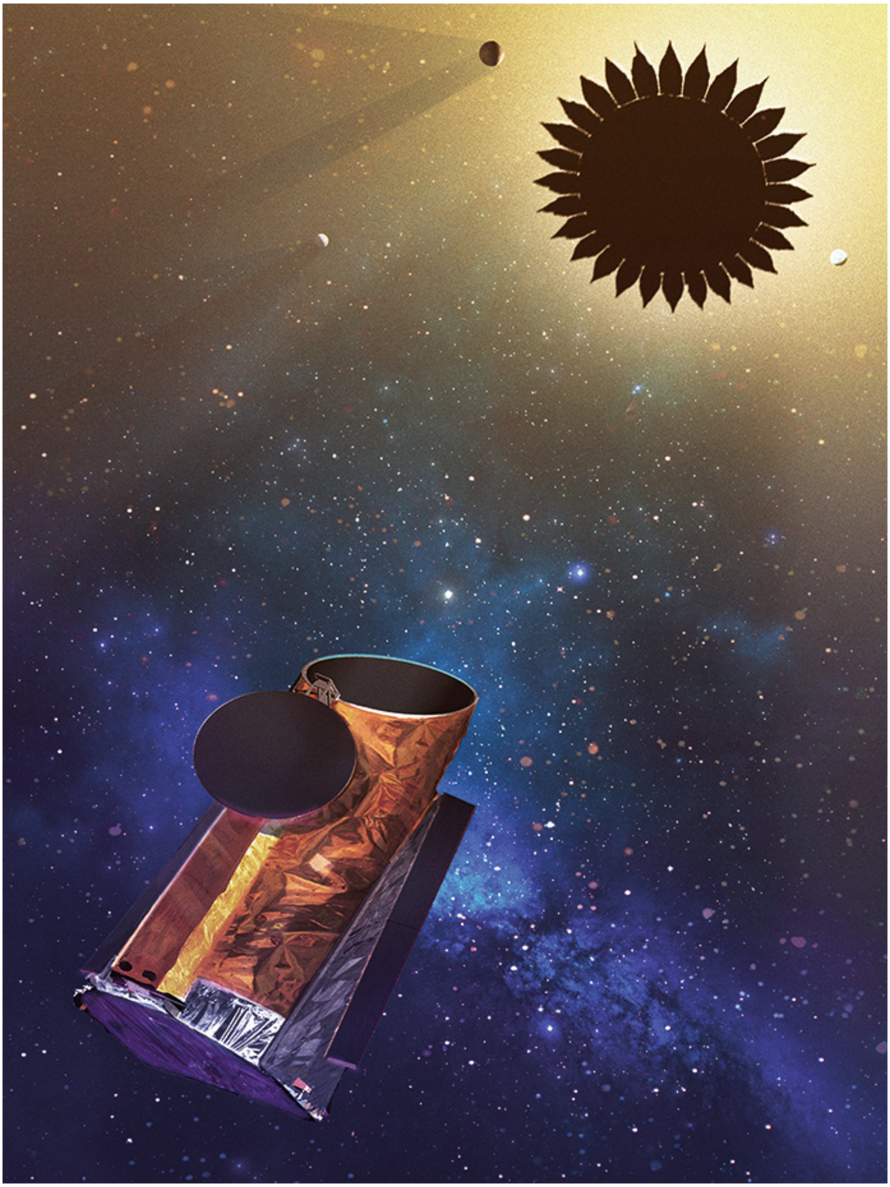

Figure 1.1: A concept drawing of the habitable exoplanet observatory (HabEx) with a star shield. The telescope flies in formation with a star shield that blocks the light of a star. The telescope can then directly image the faint rocky exoplanets. HABEX would image exoplanets in visible and near-infrared wavelengths. Image is from Ref. [1]. The Habitable Worlds (HWO) mission combines elements of HabEx and the Large Ultraviolet Optical Infrared Surveyor (LUVOIR).

1.1. A world in multicolor

The retina, located at the back of our eyes where the lens focuses light, is covered with photoreceptor cells. Humans have two types of these cells: rods and cones. These cells capture light and, in turn, send a signal to our visual system, forming the images we see. Both rods and cones contain proteins called opsins, which are paired with chromophores. The chromophores absorb light, triggering a chain reaction through the opsins, resulting in an electric signal traveling to the brain via the optic nerve.

Humans have cones in three varieties due to differences in opsins. Each type of opsin is sensitive to different wavelengths of light as illustrated by Fig. 1.2 and are known as short, medium, and long wavelength opsins. The short-wavelength opsin is sensitive to wavelengths close to 400 nm, which we perceive as violet/blue, while the long-wavelength opsin is most sensitive to wavelengths around 700 nm, which we perceive as red. The more familiar names for these opsins and the cones that contain them are red (R), green (G), and blue (B).

When we look at a red flower, the light reflected by the petals strongly stimulates the red cones while slightly stimulating the green cones. Conversely, the light reflected by a blue flower strongly stimulates the blue cones.

Our visual system essentially mixes these primary colors—red, green, and blue—to create the vast array of colors we can perceive. Light of various wavelengths will simulate the cones in different ratios, and our optical system translates this into a color. We can distinguish between light of two wavelengths or colors if the response of our cones to both wavelengths is different—it results in a different RGB ratio. To better understand the colors we can see, we will explore a few of the eyes we can find in the animal kingdom.

1.1.1. A plethora of eyes

The sensitivity of our three opsins limits the range of wavelengths humans can see. For most people, this ranges from approximately 380 nm (violet) to 700 nm (red), as illustrated in Fig. 1.2. This range is known as the visible (VIS) wavelength range, encompassing all the colors of the rainbow.

However, not all eyes are limited to this wavelength range. The melanophila, or "fire" beetles, rely on forest fires for reproduction, laying their eggs in freshly scorched bark. To locate forest fires, these beetles can "see" infrared radiation at longer wavelengths (2.5-4 µm)—which we feel as heat emanating from a campfire [4]. With their specialized sensors, these "fire-loving" beetles can detect forest fires up to 130 km away [5].

Furthermore, the number of different types of cones is not universally limited to three. Most birds have a fourth cone sensitive to shorter wavelengths, the UV, as

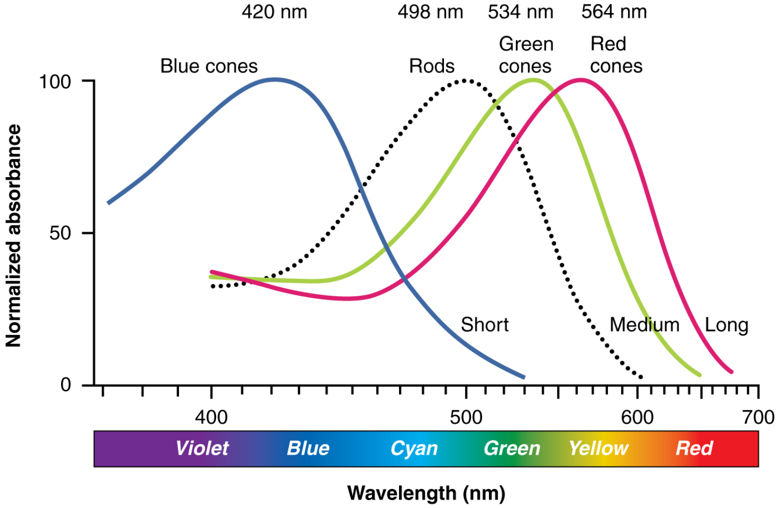

Figure 1.2: The spectral sensitivity of cones and rods in the human eyes. Each of the three types of cones is sensitive to a different range of wavelengths. Photons at the violet end of the spectrum will mostly trigger the blue cones, while photons at the red side of the spectrum will mainly trigger the red cones. Together, these cones give us our color vision, and the horizontal bar indicates the range of colors we can see. The rods in our eyes are sensitive to wavelengths around 498 nm and are great at seeing low-light levels. Image from [2]

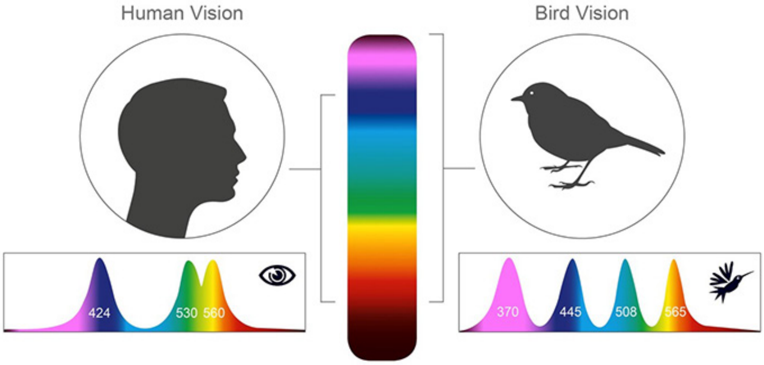

Figure 1.3: Humans are trichromats; we have three types of cones as depicted in Fig. 1.2. Most birds, on the other hand, are tetrachromats; they have a fourth type of cone that is sensitive to shorter wavelengths, the UV. Note that the UV range is depicted with a bright violet in this image, while in reality, there is no color associated with these wavelengths since we can not see it. Image from [3]

illustrated in Fig. 1.3. Research shows that some species of birds, like the blue tit (*NL: pimpelmees*) and the Saw-whet owl, have markings that light up brightly in UV as shown in Fig. 1.4. There are bird species, like the blue tit, where the male and female look identical to us but appear different to each other [6]. Other birds, like the American kestrel, might use their UV vision to spot their prey, as small rodents leave trails of urine that reflect ultraviolet light, with the freshest trails reflecting the strongest.

Human blue cones are actually sensitive to UV light, but our lenses block it. This is why people who lost their lenses to surgeries or accidents, like Claude Monet [7], start to see UV as a whitish blue.

Our electronic eyes-the cameras in our smartphones-mimic the human eye and are generally sensitive to the same wavelengths. However, these electronic cameras can be designed to detect different wavelengths, such as the infrared cameras popular in spy movies. Exoplanets reflect and emit light over a much broader wavelength range than the human eye perceives. In the next section we will see that to find life on these distant worlds, we need detectors sensitive to a far wider range of wavelengths than our eyes.

1.1.2. How do we see different colors?

Now to revisit our earlier question, "Why do we see different colors?" Researchers estimate that humans can discriminate between a few million colors [9]. We can differentiate between two colors if their wavelengths produce a unique RGB response. This means the ratio of stimulation among the three types of cones (red, green, and blue) must be different for each wavelength. If the wavelengths are too close to each other, they will stimulate the same cones equally, resulting in an indistinct signal for our brains since every color we perceive is a mix of red, green, and blue.

Some animals, such as dogs, have only two types of cones and see a world in a limited color spectrum, primarily in shades of blue, yellow, and gray. Similarly, People with color blindness lack one of the three cones and are dichromats as well Deuteranopes, a subset of "color-blind" people that miss the green cone, still see color but in a narrower range, making it hard, for example, to distinguish red and greens. Dichromats can see roughly 1% of the colors that trichromats can see-tens of thousands instead of millions [10]. On the other hand, tetrachromats, like most birds with four types of cones, likely perceive a hundred times more colors than we do. Adding an extra cone means that colors become more distinct, as the additional cone allows for finer discrimination of wavelengths and, thus, a broader and more nuanced perception of colors. Later, we will see how wavelength discrimination is crucial to learn more about the conditions on an exoplanet.

Figure 1.4: Porphyrin pigments make the feathers of owls fluoresce bright pink when exposed to a UV lamp. Since the intensity of the fluorescence depends strongly on the age of the feathers, these markings are used to determine an owl's age. Normally, we would not be able to see these markings, but with a bright UV source and a camera that is sensitive to shorter wavelengths, translating UV light to a bright pink, we can get a glimpse of the world birds see. Image from [8]

1.1.3. Seeing single photons

If the cones in our retinas give us color vision, why do we also have an extra set of photoreceptors called rods? While rods do not provide color vision, they are significantly more sensitive than cones and continue to function at low light levels where cones stop working. Researchers have found that our rods are sensitive enough to detect light at the single-photon level [11], [12].

Using short flashes of faint green (510 nm) light, researchers discovered that humans could detect flashes containing as few as 90 photons. Only about ten percent of these photons reach the retina; the rest are reflected by the cornea or absorbed elsewhere. Since the 9 photons that reach the retinas are spread over an area containing around 350 rods, the researchers concluded that rods are sensitive to single photons. In 1999, researchers connected a toad's rods to an electric circuit, demonstrating their sensitivity to single photons [13].

However, our rods can be fooled. If you close your eyes and cover them with your hands to block out all light, you might see faint static ("snow") instead of complete darkness. This is because photoreceptors can accidentally fire on their own, and in the absence of light, these false signals can outnumber the actual photons hitting our eyes. So, while rods can detect single photons, they do so amidst a sea of misfires. The light our telescopes will see from an exoplanet will be extremely faint, less than a photon per second. If our detectors suffer the same misfires as our eyes, the exoplanet's signal will drown in the background static.

1.2. Exoplanet atmospheric spectroscopy

A space telescope equipped with something that blocks the light from the host star to a sufficient degree, like the star shade in Fig. 1.1, will be able to directly detect the faint light reflected by an exoplanet. The light the planet reflects from its host star is filtered by the atmosphere of the planet. Molecules in the atmosphere will absorb light at specific wavelengths and leave a specific "fingerprint" in the light our telescope detects. This fingerprint will be different for different types of planets, as illustrated by Fig. 1.5.

Identifying the gasses responsible for the "fingerprint" in the detected light, like in Fig. 1.6, can tell us a lot about the atmospheric chemistry of that planet. Some of these gasses are caused by biological processes, like the oxygen created as a byproduct of photosynthesis in plants and bacteria. However, for a lot of these gasses, false-positive mechanisms exist, where the same gass can also be created by non-biological processes like volcanic activity or, in the case of oxygen, by photolysis.

A few combinations of gasses, in specific ratios, have been identified as bio-

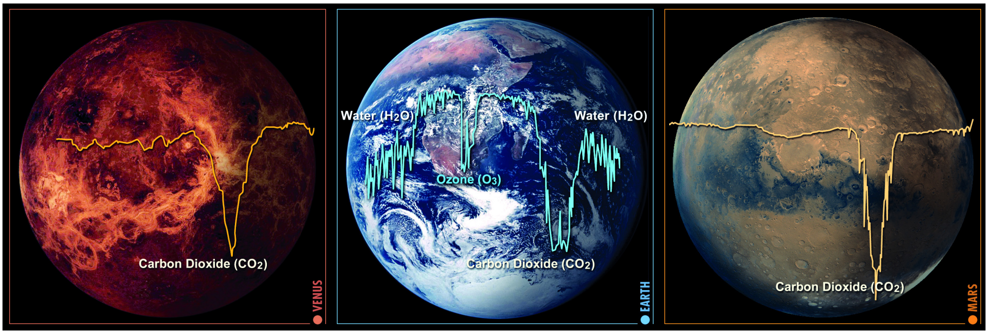

Figure 1.5: Atmospheric spectra for three planets in our solar system. While our atmosphere contains a variety of gasses, like water and ozone, the atmospheres of Mars and Venus contain mainly carbon dioxide. Image from [14]

signatures, which means that they can, in that specific balance, only be created by biological life on that planet. The bio-signatures in Fig. 1.6 are present at longer wavelengths than we can see. For the habitable worlds observatory, the interesting bio-signatures lie in the visible (VIS) and near-infrared (NIR) wavelengths, between 400 nm and 1700 nm, a range a factor four bigger than what we can see with our eyes.

To find these signatures, it is not enough to reduce the wavelength information to a single color as our visual system does; we need full wavelength information in order to obtain the spectrum in Fig. 1.6. In addition, the exoplanet is so faint that we would expect less than a photon per second to hit the detector. While our eyes use millions of photons to determine color by observing the ratio between red, green, and blue, we need a detector that can determine the "color" of a single photon.

1.3. Our electronic eyes

The most common optical detectors are based on semiconductors, similar to the camera in your smartphone. In these semiconductor detectors, there exists a specific energy barrier known as the material's energy gap, which must be overcome to mobilize an electron. The wavelength of a photon corresponds to a photon's energy, with shorter wavelength photons having a higher energy. When a photon is absorbed in a semiconductor, this energy can be used to excite one electron across the barrier. For silicon (Si) this energy barrier is 1.1 eV, which corresponds to a photon with a wavelength of ~1.1 µm. Photons with longer wavelengths don't have enough energy to excite an electron and photons in the visible range (400 - 700 nm) still only have

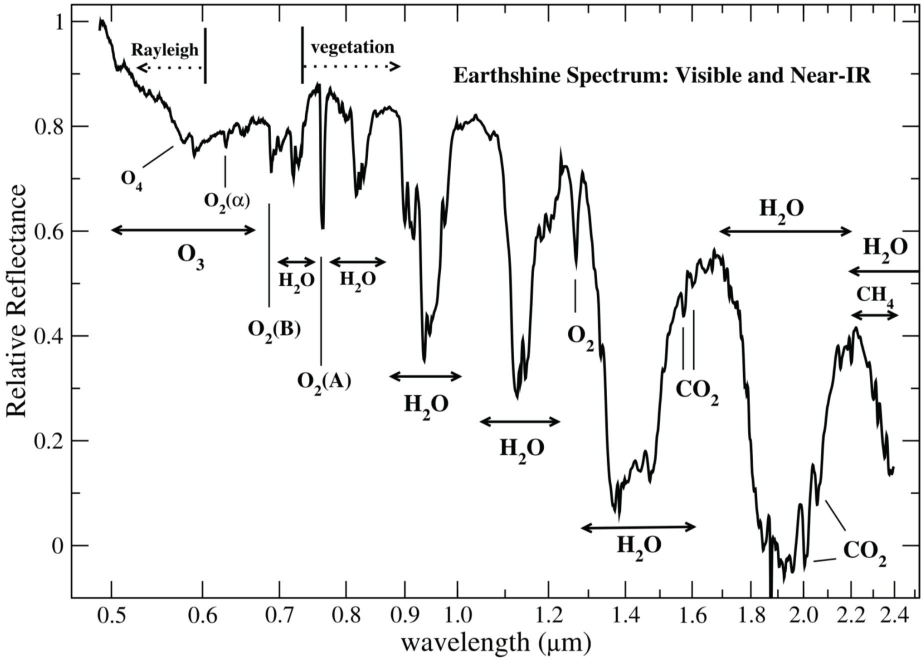

Figure 1.6: The atmospheric spectrum of our Earth contains fingerprints from a lot of different gasses in the visible and near-infrared wavelengths. Finding an exoplanet with a similar spectrum would be a strong indication of the presence of life. Our eyes only cover this graph's left side, up to 0.7 µm. The habitable worlds observatory aims at finding the biosignatures between roughly 0.4 µm and 1.7 µm. Image from [15]

enough energy to excite one, maybe two, electrons, as illustrated in Fig. 1.7.

Measuring the number of electron excitations within a time interval provides a measure of the brightness of a light source. However, these detectors alone cannot distinguish between photons of different wavelengths because each photon creates the same type of excitation since, no matter the wavelength, there is only enough energy to excite one electron across the barrier, see Fig. 1.7. To address this, colored filters placed above the detectors mimic the response of our cone cells, effectively creating an electronic version of our eye. Each pixel in your smartphone's camera consists of at least three detectors: one with a blue filter, one with a red filter, and one with a green filter.

Just like our eyes, these cameras do not determine the wavelength of a photon but group them into one of three categories: red, green, or blue. The ratio between these three then determines the color in your picture. In addition, these detectors are susceptible to noise—similar to the visual static we experience in low light conditions—where detectors may accidentally trigger, creating an electron excitation without a photon being absorbed. These excitations cannot be distinguished from real photon events. At the light levels relevant for exoplanet direct imaging, less than a photon per second, these false triggers can easily outnumber the real photons coming from our planet.

1.3.1. Superconducting single photon detectors

This all changes when we move to superconducting detectors. At low temperatures, the electrons in a superconductor form so-called Cooper pairs. These pairs are bound but can be broken by photons with enough energy, as in Fig. 1.7. However, in contrast to the semiconductor-based detectors, this binding energy is more than a thousand times smaller than the energy of visible photons. For example, for beta-phase Tantalum (β-Ta) this binding energy is $\sim 300\,\mu\text{eV}$ (2Δ, $T_c = 1$ K). This means a single VIS-NIR photon will not create a single excitation, but can break thousands of Cooper pairs to create thousands of excitations.

We can create superconducting resonators—ultra-pure tuning forks—that are extremely sensitive to these excitations. In the absence of light these resonators produce a single tone, of a specific pitch and with a certain duration. When hit by a photon, these resonators will respond by shifting to a lower pitch and holding their tone for a shorter duration. How far they shift depends on the number of excitations created by the absorbed photon. These resonators are the kinetic inductance detectors (KIDs) [16], [17] from the title of this thesis.

Since the photon's wavelength (= energy) determines how many excitations were created, photons of a specific wavelength will create a specific, unique response. This is an entirely different story than for our eyes, where photons are effectively only

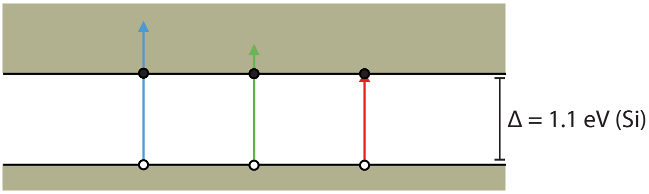

Semiconductor

The gap is on the same order as the energy in a visible photon,
a 400 nm (blue) photon creates one excitation

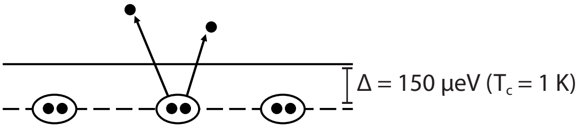

Superconductor

The binding energy of a Cooper pair (2Δ) is way smaller than the energy in a visible photon,
a 400 nm (blue) photon can create thousands of excitations

Figure 1.7: Energy gap in a semiconductor and superconductor. For semiconductors, the gap (Δ)corresponds roughly to the energy of a single visible photon. A single photon, no matter its color, can thus excite only one electron across the barrier. The responses to photons of different wavelengths or colors are indistinguishable. For a superconductor the energy required to break a Cooper pair into quasiparticles (2Δ) is more than a thousand times smaller than the energy of a VIS-NIR photon. A single photon thus has enough energy to create thousands of excitations. Since a blue photon has more energy than a red photon, a blue photon will create more excitations than a red photon, in a superconductor.

classified as red, green, or blue. The property that a superconducting detector can determine the wavelength of each individual photon is known as energy resolving.

Over the observation time, measuring photon by photon and determining the wavelength of each photon from its unique response, we can build up the spectrum in Fig. 1.6 with a single detector. The superconducting detector can do this over an extremely wide band. The work in this thesis shows measurements between 400 nm and 1550 nm, but single photon measurements have been demonstrated even at 25 µm [18]. Moreover, there are no false photon pulses when the detector accidentally triggers, and we can reject out-of-band photons at wavelengths outside our range of interest.

1.4. Outline of this thesis

Chapter 2 introduces the concepts of superconductivity necessary to describe the superconducting resonators that lie at the basis of kinetic inductance detectors (KIDs). The resonator's circuit representation, which includes the complex conductivity of the superconductor, is used to derive the resonator's response to the intentional creation of excess quasiparticles. The chapter then dives into single photon detection, where we present the photon absorption mechanism and the single photon pulse response. Since the response is energy-dependent, these detectors can resolve the energy of a single photon. We discuss the fundamental and experimental limits to the energy resolution of a KID and how the energy of a photon can be retrieved from the photon pulse through the optimal filter.

Chapter 3 introduces several topics that are useful as an experimental background for the work in this thesis. This chapter gives an overview of several design and simulation considerations, discusses the microwave readout system and the associated system noise level, and finally describes the experimental setup used for the efficiency measurements in Chapter 6.

Chapter 4 focusses on the energy resolution of hybrid β-Ta/NbTiN KIDs with 3D-printed microlenses. The resolving power is measured at four wavelengths between 400 nm and 1550 nm, and we conclude that the SNR of the detectors does not limit the resolving power. The phase response saturates for shorter wavelengths, so an alternative linear readout coordinate system is used to see if it improves the resolving power of the detectors. Although we observe a small improvement in resolving power, the measured resolving powers still do not follow the SNR or phonon-loss limited energy dependency. The response to two sources, a laser and a monochromator, at different wavelengths is used to demonstrate the line-resolving capabilities of KIDs.

Chapter 5 describes the optical stacks that can be used to improve the absorption efficiency of KIDs. A transmission line model is introduced that uses ellipsometric measurement data from the deposited superconducting film to predict the absorption efficiency of both bare films and optical stacks. An optical stack based on thin layers of SiN and an aluminum backing reflection yield near unity absorption over a broad wavelength for a TiN KID. The predicted absorption efficiency is in good agreement with reflection-transmission measurements of an unpatterned version of the stack.

Chapter 6 shows detector efficiency measurements of 61% at 500 nm, achieved by coating the entire KID array with a thin AR-layer of SiN. We use the detector efficiency setup as described in Chapter 3 to measure the photon count rate of lens-coupled 5 KIDs and compare it to the expected count rate based on the power in the beam that illuminates the array. The measured detector efficiency includes the efficiency of the AR-coated microlens array, the effective filling-ratio of the inductors, and the absorption efficiency of a a 40-nm thick film of β-Ta coated with a 54-nm thick layer of SiN.

Chapter 7: is focussed on the noise of parallel plate capacitors. Since these capacitors have a high capacitance per unit area, they can be used to decrease the pixel size of visible to near-infrared (VIS-NIR) KIDs. However, the two-level systems in the dielectric between the parallel plates increase the noise level of the detectors. We study these parallel plate capacitors within the TLS framework by measuring both the power-dependent microwave loss and the frequency noise levels as a function of parallel plate area and dielectric thickness. We observe that the microwave loss is affected by surface layers, where a thicker dielectric layer gives lower loss, and that the frequency scales roughly as $1/V$, with V the volume of the dielectric, as predicted by theory. We do not find evidence for surface layers in the noise measurements, while the surface layers clearly impact the microwave loss. The chapter finishes with design considerations for parallel plate capacitor KIDs based on the observed noise level scalings.

Bibliography

[1] B. S. Gaudi, S. Seager, B. Mennesson, *et al.*, "The Habitable Exoplanet Observatory," *Nature Astronomy*, vol. 2, no. 8, pp. 600–604, 2018. DOI: `10.1038/s41550-018-0549-2`.

[2] Chromatone center. "Human color perception." (n.d.), [Online]. Available: `https://chromatone.center/theory/color/perception/`.

[3] Klaus Schmitt. "How to simulate what birds may see: Simulated bird vision." (2017), [Online]. Available: `http://photographyoftheinvisibleworld.blogspot.com/2017/09/how-to-simulate-what-birds-may-see.html`.

[4] D. Klocke, A. Schmitz, H. Soltner, H. Bousack, and H. Schmitz, "Infrared receptors in pyrophilous ("fire loving") insects as model for new un-cooled infrared sensors," *Beilstein journal of nanotechnology*, vol. 2, pp. 186–97, Mar. 2011.

[5] H. Schmitz and H. Bousack, "Modelling a Historic Oil-Tank Fire Allows an Estimation of the Sensitivity of the Infrared Receptors in Pyrophilous Melanophila Beetles," *PLOS ONE*, vol. 7, no. 5, e37627, May 2012.

[6] S. Hunt, A. T. D. Bennett, I. C. Cuthill, and R. Griffiths, "Blue tits are ultraviolet tits," *Proc. R. Soc. Lond. B Biol. Sci.*, Mar. 1998.

[7] Carl Zimmer, "Monet's Ultraviolet Eye," Blog Post, Apr. 2012.

[8] Wild Bird Research Group, Inc. "Adopted owls." (n.d.), [Online]. Available: `https://wildbirdresearch.org/adopted/`.

[9] M. R. Pointer and G. G. Attridge, "The number of discernible colours," *Color Res. Appl.*, vol. 23, no. 1, pp. 52–54, 1998.

[10] J. Carroll, C. J. Murphy, M. Neitz, J. N. Ver Hoeve, and J. Neitz, "Photopigment basis for dichromatic color vision in the horse," *J. Vision*, vol. 1, no. 2, p. 2, Oct. 2001.

[11] J. N. Tinsley, M. I. Molodtsov, R. Prevedel, *et al.*, "Direct detection of a single photon by humans," *Nat. Commun.*, vol. 7, no. 1, pp. 1–9, Jul. 2016.

[12] R. Holmes, "Seeing single photons," *Phys. World*, vol. 29, no. 12, p. 28, Dec. 2016.

[13] G. G. Whitlock and T. D. Lamb, "Variability in the time course of single photon responses from toad rods: Termination of rhodopsin's activity," *Neuron*, vol. 23, no. 2, pp. 337–351, Jun. 1999.

[14] The European space agency. “Spectra from different Earth-like planets.” (2006), [Online]. Available: `https://www.esa.int/ESA_Multimedia/Images/2003/04/Spectra_from_different_Earth-like_planets`.

[15] R. Claudi and E. Alei, “Biosignatures Search in Habitable Planets,” *Galaxies*, vol. 7, no. 4, 2019.

[16] J. Zmuidzinas, “Superconducting microresonators: Physics and applications,” *Annu. Rev. Conden. Ma. P.*, vol. 3, no. Volume 3, 2012, pp. 169–214, Mar. 2012, ISSN: 1947-5462. DOI: `10.1146/annurev-conmatphys-020911-125022`.

[17] J. Baselmans, “Kinetic Inductance Detectors,” *J. Low Temp. Phys.*, vol. 167, no. 3-4, pp. 292–304, Jan. 2012, ISSN: 1573-7357. DOI: `10.1007/s10909-011-0448-8`.

[18] P. K. Day, N. F. Cothard, C. Albert, *et al.*, “A 25-micron single photon sensitive kinetic inductance detector,” 2024. DOI: `10.48550/arxiv.2404.10246`. arXiv: `2404.10246 [astro-ph.IM]`.

Chapter 2

A pair-breaking detector: superconducting resonators and single photons

2.1. Superconductivity

Motivated by the liquefaction of helium, Heike Kamerlingh Onnes began investigating the reduction of a metal's resistance at low temperatures. On July 10, 1908, in Leiden, he serendipitously found that the resistance of "a mercury resistance" suddenly drops to zero when cooled to below a temperature of 4.19 Kelvin [1] (April 8, 1911, Leiden). In his initial articles, Kamerlingh Onnes dubbed this phenomenon "supraconductivity" and, only later, started using the term "superconductivity". Kamerlingh Onnes showed that a superconductive ring would maintain an induced current after removing the battery source. An hour later, the researchers did not observe a measurable change in the current flowing through the ring, showing that the ring had indeed zero resistance and was thus lossless.

To explain the absence of resistance in a superconductor below a specific temperature, we look at the motion of electrons in a metal. In a metal, the valence electrons are so weakly bound to their host atoms that they essentially behave as a free-flowing gas of electrons [2]. When an external electric field $\vec{E}$ is applied to a metal conductor, the free electrons experience a force $\vec{F} = -e\vec{E}$ and start moving in the opposite direction of the field. The current density $\vec{J}$ induced in the conductor is given by the total charge passing through the conductor's cross-sectional area (A) per unit time when the field $\vec{E}$ is applied.

The Drude model [3], [4] assumes that the interaction between electrons can be ignored and that we can describe the response to the electric field by considering the dynamics of independent electrons. For a constant field (DC), the electrons experience a force $\vec{F} = -e\vec{E} = ma$, which accelerates them in the opposite direction with respect to the electric field. Here, $-e$ is the elementary charge of an electron, m is the mass of an electron, and a is the acceleration.

Instead of moving freely through the metal, some inelastic scattering process dampens the electron's velocity. The scattering time is defined such that the time between two scattering events is 2τ. This means that an electron will, on average, travel a time τ until the next collision and has been traveling for a time τ since its last collision. The Drude model assumes that the electrons are scattered in a random direction by each collision. Averaging all possible random directions, we can say that the average momentum after a collision is 0. This means that, instead of being accelerated indefinitely, the electron picks up an average drift velocity $\vec{v}_d = \frac{1}{2}a \cdot 2\tau$ between collisions. The acceleration during this period (2τ) is given by $\vec{a} = \frac{-e}{m}\vec{E}$ and the drift velocity becomes $\vec{v}_d = -\frac{e\tau_e}{m}\vec{E}$.

The current density is then given by

$$\vec{J} = -ne\vec{v}_d = \frac{ne^2\tau}{m}\vec{E}, \tag{2.1}$$

with n the electron density. Here, we recognize Kirchhoff's reformulation of Ohm's law [5], where $J = \sigma\vec{E}$ with σ the material's conductivity,

$$\sigma = \frac{ne^2\tau}{m}. \tag{2.2}$$

Scatters such as phonons, electrons, or excitations, will dominate at high temperatures ($T \gtrsim 50$ K), where the resistivity ($\rho = \sigma^{-1}$) is temperature dependent [6],

$$\rho(T) = \rho(0) + A\left(\frac{T}{\Theta_R}\right)^n \int_{x=0}^{\Theta_R/T} \frac{x^n}{(e^x-1)(1-e^{-x})}dx, \tag{2.3}$$

with Θ_R the Debye temperature from resistivity measurements, A is a constant that depends on the velocity of electrons at the Fermi surface, the Debye radius, and on the number of electrons in the metal. The integer n depends on the type of scatterer, where $n = 5$ for electron-photon interactions and $n = 2$ for electron-electron interactions, for which we obtain different temperature dependencies. For "normal" metals, such as gold, the resistivity keeps decreasing with temperature until it plateaus to $\rho(0)$ where the residual scattering time τ is dominated by electron-impurity scattering.

However, Kamerlingh Onnes noted that for some pure metals, the resistivity suddenly drops to zero below a specific temperature. This effect becomes apparent in the Drude model if we assume that for a certain temperate T, some superconducting electrons (n_s) exist that no longer collide with the ion lattice ($\tau \to \infty$). In this case, the conductivity for those electrons (2.1) tends to infinity (resistivity drops to zero), and we have an accelerating super-current

$$\frac{d\vec{J}_s}{dt} = \frac{e^2 n_s}{m_e}\vec{E} = \frac{\vec{E}}{\Lambda}. \tag{2.4}$$

If we introduce $\Lambda = \frac{m}{n_s e^2} = \mu_0 \lambda^2$ with λ the penetration depth, Equation 2.4 is the first of the two London equations proposed by the brothers F. and H. London to describe the local electric and magnetic fields in a superconductor [7]: a time-dependent electric field is screened out exponentially with depth λ.

$$\nabla^2 \vec{E} = \vec{E}/\lambda^2. \tag{2.5}$$

The second London equation, which cannot be derived in this classical way, is valid for time-dependent magnetic fields

$$\nabla^2 \vec{h} = (1/\lambda^2)\vec{h}, \tag{2.6}$$

where $\vec{h}$ is the flux density on a microscopic scale.

Combined, the Londen equations show that electromagnetic fields are screened from the interior of a superconductor with penetration depth λ

$$\lambda = \sqrt{\frac{m}{\mu_0 n_s e^2}}, \tag{2.7}$$

which is related to the superconducting electron density. We save a discussion on the nature of these superconducting electrons and how the collision time τ vanishes for later and focus first on the response of a superconductor to a time-dependent field.

2.1.1. Two-fluid model

Consider that for a specific temperature T, a fraction of the total electrons, n, are in the superconducting state, n_s, while the remaining electrons are in the normal state, n_n. In this case, we can assume that two parallel channels carry the current in the conductor [8].

From the Drude approach in the previous section, the first channel, which consists of normal electrons with some average collision time τ_n, has an ohmic current response

$$\vec{J} = \frac{n_n e^2 \tau_n}{m} \vec{E} = \sigma_n \vec{E}. \tag{2.8}$$

The second channel of superconducting electrons ($\tau_s \to \infty$) has a current response

$$\frac{d\vec{J}}{dt} = \frac{n_s e^2}{m} \vec{E} \tag{2.9}$$

If we take a high-frequency field ($Ee^{i\omega t}$), as is relevant for a microwave resonator, we get the imaginary conductivity

$$\vec{J} = i\frac{n_s e^2}{m_e \omega} = i\sigma_s \vec{E}. \tag{2.10}$$

The combination of the two channels gives the complex conductivity

$$\sigma(\omega) = \sigma_n(\omega) - i\sigma_s(\omega), \tag{2.11}$$

with

$$\sigma_n(\omega) = \frac{n_n e^2 \tau_n}{m_e}, \tag{2.12}$$

$$\sigma_s(\omega) = \frac{n_s e^2}{m_e \omega}. \tag{2.13}$$

The two channels of Eqs. 2.12 and 2.13 describe two different responses to the AC field. The normal electrons in Eq. 2.12 dissipate energy by exchanging energy with the ion-lattice (Joule heating). The superconducting electrons of eq. 2.13 do not dissipate energy, but since the superconducting electrons have mass, they have a delayed response to a change in the electric field's direction. This means the current response lags to the voltage change ($\vec{E}$) over the inductor, which is an inductive behavior. Since this inductive behavior is associated with the momentum of the electrons, it is referred to as kinetic inductance. If we take the response of a uniform volume of superconducting electrons to an uniform electric field and equate the total kinetic energy of these electrons to an equivalent inductive energy

$$\frac{1}{2}(m_e v^2)(n_s l A) = \frac{1}{2} L_k I^2. \tag{2.14}$$

Given the current $I = J \cdot A = n_s e v A$ [9],

$$L_k = \left(\frac{m_e}{n_s e^2}\right)\left(\frac{l}{A}\right), \tag{2.15}$$

which is the kinetic inductance. Note that the kinetic inductance increases with decreasing n_s.

2.1.2. Surface impedance

The two channels in the two-fluid model give a surface impedance with a real part given by the dissipative behavior of the normal electrons, which gives rise to the sheet resistance R_s, and the inductive behavior from the superconducting electrons, which gives rise to the sheet kinetic inductance L_s,

$$Z_s = R_s + i\omega L_s. \tag{2.16}$$

For a superconducting film of arbitrary thickness d, the surface impedance is given by [10]

$$Z_s = \sqrt{\frac{i\mu_0\omega}{\sigma_1 - i\sigma_2}} \coth\left(d\sqrt{i\omega\mu_0\sigma}\right). \tag{2.17}$$

The term $\coth\left(d\sqrt{i\omega\mu_0\sigma}\right)$ accounts for films with a thickness comparable to or lesser than λ. For thick films ($d > \lambda$), this term is equal to unity, and the surface impedance is given by

$$Z_s = \sqrt{\frac{i\mu_0\omega}{\sigma_1 - i\sigma_2}}. \tag{2.18}$$

For thick films and low temperatures ($\sigma_2 \gg \sigma_1$), the surface resistance and kinetic inductance are given by

$$R_s = \sqrt{\frac{\mu_o\omega}{\sigma_2}}\frac{\sigma_1}{2\sigma_2} \qquad L_s = \sqrt{\frac{\mu_0}{\omega\sigma_2}} = \mu_0\lambda. \tag{2.19}$$

For thin films, where the electric field $\vec{E}$ is almost uniform across the film, and low temperatures ($\sigma_2 \gg \sigma_1$) [11]

$$Z_s = \frac{1}{(\sigma_1 - i\sigma_2)d}, \tag{2.20}$$

and,

$$R_s = \frac{\sigma_1}{{\sigma_2}^2}\frac{1}{d} \qquad L_s = \frac{1}{\omega\sigma_2}\frac{1}{d} = \mu_0\lambda_\perp. \tag{2.21}$$

Here we used

$$\lambda_\perp \approx \lambda^2/d = \frac{m_e}{\mu_0 n_s e^2}\frac{1}{d}, \tag{2.22}$$

which is the Pearl length [12], the penetration length relevant for thin superconducting strips. Together, Eqs. 2.21 and 2.22 yield the same result for the kinetic inductance as Eq. 2.15 since $L_k = L_s \cdot (l/w)$.

2.1.3. Microscopic description of superconductors and their conductivity

The theory of Bardeen, Cooper, and Schrieffer (BCS) gave a microscopic foundation for the existence of the "superconducting electrons" [13]: two electrons of opposite spin and momentum can pair up, forming a so-called Cooper pair if they experience an attractive force that overcomes the screened Coulomb repulsion[1]. The attractive force arises due to the movement of lattice ion cores, which are attracted to a passing electron, leaving a zone with a net positive charge in the wake of an electron. This zone can attract a second electron, creating an effective attraction between the two electrons.

All conduction electrons will form pairs as long as it is energetically favorable, so at T = 0 K, all free electrons will be paired into Cooper pairs. Cooper pairs are bosonic particles, for which the Pauli exclusion principle does not apply, so they condense into a single collective groundstate described by the macroscopic wavefunction [13]

$$\Psi = ||\Delta|| \exp(i\phi), \tag{2.23}$$

with Δ the energy gap and ϕ the phase.

At finite temperatures, there are excitations above the ground state, which are a mixture of electrons and holes. The superposition of an electron and a hole is described as single superconducting quasiparticle. The energy required to break a Cooper pair is 2Δ, and a broken Cooper pair creates two quasiparticles with a minimum energy $E \geq \Delta$ where Δ is the energy gap of the superconductor. The resulting quasiparticle density can be described by:

$$n_{qp} = 4N_0 \int_0^\infty N_s(E) f(E) dE \tag{2.24}$$

where $N_s(E)$ is the normalized quasiparticle density of states

$$N_s = \mathrm{Re}\left(\frac{E}{\sqrt{E^2 - \Delta^2}}\right) \tag{2.25}$$

and $f(E)$ is given by the Fermi-Dirac distribution

$$f(E) = \frac{1}{1 + \exp(E/k_B T)}. \tag{2.26}$$

If we consider low temperatures ($k_B T \ll \Delta$), the thermal quasiparticle density can be approximated by

---

[1] To adopt the formalism in the previous section for Cooper pairs, we would need to change $n_{cp} = \frac{1}{2} n_s$ and $m_{cp} = 2m_e$, since it takes two superconducting electrons to form one Cooper pair.

$$n_{qp} \approx 2N_0\sqrt{2\pi k_B T\Delta}e^{-\Delta/k_BT}. \tag{2.27}$$

Mattis-Bardeen theory

The two-fluid model allows us to describe the electron dynamics in a superconducting material. Mattis and Bardeen [14] derived expressions for σ_1 and σ_2 for a BCS superconductor:

$$\frac{\sigma_1}{\sigma_N} = \frac{2}{\hbar\omega}\int_{\Delta}^{\infty}[f(E)+f(E+\hbar\omega)]g_1(E)dE \tag{2.28}$$

$$+\frac{1}{\hbar\omega}\int_{min(\Delta-\hbar\omega,-\Delta)}^{-\Delta}\left[1-2f(E+\hbar\omega)\right]g_1(E)dE, \tag{2.29}$$

$$\frac{\sigma_2}{\sigma_N} = \frac{1}{\hbar\omega}\int_{max(\Delta-\hbar\omega,-\Delta)}^{-\Delta}\left[1-2f(E+\hbar\omega)\right]g_2(E)dE, \tag{2.30}$$

where

$$g_1(E) = \frac{E^2+\Delta^2+\hbar\omega E}{(E^2-\Delta^2)^{1/2}\left[(E+\hbar\omega)^2-\Delta^2\right]^{1/2}}, \tag{2.31}$$

$$g_2(E) = \frac{E^2+\Delta^2+\hbar\omega E}{(\Delta^2-E^2)^{1/2}\left[(E+\hbar\omega)^2-\Delta^2\right]^{1/2}}, \tag{2.32}$$

and $\sigma_N = 1/\rho_N$ is the normal state conductivity related to the total number of electrons in the system.

The first integral in Eq. 2.29 describes the conductivity due to a thermal quasiparticle population. The second integral of Eq. 2.29 describes the effect of breaking Cooper pairs by radiation absorption and is only relevant for $\hbar\omega > 2\Delta$.

For a thermal quasiparticle distribution and $k_BT, \hbar\omega < 2\Delta$, Eqs. 2.29 and 2.30 can be simplified to [11], [15]

$$\frac{\sigma_1}{\sigma_N} = \frac{4\Delta}{\hbar\omega}\exp(-\Delta/k_BT)\sinh\left(\frac{\hbar\omega}{2k_BT}\right)K_0\left(\frac{\hbar\omega}{2k_BT}\right), \tag{2.33}$$

$$\frac{\sigma_2}{\sigma_N} = \frac{\pi\Delta}{\hbar\omega}\left[1-2\exp(-\Delta/k_BT)\exp\left(\frac{-\hbar\omega}{2k_BT}\right)I_0\left(\frac{\hbar\omega}{2k_BT}\right)\right], \tag{2.34}$$

where K_0 and I_0 are the Bessel functions of the first and second kind, respectively. In Section 2.3, we will discuss the intentional breaking of Cooper pairs by absorbing radion with $\hbar\omega > 2\Delta$.

2.2. Superconducting Resonators

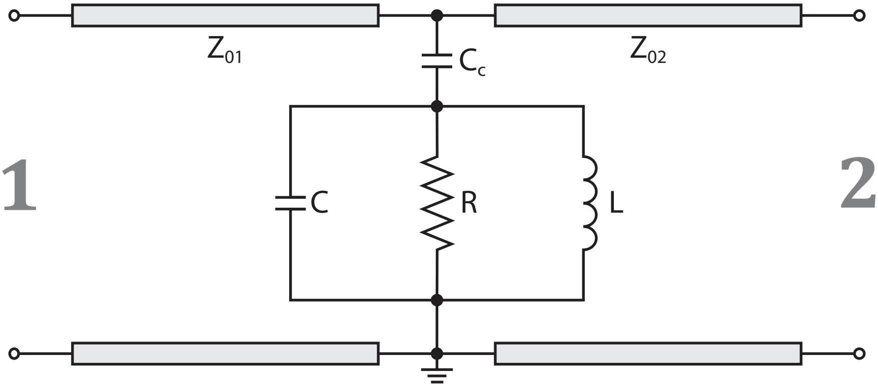

Figure 2.1: Circuit of an RLC-resonator capacitively coupled to a readout line through coupling capacitor C_c. The capacitor C and inductor L are considered to be lossless. Dissipation in the resonator is given by the resistance R. The readout line has characteristic impedances Z_{01} and Z_{02} towards ports 1 and 2, which can be complex. For a superconducting resonator, the resistance R and the kinetic inductance, which is part of the total inductance L [Eq. 2.39], are given by the superconductor's surface impedance [Eq. 2.17]. The resonance frequency is given by $\omega_r = 1/(\sqrt{C_t L})$ with $C_t = C + C_c$. This circuit diagram is a relatively accurate description of the resonator pictured in Fig. 2.2

To analyze the behavior of a superconducting resonator, we consider the RLC-resonator circuit in Fig. 2.1. This resonator is capacitively coupled to a readout line through coupling capacitor C_c. At the resonator's driven resonance frequency, f_r, the time-averaged stored magnetic energy W_m

$$W_m = \frac{1}{4} L |I_{\max}|^2, \tag{2.35}$$

is equal to the time-averaged stored electric energy (W_e)

$$W_e = \frac{1}{4} C_t |V_{\max}|^2, \tag{2.36}$$

with $C_t = C + C_c$ the total capacitance of the circuit. For this condition to be met, the total reactance of the resonator has to be zero,

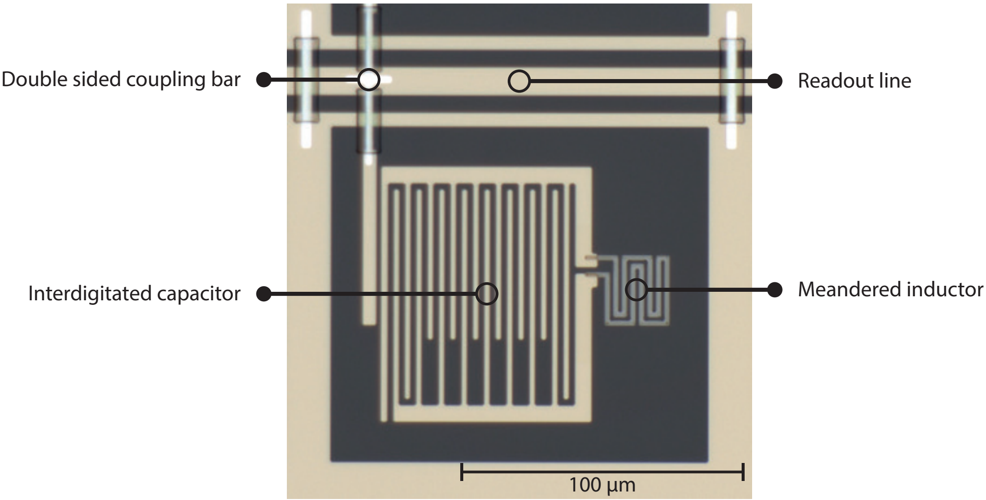

Figure 2.2: Microscope image of a superconducting lumped element resonator. The pictured resonator matches the circuit in Fig. 2.1: The capacitance C is realized by a NbTiN interdigitated capacitor (IDC) consisting of several interlocked lines. The inductance is mainly due to the high sheet kinetic inductance of the β-Ta paired meander, such that α_k is close to one (Eq. 2.39). The thick bar alongside each IDC that connects directly to the coplanar waveguide (CPW) readout line realizes the coupling capacitor C_c. The lines of both the inductor and the IDC are 2-µm wide.

$$\omega L = \frac{1}{\omega C_t}, \tag{2.37}$$

which is true for

$$\omega_r = \frac{1}{\sqrt{LC_t}}, \tag{2.38}$$

with ω_r the resonance frequency of the circuit. We typically use weakly coupled resonators for which $C_c \ll C$ so the resonance frequency can be approximated by the unloaded resonance frequency $\omega_r \approx 1/\sqrt{LC}$.

For a superconducting resonator, the loss in the resonator is given by the superconducting film's sheet resistance R_s (Eq. 2.19). The total inductance of the resonator, L, consists of the resonator's geometrical inductance plus the kinetic inductance of the line L_k (Eq. 2.19)

$$L = L_g + L_k = \alpha^{-1} L_k, \tag{2.39}$$

where $\alpha = L_k/L$ is the kinetic inductance fraction.

In this thesis, we will mainly discuss planar lumped element LC-resonators. An optical micrograph of such a resonator is given in Fig. 2.2. The inductance (L) and capacitance (C) of the circuit in Fig. 2.1 are realized by a meandering inductor and an interdigitated capacitor (IDC), respectively. The total kinetic inductance of the meandering strip of Fig. 2.1 is given by

$$L_k = L_k/\square \left(\frac{l}{w}\right) \tag{2.40}$$

with $L_k/\square$ the sheet kinetic inductance (per square) of the superconductor, l the length of the strip, and w the width of the strip.

The resonator is externally driven through the coplanar waveguide (CPW) readout line via the coupling bar that capacitively couples to the IDC of the resonator. If the external probe's frequency matches the circuit's resonance frequency (Eq. 2.38), the resonator stores energy, which is dissipated in R_s or leaks back out of the resonator to the readout lines through the coupling capacitor C_c.

2.2.1. Q-factors

The quality factor of the resonator is defined as

$$Q = \omega_r \frac{\text{energy stored}}{\text{power lost}} \tag{2.41}$$

The time-averaged energy stored in the resonator is

$$W = W_e + W_m \tag{2.42}$$

and time-averaged power dissipated in the resonator is

$$P_{diss} = \frac{1}{2}|V_{max}|^2/R. \tag{2.43}$$

Combined, we find the intrinsic quality factor

$$Q_i = \omega_r C_t R = \frac{R}{\omega_r L}, \tag{2.44}$$

which describes the power dissipated in the resonator by the normal electrons in the superconducting film. In Section 2.5.1, we will see that the capacitor C, which in Fig. 2.1 is assumed to be lossless, will be lossy, introducing an extra loss channel. For example, the resonators in Chapter 7 have a Q_i dominated by the microwave loss in the dielectric.

The power lost from the resonator to the readout line is given by

$$Q_c = \omega_r C_t R_{out}, \tag{2.45}$$

where R_{out} is the resistance seen by the resonator through the coupling capacitor

$$R_{out} = \frac{2}{Z_0(\omega_r C_c)^2}, \tag{2.46}$$

with Z_0 the characteristic impedance of the readout lines.

Using the Norton/Thevenin equivalent circuits, one can show that the circuit's total resistance is the parallel combination of R and R_{out} [16]. The total, or loaded, Q-factor of the circuit is then given by

$$Q_l = \omega_r (C_t) R_{//}. \tag{2.47}$$

Since $1/R_{//} = 1/R + 1/R_{out}$,

$$\frac{1}{Q_l} = \frac{1}{Q_c} + \frac{1}{Q_i}. \tag{2.48}$$

2.2.2. Input impedance

The impedance seen from the readout line in Fig. 2.2 is

$$Z_{in} = Z_{\mathrm{KID}} + Z_c, \tag{2.49}$$

with Z_{KID} the complex impedance of the resonator circuit and Z_c the impedance of the capacitive coupler. The impedance of the resonator is

$$Z_{\mathrm{KID}} = \left(\frac{1}{R} + \frac{1}{j\omega L} + i\omega C\right)^{-1} \tag{2.50}$$

which we can write for small deviations, $\delta\omega$, from the resonance frequency ω_r as

$$\frac{1}{Z_{\mathrm{KID}}} = \frac{1}{R} + \frac{1}{i(\omega_r + \delta\omega)L} + i(\omega_r + \delta\omega)C. \tag{2.51}$$

This can be rearranged,

$$\frac{1}{Z_{\mathrm{KID}}} = \frac{1}{R} + \frac{1}{i\omega_r L}\frac{1}{(1 + \delta\omega/\omega_r)} + i(\omega_r + \delta\omega)C, \tag{2.52}$$

and rewritten as

$$\frac{1}{Z_{\mathrm{KID}}} = \frac{1}{R} + 2i\delta\omega C. \tag{2.53}$$

Here we used $\omega_r^2 = 1/LC$. This yields

$$Z_{\text{KID}} = \frac{R}{1 + 2i\delta\omega RC} \tag{2.54}$$

in which we can recognize $Q_i = \omega_r RC$, so that we can rewrite

$$Z_{\text{KID}} = \frac{R}{1 + 2iQ_i x} \tag{2.55}$$

with the fractional frequency detuning

$$x = \frac{\omega - \omega_r}{\omega_r} = \frac{\delta\omega}{\omega_r}. \tag{2.56}$$

2.2.3. Scattering parameters

The scattering parameters (S-parameters) give the ratio between the in- and outgoing voltage waves at the two ports in Fig. 2.1. Transmission from port 1 to port 2 is then given by $S_{21} = V_2^-/V_1^+$, with V_1^+ the incident wave at port 1, and V_2^- the outgoing wave at port 2. The S-parameters are complex, as in Fig. 2.3, reflecting a change in amplitude and phase between ports 1 and 2. Off-resonance, the resonator is seen as an open in the readout line ($|Z_{\text{KID}}| \to \infty$), so there is full transmission from port 1 to port 2, $|S_{21}|^2 = 1$.

The full, frequency-dependent, S-parameters of the circuit in Fig. 2.1 can be obtained by using the ABCD matrix for a shunt impedance,

$$\begin{bmatrix} A & B \\ C & D \end{bmatrix} = \begin{bmatrix} 1 & 0 \\ Y_{shunt} & 1 \end{bmatrix}, \tag{2.57}$$

with the shunt impedance given by the resonator circuit

$$Y_{shunt} = Z_{in}^{-1} = (i\omega C_c + Z_{KID})^{-1}. \tag{2.58}$$

If the characteristic impedances of the readout lines are real and equal ($Z_{01} = Z_{02} = Z_0$) on both sides, the complex transmission coefficient S_{21} is given by [17]

$$S_{21} = \frac{2Z_0}{AZ_0 + B + CZ_0^2 + DZ_0} \tag{2.59}$$

For the circuit of Fig. 2.1 and Eq. 2.58,

$$S_{21} = \frac{2Z_{in}}{2Z_{in} + Z_0} \tag{2.60}$$

with Z_0 the characteristic impedance of the readout line. More complex situations, where the characteristic impedance is complex or not equal on both sides of the resonator, can be treated with the conversion charts in [17].

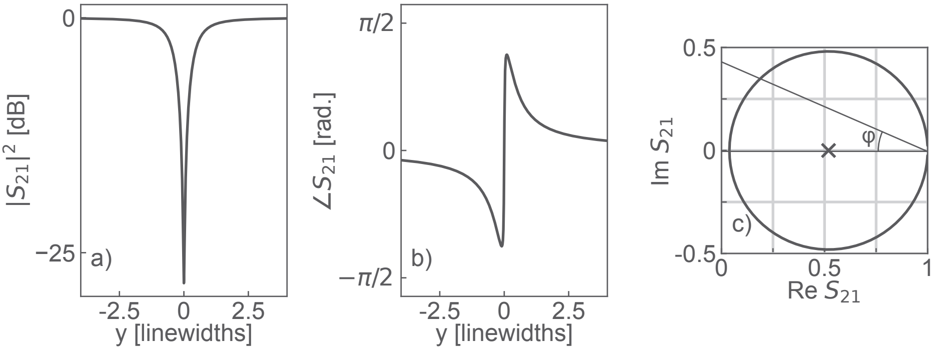

Figure 2.3: Complex scattering parameter S_{21} as a function of frequency in terms of linewidths $y = xQ_l$, where $x = (\omega - \omega_r)/\omega_r$. **a)** Power transmitted from port 1 to port 2, $|S_{21}|^2$, see Fig. 2.1. **b)** Phase difference incurred by the wave between ports 1 and 2 due to the resonator, see Fig. 2.1. **c)** Combined, the frequency-dependent magnitude and angle of the complex transmission S_{21} trace a circle in the complex plane. Off resonance, the circle approaches $\mathrm{Re(S_{21})} = 1$. On resonance $\mathrm{Re(S_{21})} = \mathrm{S_{21,min}} = \mathrm{Q_l/Q_i}$. For an asymmetric resonance dips [18], see Eq. 2.64, the resonance circle will be rotated by an angle ϕ with respect to the off-resonance point. In addition, the resonance circle grows with a factor $1/\cos(\phi)$.

For the admittance in Eq. 2.58, there exists an analytical form that describes the Lorentzian, symmetric, resonance dip in S_{21} in terms of the Q-factors and the fractional frequency detuning [16]

$$S_{21} \approx 1 - \frac{Q_l/Q_c}{1 + 2iQ_l x}, \tag{2.61}$$

Another commonly seen form is

$$S_{21} \approx \frac{Q_l/Q_i + 2iQ_l x}{1 + 2iQ_l x}. \tag{2.62}$$

On resonance $x = \delta\omega/\omega_r = 0$ and $|S_{21,min}| = Q_l/Q_i$. In Fig. 2.3a) the resonance dip of Eq. 2.61 and Eq. 2.62 is plotted against frequency.

The complex transmission $S_{21}(\omega)$ traces the circle in Fig. 2.3c (clockwise with increasing frequency) in the complex plane with diameter $1 - |S_{21,min}|$. The center of the resonance circle is

$$r_c = \frac{1 + |S_{21,min}|}{2} = \frac{1 - Q_l/Q_i}{2}. \tag{2.63}$$

Assymetric dips

In Ref. [18], the authors expand the circuit of Fig. 2.1 to include both capacitive and inductive coupling and mismatched readout lines. Due to the mismatched readout lines, the resonance circle is rotated by an angle ϕ, with respect to the horizontal axis and the off-resonance point, see Fig. 2.3, and grows by $1/\cos(\phi)$, creating an asymmetric resonance dip. The asymmetry is captured by introducing the complex coupling quality factor ($\hat{Q}_e = |Q_e|e^{i\phi}$) and the factor $(1+\hat{\epsilon})$ in Eq. 2.61 [18]

$$S_{21} \approx (1+\hat{\epsilon})\left(1 - \frac{Q_l/\hat{Q}_e}{1+2iQ_l x}\right). \tag{2.64}$$

Here $|Q_e| = Q_c$ as in Section 2.2.1 and in Eq. 2.61.

2.2.4. Internal power

From the scattering parameters, we get $|S_{11}|^2$ as the fraction of power reflected at port 1 and $|S_{21}|^2$ as the fraction of the power transmitted to port 2. If we take P_{read} as the power incident on port 1 in Fig. 2.1, the power dissipated in the KID is

$$P_{diss} = P_{read}\left(1 - |S_{11}|^2 - |S_{21}|^2\right). \tag{2.65}$$

For a shunt impedance, as in Fig. 2.1, $S_{11} = S_{21} - 1$, and substituting Eq. 2.61 in Eq. 2.65 yields the result [19]

$$P_{diss} = P_{read}\left(\frac{2Q_l^2}{Q_c Q_i}\frac{1}{1+4Q_l^2 x^2}\right). \tag{2.66}$$

Using the definition of Q_i from 2.41 and 2.44, which relates the dissipated power to the total microwave energy stored in the resonator

$$Q_i = \omega_r \frac{E_{res}}{P_{diss}} \tag{2.67}$$

we find

$$E_{res} = \frac{2Q_l^2}{Q_c}\frac{1}{1+4Q_l^2 x^2}\frac{P_{read}}{\omega_r}, \tag{2.68}$$

which at resonance ($x = 0$) reduces to

$$E_{res} = \frac{2\pi P_{int}}{\omega_r} = \frac{2Q_l^2}{Q_c}\frac{P_{read}}{\omega_r}, \tag{2.69}$$

with P_{int}, the internal power of the resonator at resonance. The stored microwave energy is typically translated to an average number of microwave photons

$$\langle n\rangle = \frac{E_{res}}{\hbar\omega_r} = \frac{2Q_l^2}{Q_c}\frac{P_{read}}{\hbar\omega_r^2}. \tag{2.70}$$

2.2.5. Magnetic and electric energy

At a certain moment in time, the total energy in the resonator is stored in the magnetic field, at which the current in the inductor wires is maximum[2]

$$E_m = \frac{1}{2}LI_{max}^2 = \frac{1}{2}\frac{L_k}{\alpha_k}I_{max}^2. \tag{2.71}$$

If we assume that $Q_l = Q_c$, the energy stored for a certain read-power is given by Eq. 2.69

$$E = \frac{2Q_c}{\omega_r}P_{read}. \tag{2.72}$$

The maximum current density flowing through the inductor, given the power on the readout line, is then

$$J_{max} = \frac{2}{wd}\sqrt{\frac{\alpha_k Q_c}{\omega_r L_{k,s}}\frac{w}{l}P_{read}}. \tag{2.73}$$

where the total kinetic inductance is expressed as the sheet kinetic inductance times the number of squares in the inductor (Eq. 2.40) and wd is the cross-sectional area of the inductor wire.

In a similar way, the electric energy stored in the resonator

$$E_e = \frac{1}{2}CV_{max}^2 = \frac{1}{2}VQ, \tag{2.74}$$

with Q the electric charge. The maximum voltage in the capacitor is then

$$V_{max} = 2\sqrt{\frac{Q_c}{\omega_r C}P_{read}}, \tag{2.75}$$

and since $V = Q/C$, the electric charge in the capacitor is

$$Q_{max} = 2\sqrt{C\frac{2Q_c}{\omega_r}P_{read}}. \tag{2.76}$$

---

[2] In Eq. 2.35 we used the average stored energy instead of the maximum stored energy in time, $I_{\mathrm{RMS}} = I_{max}/\sqrt{2}$

In Chapter 7 we use Eq. 2.76 to calculate the electric field in a parallel plate capacitor for which $C = (\varepsilon A)/d$ and the electric field is given by Gauss' law $\vec{E} = q/\varepsilon$, with q the plate charge density (Q/A).

2.3. Pair breaking detectors

Cooper pairs can intentionally be broken into quasiparticles by exposing the superconducting film to a photon flux with sufficient energy to break Cooper pairs $(hc_0)/\lambda \geq 2\Delta$, with c_0 the speed of light in vacuum and λ the photon's wavelength. The change in Cooper pair and quasiparticle density (n_{qp}) changes the complex conductivity of the film [20]. From Eqs. 2.27, 2.33, and 2.34

$$\frac{d\sigma_1}{dn_{qp}} \approx \sigma_N \sqrt{\frac{2\Delta_0}{\pi k_B T}} \sinh\left(\frac{\hbar\omega}{2k_B T}\right) K_0\left(\frac{\hbar\omega}{2k_B T}\right), \tag{2.77}$$

$$\frac{d\sigma_2}{dn_{qp}} \approx \sigma_N \frac{-\pi}{2N_0\hbar\omega}\left[1 + \sqrt{\frac{2\Delta_0}{\pi k_B T}} \exp\left(\frac{-\hbar\omega}{2k_B T}\right) I_0\left(\frac{\hbar\omega}{2k_B T}\right)\right]. \tag{2.78}$$

2.3.1. Resonator response

From Eq. 2.19 we know that the surface impedance of the superconducting film responds to a change in conductivity,

$$\frac{\delta L_s}{L_s} = -\frac{\delta\sigma_2}{\sigma_2} \qquad \frac{\delta R_s}{L_s} = \frac{\delta\sigma_1}{\sigma_2}, \tag{2.79}$$

with $|\sigma| \approx \sigma_2$ for $T \ll T_c$. Since $\omega_r = 1/\sqrt{LC}$, the new resonance frequency is

$$\omega_r' = \frac{1}{\sqrt{(L+\delta L)C}}. \tag{2.80}$$

For small changes in L,

$$\omega_r' = \omega_r - \frac{1}{2}\omega_r\frac{\delta L}{L}, \tag{2.81}$$

$$\frac{\omega_r' - \omega_r}{\omega_r} = -\frac{1}{2}\frac{\delta L}{L}. \tag{2.82}$$

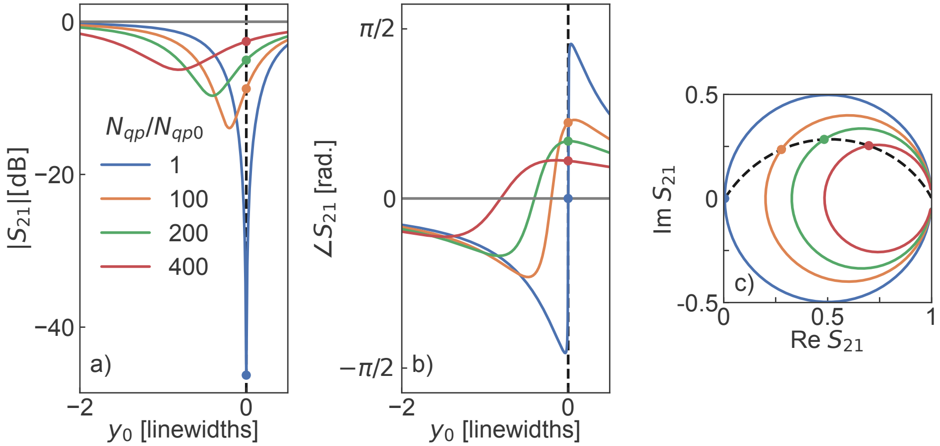

Figure 2.4: Change in S_{21} due to a change in quasiparticle density. **q)** The resonance frequency decreases (Eq. 2.86) and Q_i drops (Eq. 2.87) as the quasiparticle density increases. **b)** Change in the phase angle of S_{21} due to a change in quasiparticle density. **c)** KID response in the resonance circle. We measure the response as the change in S_{21} with respect to the resonance frequency of the KID, represented by the markers on the black dashed line in all three plots.

Since L is given by the combination of the film's kinetic inductance and the resonator's geometric inductance (Eq. 2.39), the latter of which does not respond to a change in quasiparticle density,

$$x' = \frac{\omega_r' - \omega_r}{\omega_r} = -\frac{1}{2}\frac{\delta L_k}{(L_k + L_g)}. \tag{2.83}$$

Substituting Eq. 2.17 gives

$$x' = -\frac{\alpha_k}{2}\frac{\delta L_k}{L_k} = \frac{\alpha\beta}{4}\frac{\delta\sigma_2}{\sigma_2}, \tag{2.84}$$

with $\beta = 1 + \frac{2d/\lambda}{\sinh(2d/\lambda)}$. In Section 2.1.1 we saw that $L_k \propto n_s^{-1}$, so L_k increases when cooper pairs are broken which means that $\omega_r' < \omega_r$.

Similarly, we can find the change in Q_i due to a change in surface resistance,

$$\delta {Q_i}^{-1} = \frac{\delta R}{\omega(L_k + L_g)} = \frac{\alpha\beta}{2}\left(\frac{\delta\sigma_1}{\sigma_2} - \frac{\sigma_1}{\sigma_2^2}\delta\sigma_2\right). \tag{2.85}$$

So, upon a change in quasiparticle density (n_{qp}) the resonator shifts to a lower frequency (Fig. 2.4a)

$$\frac{x'}{dN_{qp}} = \frac{\alpha_k \beta}{4|\sigma| V} \frac{d\sigma_2}{dn_{qp}}, \tag{2.86}$$

and the internal losses in the resonator increase,

$$\frac{d{Q_i}^{-1}}{dN_{qp}} = \frac{\alpha_k \beta}{2|\sigma| V} \frac{\delta\sigma_1}{dn_{qp}}, \tag{2.87}$$

where we used $\sigma_2 \gg \sigma_1$ and $N_{qp} = n_{qp} V$.

Fig. 2.4 shows the resonator's response upon a change in quasiparticle number (Eqs. 2.86 and 2.87) in three different representations. We generate a model resonator based on a thermal quasiparticle distribution ($N_{qp}(T)$) and Eq. 2.61 and plot the complex S_{21} in Fig. Fig. 2.4. We then introduce a number of excess quasiparticles and see, in Fig.2.4a, that the resonator shifts to lower frequencies (Eq. 2.86) and that the dip depth decreases since the losses increase (Eq. 2.87). The second panel, Fig. 2.4b, shows the same response but in S_{21} phase. Combined, panels a and b result in the KID circle representation of Fig. 2.4c, where each point on the circle is described by the magnitude (Fig. 2.4a) and angle (Fig. 2.4b) of $S_{21}(\omega)$.

2.3.2. Observables

The change in the complex scattering parameter S_{21} upon a change in quasiparticle number is summarized in Fig. 2.4, from which it is clear that we can measure a change in quasiparticle density by observing changes in $S_{21}(\omega)$. However, the frequency sweep required to obtain S_{21} as a function of frequency is time-intensive. When reading out a real detector, this will make it impossible to read out fast phenomena such as the single photon pulses we want to detect. Instead, we use a homo-dyne readout scheme to measure changes in transmission with a continuous signal at the resonance frequency $S_{21}(\omega = \omega_r)$. The two components from the demodulation mixer, in-phase (I) and quadrature (Q) are the real and imaginary parts of S_{21}, respectively; see the dots on the black dashed line Fig. 2.4. The readout scheme is discussed in more detail in Chapter 3.

The measured IQ-data is typically transformed into a polar coordinate system since each point in the complex S_{21} plane can be described by an amplitude and angle (phase) with respect to the center of the resonance circle (Eq. 2.63) as illustrated by the polar grid in Fig. 2.5a. This polar amplitude and phase coordinate system is linear for small changes in S_{21} but saturates for higher responses and becomes non-monotonous in the case of amplitude, as shown in Fig. 2.5c and Ref. [21].

To calculate the amplitude and phase response with respect to the circle, we use the radius of the circle $r_c = (1 + S_{21,min})/2$ so the center of the circle lies at $1 - r_c = Q/2Q_c$. The amplitude with respect to the center of the circle is then

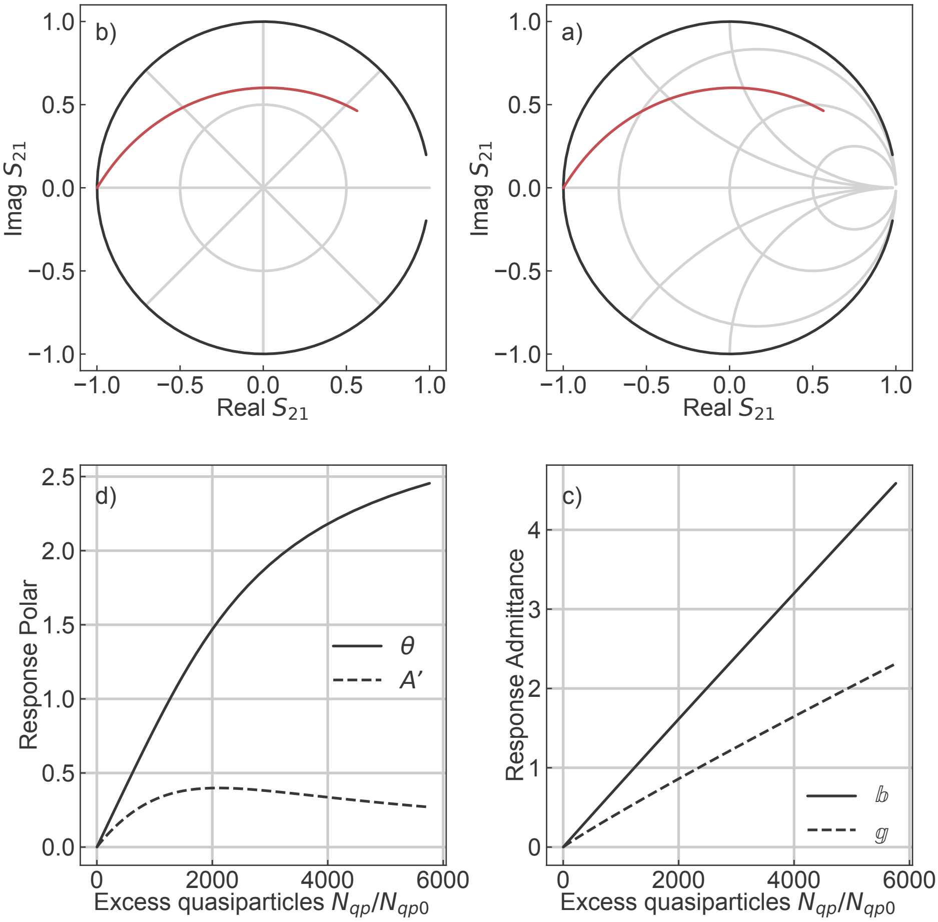

Figure 2.5: **Top)** KID IQ-response to a change in quasiparticle density (red) plotted in the resonance circle (black) for both admittance and polar coordinate systems. **Bottom)** KID response for both coordinates each coordinate system. **Left column)** KID response in the polar coordinates of Eqs. 2.93 (amplitude A') and 2.94 (phase θ). The amplitude and phase response is linear for small changes in N_{qp} but saturate at higher excess N_{qp}. The amplitude response becomes non-monotonous for larger excess N_{qp}. **Right column)** KID response in the admittance coordinates of eqs. 2.98 and Eq. 2.99. The inward circles are a change in the real part $\mathbb{g}$ (increase in R), while the arcs are a change in $\mathbb{b}$, where the top half is reserved for positive sign (increase in inductance). The response with excess N_{qp} is linear in both coordinates ($\mathbb{g}$, $\mathbb{b}$).

$$A = \frac{\sqrt{(\mathrm{Re}(S_{21}) - r_c)^2 + \mathrm{Im}(S_{21})^2}}{1 - r_c}, \tag{2.88}$$

and the phase is given by the clockwise angle inclined from the real axis $[0, \pi]$

$$\tan(\theta) = \frac{\mathrm{Im}(S_{21})}{r_c - \mathrm{Re}(S_{21})}. \tag{2.89}$$

Equation 2.62 gives us the real and imaginary part of S_{21}

$$\mathrm{Re}(S_{21}) = \frac{S_{21}^{min} + 4Q_l^2 x^2}{1 + 4Q_l^2 x^2} \approx \frac{Q_l}{Q_i}, \tag{2.90}$$

$$\mathrm{Im}(S_{21}) = \frac{2Q_l x(1 - S_{21,min})}{1 + 4Q_l^2 x^2} \approx 2Q_l x(1 - S_{21}^{min}) \tag{2.91}$$

where the approximation is based on the first order in x. For small changes in Q_i

$$\delta\mathrm{Re}(S_{21}) = -\frac{Q_c Q_i}{(Q_c + Q_i)^2}\frac{\delta Q_i}{Q_i}. \tag{2.92}$$

which yields

$$A' = -\frac{\delta\mathrm{Re}(S_{21})}{1 - r_c} = \frac{2Q}{Q_i}\frac{\delta Q_i}{Q_i} \tag{2.93}$$

$$\theta = \frac{\mathrm{Im(S_{21})}}{r_c - \mathrm{Re(S_{21})}} = -4Q\frac{\delta\omega}{\omega_r}. \tag{2.94}$$

Here, we used $A' = 1 - A$ as the decrease in amplitude with respect to the maximum amplitude at resonance.

From Eqs. 2.85 and 2.84 we get

$$A' = -\alpha_k \beta Q \frac{\delta\sigma_1}{\sigma_2} \qquad \theta = -\alpha_k \beta Q \frac{\delta\sigma_2}{\sigma_2} \tag{2.95}$$

from which the response to a change in the number of quasiparticles can be derived

$$\frac{dA'}{dN_{qp}} = -\frac{\alpha_k \beta Q_l}{|\sigma| V}\frac{d\sigma_1}{dn_{qp}} \qquad \frac{d\theta}{dN_{qp}} = -\frac{\alpha_k \beta Q_l}{|\sigma| V}\frac{d\sigma_2}{dn_{qp}} \tag{2.96}$$

where $|\sigma| \approx \sigma_2$ for $T \ll T_c$ and we assume that the resonator is under-coupled ($Q_l \approx Q_c$) such that the loaded Q-factor does not change upon a change in quasiparticle density.

Alternatively, in Eq. 2.60, we can recognize the Möbius projection, familiar from Smith chart analysis [22], where the frequency-dependent input reflection from short or open-ended transmission line is mapped as a circle in the complex reflection coefficient (S_{11}). In this case, Eq. 2.60 projects the complex shunt admittance of Eq. 2.58 onto the circles in the complex transmission coordinates we see in Fig. 2.3 and Fig. 2.4, on the Smith chart like grid of Fig. 2.5b. Since the input admittance of the KID (Eq. 2.58) is directly related to the complex conductivity, the projection

$$S_{21} = I + iQ = \frac{2}{2 + \mathbb{y}} \tag{2.97}$$

gives us a linear response coordinate system. Here $\mathbb{y} = \mathbb{z}^{-1} = Z_0/Z_{in}$ the normalized input admittance (2.58) with respect to the characteristic impedance of the readout line. The admittance can then be extracted from the measured $S_{21} = I + iQ$ data as

$$\mathbb{y} = \frac{2 - 2S_{21}}{S_{21}} \tag{2.98}$$

the two readout coordinates are then the normalized conductance ($\mathbb{g}$) and susceptance ($\mathbb{b}$),

$$\mathbb{y} = \mathbb{g} + i\mathbb{b}, \tag{2.99}$$

which are both linear and monotonous with a change in quasiparticle density as highlighted by Fig. 2.5d.

2.4. Single-photon response

In the optical to near-IR, a single photon has enough energy to create a few thousand excess quasiparticles since $E_{ph} \gg 2\Delta$, sparking a pulse in the KID response. The pulse height depends on the number of generated quasiparticles, see Fig. 2.5, which in turn depends directly on the energy of the absorbed photon, giving a KID intrinsic energy resolving capabilities for optical to near-IR photons.

2.4.1. Photon absorption

The interaction between an electromagnetic wave and a medium can be described if we introduce the complex dielectric function[3]

---

[3] The sign of the imaginary part depends on the convention used for the time dependence of a propagating wave: $\exp(-i\omega t)$ for which the sign is negative, popular with physicists, or $\exp(i\omega t)$

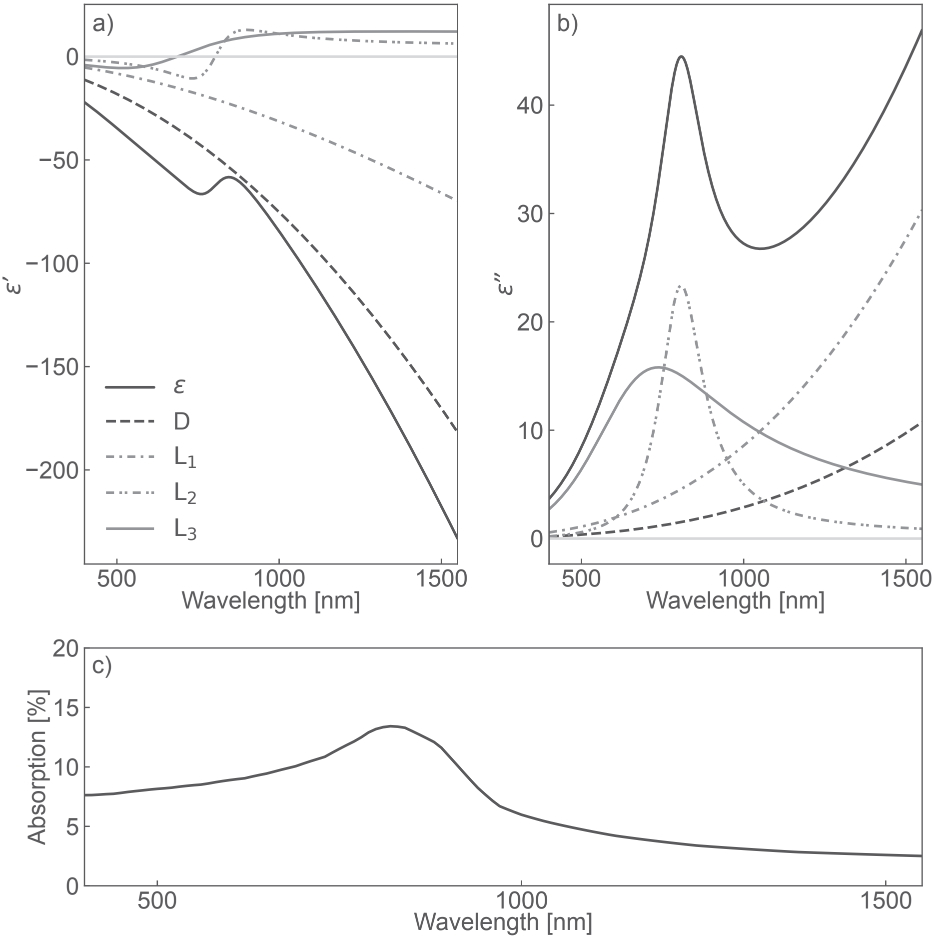

Figure 2.6: Complex dielectric function derived from the complex conductivity of aluminum based on the Drude response and the sum of three Lorentz oscillators (Eq. 2.107). Values for Eq. 2.107 for the Drude term and the Lorentz oscillators of aluminum are available in Ref. [23] or in the Matlab function of Ref. [24]. Panel **a)** and **b)** are the real and imaginary parts, respectively. **c)** Absorption in a 100-nm thick Al film. The peak in both ε' and ε'' around 800 nm is responsible for an absorption peak common for aluminum mirrors, which is visible in the commercial mirrors used for the QE-setup in Fig. 3.7a. The complex dielectric function of a metal can be retrieved with spectroscopic ellipsometry measurements; see Chapter 5.

$$\varepsilon(\omega) = \varepsilon'(\omega) + i\varepsilon''(\omega) \tag{2.100}$$

which relates to the complex refractive index ($\tilde{n} = n + ik$) as

$$n(\omega) = \sqrt{\frac{|\varepsilon(\omega)| + \varepsilon(\omega)}{2}} \qquad k(\omega) = \sqrt{\frac{|\varepsilon(\omega)| - \varepsilon(\omega)}{2}}. \tag{2.101}$$

Here, n is the refractive index, which indicates a decrease in the phase velocity of a wave propagating through a medium, and k is the optical extinction coefficient, which corresponds to absorption in the medium.

For a metal with complex conductivity, $\tilde{\sigma}$,

$$\varepsilon(\omega) = 1 + i\frac{\tilde{\sigma}(\omega)}{\epsilon_0 \omega}. \tag{2.102}$$

We can define two contributions to $\tilde{\sigma}(\omega)$, which are plotted in Fig. 2.6 for aluminum [23], [24]. The first comes from the Drude free electron model as discussed in Section 2.1. The incident field can excite the free electrons to a higher energy within a band (intraband-transitions), which are relaxed by collisions with the ion lattice over an average time τ, as discussed in Section 2.1. This gives rise to the complex, frequency-dependent Drude contribution

$$\sigma_D(\omega) = \frac{\sigma_0}{1 - i\omega\tau} \tag{2.103}$$

with σ_0 the DC conductivity of Eq. 2.1. Substituting Eq. 2.103 in Eq. 2.102 we get the dielectric function

$$\frac{\varepsilon(\omega)}{\varepsilon_0} = 1 - \frac{ne^2}{\varepsilon_0 m}\frac{1}{\omega^2 - i\Gamma_D\omega} \tag{2.104}$$

with $\Gamma_D = 1/\tau$. Here n is the conduction electron density, e is the charge of an electron, and m is the mass of an electron as in Section 2.1.

At the plasma frequency

$$\omega_p = \sqrt{\frac{ne^2}{m\epsilon_0}} \tag{2.105}$$

the real part of the dielectric function in Eq. 2.104 crosses zero. Below ω_p, the real part of $\varepsilon(\omega)$ tends to $-\infty$, and the medium is opaque; see the Drude contribution in Fig. 2.6a). Above ω_p, which lies in the ultraviolet (UV) for most metals, the metal acts as an insulator and is transparent.

---

for which the sign is positive, popular among electrical engineers. In both conventions $\varepsilon'' \geq 0$.

The second contribution is from bound electrons that can be excited from one band to another (interband transitions). The bound-electrons are modeled as Lorentz oscillators, and their contribution to the dielectric function is found by introducing a Hooke's law restoring force ($m\omega_0^2 r$) in Eq. 2.104

$$\frac{\varepsilon(\omega)}{\varepsilon_0} = 1 + \frac{ne^2}{\varepsilon_0 m} \frac{1}{(\omega_0^2 - \omega^2) + i\gamma\omega} \tag{2.106}$$

with γ the damping of the bound electron. A real solid contains multiple possible interband transitions, each modeled by a separate Lorentzian oscillator, such that the dielectric function of a metal can be described by

$$\frac{\varepsilon(\omega)}{\epsilon_0} = \varepsilon_\infty - \frac{\omega_p^2}{\omega^2 - i\Gamma_D\omega} + \sum_{j=1}^{n} \frac{f_j \cdot \omega_{oj}^2}{\omega_{oj}^2 - \omega^2 + i\gamma_j\omega} \tag{2.107}$$

where ε_∞ is a background constant (> 1) due to transitions that are not taken into account by the Drude-Lorentz model. The dielectric function is thus given by the Drude term located at the plasma energy ω_p, and a sum of Lorentz oscillators located at energy positions ω_{oj} with strength f_j and dampening γ_j. Fig. 2.6 gives the Drude term and three Lorentz oscillators for aluminum, with values for Eq. 2.107 taken from Refs. [23], [24].

For highly resistive disordered superconductors, the plasma frequency typically lies around the visible-to-UV transition [25]. The Drude term at optical wavelengths is then close to zero, and the Lorentz oscillators effectively screen the plasma frequency (Eq. 2.107), such that the transition from a negative to positive sign of ε' happens somewhere in the optical to near-infrared wavelength regime. For most of the optical and near-infrared range, absorption in the metal is dominated by interband transitions [25], see Fig. 2.6b.

A superconductor commonly used for sub-millimeter and far-infrared KIDs is aluminum [26]. In the visible wavelength range, where we rely on direct absorption in the superconductor, the bare aluminum layer of Fig. 2.6c absorbs at most 15% of the incoming radiation, the rest being reflected. Disordered superconductors, such as TiN and β-Ta, which are more resistive, absorb more of the incoming radiation, with ~50% absorption at 400 nm in Fig. 5.1.

We can enhance the absorption in the disordered superconductor by embedding it in a stack that consists of an aluminum backing reflector and a dielectric anti-reflection layer. In Chapter 5, we discuss the optical stack design in detail and show that we can increase the absorption efficiency of KIDs over a wide bandwidth. In Chapter 6, we focus on the measurements of the absorption efficiency.

2.4.2. Single photon pulse shapes

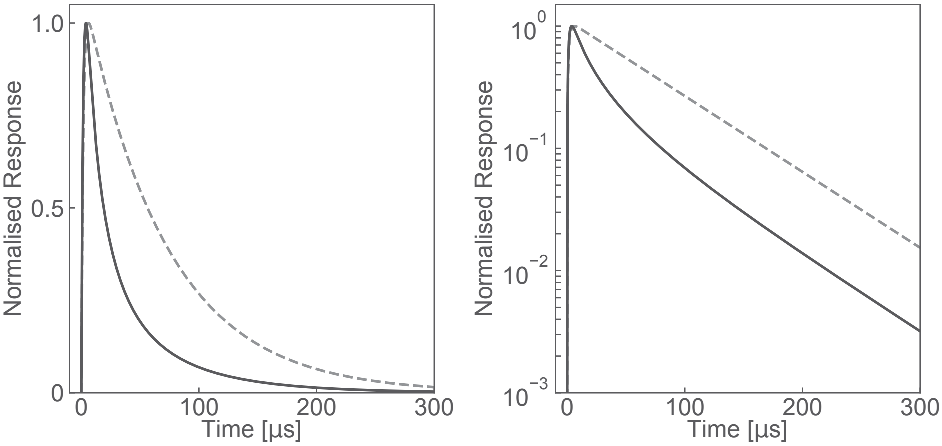

Figure 2.7: Normalised photon pulse shapes in linear and logarithmic scales for the two cases of Eq. 2.111. In the first case (solid) the excess number of quasiparticles ($\delta N_{qp}(t=0)$) is large compared to the equilibrium number of quasiparticles (N_{qp}^0) and the pulse has an initial $1/t$ decay before it settles to an exponential decay ($\exp\left(-t/\tau_{qp}^*\right)$). In the second case (dashed) $N_{qp}^0/\delta N_{qp}(0) \gg 1$, the pulse has a single exponential decay. The exponential pulse rise time depends on the resonator ring time of Eq. 2.109. Plotted pulse shapes are the convolution between the exponential rise time and the decay from Eq. 2.111 using a τ_{res} of 7 µs and a τ_{qp}^* of 70 µs. For the fast pulse $\delta N_{qp}(t=0)/N_{qp}^0 = 10$.

An absorbed photon with $E \gg 2\Delta$ releases its energy as a fast photoelectron [27], [28]. This initial, large energy excitation is down-converted to quasiparticles at the superconducting gap with energy $[\Delta, 2\Delta]$ and a set of phonons with energies below 2Δ. In the first stage, the downconversion is dominated by electron-electron interactions and ends in strongly interacting electrons and holes. The second stage, which happens below the Debye energy, takes the non-equilibrium distribution of quasiparticles down to a characteristic energy through electron-phonon scattering, which releases a large number of phonons. Combined, these two stages last no longer than a few nanoseconds, but the exact duration is strongly material-dependent. Over the third stage, the mixed distribution of quasiparticles and phonons evolves to a quasiparticle distribution at the superconducting gap Δ. The result is an excess number of quasiparticles $\delta N_{qp}(t=0)$ and a phonon cloud of non-pairbreaking phonons with energies below 2Δ.

The maximum number of generated excess quasiparticles for a photon with wavelength λ_{ph} is

$$N_{qp} = \frac{hc_0}{\lambda_{ph}} \frac{\eta_{pb}^{max}}{\Delta} \tag{2.108}$$

with $\eta_{pb}^{max} = 0.6$ the maximum pair breaking efficiency [28]–[30], a result from detailed modeling of the aforementioned downconversion, which implies that 40% or more of the photon energy is converted in phonons with $E < 2\Delta$. Consequently, due to the energy lost in non-pairbreaking phonons, the mean energy necessary to generate a single quasiparticle is $\epsilon = 1.7\Delta = \Delta/\eta_{pb}^{max}$ [28], [31].

The resonator responds to created excess quasiparticles as described in Section 2.3. The resonator's response to the creation of excess quasiparticles is not instantaneous but has a time scale given by the resonator ring time

$$\tau_{res} = \frac{2Q_l}{\omega_r}, \tag{2.109}$$

which is much slower, in the order of microseconds, than the energy downconversion process. The resonator relaxes back to the equilibrium quasiparticle distribution through recombination with timescale τ_{qp}, the quasiparticle lifetime. For a thermal distribution, $T \ll T_c$, and $E_{qp} = \Delta$, the quasiparticle lifetime can be approximated by [32]

$$\tau_{qp} = \frac{\tau_0}{\sqrt{\pi}} \left(\frac{k_B T_c}{2\Delta}\right)^{5/2} \sqrt{\frac{T_c}{T}} \exp\left(\Delta/k_B T\right) = \frac{\tau_0}{n_{qp}} \frac{N_0 (k_B T_c)^3}{2\Delta^2} \tag{2.110}$$

In [33], the authors show that the pulse decay can be captured by introducing the time-dependent excess quasiparticle number

$$\delta N_{qp}(t) = \frac{2N_{qp}^0}{\left(1 + 2N_{qp}^0/\delta N_{qp}(t=0)\right) \exp\left(t/\tau_{qp}^*\right) - 1} \tag{2.111}$$

with $\delta N_{qp}(t=0)$ the number excess quasiparticles introduced at $t = 0$, N_{qp}^0 the equilibrium number of quasiparticles and τ_{qp}^* the apparent lifetime defined as [34]

$$\tau_{qp}^* = \tau_{qp}(1 + \tau_{esc}/\tau_{pb})/2 \tag{2.112}$$

with $(1 + \tau_{esc}/\tau_{pb})$ the phonon trapping factor, in which τ_{pb} is the pair breaking time and τ_{esc} is the phonon escape time [32]. Eq. 2.111 has two regimes, visible in Fig. 2.7. If $N_{qp}^0/\delta N_{qp}(0) \ll 1$, i.e. the excess number of quasiparticles is large compared to the equilibrium number,

$$\delta N_{qp}(t) \approx \frac{2N_{qp}^0}{\exp\left(t/\tau_{qp}^*\right) - 1} \tag{2.113}$$

which behaves as $1/t$ for $t \ll \tau^*_{qp}$. The second regime, $N^0_{qp}/\delta N_{qp}(0) \gg 1$, has an exponential decay

$$\delta N_{qp}(t) \approx \delta N_{qp}(0) \exp\left(-t/\tau^*_{qp}\right). \tag{2.114}$$

2.4.3. Energy resolution

Since the pulse height is directly related to the energy (E) of the incoming photon through Eqs. 2.108, and 2.86 - 2.87, each photon pulse gives a measurement of the photon energy. However, several processes introduce variance in the number of generated quasiparticles for a photon pulse. Assuming that any noise process results in a normal distribution of observed pulse heights, with variance σ_E, the resolving power of the detector is given by

$$R = \frac{E}{\delta E} \tag{2.115}$$

where δE is the full-width half maximum of the normal distribution given by

$$\delta E = 2\sqrt{2\ln(2)}\sigma_E \sim 2.355\sigma_E \tag{2.116}$$

The fundamental limit in resolving power is related to the maximum pair breaking efficiency, η^{max}_{pb}, introduced in Eq. 2.108: there are statistical fluctuations in the number of subgap phonons created and thus uncertainty in the number of generated quasiparticles [27], [28], [31]. The statistical relation between the mean number of generated quasiparticles and the variation in the number of generated quasiparticles is described by the Fano factor

$$F = \frac{\sigma^2}{\mu}. \tag{2.117}$$

For a Poisson process, $F = 1$, but the creation of quasiparticles due to the absorption of a single photon is partially correlated, so $F < 1$ and depends on the electron system: $F \sim 0.4$ for semiconductors and $F \sim 0.2$ for superconductors. The Fano noise yields an upper limit to the detector's energy resolution. Inserting the variance $\sigma_E = F\epsilon E$ in Eq. 2.116

$$\delta E = 2\sqrt{2\ln(2)}\sqrt{F\epsilon E} \tag{2.118}$$

with E the deposited energy (photon energy). Inserting Eq. 2.118 in Eq. 2.115 yields the Fano-limited resolving power

$$R = \frac{E}{\delta E} = \frac{1}{2\sqrt{2\ln(2)}}\sqrt{\frac{\eta_{pb}^{max}E}{\Delta F}} \tag{2.119}$$

If we consider thin superconducting strips deposited on a thick substrate, phonons can escape from the superconductor into the substrate. The loss of phonons during the downconversion process removes energy available to the quasiparticle system $E' = E - E_{loss}$ with E the photon energy. The variance introduced by this process is captured by the phonon noise term $J(E)$, which can be energy-dependent [28]

$$\delta E = 2\sqrt{2\ln(2)}\sqrt{\left(F + J(E)\frac{E}{E'}\right)\epsilon E'}. \tag{2.120}$$

Since both processes are independent, the variance introduced by the Fano noise and phonon loss is additive. The factor E/E' accounts for the fact that the Fano factor F is with respect to the deposited energy, E', while J is with respect to the originally absorbed photon energy E. In the case of perfect phonon trapping, $E = E'$.

The phonon loss can be reduced by placing the detector on a thin membrane, recycling the phonons that would otherwise be lost in the substrate [35], or by creating a phonon-barrier between the superconductor and the substrate [36].

2.5. Photon energy estimation: Optimal filter

To find the pulse height in the presence of noise, we use an "optimal filter." A KID timestream containing a single photon pulse in an arbitrary KID response coordinate has the form

$$d(t) = H(E)m(t) + n(t), \tag{2.121}$$

with $H(E)$ the photon energy dependent pulse height, $m(t)$ the normalized pulse shape (or model) as in Fig. 2.7, and $n(t)$ a particular realisation of the noise. Here, we assume that all pulses have the same pulse shape $m(t)$, that the pulse shape is independent of the photon energy, and that the pulse arrival time t_0 is known. We assume that the noise is stationary, i.e., it does not change during a pulse, such that the noise is simply additive and independent of H and $m(t)$. In this case, the noise during a pulse can be estimated by measuring the noise level of several timestreams without photon pulses.

Instead of simply taking the maximum value in the raw timestream as the pulse height, which will be affected by noise, we want to determine the best estimate of $H(E)$ from the measured pulse using the pulse shape $m(t)$ and the noise power spectral density.

The best estimate of the pulse height ($\hat{H}$) is the pulse height that minimizes the error

$$\chi^2 = \int_{-\infty}^{\infty} \frac{|\tilde{d}(f) - H(E)\tilde{m}(f)|^2}{N(f)} df, \tag{2.122}$$

which is calculated in the frequency domain since, for linear systems, different frequency components are independent such that

$$\tilde{d}(f) = H(E)\tilde{m}(f) + \tilde{n}(f). \tag{2.123}$$

Here, $\tilde{d}(f)$, $\tilde{m}(f)$, and $\tilde{n}(f)$ are the Fourier transforms, denoted by a tilde, of $d(t)$, $m(t)$ and $n(t)$, respectively. $N(f)$ is the measured noise power spectral density of the detector.

This estimator is based on the fact that there is a pulse height for which the noise during a timestream can be obtained by subtracting the model pulse from the timestream $n(t) = d(t) - H(E)m(t)$. The noise $n(t)$ obtained this way is compared to the noise power spectral density of the detector $N(f)$. In the numerator of Eq. 2.122, we find the noise $\tilde{n}(f)$ obtained by subtracting the expected pulse $H(E)\tilde{m}(f)$ from the measured data $\tilde{d}(f)$, which is weighed against the power spectral density of the noise $N(f)$. If we would know the exact pulse height H, this would yield [37]

$$\chi^2 = \int_{-\infty}^{\infty} \frac{|\tilde{d}(f) - H(E)\tilde{m}(f)|^2}{N(f)} df = \int_{-\infty}^{\infty} \frac{|\tilde{m}(f)|^2}{N(f)} df = 1 \tag{2.124}$$

Following Ref. [37], the best estimator for the pulse height $\hat{H}$ is found by minimizing χ^2 with respect to H:

$$\hat{H} = \int_{-\infty}^{\infty} \frac{\tilde{d}(f)\tilde{m}^*(f) + \tilde{m}(f)\tilde{d}^*(f)}{2N(f)} df \Bigg/ \int_{-\infty}^{\infty} \frac{|\tilde{m}(f)|^2}{N(f)} df\ . \tag{2.125}$$

This equation can be simplified [38]

$$\hat{H} = \int_{-\infty}^{\infty} \frac{\tilde{m}^*(f)\tilde{d}(f)}{N(f)} df \Bigg/ \int_{-\infty}^{\infty} \frac{|\tilde{m}(f)|^2}{N(f)} df. \tag{2.126}$$

This equation is the linear optimal filter that gives the best estimate $\hat{H}$ of the pulse height $H(E)$. Conceptually Eq. 2.126 shows that an estimate of pulse height is made for every frequency point in the spectra. The estimate $\hat{H}$ is then obtained by averaging the estimate at each frequency with a weight given by $|\tilde{m}(f)|^2/N(f)$. The above formalism is only valid if all the pulses have the same pulse shape and if the pulse height $H(E)$ is linear with respect to the photon energy.

In practice, we obtain the pulse shape by averaging a large number of pulse events ($d(t)$), which we align with respect to the rising edge of the pulse. The noise power spectral density $N(f)$ is computed by averaging multiple individual noise spectra of timestreams without pulse events of the same length as $d(t)$. Fig.2.8a shows the frequency spectra of the average pulse and the noise power spectral density.

Estimator variance

Following Ref. [37], the expected variance of the estimator is $\sigma_H^2 = \langle [\hat{H} - H]^2 \rangle$, which, in general, is given by

$$\sigma_A^2 = \left(\frac{1}{2} \frac{\partial^2 \chi^2}{\partial H^2} \right)^{-1}. \tag{2.127}$$

This yields

$$\sigma_H^2 = \left[\int_{-\infty}^{\infty} \frac{|\tilde{m}(f)|^2}{N(f)} df \right]^{-1}. \tag{2.128}$$

The variance in energy is then

$$\sigma_E^2 = \left(\frac{E}{H} \right)^2 \sigma_H^2, \tag{2.129}$$

where E/H is the inverse of the KIDs responsivity. The FWHM of the normal distribution is (Eq. 2.116),

$$\delta E = 2\sqrt{2\ln(2)} \sigma_E = 2\sqrt{2\ln(2)} \left(\frac{E}{H} \right) \left[\int_{-\infty}^{\infty} \frac{|\tilde{m}(f)|^2}{N(f)} df \right]^{-1/2}. \tag{2.130}$$

The maximum obtainable resolving power based on the noise power spectral density $N(F)$ and the average pulse $\overline{H}\tilde{m}(f)$ is then

$$R_{SN} = \frac{E}{\delta E} = \frac{\overline{H}}{2\sqrt{2\ln(2)}} \sqrt{\int_{-\infty}^{\infty} \frac{|\tilde{m}(f)|^2}{N(f)} df}, \tag{2.131}$$

with $\overline{H}$ the average pulse height. Fig. 2.8 shows both power spectra $|\overline{H}\tilde{m}(f)|^2$ and $N(F)$, where the signal-to-noise resolving power R_{SN} is proportional to the square root of the area (in a logarithmic plot) between $|\overline{H}\tilde{m}(f)|^2$, and $N(f)$. The bigger the area, the higher R_{SN} will be. Alternatively, R_{SN} can be expressed in terms of the detector's NEP, see Ref. [39].

Since $R \propto 1/\sqrt{\sigma_E}$ the total resolving power due to different independent processes is

$$\frac{1}{R^2} = \frac{1}{R_{SN}^2} + \frac{1}{R_F^2} + \ldots, \tag{2.132}$$

where R_F relates to the variance in the number of quasiparticles created and R_{SN} to how accurately we can measure the photon pulse.

Two-dimensional filter

We can use the same estimator methodology to estimate the photon energy from the pulse in phase and amplitude in conjunction. In this case, we have a pulse with different heights in both coordinates due to the difference in responsivity between amplitude and phase (Fig. 2.5),

$$\begin{bmatrix} d_\theta(t) \\ d_A(t) \end{bmatrix} = \begin{bmatrix} H_\theta(E)m_\theta(t) \\ H_A(E)m_A(t) \end{bmatrix} + \begin{bmatrix} n_\theta(t) \\ n_A(t) \end{bmatrix} \tag{2.133}$$

for which the χ^2 estimator in frequency domain is

$$\chi^2 = \int_{-\infty}^{\infty} (\tilde{\mathbf{d}} - \mathbf{H}\tilde{\mathbf{m}})^\dagger \mathbf{S}^{-1} (\tilde{\mathbf{d}} - \mathbf{H}\tilde{\mathbf{m}}) df, \tag{2.134}$$

with $\mathbf{D}$, $\mathbf{H}$ and $\mathbf{M}$ the data, pulse height, and pulse shape column vectors, in frequency domain respectively, and S is the noise covariance matrix

$$\mathbf{S}(f) = \begin{bmatrix} S_{\theta\theta}(f) & S_{\theta A}(f) \\ S_{A\theta}(f) & S_{AA}(f) \end{bmatrix}. \tag{2.135}$$

The photon energy estimate is then obtained by minimizing χ^2 with respect to H.

An analytical form that is not dependent on a known responsivity ratio between A and θ, assuming both are linear with respect to E (Fig. 2.5), is found by normalizing the pulse shapes with respect to one unknown amplitude

$$\begin{bmatrix} d_\theta(t) \\ d_A(t) \end{bmatrix} = H(E) \begin{bmatrix} \frac{A_\theta}{A_\theta + A_d} m_\theta(t) \\ \frac{A_d}{A_\theta + A_d} m_A(t) \end{bmatrix} + \begin{bmatrix} n_\theta(t) \\ n_A(t) \end{bmatrix}. \tag{2.136}$$

The solution is

$$\hat{H} = \frac{\int_{-\infty}^{\infty} \tilde{\mathbf{m}}(f)^\dagger \mathbf{S}^{-1} \tilde{\mathbf{d}}(f) df}{\int_{-\infty}^{\infty} \tilde{\mathbf{m}}(f)^\dagger \mathbf{S}^{-1} \tilde{\mathbf{m}}(f) df}. \tag{2.137}$$

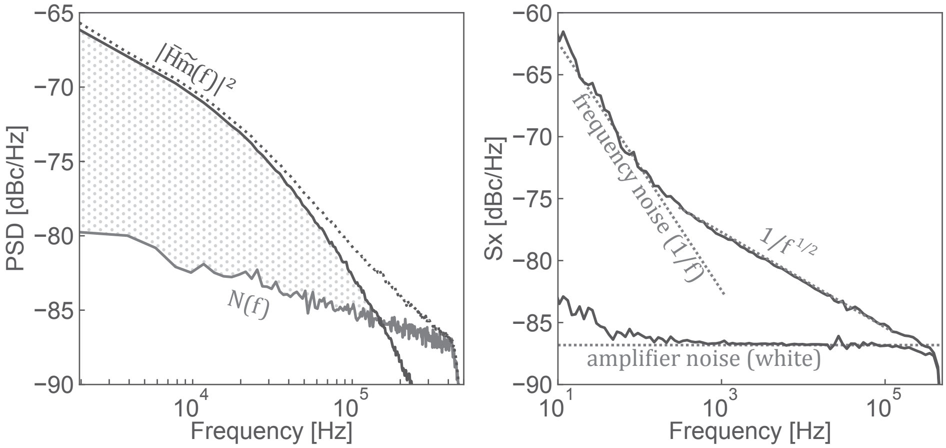

Figure 2.8: **Left)** The optimal filter is presented by the frequency spectra of its components. $|\overline{H}\tilde{m}(f)|^2$ is the power spectrum of the average pulse. $N(f)$ is the noise PSD. The useful bandwidth of Eq. 2.131 is illustrated by the shaded area between $|\overline{H}\tilde{m}(f)|^2$ and $N(f)$. The frequency range of interest is limited by the length of the pulse window, for this analysis 512 μs, and the sample frequency (1 Msample/s). For completeness, the dotted line gives the average spectrum of individual pulses. Spectra are plotted for the phase readout coordinate. **Right)** Phase and Amplitude (dark) noise spectra to illustrate the different contributions to $N(f)$. The phase response is dominated by frequency noise (f^{-1} or $f^{-0.5}$). The white amplifier noise dominates the amplitude noise spectra, but there is some f^{-1} noise at lower frequencies, likely due to the electronics. Data for both panels is from a typical KID from Chapter 4.

2.5.1. Noise contributions

The noise power spectral density $N(f)$ in Fig. 2.8 has two main contributions, as indicated in Fig. 2.8b; the readout system's amplifier noise and the frequency noise from the resonator. The quasiparticle generation-recombination (GR) noise level [40] is not visible in the noise measurements in this thesis [41].

System noise: Amplifier noise

The white amplifier noise level, primarily visible in the amplitude noise spectra, is the noise level set by the amplifiers and attenuators in the readout system. The readout system will be discussed in detail in Chapter 3, but the noise level is given by

$$S_{A,\theta}^{system} = \frac{k_B T_{sys}}{r_c^2 P_{read}}. \tag{2.138}$$

Here, T_{sys} is the readout's equivalent noise temperature, dominated by the first cryogenic amplifier. The radius of the resonance circle, r_c, is given by $r_c = Q_l/2Q_c$ which, for an overcoupled KID ($Q_c \ll Q_i$, $Q_l = Q_c$) is 0.5. The system noise temperature of our microwave readout system is discussed in detail in Chapter 3.

Resonator noise: Two Level System noise

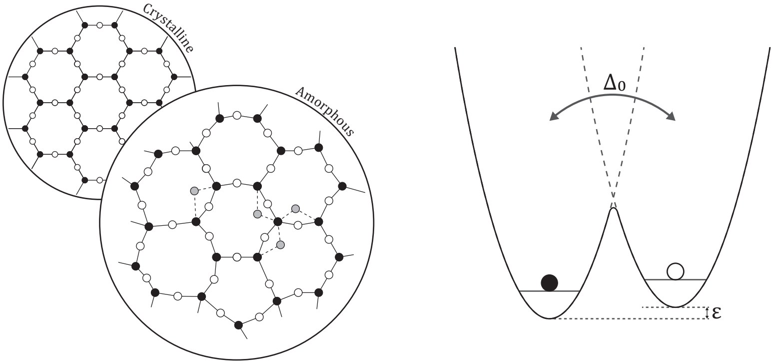

Figure 2.9: Two-level-tunneling systems (TLSs) can arise among others from tunneling atoms, or tunneling groups of atoms, that exist due to defects in amorphous materials. These systems are modeled as particles in asymmetric double-well potentials with asymmetry energy ϵ and tunneling barrier energy Δ_0. Tunneling transitions between the two energy minima result in changes in the dielectric constant of the host volume and introduce microwave losses in the capacitive element of the resonator.

The phase noise spectra of Fig. 2.8 show a significant amount of excess noise with a $f^{-\alpha}$ spectrum compared to the amplitude noise spectrum, which is typical for microwave kinetic inductance detectors [42] and is associated with frequency fluctuations [43]–[46]. Experimental studies showed that the noise level has a $P_{int}^{-0.5}$ dependency and is dependent on the substrate [42]. In addition, the noise level rises when a dielectric layer ($\mathrm{SiO_x}$) is deposited on top of a NbTiN CPW resonator [47]. Based on these observations, the excess noise can be explained by the presence of switching two-level systems (TLS) in amorphous ("glassy") dielectric layers, as in Fig. 2.9.

Every resonator we make will contain such amorphous layers, either intentionally, like the deposited dielectric between the plates of a parallel plate capacitor, or due to surface oxides on metals and substrates. At low temperatures, the electromagnetic properties of these amorphous layers are dominated by crystalline lattice defects. An example of such a defect is an atom that can tunnel ("move") between two energetically similar potential minima in the lattice (Fig. 2.9). In the Standard Tunneling Model (STM) model, this two-level system (TLS) is modeled as a particle in an asymmetric double-well potential. The TLS couples to the electric field of the resonator ($\vec{E}$) through its electric dipole moment d_0. Each TLS will have a different asymmetry energy ϵ and barrier tunneling energy Δ_0 due to the random nature of amorphous materials. The STM assumes that ε and Δ_0 are independent and are uniformly distributed over a broad range. As an ensemble, the TLSs contribute to the complex dielectric constant[4] ($\tilde{\varepsilon} = \varepsilon' - i\varepsilon''$) of the amorphous dielectric (in the weak field) as

$$\tilde{\varepsilon}_{TLS}(\omega) = -\frac{2Pd_0^2}{3}\left[\Psi\left(\frac{1}{2} - \frac{\hbar\omega - j\Gamma}{2j\pi k_B T}\right) - \log\frac{\epsilon_{max}}{2\pi k_B T}\right], \tag{2.139}$$

with P the TLS-density, d_0 the electric dipole moment, Ψ the complex digamma function, Γ the linewidth (related to the dephasing time) and ϵ_{max} the maximum splitting energy [11]. Since the capacitance of the resonator depends on the dielectric constant of the surrounding medium (media), ε_h, the TLS will have two effects on the resonator. The real part of $\tilde{\varepsilon}_{TLS}$ is responsible for a frequency shift of the resonator

$$\frac{\Delta f_r}{f_r} = -\frac{\int_{V_h} \varepsilon'_{TLS}|\vec{E}|^2 d\vec{r}}{2\int_{V_h} \varepsilon_h|\vec{E}|^2 d\vec{r}} = \frac{p\delta^0_{TLS}}{\pi}\left[\mathrm{Re}\Psi\left(\frac{1}{2} - \frac{\hbar\omega}{2j\pi k_B T}\right) - \log\frac{\epsilon_{max}}{2\pi k_B T}\right] \tag{2.140}$$

while the imaginary part gives rise to microwave loss

$$\frac{1}{Q_i} = -\frac{\int_{V_h} \varepsilon''_{TLS}|\vec{E}|^2 d\vec{r}}{\int_{V_h} \varepsilon_h|\vec{E}|^2 d\vec{r}} = p\delta^0_{TLS}\tanh\frac{\hbar\omega}{2k_B T}. \tag{2.141}$$

Here $\delta^0_{TLS} = 3Pd_0^2/2\varepsilon_h$, with ε_h the dielectric constant of the host volume, and we assume that TLS dominates the internal loss of the resonator. p is the participation ratio that takes into account that for some structures, only part of the electric field is in the TLS volume V_h and is given by the ratio between the electric energy in the TLS host volume (w_h^e) and the total electric energy (w_e)

$$p = \frac{\int_{V_h} \epsilon_h \vec{E}(\vec{r})^2 d\vec{r}}{\int_V \epsilon \vec{E}(\vec{r})^2 d\vec{r}} = \frac{w_h^e}{w^e}. \tag{2.142}$$

At higher fields the TLS induced loss ($1/Q_i$) depends on the applied electric field $\vec{E}$ as

---

[4] In Section 2.4 we used the sign convention common among electrical engineers. Here, we switch to the sign convention commonly used by physicists to adhere to the literature references.

$$\frac{1}{pQ_i} = \delta^0_{TLS} \tanh \frac{\hbar\omega}{2k_BT} \left(1 + \frac{|\vec{E}|}{E_c}\right)^{-\beta} + \tan \delta_{HP}. \tag{2.143}$$

Above the critical field E_c, the TLSs are excited with an effective Rabi-frequency that exceeds their dissipation rates, and $\tan \delta_{HP}$ is the loss that dominates at high internal resonator powers. In the STM $\beta = 0.5$, but values between 0.15-0.35 have been observed [48]–[50].

The TLS properties of a material are typically extracted by fitting Eq. 2.140 to the temperature-dependent resonance frequency of a resonator and by fitting Eq. 2.143 to the power-dependent microwave loss ($1/Q_i$).

The frequency noise of a resonator originates from the same TLS. The TLSs randomly switch between their two states, which introduces a time-fluctuating dielectric constant ε_{TLS}. Since each TLS has a different coupling strength and timing, which are uniformly spread over a broad range, the resulting noise contribution has a 1/f spectrum [11], [51]. The STM makes the ansatz that the frequency noise level should depend on the applied electric field in the same way as the TLS loss (eq. 2.143) to explain the observed $S_f \propto P_{int}^{-0.5}$.

Recent focus has been on the "interacting tunneling model," or generalized tunneling model (GTM), which splits the TLS into two entities. The microwave loss is caused by high-frequency resonant TLSs that couple to the electric field of the resonator. In addition, the volume is filled with slow classical fluctuators that do not couple directly to the resonator but can couple to the high-frequency TLS. These strongly coupled fluctuators can bring the high-frequency TLS in and out of resonance with the resonator. The fractional frequency power spectral density predicted by the interacting tunneling model is

$$\frac{S_f}{f_r^2}(\omega) \sim \frac{\chi}{\omega} \left(\frac{f_r}{E_{max}}\right)^{\mu} \frac{U_0}{\Gamma_2} \begin{cases} \frac{\int_{V_h} E_c|\vec{E}|^3 dV}{4(\int_V \epsilon|\vec{E}|^2 dV)^2} & \text{if } |\vec{E}| \gg E_c \\ \frac{\int_{V_h} E_c|\vec{E}|^4 dV}{4(\int_V \epsilon|\vec{E}|^2 dV)^2} & \text{if } |\vec{E}| \ll E_c, \end{cases} \tag{2.144}$$

In both cases, the spectrum has a $1/f$ spectrum, and in a strong field, the spectrum scales with $P_{int}^{-0.5}$ ($1/\vec{E}$). The GTM explains the observed deviation from $\beta = 0.5$ in Eq. 2.143 [48]–[50], [52] and the temperature dependence of the frequency noise level [53] which could not be explained with the STM. The GTM also shows that the sources of loss and noise are two separate entities, which can explain why, in [54], the removal of surface spins resulted in a large noise reduction but a small reduction in loss. This could potentially explain the discrepancy between observed noise and loss dependencies in [47] and Chapter 7 of this thesis. The theory discussed here forms the basis for the experiments in Chapter 7, where we study how the TLS-noise level changes for different parallel plate capacitor dimensions. For a detailed discussion on two-level systems in amorphous solids, refer to [51].

2.5.2. Other limitations

Undersampled pulses

The observed photon pulse is narrow due to the fast $1/t$ decay, which can easily result in an undersampled pulse for our standard sampling rate of 1 Msample/s. An undersampled pulse has a direct negative effect on the reachable energy resolution and, in addition, makes the alignment between pulses, and thus the creation of an average pulse shape difficult. Ref. [55] gives a simple estimate of variation in pulse height based on the pulse shape and sample rate. We believe the undersampled peaks can be a limiting factor in the achievable energy resolution for our β-Ta hybrid KIDs presented in Chapter 4.

Current non-uniformity

In the previous sections, we have always assumed that the current along the lumped element, meandered inductor, is uniform. However, due to the inductor's physical dimensions, the current density will be location-dependent [56]. In addition, current crowding effects [57]–[59] increase the current density near the inner bends of the inductor. For the designs we use, a SONNET simulation of these effects is given in Fig. 2.10.

Due to the current density inhomogeneity, the photon response of a KID will be location-dependent since the quasiparticles do not diffuse fast enough in disordered superconductors (~ 10 μm in TiN [56]) to even out over the inductor. The response to a local injection of quasiparticles scales with the square of the location-dependent current density [56], [60]. One way to derive this dependency is through the cavity perturbation method [22], which shows that the resonance frequency shift of a resonator depends linearly on the change in energy in the perturbed resonators. From Eq. 2.35, the change in stored energy on a local change in L_k is

$$\delta E_m = \int_{l_1}^{l_2} \delta L_k(l) |I_{max}(l)|^2 dl, \tag{2.145}$$

where we only consider current variation in the length of the strip since the width of the strip is typically small compared to the quasiparticle diffusion length. Both the admittance and polar coordinate systems in Fig. 2.5 are linear with changes in

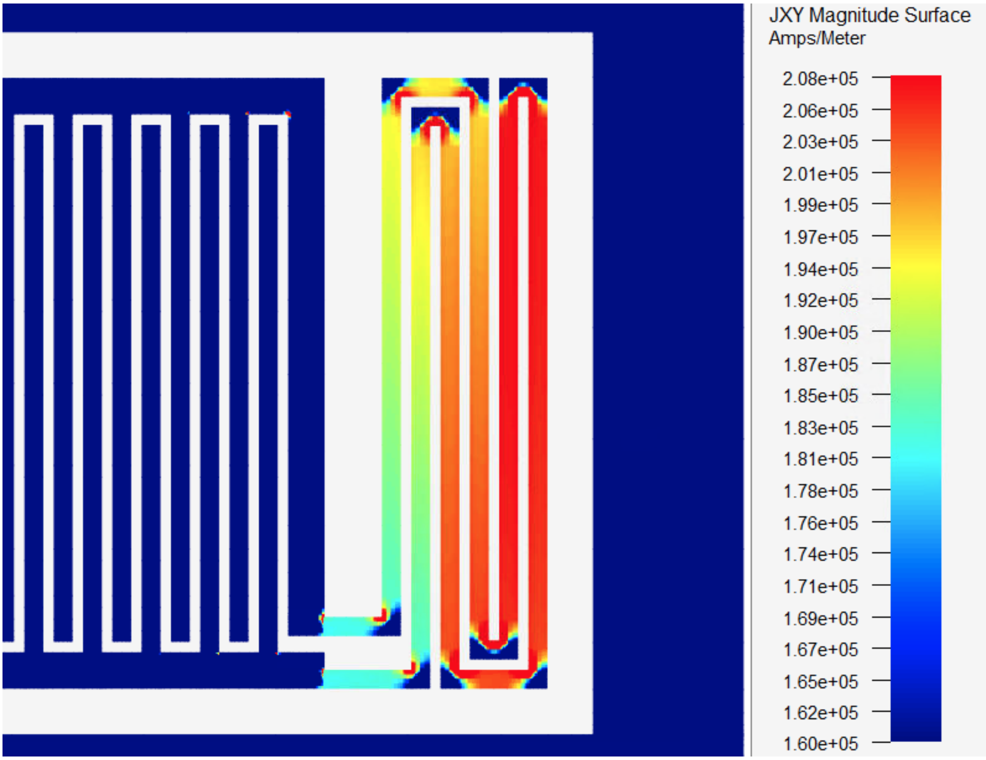

Figure 2.10: SONNET current density simulation for a 3-μm β-Ta inductor with a sheet kinetic inductance of 84 pH/□ (40 nm). Current crowding changes the current density in each turn and corner. The difference in current density between the leftmost and rightmost lines is around 10%. The cell size is 0.25 μm.

δE_m, although the polar system is only linear for small angles, see Section 2.3.1. If I_{max} is location dependent, as in Fig. 2.10, the pulse height will depend on the the position where the photon was absorbed, introducing an additional variance σ_H^2 possible limiting the energy resolution of the detector.

The cavity perturbation method assumes that the change in δL_k is small enough such that the current distribution in the perturbed resonator can still be approximated by the distribution of the unperturbed resonator. The same result is reached using different approaches in Refs. [11], [60].

In the simulation of a beta-Ta inductor in Fig. 2.10, the current density in the inductor's leftmost vertical wire is 90% of the current density in the rightmost vertical wire. The current uniformity can be improved by increasing the inductor leg width according to the increase in current density, which peaks at the point furthest from the capacitor contacts. The current crowding effects in the corners of the meandering inductor can be decreased by shaping the corners [57]. For optical lithography, the corners of structures are already naturally rounded with respect to the mask due to optical effects.

Bibliography

[1] H. K. Onnes, *Further experiments with Liquid Helium. G. On the Electrical Resistance of Pure Metals, etc. VI. On the Sudden Change in the Rate at which the Resistance of Mercury Disappears.* K. Gavroglu and Y. Goudaroulis, Eds. Dordrecht: Springer Netherlands, 1991, pp. 267–272.

[2] J. R. Hook and H. E. Hall, *Solid State Physics* (Manchester Physics Series). Wiley, 2013, ISBN: 9781118790885.

[3] P. Drude, "Zur Elektronentheorie der Metalle," *Ann. Phys. (Berl.)*, vol. 306, no. 3, pp. 566–613, 1900.

[4] P. Drude, "Zur Elektronentheorie der Metalle; II. Teil. Galvanomagnetische und thermomagnetische Effecte," *Ann. Phys. (Berl.)*, vol. 308, no. 11, pp. 369–402, 1900.

[5] G. S. Ohm, *Die galvanische Kette, mathematisch bearbeitet* (Landmarks of Science). Riemann, 1827.

[6] E. Grüneisen, "Die Abhängigkeit des elektrischen Widerstandes reiner Metalle von der Temperatur," *Ann. Phys. (Berl.)*, vol. 408, no. 5, pp. 530–540, 1933.

[7] F. London, H. London, and F. A. Lindemann, "The electromagnetic equations of the supraconductor," *Proc. R. Soc. London A - Math Phys. Sci.*, vol. 149, no. 866, pp. 71–88, 1935.

[8] C. J. Gorter and H. Casimir, "On supraconductivity I," *Physica*, vol. 1, no. 1, pp. 306–320, 1934, ISSN: 0031-8914. DOI: `10.1016/S0031-8914(34)90037-9`.

[9] A. J. Annunziata, D. F. Santavicca, L. Frunzio, *et al.*, "Tunable superconducting nanoinductors," *Nanotechnology*, vol. 21, no. 44, p. 445 202, Oct. 2010, ISSN: 1361-6528. DOI: `10.1088/0957-4484/21/44/445202`.

[10] R. L. Kautz, "Picosecond pulses on superconducting striplines," *J. Appl. Phys.*, vol. 49, no. 1, pp. 308–314, Jan. 1978, ISSN: 0021-8979. DOI: `10.1063/1.324387`.

[11] J. Gao, "The Physics of Superconducting Microwave Resonators," Ph.D. dissertation, California Institute of Technology, 2008. [Online]. Available: `http://web.physics.ucsb.edu/~bmazin/Papers/2008/Gao/Caltech%20Thesis%202008%20Gao.pdf`.

[12] J. Pearl, "Current Distribution in Superconducting Films Carrying Quantized Fluxoids," *Appl. Phys. Lett.*, vol. 5, no. 4, pp. 65–66, Aug. 1964, ISSN: 0003-6951. DOI: `10.1063/1.1754056`.

[13] J. Bardeen, L. N. Cooper, and J. R. Schrieffer, “Theory of Superconductivity,” *Phys. Rev.*, vol. 108, pp. 1175–1204, 5 Dec. 1957. DOI: `10.1103/PhysRev.108.1175`.

[14] D. C. Mattis and J. Bardeen, “Theory of the anomalous skin effect in normal and superconducting metals,” *Phys. Rev.*, vol. 111, no. 2, pp. 412–417, 2 Jul. 1958. DOI: `10.1103/PhysRev.111.412`.

[15] R. Barends, “Photon-detecting superconducting resonators,” en, Publisher: R. Barends, Ph.D. dissertation, Delft University of Technology, 2009. [Online]. Available: `https://repository.tudelft.nl/islandora/object/uuid%3A574944e6-c3ce-4c86-a511-a88385b22379`.

[16] O. Noroozian, “Superconducting microwave resonator arrays for submillimeter/far-infrared imaging,” Ph.D. dissertation, California Institute of Technology, 2012. [Online]. Available: `https://resolver.caltech.edu/CaltechTHESIS:06122012-091920562`.

[17] D. A. Frickey, “Conversions between S, Z, Y, H, ABCD, and T parameters which are valid for complex source and load impedances,” *IEEE Trans. Microw. Theory Techn.*, vol. 42, no. 2, pp. 205–211, Feb. 1994, Conference Name: IEEE Transactions on Microwave Theory and Techniques, ISSN: 1557-9670. DOI: `10.1109/22.275248`.

[18] M. S. Khalil, M. J. A. Stoutimore, F. C. Wellstood, and K. D. Osborn, “An analysis method for asymmetric resonator transmission applied to superconducting devices,” *J. Appl. Phys.*, vol. 111, no. 5, p. 054 510, Mar. 2012, ISSN: 0021-8979. DOI: `10.1063/1.3692073`.

[19] L. J. Swenson, P. K. Day, B. H. Eom, *et al.*, “Operation of a titanium nitride superconducting microresonator detector in the nonlinear regime,” *J. Appl. Phys.*, vol. 113, no. 10, p. 104 501, Mar. 2013, ISSN: 0021-8979. DOI: `10.1063/1.4794808`.

[20] J. Gao, J. Zmuidzinas, A. Vayonakis, P. Day, B. Mazin, and H. Leduc, “Equivalence of the Effects on the Complex Conductivity of Superconductor due to Temperature Change and External Pair Breaking,” *J. Low Temp. Phys.*, vol. 151, no. 1, pp. 557–563, 2008. DOI: `10.1007/s10909-007-9688-z`.

[21] N. Zobrist, N. Klimovich, B. Eom, *et al.*, “Improving the dynamic range of single photon counting kinetic inductance detectors,” *J. Astron. Telesc. Instrum. Syst.*, vol. 7, no. 1, p. 010 501, Feb. 2021, ISSN: 2329-4124. DOI: `10.1117/1.JATIS.7.1.010501`.

[22] D. M. Pozar, *Microwave Engineering.* Wiley, 2012, ISBN: 9781118213636.

[23] A. D. Rakić, "Algorithm for the determination of intrinsic optical constants of metal films: Application to aluminum," EN, *Applied Optics*, vol. 34, no. 22, pp. 4755–4767, Aug. 1995, Publisher: Optica Publishing Group, ISSN: 2155-3165. DOI: `10.1364/AO.34.004755`.

[24] B. Ung. "Drude-lorentz and debye-lorentz models for the dielectric constant of metals and water." MATLAB Central File Exchange. (2024), [Online]. Available: `https://nl.mathworks.com/matlabcentral/fileexchange/18040-drude-lorentz-and-debye-lorentz-models-for-the-dielectric-constant-of-metals-and-water`.

[25] P. Patsalas and S. Logothetidis, "Optical, electronic, and transport properties of nanocrystalline titanium nitride thin films," *J. Appl. Phys.*, vol. 90, no. 9, pp. 4725–4734, Nov. 2001, ISSN: 0021-8979. DOI: `10.1063/1.1403677`.

[26] J. J. A. Baselmans, F. Facchin, A. P. Laguna, *et al.*, "Ultra-sensitive THz microwave kinetic inductance detectors for future space telescopes," *Astron. Astrophys.*, vol. 665, A17, Sep. 2022. DOI: `10.1051/0004-6361/202243840`.

[27] A. G. Kozorezov, A. F. Volkov, J. K. Wigmore, A. Peacock, A. Poelaert, and R. den Hartog, "Quasiparticle-phonon downconversion in nonequilibrium superconductors," *Phys. Rev. B*, vol. 61, no. 17, pp. 11 807–11 819, 17 May 2000. DOI: `10.1103/PhysRevB.61.11807`.

[28] A. G. Kozorezov, J. K. Wigmore, D. Martin, P. Verhoeve, and A. Peacock, "Electron energy down-conversion in thin superconducting films," *Phys. Rev. B*, vol. 75, p. 094 513, 9 Mar. 2007. DOI: `10.1103/PhysRevB.75.094513`.

[29] T. Guruswamy, D. J. Goldie, and S. Withington, "Quasiparticle generation efficiency in superconducting thin films," *Supercond. Sci. Technol.*, vol. 27, no. 5, p. 055 012, Mar. 2014. DOI: `10.1088/0953-2048/27/5/055012`.

[30] P. J. de Visser, S. J. C. Yates, T. Guruswamy, *et al.*, "The non-equilibrium response of a superconductor to pair-breaking radiation measured over a broad frequency band," *Appl. Phys. Lett.*, vol. 106, no. 25, p. 252 602, Jun. 2015, ISSN: 0003-6951. DOI: `10.1063/1.4923097`.

[31] A. Kozorezov, "Energy Down-Conversion and Thermalization in Metal Absorbers," *J. Low Temp. Phys.*, vol. 167, no. 3, pp. 473–484, May 2012. DOI: `10.1007/s10909-011-0426-1`.

[32] S. B. Kaplan, C. C. Chi, D. N. Langenberg, J. J. Chang, S. Jafarey, and D. J. Scalapino, "Quasiparticle and phonon lifetimes in superconductors," *Phys. Rev. B*, vol. 14, pp. 4854–4873, 11 Dec. 1976. DOI: `10.1103/PhysRevB.14.4854`.

[33] T. Rugers, "Quasiparticle dynamics in disordered superconductors," en, Bachelor Thesis, Dec. 2023. [Online]. Available: `https://repository.tudelft.nl/islandora/object/uuid%3A3097e7ce-73aa-4312-ad5c-eb105cc97091?collection=education`.

[34] S. de Rooij, “Quasiparticle Dynamics in Optical MKIDs: Single Photon Response and Temperture Dependent Generation-Recombination Noise,” Ph.D. dissertation, 2020. [Online]. Available: `https://repository.tudelft.nl/islandora/object/uuid:1d935dc8-58d1-438f-995b-872e9d5f077e`.

[35] P. J. de Visser, S. A. de Rooij, V. Murugesan, D. J. Thoen, and J. J. Baselmans, “Phonon-Trapping-Enhanced Energy Resolution in Superconducting Single-Photon Detectors,” *Phys. Rev. Applied*, vol. 16, no. 3, p. 034 051, Sep. 2021. DOI: `10.1103/PhysRevApplied.16.034051`.

[36] N. Zobrist, W. H. Clay, G. Coiffard, *et al.*, “Membraneless Phonon Trapping and Resolution Enhancement in Optical Microwave Kinetic Inductance Detectors,” *Phys. Rev. Lett.*, vol. 129, no. 1, p. 017 701, Jul. 2022. DOI: `10.1103/PhysRevLett.129.017701`.

[37] S. R. Golwala, “Exclusion limits on the WIMP-nucleon elastic-scattering cross section from the cryogenic dark matter search,” Ph.D. dissertation, University of California, Berkley, 2000.

[38] K. D. Irwin, “Phonon-mediated particle detection using superconducting tungsten transition-edge sensors,” en, Ph.D. dissertation, Stanford University, Feb. 1995. DOI: `10.2172/1423679`.

[39] M. E. Eckart, “Measurements of X-Ray Selected AGN and Novel Superconducting X-Ray Detectors,” phd, California Institute of Technology, 2007. DOI: `10.7907/SZAB-0Y07`.

[40] P. J. de Visser, J. J. A. Baselmans, P. Diener, S. J. C. Yates, A. Endo, and T. M. Klapwijk, “Number fluctuations of sparse quasiparticles in a superconductor,” *Phys. Rev. Lett.*, vol. 106, p. 167 004, 16 Apr. 2011. DOI: `10.1103/PhysRevLett.106.167004`.

[41] S. A. H. de Rooij, J. J. A. Baselmans, V. Murugesan, D. J. Thoen, and P. J. de Visser, “Strong reduction of quasiparticle fluctuations in a superconductor due to decoupling of the quasiparticle number and lifetime,” *Phys. Rev. B*, vol. 104, p. L180506, 18 Nov. 2021. DOI: `10.1103/PhysRevB.104.L180506`.

[42] P. K. Day, H. G. LeDuc, B. A. Mazin, A. Vayonakis, and J. Zmuidzinas, “A broadband superconducting detector suitable for use in large arrays,” *Nature*, vol. 425, no. 6960, pp. 817–821, Oct. 2003. DOI: `10.1038/nature02037`.

[43] J. Gao, J. Zmuidzinas, B. A. Mazin, H. G. LeDuc, and P. K. Day, “Noise properties of superconducting coplanar waveguide microwave resonators,” *Appl. Phys. Lett.*, vol. 90, no. 10, p. 102 507, Mar. 2007. DOI: `10.1063/1.2711770`.

[44] J. Gao, L. R. Vale, J. A. B. Mates, *et al.*, “Strongly quadrature-dependent noise in superconducting microresonators measured at the vacuum-noise limit,” *Appl. Phys. Lett.*, vol. 98, no. 23, p. 232 508, Jun. 2011. DOI: `10.1063/1.3597156`.

[45] S. Takei, V. M. Galitski, and K. D. Osborn, “Squeezed noise due to two-level system defects in superconducting resonator circuits,” *Phys. Rev. B*, vol. 85, no. 10, p. 104 507, Mar. 2012, ISSN: 1550-235X. DOI: `10.1103/PhysRevB.85.104507`.

[46] C. Neill, A. Megrant, R. Barends, *et al.*, “Fluctuations from edge defects in superconducting resonators,” *Appl. Phys. Lett.*, vol. 103, no. 7, p. 072 601, Aug. 2013, ISSN: 0003-6951. DOI: `10.1063/1.4818710`.

[47] R. Barends, H. L. Hortensius, T. Zijlstra, *et al.*, “Contribution of dielectrics to frequency and noise of NbTiN superconducting resonators,” *Appl. Phys. Lett.*, vol. 92, no. 22, p. 223 502, Jun. 2008, ISSN: 0003-6951. DOI: `10.1063/1.2937837`.

[48] J. Burnett, L. Faoro, and T. Lindström, “Analysis of high quality superconducting resonators: Consequences for TLS properties in amorphous oxides,” *Supercond. Sci. Technol.*, vol. 29, no. 4, p. 044 008, Mar. 2016, ISSN: 1361-6668. DOI: `10.1088/0953-2048/29/4/044008`.

[49] P. Macha, S. H. W. van der Ploeg, G. Oelsner, *et al.*, “Losses in coplanar waveguide resonators at millikelvin temperatures,” *Appl. Phys. Lett.*, vol. 96, no. 6, p. 062 503, Feb. 2010, ISSN: 0003-6951. DOI: `10.1063/1.3309754`.

[50] J. M. Sage, V. Bolkhovsky, W. D. Oliver, B. Turek, and P. B. Welander, “Study of loss in superconducting coplanar waveguide resonators,” *J. Appl. Phys.*, vol. 109, no. 6, p. 063 915, Mar. 2011, ISSN: 0021-8979. DOI: `10.1063/1.3552890`.

[51] C. Müller, J. H. Cole, and J. Lisenfeld, “Towards understanding two-level-systems in amorphous solids: Insights from quantum circuits,” *Rep. Progr. Phys.*, vol. 82, no. 12, p. 124 501, Oct. 2019. DOI: `10.1088/1361-6633/ab3a7e`.

[52] L. Faoro and L. B. Ioffe, “Internal Loss of Superconducting Resonators Induced by Interacting Two-Level Systems,” *Phys. Rev. Lett.*, vol. 109, no. 15, p. 157 005, Oct. 2012, ISSN: 1079-7114. DOI: `10.1103/PhysRevLett.109.157005`.

[53] L. Faoro and L. B. Ioffe, “Interacting tunneling model for two-level systems in amorphous materials and its predictions for their dephasing and noise in superconducting microresonators,” *Phys. Rev. B*, vol. 91, no. 1, p. 014 201, 1 Jan. 2015. DOI: `10.1103/PhysRevB.91.014201`.

[54] S. E. de Graaf, L. Faoro, J. Burnett, *et al.*, “Suppression of low-frequency charge noise in superconducting resonators by surface spin desorption,” *Nat. Commun.*, vol. 9, no. 1, p. 1143, 2018. DOI: `10.1038/s41467-018-03577-2`.

[55] M. De Lucia, G. Ulbricht, E. Baldwin, *et al.*, “Limitations to the energy resolution of single-photon sensitive microwave kinetic inductance detectors,” *AIP Adv.*, vol. 13, no. 12, p. 125 026, Dec. 2023, ISSN: 2158-3226. DOI: `10.1063/5.0168365`.

[56] B. A. Mazin, B. Bumble, S. R. Meeker, K. O'Brien, S. McHugh, and E. Langman, "A superconducting focal plane array for ultraviolet, optical, and near-infrared astrophysics," *Opt. Express*, vol. 20, no. 2, pp. 1503–1511, Jan. 2012. DOI: `10.1364/OE.20.001503`.

[57] J. R. Clem and K. K. Berggren, "Geometry-dependent critical currents in superconducting nanocircuits," *Phys. Rev. B*, vol. 84, no. 17, p. 174 510, 17 Nov. 2011. DOI: `10.1103/PhysRevB.84.174510`.

[58] H. L. Hortensius, E. F. C. Driessen, T. M. Klapwijk, K. K. Berggren, and J. R. Clem, "Critical-current reduction in thin superconducting wires due to current crowding," *Appl. Phys. Lett.*, vol. 100, no. 18, p. 182 602, May 2012, ISSN: 0003-6951. DOI: `10.1063/1.4711217`.

[59] J. R. Clem, Y. Mawatari, G. R. Berdiyorov, and F. M. Peeters, "Predicted field-dependent increase of critical currents in asymmetric superconducting nanocircuits," *Phys. Rev. B*, vol. 85, p. 144 511, 14 Apr. 2012. DOI: `10.1103/PhysRevB.85.144511`.

[60] B. A. Mazin, "Microwave kinetic inductance detectors," Ph.D. dissertation, California Institute of Technology, 2004. [Online]. Available: `http://web.physics.ucsb.edu/~bmazin/Papers/2004/Mazin/Caltech%20Thesis%202004%20Mazin.pdf`.

Chapter 3

Experimental Background

3.1. LEKID design, simulations, and useful resources

A starting point of most designs is an analytical calculation of the capacitance C and the kinetic inductance L_k of the circuit in Fig. 2.1, to estimate the KIDs resonance frequency.

3.1.1. Interdigitated capacitors

For an IDC, as in Fig. 2.2, Ref. [1] gives the analytical equations necessary to calculate C. We are typically interested in the simplest stratification described in Ref. [1], with infinite media below (substrate) and above (air) the IDC. The metallization ratio of an IDC is

$$\eta = \frac{W}{W+G}, \tag{3.1}$$

with W the width of a finger and G the gap between two fingers. For $N > 3$ fingers with an overlap between electrodes of length L and on a substrate with relative dielectric constant ε_s

$$C_{IDC} = (N-3)\frac{C_I}{2} + 2\frac{C_I C_E}{C_I + C_E}. \tag{3.2}$$

Here C_I and C_E are the results of conformal mapping techniques

$$C_I = \varepsilon_0 L \left(\frac{K(k_{I\infty})}{K(k'_{I\infty})} + \varepsilon_s \frac{K(k_{I\infty})}{K(k'_{I\infty})} \right), \tag{3.3}$$

$$C_E = \varepsilon_0 L \left(\frac{K(k_{E\infty})}{K(k'_{E\infty})} + \varepsilon_s \frac{K(k_{E\infty})}{K(k'_{E\infty})} \right), \tag{3.4}$$

where $K(k)$ is the complete elliptic integral of the first kind with modulus k and $k' = \sqrt{1-k^2}$. For infinite media

$$k_{I\infty} = \sin\left(\frac{\pi}{2}\eta\right), \tag{3.5}$$

$$k_{E\infty} = \frac{2\sqrt{\eta}}{1+\eta}. \tag{3.6}$$

The equations in Ref. [1] include an additional thin dielectric layer on top of the IDC with relative dielectric constant ε_1. The capacitance of an IDC is thus given by its total size through L and N and increases for a smaller gap between fingers due to the metallization ratio η. The pixel pitch gives the upper limit for the IDC's size, while the minimum finger and gap widths are limited by the minimum achievable dimensions in fabrication.

For planar capacitors, like an IDC, dominated by the TLSs in a thin surface layer, a larger finger width and spacing will reduce the electric field density in the TLS layer, see Sec. 2.5.1. The reduction in participation ratio (Eq. 2.142) means that Q_i will be higher and the TLS frequency noise level will be reduced for a bigger capacitor [2].

3.1.2. Kinetic inductance from thin superconducting strips

We measure the DC resistance of narrow wires from room temperature to below the critical temperature using 4-probe DC structures patterned on each wafer we fabricate. From these measurements, we can determine the critical temperature of the superconductor and the sheet resistance of the superconductor R_s. The sheet kinetic inductance per square for $k_B T, \hbar\omega \ll 2\Delta$ is then given by

$$L_s \approx \frac{\hbar R_s}{\pi\Delta}, \tag{3.7}$$

where

$$\Delta \approx 1.76 k_B T_c. \tag{3.8}$$

A full calculation of the sheet kinetic inductance can be done from Eq. 2.17 and Eqs. 2.33 and 2.34.

The total kinetic inductance for the resonator is

$$L_k = L_s N_{sq}. \tag{3.9}$$

Here $N_{sq} = l/w$, the number of $w \times w$ squares in the total length of the inductor l, with w the width of the strip.

For the hybrid KIDs in Chapter 4, the inductance per square of the β-Ta inductor is high compared to the NbTiN IDC, 54.6 pH/□ against ∼1 pH/□ respectively. In addition, the kinetic inductance of the β-Ta is large compared to the geometric inductance of the inductor ($\alpha_k > 0.9$), so we can estimate the resonance frequency of the KID by

$$\omega_r \approx \frac{1}{\sqrt{L_k C_{IDC}}}, \tag{3.10}$$

where we have ignored the geometric inductance and the capacitance of the coupler.

3.1.3. Three port simulation method

We simulate the resonators in the commercial EM-solver SONNET to get realistic estimates of the resonator's resonance frequency and coupling quality factor. We simulate the resonator as pictured in Fig. 3.1, including a small section of the readout line without readout line bridges. Two ports, one at each side of the readout line at the edge of the simulation box, allow us to simulate the full scattering parameters of the resonator. We find the resonance frequency and coupling quality factor from the simulated S_{21} with Eq. 2.61. Although we can find the resonance with a wide frequency sweep, to get an accurate estimate of ω_r and Q_c, we need a lot of frequency points in a small bandwidth around f_r. In practice, this means that we run a number of frequency sweeps over increasingly narrower frequency ranges until we can retrieve ω_r and Q with a fit to Eq. 2.61.

This approach is time-consuming and will become impractical for a big KID array, where we need to simulate the resonance frequency of each pixel since the IDC finger length will vary between pixels. The authors in Ref. [3] introduced a simulation method worth mentioning here, as it greatly reduces the time it takes to get the resonance frequency and coupling quality factor. We do not need to simulate the full scattering matrix $\mathbf{S}$ to retrieve ω_r and Q_c. Instead, knowing the frequency dependence of the impedances in Eqs. 2.49 and 2.50 is enough. The aptly called "three-port method" introduces a third port in the LEKID, at the connection between the meandered inductor and the interdigitated capacitor, see Fig. 3.1. This port sees the frequency-dependent impedance

$$Z_{in,3} = j\omega L + \frac{1}{j\omega C_t} + R. \tag{3.11}$$

Since all metals and dielectrics in the simulation are lossless, R is not the surface resistance of the superconductor, but the impedance of the readout line as seen through the coupler see Eqs. 2.45 and 2.49.

At ω_r the imaginary part of Eq. 3.11 is 0, as discussed in Sec. 2.2. On resonance $Z_{in,3} = R$, since the imaginary part vanishes. The coupling quality factor Q_c is ob-

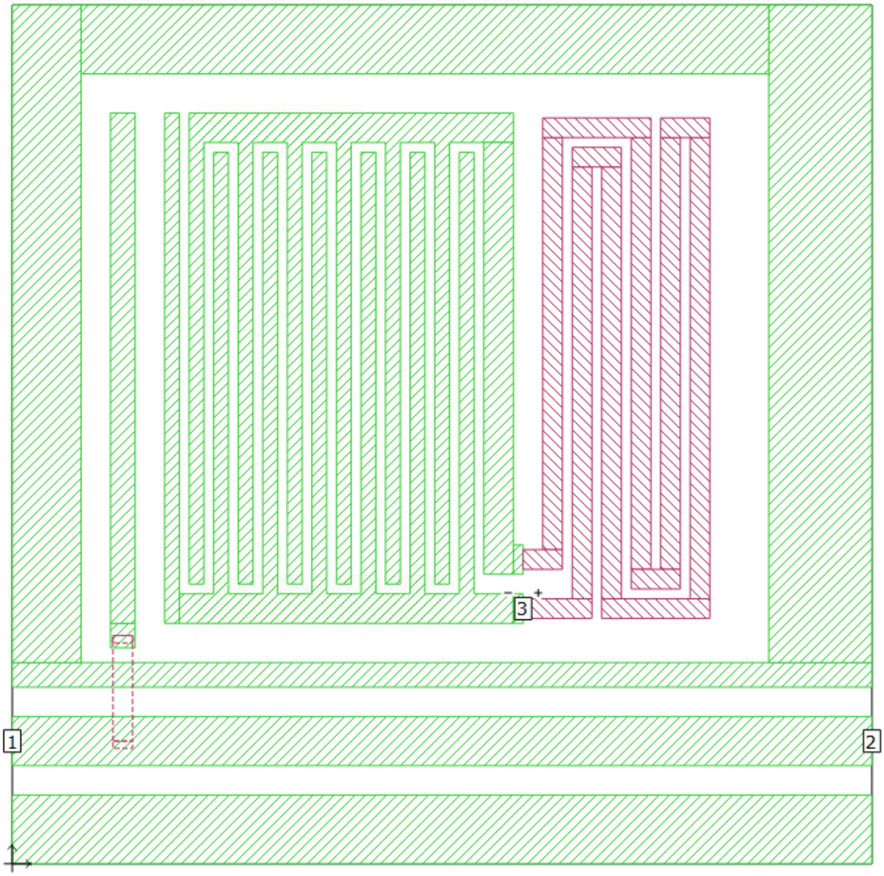

Figure 3.1: Geometry view in Sonnet V18 of a lumped element resonator simulated using the three-port method. Green dashed area is NbTiN with L_s = 1.0 pH/□ and red dashed is β-Ta with L_s = 84.0 pH/□ (40 nm). The coupling bar, which is pictured here at its maximum length (lowest Q_c), runs vertically along the IDC and is connected to the readout line by two vias that pass through a thin layer (0.3 µm) of air $\epsilon_r = 1.0$. Two side-wall ports are connected to the sides of the CPW readout line. A third delta-gap port is placed at the connection between the capacitive (IDC) and inductive (meandered line) of the resonator.

tained from R, on resonance, and the local linear slope in frequency k in the imaginary part of Eq. 3.11

$$Q_c = \frac{k f_r}{2R}. \tag{3.12}$$

Since Eq. 3.11 is linear in frequency, we only need to simulate a few frequency points over a wide frequency range to obtain ω_r and Q_c.

3.1.4. Material selection

There are several considerations when selecting a superconductor for the inductor of the hybrid LEKID. In Eqs. 3.7 and 3.9, we see that for a superconductor with a higher resistivity, we obtain the same L_k, and thus the same resonance frequency, with a shorter inductor. A shorter inductor reduces the size of a KID size, which in turn reduces the pixel pitch of our arrays.

In addition, in Section 2.3.1, we saw that the responsivity of a KID is given by

$$\frac{d\theta}{dN_{qp}} = -\frac{\alpha_k \beta Q_l}{|\sigma| V}\frac{d\sigma_2}{dn_{qp}}, \tag{3.13}$$

which increases for a shorter inductor with a smaller volume. Equation 3.13 depends on the kinetic inductance fraction, α_k, as well, which increases for a higher L_s.

Thus, a high resistivity superconductor, typically a disordered superconductor, provides high responsivity. Furthermore, in Section 2.4, we saw that these superconductors have a higher absorption efficiency. This is why we use β-Ta for the KIDs in Chapter 4 to get a compact KID with a high responsivity and a decent absorption efficiency.

The fundamental limit in resolving power is given by the Fano limit of Eq. 2.119, which scales with $1/\sqrt{\Delta}$. So, for the ultimate resolving power, we want a superconductor with a small gap (Δ) and, thus, a low T_c. A smaller Δ will also increase the sheet kinetic inductance of the film in Eq. 3.7.

To highlight the difference between β-Ta and aluminum, and to give a range of typical values, Table 3.1 gives the properties of different superconductors. The biggest difference between Al and β-Ta is the resistivity, so β-Ta KIDs can be smaller and have a higher responsivity. The values for TiN indicate that, for a given superconductor, a wide range of microwave properties can be obtained by varying the film's thickness or composition.

There is, however, a caveat: using Eq. 2.73, [8], [9], and [10], the bifurcation power, the maximum read power at which we operate the KID, is given by[1]

---

[1] De Rooij, in preparation

Table 3.1: Typical values for different superconductors. The gap Δ is calculated using the BCS relation. The range of values for TiN shows that film thickness or composition can be used to tune the microwave properties of a layer.

Material	T_c (K)	Δ (μeV)	ρ_N ($\mu\Omega$cm)	Reference (and t)
Al	1.29	196	0.8	[4] (55 nm)
TiN	0.7-4.5	100-650	100-1000	[5]–[7]
β-Ta	1.0	152	239	Chapter 4 (60 nm)

$$P_{read}^{bif} = N_0\Delta_0^2 \frac{V\omega_r}{\alpha_k^2}\frac{Q_c}{Q_l^3}, \tag{3.14}$$

and the internal power (Eq. 2.69)

$$P_{int}^{bif} = \frac{N_0\Delta_0^2}{\pi}\frac{V\omega_r}{\alpha_k^2}\frac{1}{Q_l}, \tag{3.15}$$

Here, we assume that the bifurcation power is set by the kinetic inductance non-linearity [8]–[10]. The lowest system- and TLS-noise levels are obtained by operating the KID just below the bifurcation power. The system (amplifier) noise scales inversely with the power on the readout line (Eq. 2.138) and Ref. [11],

$$S_\theta^{system} = \frac{4Q_c^2 k_B T_{noise}}{Q_l^2 P_{read}}, \tag{3.16}$$

such that,

$$S_\theta^{system}(P = P_{bif}) \propto \frac{\alpha_k^2}{N_0\Delta_0^2}\frac{Q_c Q_l}{V\omega_r} \tag{3.17}$$

The TLS frequency noise scales inversely with the square root of the internal resonator power

$$S_f(P = P_{bif})/f^2 \propto P_{int,bif}^{-0.5} \propto \sqrt{\frac{\pi\alpha_k^2}{N_0\Delta_0^2}\frac{Q_l}{V\omega_r}}. \tag{3.18}$$

Converted to phase noise ($S_f/f^2 = S_\theta/(4Q_l)^2$),

$$S_\theta^{TLS}(P = P_{bif}) \propto (4Q_l)^2\sqrt{\frac{\pi\alpha_k^2}{N_0\Delta_0^2}\frac{Q_l}{V\omega_r}}. \tag{3.19}$$

From Eq. 2.131, we know the SNR limited resolving power is proportional to $\overline{H}/\sqrt{N(f)}$ if we assume that the pulse shape is independent of the pulse height. Here H is the average pulse height, which depends on the responsivity in Eq. 3.13 and $N(f)$ is the noise power spectral density which is a combination of the white amplifier noise from Eq. 3.17 and the 1/f frequency noise from Eq. 3.19.

If we consider a detector at a set resonance frequency ω_r and with the same superconductor for the inductor, so N_0, Δ_0 remain unchanged, the SNR for system noise can be optimized as

$$SNR_{system} \propto \sqrt{\frac{Q_l}{Q_c}\frac{1}{V}}. \tag{3.20}$$

In practice, we design our resonators with $Q_l = Q_c$, so the remaining scaling is $1/\sqrt{V}$. For TLS noise

$$SNR_{TLS} \propto \sqrt{\alpha_k} V^{-3/4} Q_l^{-1/4}. \tag{3.21}$$

Depending on the dominating noise contribution, one could increase the kinetic inductance fraction α_k or reduce the quality factor to improve the SNR with respect to the 1/f TLS noise level. Reducing the volume helps improve the SNR with respect to both noise contributions but with varying effects. Note that these relations are purely based on theoretical assumptions and must be experimentally verified to prove their usefulness.

3.2. Cryogenic Setup

The cryogenic system is a pulse tube pre-cooled dilution refrigerator that can reach a base temperature of around 20 mK. This base temperature is reached by mixing the two helium isotopes ^{3}He/^{4}He. Below 1 K this mixture separates in a ^{3}He-rich, or concentrated, and a ^{3}He-poor, or dilute, phase. The concentrated phase is almost pure ^{3}He, while the dilute phase contains a ratio of 6.6% ^{3}He to 93.4% ^{4}He.

As ^{3}He evaporates from the dilute phase, with a rate set by a heater, ^{3}He from the concentrated phase will refill the ^{3}He content in the dilute phase. Diluting ^{3}He from the rich phase into the dilute phase requires heat, which is taken from the sample stage, thus cooling it down.

The cryostat has three shields, one vacuum shield, and shields at 30 K and 3 K. Fig. 3.2 shows a cut of the cryostat shields and sample stage, in which the filter holders on each shield are visible. The sample stage pictured in Fig. 3.3 has two additional filter holders, one at the input of the corrugated snout and one at the sample holder. The sample stage has a box-in-box design, conceptually similar to

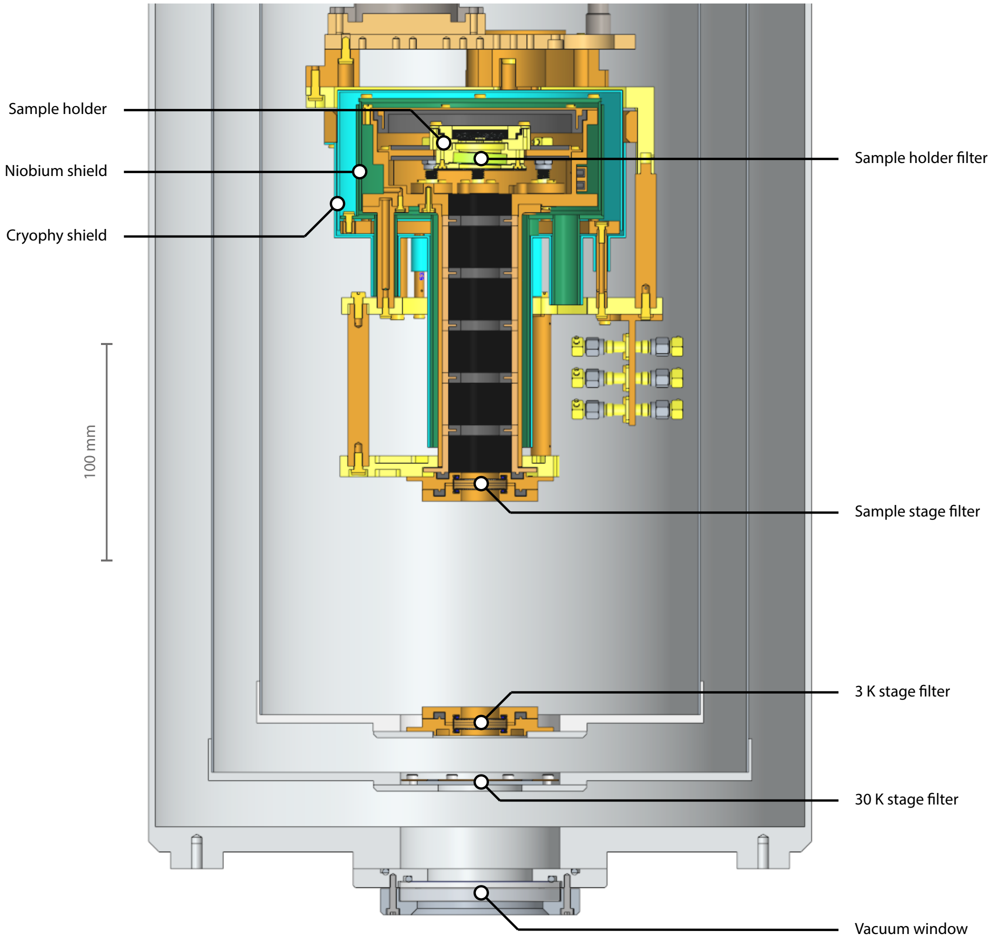

Figure 3.2: Cut of the cryostat shield and sample stage. Each shield (Vac, 30K, and 3K) is equipped with a filter for optical access to the sample stage. The filter on the vacuum shield is referred to as the vacuum or cryostat window. The sample stage has two filter holders, one at the opening of the black-coated snout and one on the sample holder. Details of the sample stage are visible in Fig. 3.3.

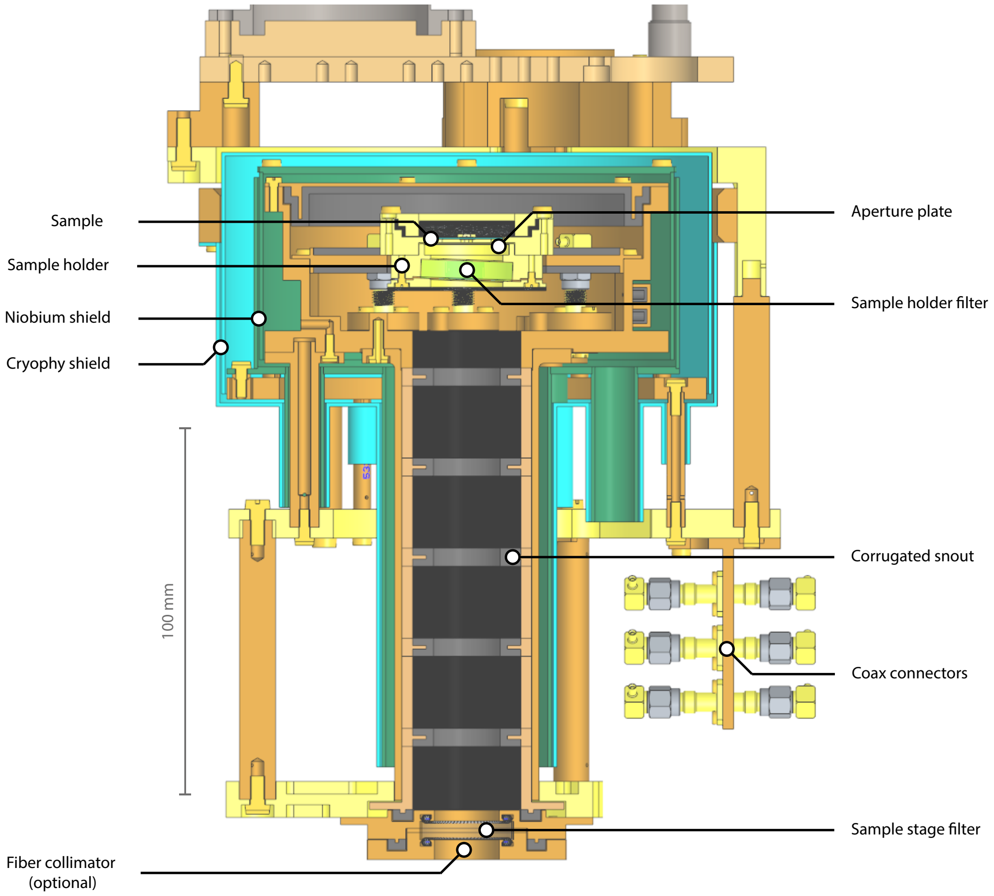

Figure 3.3: Sample stage. The entire stage is cooled down to the mixing chamber (MXC) temperature, typically 100 mK. KID chips are mounted in a box-in-box sample stage to shield them from radiation from the 3 K stage. The corrugated snout, internally coated with black, carbon-loaded epoxy, absorbs light from off-normal incidence. The sample stage is surrounded by two magnetic shields, a superconducting niobium shield, and a Cryophy shield. Coax connectors, see Fig. 3.4, are on the side of the sample holder. The sample holder contains 1 filter, and can be equipped with various aperture plates to limit the amount of light falling on the Chip. The distance between the sample holder and the opening of the snout, with a 1 inch diameter, is 150 mm, for an opening angle ($\theta = \tan^{-1}(r/l)$) of 4.8°, with r the radius of the aperture and l the distance from the sample. There is a limiting aperture with a diameter of 1 inch for the detector looking at room-temperature, located at the 30 K stage at a distance of 353 mm from the sample (see Fig. 3.3 which gives an opening angle of 2°. The filter at the entrance of the snout can be replaced with a fiber collimator mounted on a lid. This version of the setup is graphically represented in Fig. 4.2.

[12], [13], to shield the sample from stray light coming from the 3 K stage of the cooler. The stage is surrounded by two magnetic shields, a superconducting niobium shield, and a CRYOPHY® shield.

Depending on the requirements of each measurement, the filter holders can be equipped with optically transparent windows to allow for room-temperature optical access (used in Chapter 6) or with closed lids to create a dark setup (used in Chapter 7). For experiments where the sample is illuminated by a fiber, the filter holder at the entrance of the sample stage is replaced with a fiber collimator as in Fig. 4.2 (used in Chapter 4).

3.2.1. Microwave readout

We use the homodyne readout scheme illustrated in Fig. 3.4 to measure the complex transmission S_{21}, where the output of a signal generator (Agilent E8257D) with an output power of 20 dBm is split into a reference and a signal that passes through the sample. This second signal is modified by the complex transmission coefficient of the resonator (S_{21}). At the mixer (MITEQ IRM0218LC1Q), the two signals are combined with a 90-degree phase shift, which demodulates the signal in an in-phase (I) and a quadrature (Q) component. An ADC (National Instruments PXI-5922) digitalizes the output of the mixer.

The generated signal is first attenuated with between 73 and 135 dB of attenuation, set by a combination of fixed attenuators and a variable attenuator (Weinschell 8310), to reach the desired readout-signal level on the sample. The readout power at the sample, P_{read}, is calibrated by measuring the transmission through two identical input lines, including attenuation, with the sample replaced by a short cable. After the sample, the signal is amplified to the reference signal level, where a combination of amplifiers and variable attenuators (Weinschel 8310) are used to reach an input level of -5 dBm at the IQ mixer input.

Attenuators and amplifiers introduce thermal noise on the readout signal. Thermal fluctuations create a voltage over a resistor of value R given, in the Rayleigh-Jeans limit that is applicable for GHz frequenyes, by

$$V_N = \sqrt{k_B T R}\sqrt{BW} \tag{3.22}$$

with T the physical temperature of the resistor and BW the bandwidth. If the resistor matches the rest of the readout chain, i.e., the resistor sees a load of $R_l = R$, this voltage generates a power spectral density of $S_n = k_B T$, which has a unit of watts per hertz (W/Hz).

The noise contribution from an amplifier is specified by an equivalent input noise temperature T_n, where the amplifier is treated as a noiseless amplifier with input noise

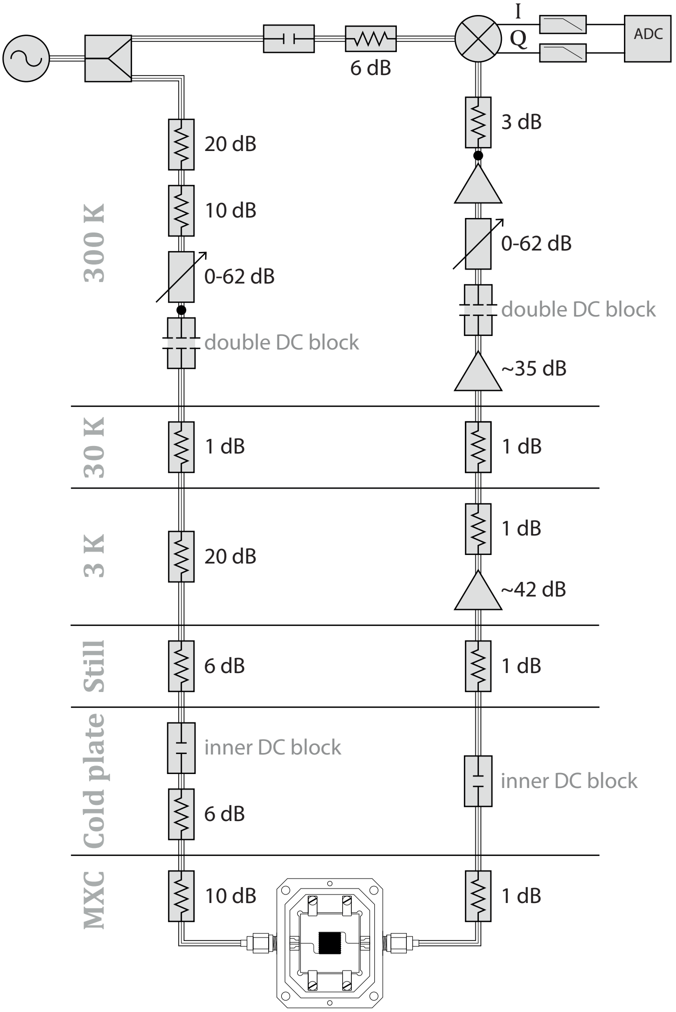

Figure 3.4: The microwave components in the readout system. The room temperature coax cables are ∅3.58 mm copper. At 30 K, the cables are ∅2.19 mm steel. At the input, the cables from the 20 dB attenuator up to the 1 dB attenuator at the mixing chamber (MXC)—or "sample stage"—are ∅0.86 mm CuNi. Between the two 1 dB attenuators, the cable is ∅2.30 mm Al, and before the first amplifier ∅0.86 mm NbTi. The adjustable attenuators (Weinschel 8310) set the read power at the sample. For measurements between 4-8 GHz, the amplifier at the 3 K stage is a Low Noise Factory LNF-LNC4_8C, and the warm amplifier at 300 K is a MITEQ LNA-30-04000800-07-10P. Alternatively, they can be replaced by a Low Noise Factory LNF-LNC2_6A and an MITEQ LNA-30-02000600-09-10P for measurements between 2-6 GHz. For the S_{21} measurements, the section above the black dots is replaced by a VNA (Keysight N5230A PNA-L).

$k_B T_n BW$. The noise contribution from a chain of amplifiers can be characterized by an equivalent system noise temperature

$$T_{sys} = T_{n1} + \frac{T_{n2}}{G_1} + \frac{T_{n3}}{G_1 G_2} + \ldots, \tag{3.23}$$

with G_i the gain of the element and T_{ni} the input noise temperature of the element. The noise spectral density (N_0) at the output of the chain is then given by

$$N_0 = G_s k_B (T_0 + T_{sys}), \tag{3.24}$$

With G_s the total gain of the chain and T_0 the input noise temperature.

Attenuators ($G < 1$) can be included by defining the equivalent noise temperature of an attenuator

$$T_{n,a} = \frac{1-G}{G} T_a \tag{3.25}$$

with T_a the physical temperature of the attenuator. The noise contribution of a single attenuator, $(1-G)T_{n,a}$, with strong attention ($G \ll 1$) is given by its physical temperature, see Eq. 3.24.

3.2.2. System Noise Temperature Calculations

Since we use a homodyne detection scheme, mixing two signals of the exact same frequency, the frequency noise of the signal generator is essentially negated. In this case, we can treat the attenuators at room temperature as an input thermal noise $T_0 = G_{300K} * T_{300K}$, with G_{300K} the total attenuation at room temperature, which is between 30 and to 92 dB, and T_{300K} the total equivalent noise temperature ($Tsys$) of the room temperature attenuators (Eq. 3.24). Since the total attenuation of the room temperature amplifiers is $\ll 1$, $T_0 = 300$ K.

To reduce the 300 K input to a noise temperature on the scale of the lowest temperature of the cold stage (20 mK), the total cold attenuation in the system (30 K → MXC @ 20 mK) has to be at least equal to the difference in temperature between (40 dB). The total thermal input noise $T_{in} = G(T_0 + T_{sys})$ of the input line, from the warm electronics to the sample, amounts to 0.16 K for an MXC temperature of 20 mK.

At the sample, we now have a signal-to-noise ratio S_i/N_i, with N_i the strongly attenuated thermal noise from the attenuators. In the output line, from the sample to the warm electronics, the signal is amplified by one cold amplifier and two warm amplifiers. The sample signal is matched to the reference signal at the mixer with the variable attenuator. In between the amplifiers are some fixed attenuators to reduce

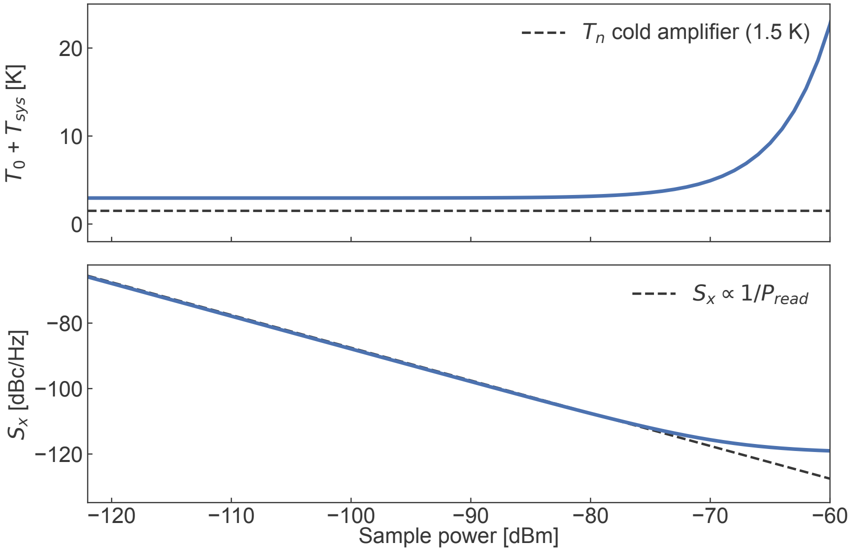

Figure 3.5: The total noise temperature and corresponding system noise level $S_{A,\theta}^{system}$ for the 4–8 GHz setup. At typical readout powers around -100 dBm, $T_{sys} = 2.72$ K. The black dashed line in the top panel indicates the equivalent noise temperature of the cold amplifier. In the bottom panel, the black dashed line indicated the expected $1/P_{read}$ scaling of the noise level for a constant system noise temperature from Eq. 3.27. At higher sample powers, the output variable attenuator in Fig. 3.4 is set to a higher attenuation, reducing the total gain of the system. Due to the reduction in total gain, the variable attenuator and subsequent RF components start to dominate the system noise temperature.

input reflections. Each of these amplifiers, and the attenuators in between, will add thermal noise to the readout signal.

The goal is to create a readout chain that is only limited by the equivalent noise temperature of the first amplifier, which has the lower noise temperature. From Eq. 3.23, we see that the product of the gain and attenuation of all preceding elements will reduce the noise temperature of each subsequent component after the first amplifier. As long as this product remains large for each subsequent element, the cold amplifier will be the dominant contribution to the system noise, and the warm amplifiers with a high noise temperature will hardly matter. In addition, we see that attenuators before the first amplifier have a relatively large impact on the system noise temperature. This is why we use superconducting cables, with 0 loss and low thermal conductivity between the sample and the first amplifier.

The first amplifier is a cryogenic LNA and is, depending on the frequency band, either a LNF-LNC4_8C (4-8 GHz) or a LNF-LNC2_6A (2-6 GHz) with average equivalent noise temperatures T_N of 1.5 K and 1.9 K respectively (@ $T_{amb} = 4$ K). Before the first amplifier, there are two attenuators of 1 dB, one at the base temperature (20 mK) and one at the still (1 K). The warm amplifier with a gain of ∼35 dB has a noise temperature of ∼42 K [4-8 GHz LNA-30-04000800-07-10P] or ∼59 K [3-6 GHz LNA-30-02000600-09-10P]. The IQ-mixer has a conversion gain of -6 dB and equivalent noise temperature of $\sim 1 \times 10^3$ K, and the ADC has an equivalent noise temperature of 10^6 K [11]. The system noise temperature of the output line, from the sample to the output of the ADC, can then be calculated using Eq. 3.27

For our highest readout power of -70 dBm we get a total system noise temperature T_{sys} (Eq. 3.24) of 4.7 K (4-8 GHz) and 5.3 K (2-6 GHz) for a sample stage temperature of 20 mK. Note that the system noise temperature depends on the desired readout power since it influences the setting of the variable attenuator, where we need more attenuation for a higher readout power, as shown in Figure. 3.5. At higher readout powers, the total gain in the system is lower, so the variable attenuator and the subsequent RF components in Fig. 3.4 start to dominate the system noise temperature.

The attenuators on the input line contribute an input noise temperature T_0 of 0.15 K for an MXC temperature of 20 mK. The total noise temperature, $T_{in} + T_{sys}$ from Eq. 3.24, is then 4.84 K (4-8 GHz) for a readout power of -70 dBm.

The two 1 dB attenuators in Fig. 3.4 at the sample stage and 1 K contribute roughly 0.33 K to the system noise temperature. We have 2 dB of attenuation before the cold amplifier to attenuate possible input reflections from the amplifier. At this moment, it is unclear if we really need the 2 dB of attenuation or if we could work with just 1 dB of attenuation or even without attenuators before the first amplifier. For a typical readout power of -100 dBm, where the coldest stages limit the system noise temperature as in Fig. 3.5, removing the 1 dB attenuator at 1 K reduces the system noise temperature by 0.85 K to a system noise temperature of 1.87 K (4-8 GHz @ 20 mK), since we reduce the added noise temperature of the attenuator itself and reduce the total attenuation before the cold amplifier (Eq. 3.27.

For a sample power of P_{read}, the amplifier noise level is given by [11]

$$S_{I,Q}^{system} = \frac{k_B T_{sys}}{P_{read}}. \tag{3.26}$$

The typical readout coordinates (A, θ) are related to (I, Q) by the size of the KID circle ($r_c = Q_l/2Q_c = (1 - S_{21,min})/2$) such that $S_\theta = S_Q/r^2$ and $S_A = S_I/r^2$ are equal if the center of the resonance circle is chosen at the origin $x_c = 0$.

$$S_{A,\theta}^{system} = \frac{k_B T_{sys}}{r_c^2 P_{read}} \tag{3.27}$$

which scales inversely with the power on the readout line P_{read}^{-1}, as long as the system noise temperature is power independent as illustrated by Fig. 3.5

For the measurement in Fig. 2.8, P_{read} = -102 dBm, T_{sys} = 2.7 K (4–8 GHz), and T_{in} = 0.22 K for a base temperature of 100 mK, and $r_c = 0.5$. According to Eq. 3.27, this should lead to an amplifier noise contribution to the power spectral density at the sample of -86 dBc/Hz (dBc: dB relative to the carrier signal), which is consistent with the white amplifier noise level in Fig. 2.8. Removing the 1 dB attenuator in the output line located at the still would reduce the system noise temperature by 0.33 K.

3.3. Detector Efficiency Measurements Setup

To measure the detector efficiency of our detectors, we need to record single photon hits on the detectors and compare the count rate to the predicted number of incident photons based on the source power. Ideally, we measure the intensity in the beam that illuminates the detectors and the photon count rate simultaneously.

We define the detector efficiency[2] as the ratio between the measured photon count rate and the number of photons incident on the KID. This efficiency includes the efficiency of the microlens array, the absorption efficiency of the superconductor, and the filling factor of the inductor lines. The setup discussed here is designed to illuminate a KID array with a uniform beam such that all KID pixels see the same incident power. This setup is used in Chapter 6 to measure the detector efficiency of an anti-reflection coated KID array. A similar setup design that, in addition, simulates the f/# and telecentricity of the telescope is discussed in Ref. [14].

3.3.1. Design

Our room temperature setup is graphically represented in Fig. 3.6. We use a commercial light source, an Oriel Cornerstone monochromator, with a quartz tungsten halogen lamp, a filter wheel, a set of three gratings, and slits on both the in- and output ports. The output of the monochromator is captured by an integrating sphere (IS), which creates a uniform illumination source. Light from this source is collimated by a single lens, after which it is split into a beam that travels to the sample mounted in the cryostat and a beam that is used for reference measurements, for which the beam is focussed on a commercial photodiode. All of the components after the IS are mounted in a standard Thorlabs 30-mm cage system. The standard size of optical components in this cage system is 25 mm ∅.

The custom Oriel Cornerstone 260 monochromator is equipped with gratings for

---

[2] Another term for this efficiency is the "quantum efficiency" of a detector which is used for both the photon-to-electron conversion ratio and the ratio between incoming and detected photons of a CCD.

the VIS-NIR. For the experiment in Chapter 6, we use the 74063 high-resolution grating, which covers 200-1400 nm, has a blaze wavelength of 350 nm, and a line density of 1200 lines/mm. The input of the monochromator is a 100-W quartz tungsten halogen (QTH) lamp. Both the in- and output of the monochromator are equipped with micrometer adjustable slits. The width of these slits gives a trade-off between throughput and resolution, and for the fully open slit (3 mm), we have a minimum energy resolution of roughly $E/\delta E = 35$. For the experiments in Chapter 6 the slits are fully open. A filter wheel with 600 and 1000-nm cut-on filters rejects the higher mode numbers from the grating.

The output bundle of the monochromator is captured by a 50-mm diameter integrating sphere (IS) [Thorlabs IS200-4]. An achromatic doublet is placed at a focal distance from one of the IS ports to create a uniform and collimated beam with a 25-mm diameter. For a point source, the irradiance at the edge of the lens can be approximated by $E_e = E_0[\cos(\phi)]^4$ [15], [16], with E_0 the irradiance at the center and ϕ the angle between the on-axis ray and the ray to the edge of the lens. The beam divergence can be estimated by $\theta = d/f$, where $\theta/2$ is the divergence angle from the propagation direction of the beam, d is the diameter of the source, in this case the IS port [3 mm], and f is the focal length of the lens. The beam divergence improves for a longer focal length lens, but at the same time, the solid angle extended from the source, and thus the power in the beam, decreases. Concerned about the power levels on the photodiode, we chose a 25-mm diameter achromatic doublet with a relatively short focal length of 100 mm and a 400-1100 nm AR coating [Thorlabs AC254-100-AB-ML]. The estimated full divergence angle for the beam is 1.72°, and the expected irradiance at the edge of the lens is 97% of the irradiance at the center of the lens.

The measurement setup is mounted on an optical table that slides underneath the cryostat. When mounted on the optical table, the output port of the monochromator does not fit underneath the cryostat, so after the collimating lens, we use two right-angle mirrors to bring the beam closer to the surface of the optical table. The last right-angle mirror in Fig. 3.6 couples the beam into the cryostat.

A cube-mounted non-polarizing 90:10 (R:T) beamsplitter (BS) splits the beam [Thorlabs BS028 or BS029, depending on the wavelength, mounted in a DFM1T4 + DFM1B/M]. Roughly 90% of the beam is reflected by the beamsplitter. It is focussed onto a calibrated photodiode [Thorlabs S130C] with the same achromatic doublet used to collimate the output of the IS [Thorlabs AC254-100-AB-ML]. The path between the collimating lens and the photodiode is covered by a 1-inch diameter lens tube, so the photodiode cannot receive power from sources other than the focusing lens. The photodiode can measure powers between 400 and 1100 nm, and the mirrors, windows, and lenses in the setup are AR-coated for the same wavelength range.

The beamsplitter transmits the other ten percent of the beam. We use an uneven, i.e., not 50:50, beamsplitter since the desired power in the input beam, which yields

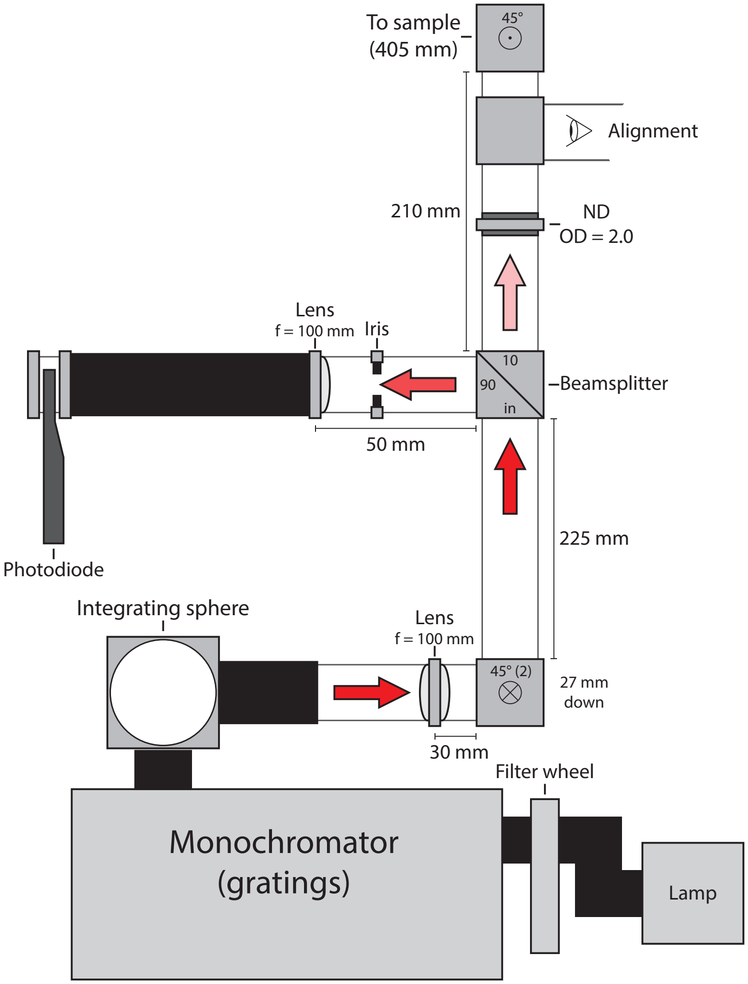

Figure 3.6: Graphical representation (not to scale) of the detector efficiency setup, mounted on an optical table (top-view). The bundle from the monochromator is captured by a 50-mm diameter integrating sphere (IS). A 100-mm focal length lens creates a collimated beam with a diameter of 25 mm. Two right-angle mirrors bring the beam closer to the surface of the optical table. A 90:10 beamsplitter splits the beam into an input- and a reference beam. The input beam passes through an ND filter with an optical density of 2.0 before it is coupled into the cryostat by a right-angle mirror (input mirror). The cryostat is centered above this final mirror. The cube before the input mirror is normally empty, but a right-angle mirror can be inserted so the cryostat window can be seen via the input mirror. This option is used to align the setup, by eye, to the cryostat vacuum window. The reference beam is focused on a commercial photodiode. The diameter of all optical components is 25 mm. Given dimensions do not include the internal distances of the cubes. The beam travels 1.5 inches in each right-angle mirror cube, 2 inches in the beamsplitter cube, and 1.9 inches in the input mirror cube. Part numbers are given in the main text.

a measurable photon count rate (∼100 photons/s), is in the order of picowatts. At the same time, the optimal range of the photodiode is in the order of nanowatts. In addition to the uneven ratio of the 90:10 beamsplitter, we place a neutral density filter (ND) with optical density 2.0 [Thorlabs ND20B] in the path of the input beam to further balance the powers between the KID and the photodiode. The input beam is coupled into the cryostat by a tip and tilt adjustable right-angle protected aluminum mirror [Thorlabs PF10-03-G01 mounted in KCB1C/M], which we refer to as the "input mirror."

The optical table is aligned to the cryostat vacuum window by placing a mirror in the "open" cube located just before the input right-angle mirror. This creates a "periscope" that looks through the vacuum window via the input right-angle mirror, as illustrated in Fig. 3.6. The field of view can be limited to slightly bigger than the vacuum window using an adjustable iris just above the input mirror. Moving the optical table, the input mirror can be aligned, by eye, with the vacuum window. In the future, a KID pixel identification setup will be attached to the currently open cube, which contains a commercial CCD camera that can be used to align the setup to the KID array.

All the optical components except the monochromator and lamp housing are enclosed in a custom optical enclosure. The enclosure is partly open on one side so the optical table can slide underneath the cryostat. On all other sides and the top, the enclosure is closed with foam panels. After alignment, the setup is blacked out with a laser curtain that is fastened around the vacuum shield of the cryostat and covers the optical enclosure on the optical table. The dark count rate of the setup is discussed in Chapter 6.

3.3.2. Verification

To verify the setup, we place the focussing lens at the location of the KID array, 375 mm above the input mirror, to directly measure the power incident on the array, without the cryostat windows. We can calculate the expected normalized monochromator output power based on the normalized intensity of the 100-W QTH lamp and the efficiency of the monochromator's grating to see how much our output power will vary over our wavelength range. The available efficiency curves are plotted in Fig. 3.7a, including the right-angle mirrors in the beam's path, but we ignore the transmission of the collimating lens and the IS reflectance since both are practically flat between 400 and 1100 nm. We do not have data on the full system efficiency of the monochromator system, which includes, in addition to the grating in Fig. 3.7, the efficiency of multiple mirrors and an F-matcher between the lamp and monochromator. In addition, the supplier specifies that the grating efficiency can only be used as a guide and not as absolute data.

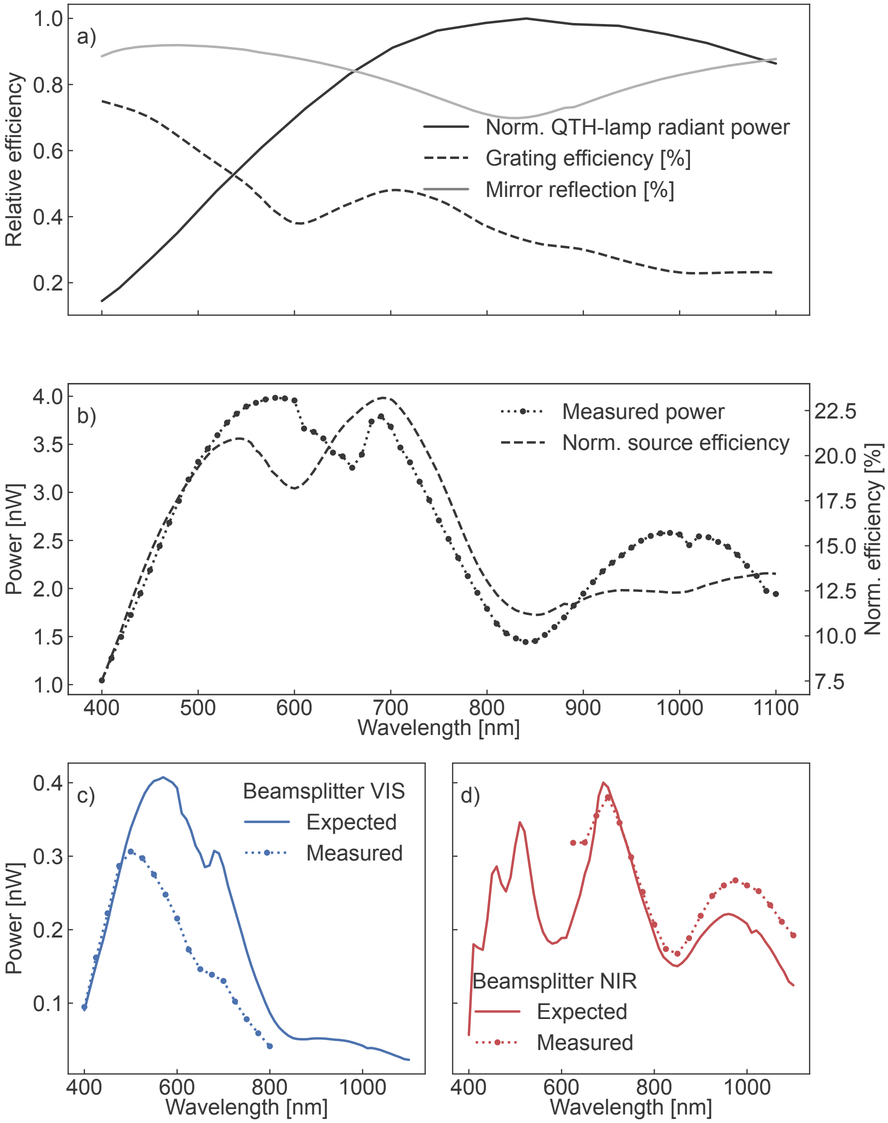

Figure 3.7: **a)** Normalised efficiency or power from the source components. The curve for the grating is the relative efficiency and was measured by the supplier with an in-plane near Littrow configuration. The grating efficiency is not the full efficiency of the monochromator. The mirror reflection is the total reflection from the three mirrors in the path between the source and sample. **b)** Measured source power at the sample location without the ND filter or beamsplitter cubes. The dashed line shows the normalized source efficiency based on the efficiencies in panel a. Note that there are three right-angle aluminum mirrors between the monochromator output and the cryostat input. **c) and d)** Measured power at the sample location with different beamsplitters compared to the expected power based on the measurement in panel b) and the beamsplitter characterization provided by the supplier.

The power recorded by the photodiode when the focussing lens is located at the KID lens surface and without the beamsplitter and ND-filter installed is given in Fig. 3.7b. From the intensity and efficiency curves in Fig. 3.7a, we know that the QTH-lamp power drops at shorter wavelengths, and we get reduced power at longer wavelengths due to the grating efficiency. The aluminum mirrors absorb power at around 850 nm. These effects are visible in Fig. 3.7b, plotting the measured power and expected relative source efficiency together.

Based on initial measurements, there was some doubt about the accuracy of the available beamsplitter transmission/reflection curves. We measured the power at the sample location with and without the beamsplitters installed. We should then be able to retrieve the measured power with the beamsplitter by combining the measured power without the beamsplitter and the beamsplitter's transmission curve from the supplier's datasheet. The different measurements and the expected power based on the beamsplitter data sheets are given in Fig. 3.7c and Fig. 3.7d. The match between measurement and calculated power is poor; see Fig. 3.7c. Since the measurements in Figs. 3.7b-d show the transmission of the beamsplitters when they are mounted in our setup, we use our own characterization of the beamsplitters in the rest of the analysis.

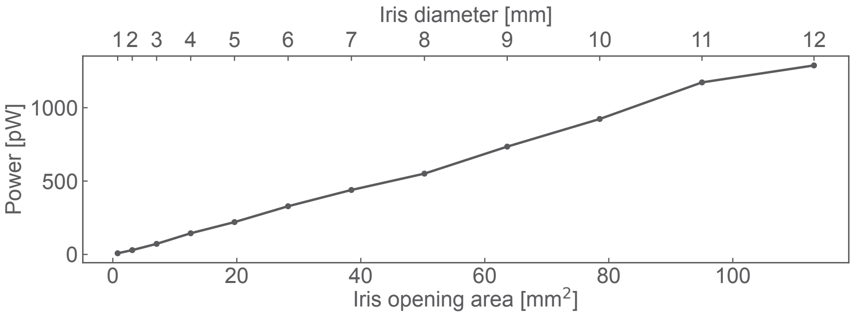

Figure 3.8: Power recorded by photodiode versus iris opening area. The iris is placed before the lens that focuses the 25-mm diameter beam on the photodiode (see Fig. 3.6). The measured power scales linearly with the opening area so the beam is radially uniform. Measurement is performed at 600 nm with 1-mm increment steps in iris diameter up to the maximum opening diameter of 12 mm.

To measure the radial uniformity of the beam, we place an iris diaphragm in front of the focusing lens [Thorlabs SM1D12C]. The opening of the iris diaphragm can be varied in diameter between 1 and 12 mm, with a laser engraved scale, to allow only a fraction of the beam to pass to the focusing lens. The measured power plotted in Fig. 3.8 scales linearly with the cross-sectional area of the iris, so the beam is radially uniform. For the measurements in Chapter 6, the entire array falls within a circle with a 3-mm diameter. We did not check the lateral uniformity of the beam.

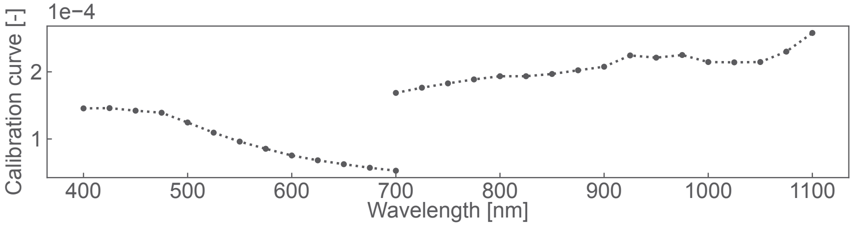

Figure 3.9: Calibration curve that links the power measured by the photodiode in the reference arm (see Fig. 3.3) to the power incident on the sample. The calibration curve ncludes the transmission of the beamsplitter and ND20 filter but not the transmission of the cryostat filters (∼80%). The magnitude of the calibration curve shows the required power level difference between the photodiode and KID. Jump in power at 700 nm is due to different beamsplitters with different wavelength ranges.

We check whether the beam is properly collimated by measuring the power at various distances from the input right-angle mirror with a focussing lens and the photodiode. We see that the measured power decreases with distance to the right angle mirror, so the beam is divergent at this distance. This means we cannot directly use the recorded power in the reference arm to calculate the power at the KID array. Since we measured the power with the photodiode located in the reference arm, as in Fig. 3.6, and at the sample location, see Figs. 3.7b–d, we can calculate a calibration curve that gives the power at the sample based on the power measured in the reference arm. This calibration curve is given in Fig. 3.9 and includes the transmission of the beamsplitter and the ND20 filter. In Chapter 6, we use this calibration curve to calculate the power at the sample when we measure single photons with the KID and use the photodiode to measure both the power and stability of the source as in Fig. 3.6. In the future, we can reduce the beam's divergence by introducing a smaller pinhole at the opening of the IS or by adjusting the setup for a collimating lens with a longer focal length.

We use the measured power from Figs. 3.7c and 3.7d and the transmission curve from the ND filter's datasheet to calculate the power plotted in Fig. 3.10. This is the total power contained in the 25-mm diameter beam incident on the KID-array. We verified the transmission curve of the ND filter by measuring the transmitted power with and without filter using the calibrated photodiode. The power in Fig. 3.10 corresponds to a photon count rate in the range of 100 to 1000 photons per second for a 100% efficient lens-coupled detector with a 150×150 μm^2 pixel size. This range matches the desired count rates, where there are enough photons per second to measure accurate count rates but not too many such that photon pulses start to overlap and become difficult to distinguish. For devices with low detector efficiency, for ex-

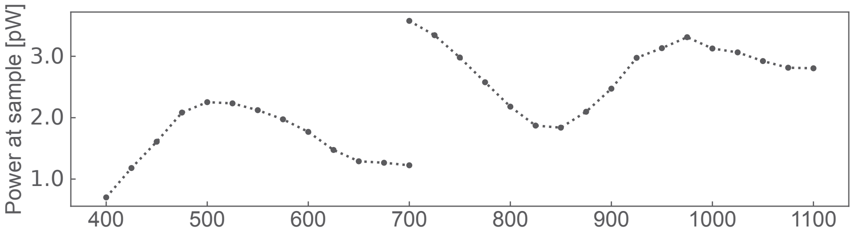

Figure 3.10: Power contained in the 25-mm beam incident on the KID array, without the cryostat filters. Calculated from the measured power in Figs. 3.7c and 3.7d and the ND20 filter transmission curve. Jump in power at 700 nm due to different beamsplitters with different wavelength ranges. For a 100% efficient lens-coupled detector with a 150×150 μm^2 pixel size, this power corresponds to a photon count rate between 100 and 1000 photons per second. If desired, the power level can be increased by replacing the ND20 filter with a filter with a lower optical density or by removing it altogether. Jump in power at 700 nm is due to different beamsplitters with different wavelength ranges.

ample, without lens arrays, the ND20 filter can be removed or replaced by a filter with a lower optical density filter.

Bibliography

[1] R. Igreja and C. J. Dias, “Analytical evaluation of the interdigital electrodes capacitance for a multi-layered structure,” *Sens. Actuators Phys.*, vol. 112, no. 2, pp. 291–301, May 2004, ISSN: 0924-4247. DOI: `10.1016/j.sna.2004.01.040`.

[2] J. Gao, M. Daal, J. M. Martinis, *et al.*, “A semiempirical model for two-level system noise in superconducting microresonators,” *Appl. Phys. Lett.*, vol. 92, no. 21, p. 212 504, May 2008, ISSN: 0003-6951. DOI: `10.1063/1.2937855`.

[3] D. S. Wisbey, A. Martin, A. Reinisch, and J. Gao, “New method for determining the quality factor and resonance frequency of superconducting micro-resonators from sonnet simulations,” *J. Low Temp. Phys.*, vol. 176, no. 3, pp. 538–544, 2014. DOI: `10.1007/s10909-014-1099-3`.

[4] Baselmans, J. J. A., Bueno, J., Yates, S. J. C., *et al.*, “A kilo-pixel imaging system for future space based far-infrared observatories using microwave kinetic inductance detectors,” *Astronomy & Astrophysics*, vol. 601, A89, 2017. DOI: `10.1051/0004-6361/201629653`.

[5] H. G. Leduc, B. Bumble, P. K. Day, *et al.*, “Titanium nitride films for ultrasensitive microresonator detectors,” *Appl. Phys. Lett.*, vol. 97, no. 10, p. 102 509, Sep. 2010, ISSN: 0003-6951. DOI: `10.1063/1.3480420`.

[6] E. F. C. Driessen, P. C. J. J. Coumou, R. R. Tromp, P. J. de Visser, and T. M. Klapwijk, “Strongly Disordered TiN and NbTiN s-Wave Superconductors Probed by Microwave Electrodynamics,” *Phys. Rev. Lett.*, vol. 109, p. 107 003, 10 Sep. 2012. DOI: `10.1103/PhysRevLett.109.107003`.

[7] P. C. J. J. Coumou, M. R. Zuiddam, E. F. C. Driessen, P. J. de Visser, J. J. A. Baselmans, and T. M. Klapwijk, “Microwave Properties of Superconducting Atomic-Layer Deposited TiN Films,” *IEEE Trans. Appl. Supercond.*, vol. 23, no. 3, pp. 7 500 404–7 500 404, 2013. DOI: `10.1109/TASC.2012.2236603`.

[8] J. Zmuidzinas, “Superconducting microresonators: Physics and applications,” *Annu. Rev. Conden. Ma. P.*, vol. 3, no. Volume 3, 2012, pp. 169–214, Mar. 2012, ISSN: 1947-5462. DOI: `10.1146/annurev-conmatphys-020911-125022`.

[9] A. V. Semenov, I. A. Devyatov, P. J. de Visser, and T. M. Klapwijk, “Coherent excited states in superconductors due to a microwave field,” *Phys. Rev. Lett.*, vol. 117, p. 047 002, 4 Jul. 2016. DOI: `10.1103/PhysRevLett.117.047002`.

[10] L. J. Swenson, P. K. Day, B. H. Eom, *et al.*, “Operation of a titanium nitride superconducting microresonator detector in the nonlinear regime,” *J. Appl. Phys.*, vol. 113, no. 10, p. 104 501, Mar. 2013, ISSN: 0021-8979. DOI: `10.1063/1.4794808`.

[11] R. Barends, “Photon-detecting superconducting resonators,” en, Publisher: R. Barends, Ph.D. dissertation, Delft University of Technology, 2009. [Online]. Available: `https://repository.tudelft.nl/islandora/object/uuid%3A574944e6-c3ce-4c86-a511-a88385b22379`.

[12] P. J. de Visser, J. J. A. Baselmans, J. Bueno, N. Llombart, and T. M. Klapwijk, “Fluctuations in the electron system of a superconductor exposed to a photon flux,” *Nat. Commun.*, vol. 5, no. 1, pp. 1–8, Feb. 2014. DOI: `10.1038/ncomms4130`.

[13] J. Baselmans, S. Yates, P. Diener, and P. de Visser, “Ultra Low Background Cryogenic Test Facility for Far-Infrared Radiation Detectors,” *J. Low Temp. Phys.*, vol. 167, no. 3-4, pp. 360–366, May 2012. DOI: `10.1007/s10909-012-0511-0`.

[14] S. R. Meeker, “Darkness: The first microwave kinetic inductance detector integral field spectrograph for exoplanet imaging,” Ph.D. dissertation, University of California, Santa Barbara, 2017.

[15] Labsphere, “Integrating sphere theory and applications,” Technical guide. [Online]. Available: `https://www.labsphere.com/wp-content/uploads/2021/09/Integrating-Sphere-Theory-and-Applications.pdf`.

[16] D. A. Kerr, “Derivation of the "cosine fourth" law for falloff of illuminance across a camera image,” Technical article, 2007. [Online]. Available: `http://dougkerr.net/Pumpkin/articles/Cosine_Fourth_Falloff.pdf`.

Chapter 4

Resolving Power of Visible to Near-Infrared Hybrid β-Ta/NbTiN Kinetic Inductance Detectors

Kinetic Inductance Detectors (KIDs) are superconducting energy-resolving detectors, sensitive to single photons from the near-infrared to ultraviolet. We study a hybrid KID design consisting of a beta phase tantalum (β-Ta) inductor and a NbTiN interdigitated capacitor (IDC). The devices show an average intrinsic quality factor Q_i of $4.3\times10^5 \pm 1.3 \times10^5$. To increase the power captured by the light sensitive inductor, we 3D-print an array of 150×150 μm resin micro lenses on the backside of the sapphire substrate. The shape deviation between design and printed lenses is smaller than 1 μm, and the alignment accuracy of this process is $\delta_x = +5.8 \pm 0.5$ μm and $\delta_y = +8.3 \pm 3.3$ μm. We measure a resolving power for 1545-402 nm that is limited to 4.9 by saturation in the KID's phase response. We can model the saturation in the phase response with the evolution of the number of quasiparticles generated by a photon event. An alternative coordinate system that has a linear response raises the resolving power to 5.9 at 402 nm. We verify the measured resolving power with a two-line measurement using a laser source and a monochromator. We discuss several improvements that can be made to the devices on a route towards KID arrays with high resolving powers.

This chapter was published as K. Kouwenhoven, D. Fan, E. Biancalani, S.A.H. de Rooij, T. Karim, C.S. Smith, V. Murugesan, D.J. Thoen, J.J.A. Baselmans, and P.J. de Visser. *Phys. Rev. Applied* **19**, 034007 (2023).

4.1. Introduction

Kinetic Inductance Detectors (KIDs) [1] are superconducting detectors in which a single visible photon (1-3 eV) creates thousands of quasiparticle excitations through which we can measure the energy of each photon. Compared to semiconductor-based detectors, where a visible photon excites just a few charge carriers, KIDs have zero dark current and read noise. This makes them ideal candidates for photon-starved experiments such as exoplanet spectroscopy, which is one of the most appealing goals of astronomy in the coming decade. Combined with their intrinsic colour resolution and photon arrival timing KIDs are promising detectors for chromatic wavefront sensors, multicolor fluorescence imaging, and order sorting detectors in a spectrometer.

A KID is a superconducting microwave resonator sensitive to a change in its complex conductivity, given by the kinetic inductance (Cooper pairs) and resistance (quasiparticles). A signal with enough energy to break Cooper pairs, creating quasiparticles in the process, will change the resonator's inductance and resistance, shifting the resonance condition. The energy gap of a superconductor is < 1 meV, so an absorbed visible photon (1-3 eV) creates thousands of quasiparticles. The number of quasiparticles created, and thus the magnitude of the response, depends on the energy of the absorbed photon, making visible to near-infrared KIDs energy resolving detectors.

The exact number of quasiparticles created for a given photon energy is uncertain due to the statistical nature of the energy down-conversion process [2], [3]. The statistical uncertainty of this process gives an upper limit to the attainable resolving power ($E/\delta E$) [4], [5] $R_{Fano} \approx (1/2.35)\sqrt{(\eta_{pb}^{max} E_{ph})/(\Delta F)}$ with E_{ph} the photon energy, Δ the superconducting gap energy, $F = 0.2$ the Fano limit for superconductors [4], [5], and $\eta_{pb}^{max} = 0.59$ the pair breaking efficiency [2], [6], [7].

KIDs in Integral Field Units for exoplanet spectroscopy require a resolving power R of $\sim$100. To reach this resolving power, the ideal superconductor for a KID has a low critical temperature T_c corresponding to a low gap Δ. Additionally, for absorber-based KIDs [8]–[12] where the incoming energy is absorbed directly in the inductor, a high resistivity (ρ) superconductor is essential for a high absorption efficiency [13]. A higher resistivity superconductor will, for any KID, reduce the pixel size and increase the responsivity due to the higher kinetic inductance.

In the ongoing search for the ideal KID material [14], several materials have been reported including sub-stoichiometric TiN ($T_c = 0.8$ K, $\rho = 100$ $\mu\Omega$cm) [9], [10], PtSi ($T_c = 0.9$ K, $\rho = 35$ $\mu\Omega$cm) [11] and Hf ($T_c = 0.4$ K, $\rho = 97$ $\mu\Omega$cm) [12]. One of the low T_c elemental superconductors that remains unexplored is beta-phase tantalum (β-Ta) [14], which has a critical temperature of around 0.6 - 1.0 K and resistivity of ≈ 200 $\mu\Omega$cm. The other phase, α-Ta [15], has a lower resistivity and a much higher T_c.

Here, we demonstrate hybrid β-Ta/NbTiN KIDs, where radiation coupling to the beta-phase tantalum (β-Ta) inductor is done using a 3D printed microlens array printed directly on the chip backside. The hybrid design consists of a light-sensitive, low-T_c inductor and a high-T_c capacitor. The inductor is made out of β-Ta, which has a T_c of 1.0 K and a resistivity of 239 $\mu\Omega$cm.

The capacitor is made out of NbTiN with a T_c of 15.2 K. This design approach has been used in Al/NbTiN KIDs to confine the quasiparticles to the sensitive part of the detector [16], [17]. Additionally, NbTiN is resistant to the Hf cleaning steps required for good galvanic contacts between the inductor and capacitor, and provides a practical readout circuit with galvanically connected bridges for high-fidelity arrays.

We show the resolving power of these devices from 402 to 1545 nm, limited by saturation in phase response from $R = 4.6$ at 1545 nm to $R = 4.9$ at 402 nm. An alternative coordinate system that is linear in photon energy, presented in [18], raises the resolving power at 402 nm to 5.9. We demonstrate that the obtained resolving power agrees with a two-line resolving measurement. Finally, we discuss the advantages, and current limitations, of our devices and present a route towards high resolving powers with β-Ta based KIDs.

4.2. Design and Fabrication

We use a hybrid lumped element design (LEKID), consisting of a high resistivity β-Ta inductor and a NbTiN interdigitated capacitor (IDC). The finger lengths of the IDC set the KID frequency spacing, see Fig. 4.1. Each KID capacitively couples to the NbTiN coplanar waveguide (CPW) readout-line through a NbTiN coupling bar, which runs alongside the IDC and galvanically connects to the central line of the CPW with an aluminium bridge on top of a polyimide dielectric support. We use a double-sided coupling bridge, where one bridge connects to both KIDs at either side of the readout-line, see Fig. 4.1. A similar bridge design galvanically connects both CPW ground planes at regular intervals. This design is similar to the one presented in [8]. We have designed two chip variations, one containing 6×6 hybrid KIDs as described here, and one containing 2×6 hybrid KIDs with the other locations in the 6×6 positions filled with design variations and lens alignment test structures.

We use a 350 μm thick c-plane sapphire substrate. The IDC and readout-line are 150 nm of reactive magnetron sputter-deposited NbTiN [19], [20]. The inductor is 60 nm of sputter-deposited β-Ta. The deposition and etching order is NbTiN, polyimide, β-Ta, protection resist, and Al. The resist cap protects the β-Ta inductor during the Al processing steps. Removing the resist patch is the final step in the fabrication process. Before each metal step, the wafer is cleaned with HF, which is critical for a good galvanic contact to the NbTiN layer.

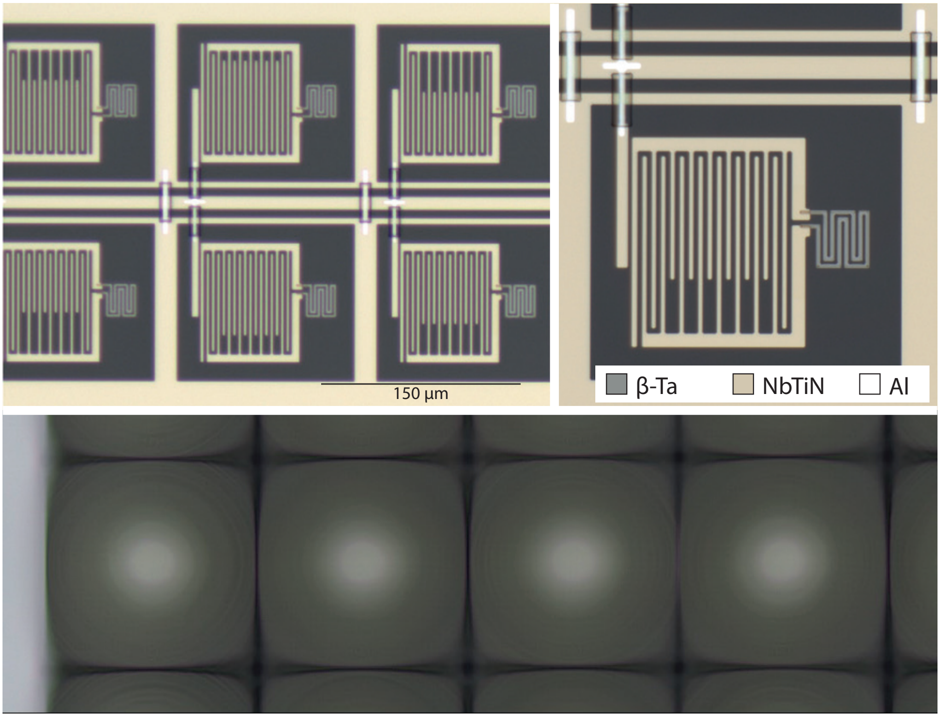

Figure 4.1: Microscope images of the NbTiN/β-Ta hybrid LEKID. **Left:** a small section of the 6×6 array with the double side coupling bar geometry. The finger length of the IDC varies from KID to KID to achieve the desired frequency spacing. The pixel pitch is 150 μm. **Right:** The hybrid KID consists of a β-Ta meandered inductor and a NbTiN IDC on a sapphire substrate. **Bottom:** A section of the 3D printed 150×150 μm lens-array. The lens array is printed on the backside of the 350 μm thick substrate. The lenses are designed with a height of 55 μm, and a conic constant of -0.405.

We use a four-probe DC structure to measure the DC properties of each layer. We measure a T_c of 1.0 K, a normal resistance of 1595 Ω just above the superconducting transition, and a room temperature (300 K) resistance of 1640 Ω which gives a residual resistivity ratio (RRR) value of 1.03. This yields a sheet resistance R_s of 39.8 Ω for the 60 nm thick β-Ta layer, resulting in a sheet kinetic inductance L_k of 54.6 pH/$\Box$. For the 120 nm NbTiN layer we measure T_c of 15.2 K and R_s of 11.0 Ω.

The photon sensitive part of the LEKID is the inductor, which makes up $\sim$2% of the total LEKID footprint. We focus the light onto the inductor by printing an array of elliptical micro-lenses on the backside of the sapphire substrate. The lenses are elliptical, instead of simply spherical, to reduce the effect of spherical abberations. Each lens is designed to have a 150 μm square base, a height of 55 μm, and a conic constant of -0.405. The lenses are printed with a Nanoscribe Photonic Professional GT2 Two-Photon Polymerization (TPP) printer in IP-S resin using a 25× immersion objective. The printer aligns the lenses to markers etched in the NbTiN layer. This method yields an alignment error of $\delta_x = +5.8 \pm 0.5$ μm and $\delta_y = +8.3 \pm 3.3$ μm, measured for 6 lenses. The measured FWHM spot size at the detector level is 6.2 ± 0.7 μm at 673 nm. The measurement procedures and a detailed analysis, including a profilometric measurement, are presented in Appendix 4.8.

4.3. Measurement setup

The samples are cooled down in a pulse-tube pre-cooled dilution refrigerator. All measurements are performed at a base temperature of 100 mK. We use a box-in-box sample stage design, conceptually similar to [21], [22], to shield the sample from stray light coming from the 4K stage of the cooler. Before reaching the sample, light travels through a corrugated snout and passes through a 5 mm thick BK7 glass window as illustrated in Fig. 4.2. Light from off-normal incidence is absorbed in the snout using black, carbon-loaded epoxy.

Located at the input of the snout is a collimator lens (Thorlabs F260FC-B) connected to an optical fiber (Thorlabs SMF-28-J9, with an 8.2 μm diameter core and 125 μm cladding, single-moded at 1550 nm). The collimator has a 3 mm beam diameter at the sample location (633 nm), while the array size is constrained to a 1 mm diameter for uniform illumination of the array. Alternatively, the lid with the collimator lens can be removed, providing optical access from outside the cryostat to the sample stage through a set of windows and filters.

The input of the fiber is either one of four fiber-coupled lasers (Thorlabs), a monochromator (Oriel Cornerstone 260) or the combination of the two through a fiber combiner (Thorlabs TW670R5F1). The fiber-coupled lasers have wavelengths 1545, 986, 673, and 402 nm, with output power from 1-10 mW in continuous wave mode and a line-width corresponding to $R > 300$. A combination of mechanical and digital attenuators set the laser power at the sample holder.

4.4. Measurements and Analysis

4.4.1. Resonator properties

To characterize the device, we perform a microwave measurement with a standard homodyne detection scheme; a detailed overview of the measurement and set-up can be found in [21]. We perform a frequency sweep to obtain the resonance circle (S21) for

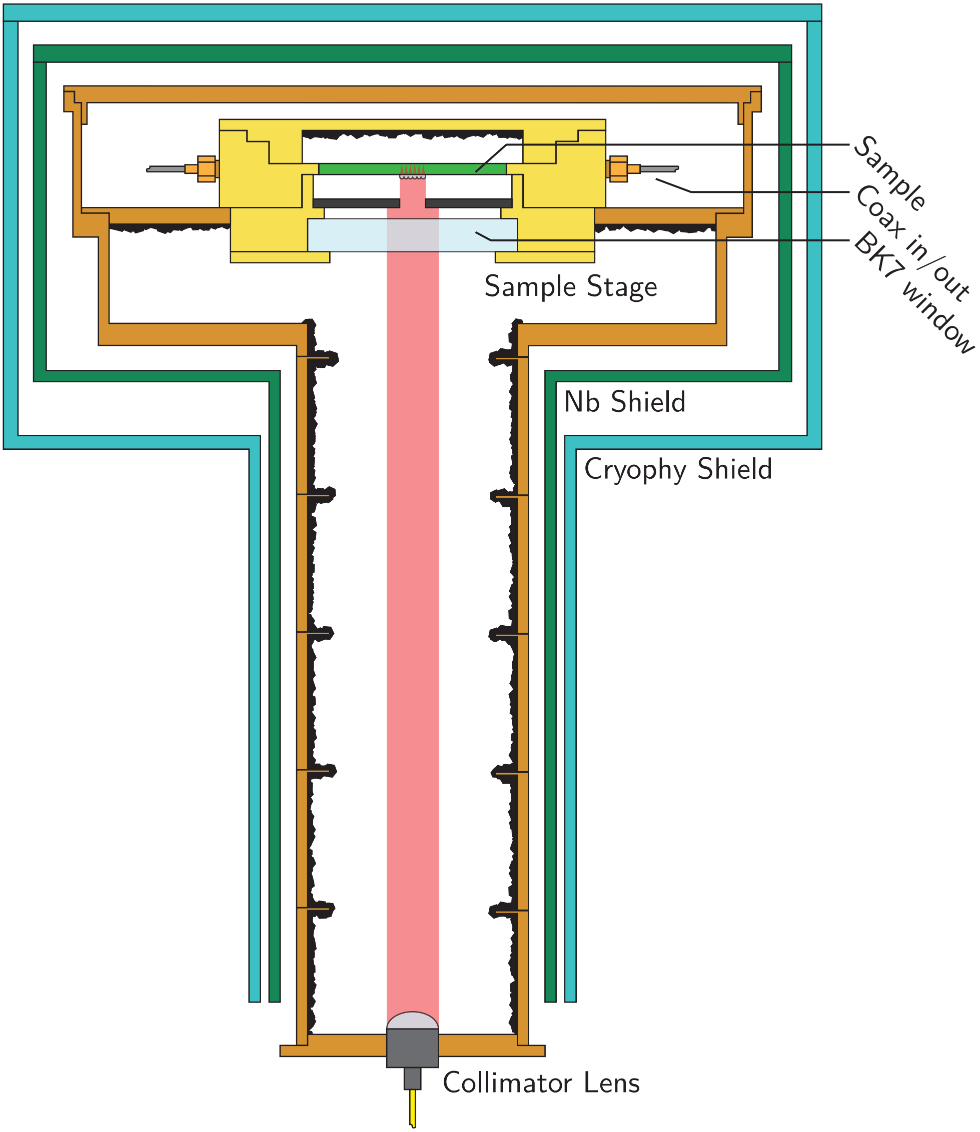

Figure 4.2: The 100 mK sample stage of the setup, parts are not to scale. Light enters the stage through a collimator lens connected to an optical fiber. The collimated bundle passes through a snout coated with black, carbon loaded epoxy. At the sample stage the bundle passes through a 5 mm thick BK7 window, and a 1 mm diameter aperture before reaching the sample. The 100 mK stage is surrounded by 2 magnetic shields, a superconducting Niobium shield, and a Cryophy shield.

each KID. Fitting the resonance dip ($|S_{21}|$) to an analytical model [21], [23] provides the resonator's resonance frequency f_0 and quality factors. We measure the resonance frequencies between 7.5 and 9.5 GHz, consistent with a SONNET simulation using the measured L_k of 54.46 pH/$\square$ from the four-probe DC measurement. For a chip with 12 hybrid β-Ta KIDs, spaced from 7.86 to 8.25 GHz, we measure an average Q_i of $4.3\times10^5 \pm 1.3 \times10^5$. The average coupler quality factor Q_c is $3.2\times10^4 \pm 2.0\times10^4$ for a designed Q_c (at 4 GHz) of 2×10^4. The optimal read power of each KID is set manually by selecting a power just below the bifurcation point. For powers at or above the bifurcation point, the resonator is operated in a non-linear regime where the resonance curve (S_{21}) shows hysteretic switching [24], [25].

We perform a noise measurement by taking two time-domain streams of the IQ-response (Appendix 4.10) at the resonance frequency, one of 40 seconds sampled at 50 ksample/s; and one of 0.5 seconds sampled at 1 Msample/s. The IQ-response is translated to the polar KID coordinates: phase, and amplitude [21]. Fig. 4.3 shows the resulting power spectral density (PSD).

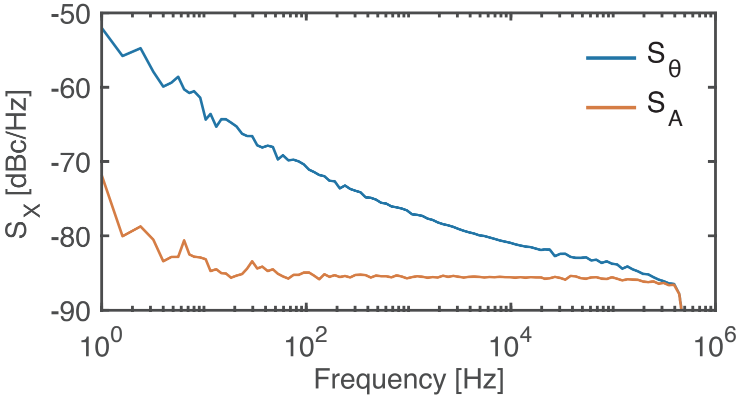

Figure 4.3: Measured Power Spectral Density (PSD) of phase and amplitude response for a hybrid β-Ta/NbTiN LEKID with f_0 = 8.15 GHz, $Q_i = 6.72 \times 10^5$, $Q_c = 1.88 \times 10^4$, KID internal power $P_{int} = -61$ dBm, and at a bath temperature of 100 mK. The measurement is performed without laser illumination.

4.4.2. Resolving power

Optimal filter

We determine the energy resolution of a KID from the histogram of photon pulse heights, obtained from a laser measurement at a single wavelength. For this measurement, we follow the approach described in [26], [27]. We consider a photon pulse in the KID response $D(f)$ which can be modelled as

$$\hat{D}(f) = H(E_{ph})M(f) + N(f), \tag{4.1}$$

where f is the frequency and $D(f)$ the Fourier transform of the time domain signal $d(t)$. The modelled photon pulse $\hat{D}(f)$ consists of a pulse shape $M(f)$ multiplied by a pulse height $H(E_{ph})$, which is a function of the photon energy E_{ph}, measured in the presence of noise $N(f)$. The measured and model pulse can be defined in any of the KID readout coordinates [21], we typically use the phase response θ unless specified otherwise: $D(f) = \theta(f)$. We assume that the pulse shape $M(f)$ and the noise $N(f)$ are not a function of the energy of the incoming photon E_{ph}. The optimal filter for the pulse height $H(E_{ph})$ is then given by [26], [28]:

$$\hat{H}(E_{ph}) = \int_{-\infty}^{\infty} \frac{D(f)M^{*}(f)}{|N(f)|^{2}} df \Big/ \int_{-\infty}^{\infty} \frac{|M(f)|^{2}}{|N(f)|^{2}} df. \tag{4.2}$$

We record an IQ timestream of 40 seconds at 1 Msample/s with enough laser attenuation to get roughly 40 photons per second. Each pulse is cut from the timestream with a window width of 512 points, corresponding to roughly 0.5 ms. Additionally, we record 20 seconds of data with the laser switched off to estimate the noise without the presence of photon hits $N(f)$. Although we assume the pulse shape in Eq. 4.2 to be independent of the photon energy, this is not always the case. Therefore, to characterize the detector at specific wavelengths, the pulse shape $M(f)$ is constructed by taking the average of a few thousand photon hits. The average pulses for each wavelength, used as the pulse shape at that wavelength, are plotted in Fig. 4.5a.

Care has to be taken to properly align the pulses on arrival time. We align the pulses on the rising edge, which we define as the point where the pulse first crosses half the pulse height. However, with a rise time in the order of 1 μs and a sample rate of 1 Msample/s the rising edge is sampled at just 1 or 2 points. To improve the pulse alignment we upsample the pulses, typically with a factor 8, improving the photon arrival time estimation to better than the sampling rate. An overview of the upsampling procedure is given in Appendix 4.9.

We apply the optimal filter to each of the individual pulses, yielding a few thousand estimates of the pulse height $\hat{H}(E_{ph})$. The pulse height estimates are translated to photon energy estimates by the KID responsivity, see Fig. 4.5b. This yields the four histograms, for four laser wavelengths, in Fig. 4.4. For some of the KIDs, we see a distinct low energy tail in the histogram as in Fig. Fig. 4.4, which is absent for other KIDs, without a clear correlation with design, front/back illumination, or lens coupling. An example of a histogram without a low energy tail is given in Appendix 4.13, Fig. 4.11.

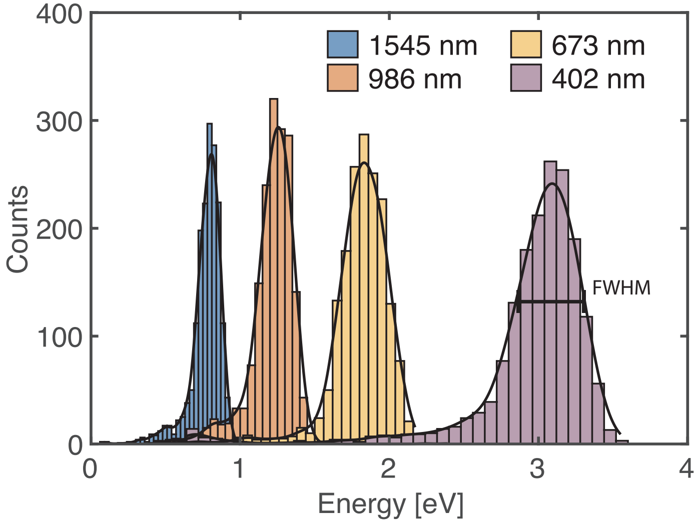

Figure 4.4: Histograms measured individually for all four laser wavelengths together with the kernel density estimates used to determine the resolving power. The corresponding photon energies are 3.08 eV for 402 nm, 1.84 eV for 673 nm, 1.26 eV for 986 nm, and 0.80 eV for 1545 nm. The number of pulses in each histogram are limited to 1718 points, to have the same number of pulses in each histogram. The resolving power at each wavelength is given in Table 4.1.

We estimate the normal probability density function of each histogram with a kernel density estimation, which yields the resolving power of the detector as $R = \mu/\mathrm{FWHM}$ with μ is the mean and FWHM the full width half maximum of the distribution. The estimated resolving powers depend on the chosen kernel width. Varying the kernel width such that the density estimate gives either a too coarse or too fine representation of the histogram shows that there is a ±5% uncertainty margin in the estimated resolving power.

All KIDs, whether lens-coupled or not, show a R that saturates at ∼5-6 for 1545 - 402 nm. The resolving power saturates at the point where the phase response saturates, which in most cases already starts at 1545 nm. A detailed discussion of the saturated phase response is presented in Section 4.4.2 while a detailed analysis of the limits in R is presented in Section 4.4.2.

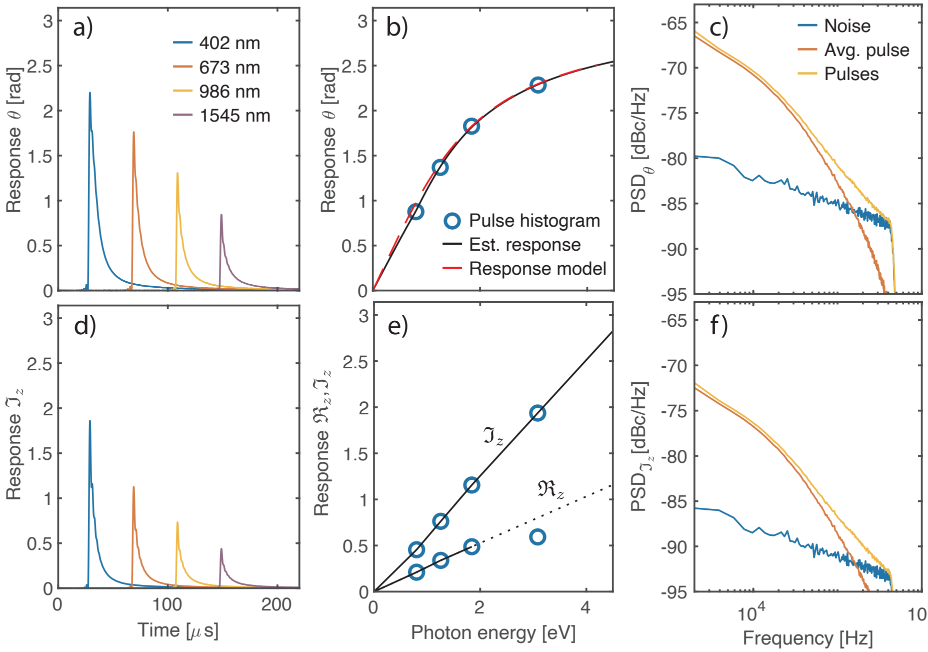

Figure 4.5: Pulse information for both coordinate systems (A, θ) and $(\mathfrak{R}_z,\ \mathfrak{I}_z)$. The corresponding photon energies are 3.08 eV for 402 nm, 1.84 eV for 673 nm, 1.26 eV for 986 nm, and 0.80 eV for 1545 nm. **a) and d)** Average pulse of ∼ 1000 pulses, used as the pulse shape for the optimal filter. **b) and e)** KID response against photon energy. The measured average pulse height, mean of the histogram, at each laser wavelength (dots) plotted against the known laser photon energy. For the phase coordinate in the top row: in red, the modelled phase responsivity as discussed in Appendix 4.12 fitted for one free parameter, the pair breaking efficiency η_{pb}. In black the θ responsivity retrieved from the linear $(\mathfrak{I}_z, \mathfrak{R}_z)$ coordinates. The modelled phase responsivity includes the free fit parameter η_{pb}. For the alternative coordinates in the bottom row: linear interpolated responsivity for $\mathfrak{I}_z$ and $\mathfrak{R}_z$. We see saturation of $\mathfrak{R}_z$ for the highest pulses in the 402 nm measurement, see section 4.4.2. **c) and f)** Typical power spectral densities of the average noise (blue), spectrum of the averaged pulse shape (orange), and the average spectrum of the pulses (yellow) for a 1545 nm laser measurement.

Responsivity

We estimate the responsivity of the KID by recording the mean of $\hat{H}$ for the four known laser wavelengths at 402, 673, 986, and 1545 nm. For devices with a phase responsivity such that pulses do not exceed $\theta = \pi/2$ radians, the response curve will be approximately linear. However, for the β-Ta devices described here, pulses easily exceed $\pi/2$ for the shorter wavelengths resulting in saturation in phase response [18], see Fig. 4.5b.

The saturation is a direct consequence of the polar coordinate system used to map the KID response into the conventional phase and amplitude response. This effect can be reproduced by a response model based on the number of excess quasiparticles N_{qp} generated by a photon, see Fig. 4.5. A detailed description is presented in Appendix 4.12.

An alternative coordinate system presented in [18] provides a response that is linear in photon energy. This coordinate system is analogous to the definition of the Smith chart, see Appendix 4.10, and is linear and monotonic in both coordinates, In this work we adopt the notation $\mathfrak{I}_z$ for the new phase component, and $\mathfrak{R}_z$ as the new dissipation component. A comparison between the two coordinate systems is presented in Fig. 4.5.

Resolving power contributions

First, we investigate the resolving power in the phase coordinate, see Table 4.1. The phase response saturates for photon energies $\gtrapprox$ 1.28 eV, which limits the obtained resolving powers by reducing the signal-to-noise ratio and, above all, introduces an error in the optimal filter. The error is twofold: saturation causes an energy-dependent pulse shape $M(f, E_{ph})$ and compresses the observed TLS-noise fluctuations, which scale with the resonator's response, causing an energy-dependent noise contribution $N(f, E_{ph})$. Since both the pulse shape and the noise contribution are now energy-dependent, the modeled pulse $\hat{D}(f) = H(E_{ph})M(f) + N(f)$ used in the optimal filter will no longer be a valid representation of the measured pulse $D(f)$, see eq. 4.2.

To estimate the effect of the response saturation on the resolving power, we analyse the measured resolving power at 1545 nm where the response is still linear, and compare it to the resolving power measured at shorter wavelengths. For this analysis we select a KID for which the full 1545 nm histogram falls in the linear phase response regime. The KID that fits this description is a front-illuminated KID without lens of which the measured resolving power is presented in Table 4.1.

For the (A, θ) coordinate, we do not present data in amplitude since the response is not only saturated but non-monotonic, which introduces an uncertainty in the translation from pulse height to photon energy.

Table 4.1: Resolving power ($E/\delta E$) for the different coordinate systems (A, θ) and $(\Re_z, \Im_z)$ obtained from the histogram mean and FWHM, see Fig. 4.4. The manual selection of the kernel width for the kernel density estimate gives the uncertainty margin on the estimated resolving powers, see Section 4.4. $R(\Re_z, \Im_z)$ is the resolving power for the combined estimator of the photon peak in both coordinate systems, see section 4.4.2 and Appendix 4.11.

λ	$R(\theta)$	$R(\Im_z)$	$R(\Re_z)$	$R(\Re_z, \Im_z)$
1545 nm	4.6 ± 0.23	4.7 ± 0.24	4.9 ± 0.25	5.0 ± 0.25
986 nm	4.7 ± 0.24	4.8 ± 0.24	5.0 ± 0.25	5.2 ± 0.26
673 nm	4.6 ± 0.23	5.0 ± 0.25	5.5 ± 0.28	5.6 ± 0.28
402 nm	4.9 ± 0.25	5.9 ± 0.30	-[1]	-[a]

At 1545 nm, in the phase coordinate, we measure a $R = 4.6 \pm 0.23$ and a R_{SN} of 13.4,

$$R_{SN} = \frac{\bar{H}}{2\sqrt{2\ln 2}}\sqrt{\int_{-\infty}^{\infty} \frac{|M(f)|^2}{|N(f)|^2} df}. \tag{4.3}$$

We can define R_i as a measure of the intrinsic resolving power contributions that are not due to noise [27] using $1/R_i^2 = 1/R^2 - 1/R_{SN}^2$. This gives an R_i of 4.9±0.28 at 1545 nm which indicates that this KID is limited by intrinsic effects, probably hot phonon loss where phonons escape to the substrate without creating quasiparticle excitations.

The definition of R_i is only valid for a linear response, which is only true for the measurement at 1545 nm. We can however extend this analysis to the shorter wavelengths under the assumption that phonon losses limit the energy resolution, using the know relation

$$R_{phonon} = \frac{1}{2\sqrt{2\ln 2}}\sqrt{\frac{\eta_{pb} E_{ph}}{\Delta(F+J)}}, \tag{4.4}$$

where the phonon-loss is represented by the additional factor J.

The phonon loss factor J depends on the depth at which photons are absorbed, since photons absorbed near the metal-substrate interface create phonons with a high probability to escape to the substrate. Since the electromagnetic penetration depth ranges from 45 nm at 1545 nm to 28 nm at 402 nm for the 60 nm β-Ta film, J can be energy dependent. If this is a dominant effect, a back- instead of frontside illuminated device will have a lower and energy dependent J. To verify that the analysis presented here is representative for the backside illuminated devices, we compare several KIDs illuminated from the front- and backside. We do not see a difference in the obtained R_i.

Since the measured resolving power, $R(\theta)$ in Table 4.1, does not follow a $\sqrt{E_{ph}}$ dependence and we do not see a difference in back- or front-side illumination, there must be an additional mechanism that limits the resolving power at higher energies. We attribute this mechanism to the saturation in phase response.

Based on the measured values of $R = 4.6 \pm 0.23$, $R_{SN} = 13.4$ and $R_i = 4.9 \pm 0.28$; and the expected E_{ph} dependancies of R_{SN} and R_i we estimate a phonon-limited R of 9.6±0.54 at 402 nm. The saturated response then limits the resolving power to the measured 4.9±0.28.

The linear Smith chart coordinates should then remove the error from the energy-dependent pulse shape $M(f)$ and noise contribution $N(f)$ caused by the saturated response. We do indeed see an increase in the measured resolving power, from 4.9 to 5.9 at 402 nm. However, the resolving power shows a much weaker energy dependence than the expected phonon-loss dominated $\sqrt{E_{ph}}$ dependence, see Table 4.1.$R(\mathfrak{I}_z)$. We attribute the deviation to the non-stationarity of the amplifier noise in the coordinates $(\mathfrak{R}_z, \mathfrak{I}_z)$, which is mapped differently at different response heights making the amplifier noise non-stationary during a photon pulse. A way to alleviate the error introduced by the non-stationarity is to measure with a parametric amplifier as is done in [18].

Combined estimator

For the linear coordinate system $(\mathfrak{R}_z, \mathfrak{I}_z)$ it can be beneficial to use a combined estimator, which combines the photon pulse data from both coordinates to estimate the photon energy, see Appendix 4.11. The combined estimator raises R slightly to 5.0 - 5.6 for 1545 - 673 nm, see Table 4.1.$R(\mathfrak{R}_z, \mathfrak{I}_z)$. However, the $\mathfrak{R}_z$ coordinate does not give an accurate pulse shape for the highest pules in the 402 nm dataset. The pulses are flattened at the top and no longer match with the estimated pulse model. This behaviour is not visible in the response model of Appendix 4.12 combined with the equations from Appendix 4.10. This makes the resolving power measurement at 402 nm unreliable and we have therefore chosen to omit the values from Table 4.1. So, even though the combined estimator gives the best resolving power, the dynamic range of this estimator is limited.

Resolving two spectral lines

The monochromator and one of the four lasers can be coupled into the cryostat simultaneously so that we can measure the KIDs response to two lines. The laser is set to 673 nm and the monochromator to 850 nm, which should be resolvable based on the measured resolving powers from Table 4.1. We measure the sources sequentially, taking 10-second timestreams for both the laser the monochromator. First we analyse the two timestreams separately, determining the pulse shapes $M(f)$, average pulse height, and resolving power at both wavelengths, see Fig. 4.6. The histograms in Fig. 4.6 are obtained with the combined estimator in $(\Re_z, \Im_z)$ discussed in Appendix 4.11 for which the KID response is linear in this wavelength range.

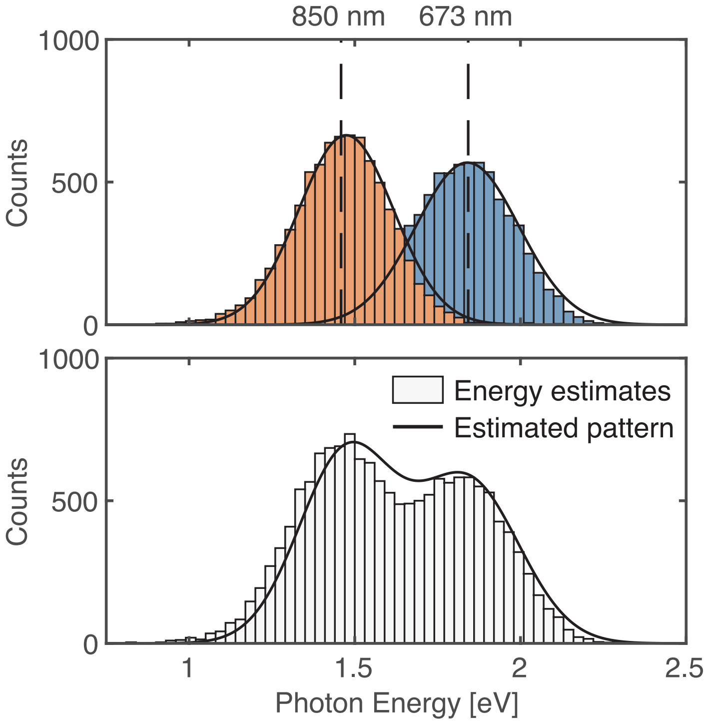

Figure 4.6: **Top:** Histograms for separate laser (673 nm) and monochromator (850 nm) measurements. In this case the pulse shape is determined individually for both measurements. The solid line is the normal distribution corresponding to the measured resolving power and mean pulse height. **Bottom:** The energy estimates when the pulse shape determined for the laser measurement is applied to both laser (673 nm) and monochromator (850 nm) measurements. The solid line is the estimated pattern, obtained by combining the normal distributions from the top panel. The energy estimates are obtained with the combined filter in $(\Re_z, \Im_z)$, presented in Appendix 4.11.

Next we process the entire 20-second timestream with the pulse shapes $M(f)$ obtained from the laser measurement. If the pulse shape is energy independent and the response is linear this should yield a histogram that is simply the sum of the laser and monochromator measurements. We can estimate the shape of this combined histogram by summing the normal distributions corresponding to the measured resolving power and mean pulse height of both sources, see Fig. 4.6. The actual histogram, when all pulses are processed with the laser pulse shape of 673 nm, is presented in the bottom panel of Fig. 4.6. The two lines can be separated from each other, as predicted from the individual measurements. We conclude that the resolving powers found for single line measurements, as in Fig. 4.4, accurately describe the energy resolving capabilities of a KID.

The shape of the total histogram deviates from the expected shape, especially in the region of the monochromator measurement (850 nm). The deviation from the expected pattern can then be explained by an energy-dependent pulse shape, such that the pulse shape determined at 673 nm is not fully representative of the pulse shape at 850 nm. Comparing the pulse shapes at 673 and 850 nm, we do indeed observe this energy dependency in the pulse tail.

4.5. Discussion

The resolving powers in Table 4.1 are representative of all the devices discussed in this work and represent the best estimate of the resolving power of these devices. A dataset which contains pulse-data from all the measured devices, is available in the reproduction package of this paper, see Sec. 4.6.

The resolving power in the phase coordinate (θ) saturates to ~5 due to the saturation in phase response. The linear coordinate $\mathfrak{I}_z$ from [18] and Appendix 4.10 raises the resolving power to 4.7 - 5.9 at 1545 - 402 nm. The combined estimator of Appendix 4.11 with both linear coordinates ($\mathfrak{R}_z, \mathfrak{I}_z$) raises the resolving power slightly for a limited dynamic range.

4.5.1. Saturated response

The non-linear, saturated response, in KID phase, as presented in Fig. 4.5b, limits the resolving power of these devices as discussed in Section 4.4.2. In Sec. 4.4.2 we discussed an alternative coordinate system that is linear in photon energy at the cost of non-stationary amplifier noise. The measurements in [18] are performed with a parametric amplifier, reducing the amplifier noise level. A lower amplifier noise level reduces the error the non-stationary noise introduces in the alternative coordinate system ($\mathfrak{R}_z, \mathfrak{I}_z$). For KIDs operated without a parametric amplifier, we think the best way forward is to reduce the KIDs responsivity enough to get a linear KID phase response over the 1545 nm - 402 nm range.

Reducing the KID response does not come without a price, as it lowers the obtained signal-to-noise resolving power R_{SN}. To reach a high resolving power, the reduction in KID response should, therefore, be compensated. One option is to improve the power handling of the devices [29], which will reduce the amplifier noise and TLS noise levels. Alternatively, the pulse decay time might increase with phonon trapping [27], raising the integrable energy (area) of a photon pulse thus improving the signal to noise ratio.

Even when the KID is operated in the linear response regime, phonon loss will still limit the resolving power as discussed in Section 4.4.2. From the measurement at 1545 nm we estimate that the phonon loss will limit the resolving power to 9.6 at 402 nm. Phonon (re)trapping, either by placing the KID on a membrane [27] or on a phonic barrier [30], can improve the phonon-loss intrinsic resolving power R_i.

4.5.2. Lifetimes

The photon pulses show two lifetimes, one fast initial decay of ≈ 7 μs and a slower second decay of ≈ 70 μs, see Fig. 4.7. The origin of these two lifetimes is currently under study. The slower decay limits the maximum photon count rate. The fast initial decay limits the integratable area underneath the pulse which limits the obtainable R_{SN}. We will investigate how the lifetimes depend on the material growth under different sputter conditions.

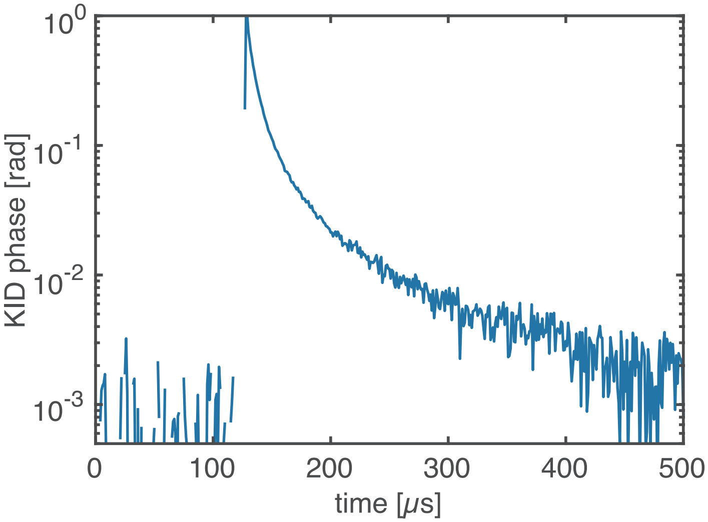

Figure 4.7: Phase (θ) pulse at 1545 nm in logarithmic scale to highlight the two pulse decay times. The pulse shows two timescales, a fast initial ≈ 7 μs decay and a slower ≈ 70 μs decay.

Increased phonon trapping increased the lifetime in Al KIDs [27], and will increase R_i improving the resolving power of these devices. We will test the effect of phonon trapping by making KIDs on a membrane [27] and on a material with different phonon properties, creating a phononic barrier [30].

4.5.3. Fabrication

The current fabrication process consists of 5 steps, as described in Sec. 4.2, where the last 2 steps are a resist layer to protect the β-Ta and the Al for readout- and coupling bridges. If we change the metal for the readout bridges from Al to β-Ta we can reduce the process to 3 steps with β-Ta as the final layer. Since there is no process step after the β-Ta, we expect a Q_i that is at least as high as measured here. We achieve a 100% fabrication yield for the 6×6 array, which is a positive sign for the development of bigger arrays in the future.

The 3D-printed lenses, described in detail in Appendix 4.8, are an interesting option for rapid prototyping of lens-coupled devices. However, with the resin we currently use, there was one isolated row of 6 lenses which came loose after 3 cooldown cycles. This is likely due to the different thermal expansion coefficients of the lenses and the substrate. More work is needed to investigate whether other resins, or an extra adhesion layer between substrate and lenses could solve this problem. For larger arrays the printing speed needs to be optimized since the 18 lenses presented here take roughly a day of printing.

4.6. Conclusion

We measure the resolving power of β-Ta hybrid LEKIDs which is limited to $R \sim 5$ for 1545-402 nm by saturation in the KID's phase response. The saturated, non-lineair, phase response distorts the pulse height histograms lowering the obtained resolving power. The β-Ta devices, with a T_c of 1.0 K and resistivity if 239 $\mu\Omega$cm, show an average Q_i of $4.3\times10^5 \pm 1.3 \times10^5$. For a small array of 6×6 pixels, we get a 100% fabrication yield. The high internal quality factor Q_i, ease of fabrication, and the possibility of a 3-layer process make β-Ta/NbTiN hybrid devices a promising option for larger, kilo-pixel, KID arrays. On the backside of the sapphire substrate we have 3D printed a micro-lens array, aligned to markers in the NbTiN layer. The lenses are printed with an alignment accuracy of of $\delta_x = +5.8 \pm 0.5$ μm and $\delta_y = +8.3 \pm 3.3$ μm and estimated FWHM spot size, fitted with a Gaussian, of 6.2 ± 0.7 μm.

All presented data, raw data, and analysis scripts are made available in a reproduction package uploaded to **Zenodo**: `https://doi.org/10.5281/zenodo.6719956`.

4.7. Acknowledgements

We acknowledge Nick de Keijzer and Robert Huiting for their work on the 100 mK sample stage.

This work is financially supported by the Netherlands Organisation for Scientific Research NWO (Projectruimte 680-91-127)

4.8. Lens analysis

We use a re-imaging setup [31] to image the microlens focal spots on the KID layer. The set-up consists of a monochromator source (673 nm), the microlens chip mounted on a manual single-axis z-stage, a re-imaging lens and a 3.45 μm pixel pitch CCD (Flir Blackfly BFLY-U3-50H5M-C). The magnification of the setup is determined from the imaged CPW read-out line. The lens misalignment is determined with respect to the imaged LEKID inductors and alignment structures as shown in Fig. 4.8.

The 3D printed micro lenses have an alignment error of $\delta_x = +5.8 \pm 0.5$ μm and $\delta_y = +8.3 \pm 3.3$ μm measured with respect to the desired focal spot location of 6 lenses.

In addition to the alignment error, we can measure the focal spot size by scanning the microlens array in the axial distance. The spot size is determined from the depth profile of each focal spot. The FWHM of the spot, fitted with a Gaussian, is 6.2 ± 0.7 μm. The diffraction limited airy disk diameter at 673 nm for an aperture with D = 150 μm and F = 525 μm (the optical length in the dielectric) is 5.75 μm, and the FWHM is 2.42 μm. The corresponding airy disk diameter for a FWHM of 6.2 μm is 14.2 μm. For the measured alignment error and estimated Airy disk diameter the complete airy disk, which contains 83.8% of the optical power, does not completely fall within the 23×25 μm inductor.

We characterise the shape of the lenses with a Keyence VK-X1000 laser confocal microscope, using a laser-based height measurement. We measure height profiles of isolated lenses, printed with the same recipe. The height profile measurement requires a height reference (a free view on the substrate surface) on at least 3 places around the lens within the field-of-view, which is not possible on a lens-array. The measured horizontal and vertical cross-section of one of the lenses is shown in Fig. 4.9, together with the designed profile. The bottom panel shows that the difference between design and realisation is better than 1 μm.

The final recipe for the Nanoscribe printer is the result of an optimization process where we have varied the scan speed and laser intensity of the printer, which together with the choice of microscope objective set the effective dose with which the resin is cured. Each iteration was evaluated with a height-profile measurement to find the

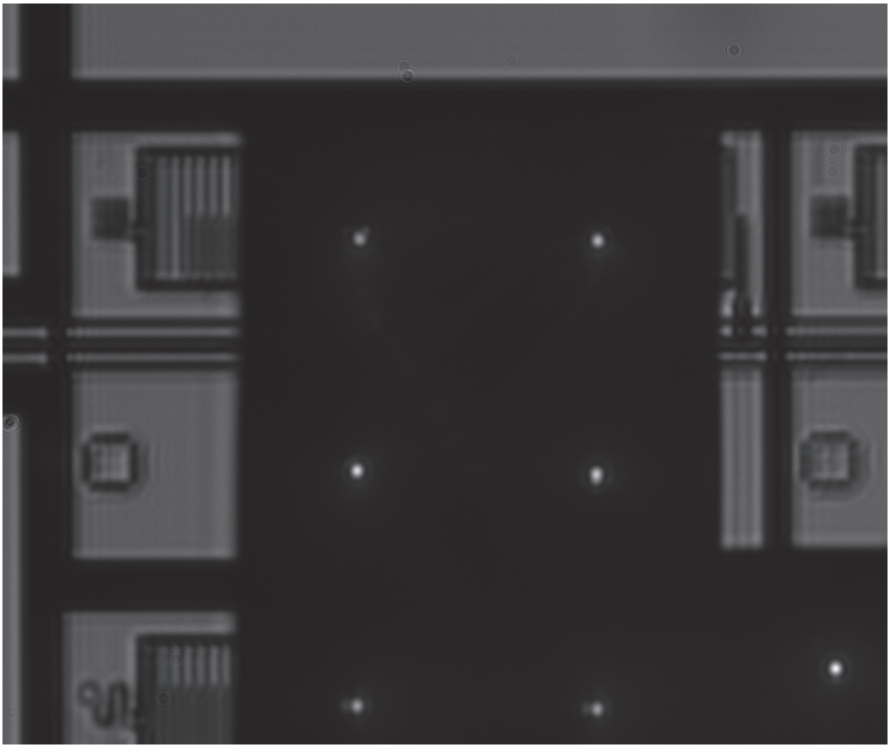

Figure 4.8: Re-imaged section of a LEKID test chip which contains a row of hybrid LEKIDs (top), alignment structures (middle), and LEKID design variations (bottom). Part of the CPW read-outline is visible between the top and middle rows. 6 lens focal spots are visible in the centre and a 7th spot, from a detached and shifted row, is visible in the lower right corner. The image is taken with a 3.5 μm pixel pitch CCD, with the array illuminated by a 673 nm laser.

conditions where the designed profile was most accurately represented. We start the writing process 1 μm below the substrate surface to ensure adhesion.

4.9. Upsampling

The pulses are aligned based on their rising slope, taken as the point where the pulse first crosses 0.5 times its final height. However, with a sample-rate of 1 Msample/s and a rise time of $\tau_{res} = 2Q/\omega_0 \approx 1$ μs, the rising edge is sampled at one or two points. To better estimate the rising edge we upsample the pulse time-stream by an integer factor, see Fig. 4.10, improving the photon arrival time estimation to better

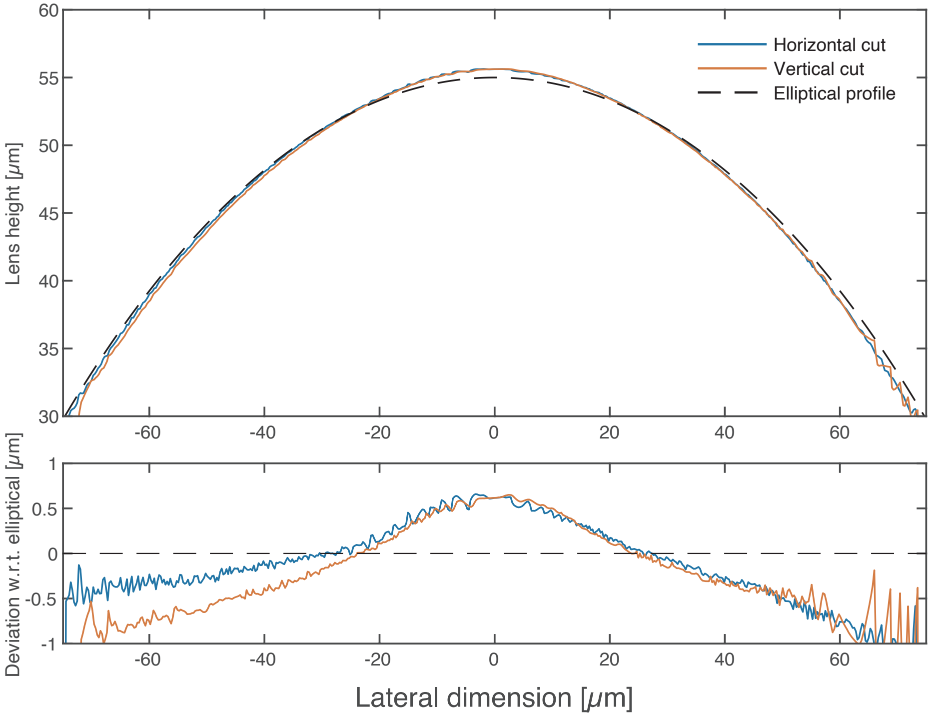

Figure 4.9: The measured horizontal and vertical cross-section of one of the Nanoscribe printed lenses together with the designed profile. The profile is measured with a Keyence VK-X1000 laser confocal microscope, using a laser-based height measurement.

than the sampling rate. The upsampling operation is done with the resample Matlab function, which resamples the input sequence at x times the original sample rate. The resample function applies a Finite Impulse Response (FIR) antialiasing lowpass filter to the input sequence and compensates for the delay introduced by the filter. The original pulse window has a length of 2^n to improve the performance of Matlab's FFT function, so we use a upsample factor that is a power of two to make sure that the upsampled pulse has a 2^n length.

The resample function is sensitive to large transients in the input signal. The photon pulses contain two of these transients, at the start of the peak where the signal rises sharply and at the under sampled peak where the signal drops suddenly. At these points the filter of the resample function slightly overestimates the actual pulse shape, see Fig. 4.10. This behaviour is however consistent for all the pulses and does not negatively affect the final energy resolution. The improved photon arrival time estimations results in a better peak-to-peak alignment, which in turn improves the estimated pulse model and the pulse-to-model alignment for the optimal filter peak height estimation.

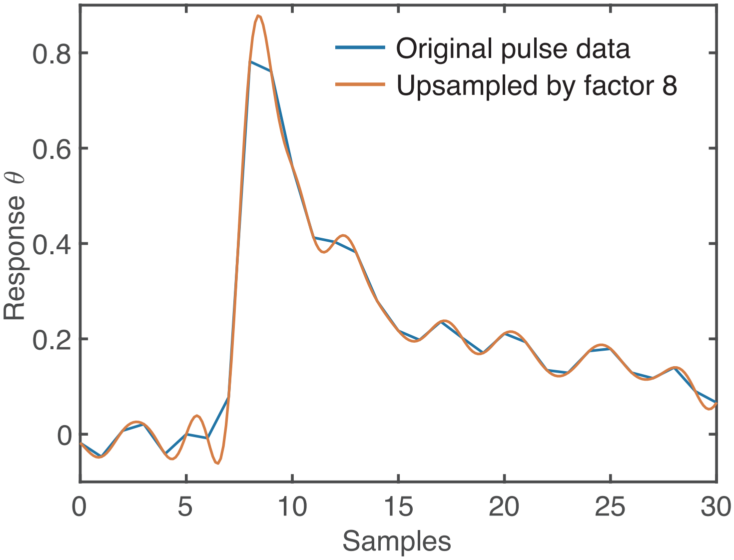

Figure 4.10: Original and factor 8 upsampled single photon pulse in KID phase response θ. Upsampled with Matlab resample function, which uses a FIR antialiasing lowpass filter.

4.10. Coordinate systems

We use a homodyne readout scheme to measure the KIDs' microwave response to an excitation by a photon absorption event. The output of the mixer is an in-phase component I and a quadrature component Q which are proportional the complex transmission coefficient S_{21}. A measurement of a KID frequency sweep at constant microwave power traces a circle in the complex IQ plane. After we calibrate for the cable delay and amplification in the readout chain, we translate the circle such that a frequency sweep measured in the dark, with the laser switched off, would trace a circle with radius 1, centered at (0,0). A noise measurement with the reference tone at the KIDs resonance frequency is then located at (-1,0).

When analyzing the response to radiation, I and Q are usually mapped on a polar coordinate system. The phase response θ is the clock-wise angle with respect to the negative x-axis. The dissipation response A is the distance from the circle's centre at

(0,0), we typically plot $\delta A = 1 - A$.

The authors of [18] show that these coordinates are linear for small signals. However, for larger signals the response becomes non-linear, and in the case of A it becomes non-monotonic. The authors then propose an alternate, Smith chart like, coordinate system $(\Re_z, \Im_z)$ that has a linear response to photon energy.

For a calibrated KID circle centered at (0,0) with a radius of 1, the equations for these new coordinates are given by

$$\Gamma = I + iQ \tag{4.5}$$

$$z = \frac{1+\Gamma}{1-\Gamma} \tag{4.6}$$

The new coordinate system $(\Re_z, \Im_z)$ is given by the real and imaginary part of z respectively.

For an asymmetric resonance dip, caused by a mismatch in the transmission line, the KID circle is rotated by ϕ and magnified by a factor $1/\cos(\phi)$ [23]. The rotation and factor $1/\cos(\phi)$ have to be corrected before equations 4.5 and 4.6 can be used. Alternatively equations 10a and 10b in [18] provide a way to compensate for the asymmetry through the factor x_a. The factor x_a relates to ϕ as

$$x_a = \frac{Q_i}{Q_i + Q_c}\frac{\tan(\phi)}{2Q}. \tag{4.7}$$

Both methods give the same response except for a scaling factor.

Until now we have assumed that one measures on resonance, where the readtone is equal to the KID resonance frequency f_0. Measuring off-resonance, which could happen when f_0 is taken from a Lorentzian fit to an asymmetric resonance dip, effectively rotates the pulse trajectory along the KID circle. Since the Smith chart is rotationally stable, the off-resonance measurement just adds an offset to the Smith chart response which can easily be corrected for in post-processing.

The reproduction package accompanying this paper contains several scripts that demonstrate the Smith chart like coordinate system and compare the obtained response with the formalism adopted in [18].

4.11. Combined estimator

The pulse model discussed in the main text can be extended to include the photon pulse in both phase and dissipation coordinates. The maximum likelihood estimator, in frequency domain is

$$\chi^2 = \int_{-\infty}^{\infty} (D - HM)^* S^{-1} (D - HM) df, \tag{4.8}$$

With D, H and M the column vectors containing the measured pulse, pulse height and pulse shape in both coordinates respectively, and S the 2×2 noise covariance matrix. The best estimate of E_{ph} is found by minimizing $\chi^2(E_{ph})$.

4.12. Responsivity model

In order to calculate the phase and amplitude response to an incoming photon, the equilibrium number of quasiparticles in the sensitive volume is calculated with, $N_{qp}^0 = 2VN_0\sqrt{2\pi k_B T_{bath}\Delta}e^{-\Delta/k_B T}$. Here, N_0 is the density of states at the Fermi energy, V is the sensitive superconducting volume, k_B is the Boltzmann constant, Δ is the superconducting order parameter and T_{bath} is the bath temperature. The equilibrium complex conductivity is calculated with the Mattis-Bardeen equations [32] at T_{bath}. With the complex conductivity, the internal quality factor, Q_i is calculated. Together with the resonance frequency, f_{res}, and coupling quality factor, Q_c, the equilibrium S_{21} circle in the complex plane is determined.

The number of excess quasiparticles generated by the photon is calculated via $\delta N_{qp} = \eta_{pb}\hbar\omega\Delta^{-1}$. Here, $\hbar\omega$ is the photon energy and η_{pb} is the pair breaking efficiency, which is the only fit parameter of the model and gives a reasonable value of 0.55. Note that this fitted value of eta_{pb} should not be interpreted as a measurement of a universal eta_{pb}. It shows that the saturation phenomena observed in the KID response can be consistently described with this simple model.

The number of quasiparticles just after the photon energy is absorbed, $N_{qp} = N_{qp}^0 + \delta N_{qp}$, is translated to an effective quasiparticle temperature, T_{eff}, by inverting the equation for N_{qp}^0. From T_{eff}, the new complex conductivity is calculated with the Mattis-Bardeen equations [32]. From this, the new Q_i and f_{res} of the KID are calculated. With these variables, the complex scattering parameter S_{21} is calculated, which is translated to an amplitude and phase, relative to the equilibrium S_{21} circle. For details, see [21], [33].

We limit ourselves here to a model of the pulse-height only. The pulse-decay could be added to the model starting with the Rothwarf-Taylor equations [34]. The comparison of such model to the observed quasiparticle dynamics is not straightforward, and beyond the scope of this work.

4.13. Low energy tail

For each laser measurement the photon energy estimates are presented as histograms, see Fig. 4.4. For some of the KIDs, we see a distinct low energy tail in the histogram, which is absent for other KIDs, without a clear correlation between design, front/back illumination, or lens coupling. Two examples of these histograms, one with and one without a low energy tail, are presented in Fig. 4.11.

Such a low energy tail is common for non-hybrid KIDs and is typically explained by quasiparticle leakage into the less sensitive capacitor [30]. This should not be an issue for hybrid KIDs due to the difference in energy gap of the low-T_c β-Ta inductor and the high-T_c NbTiN capacitor. Further study is required to pinpoint the source of this low energy tail in hybrid LEKIDs.

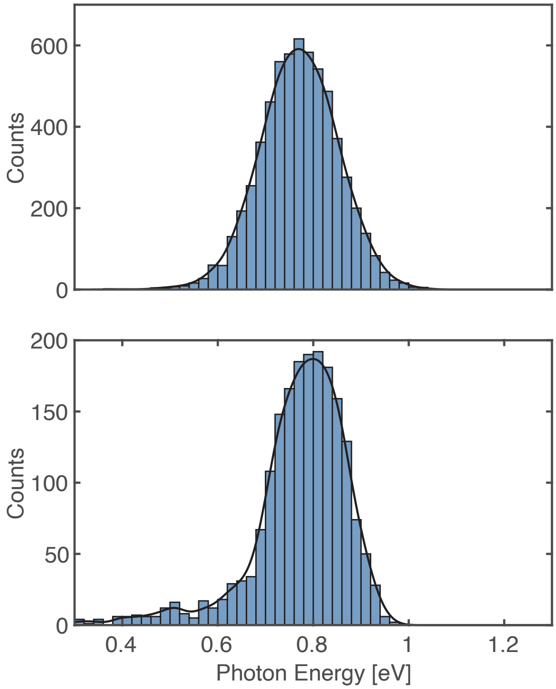

Figure 4.11: Histograms at 1545 nm for two different KIDs with the same design. The top histogram shows a symmetric distribution while the bottom histogram shows a significant low energy tail.

Bibliography

[1] P. K. Day, H. G. LeDuc, B. A. Mazin, A. Vayonakis, and J. Zmuidzinas, "A broadband superconducting detector suitable for use in large arrays," *Nature*, vol. 425, no. 6960, pp. 817–821, Oct. 2003. DOI: `10.1038/nature02037`.

[2] A. G. Kozorezov, A. F. Volkov, J. K. Wigmore, A. Peacock, A. Poelaert, and R. den Hartog, "Quasiparticle-phonon downconversion in nonequilibrium superconductors," *Phys. Rev. B*, vol. 61, no. 17, pp. 11 807–11 819, 17 May 2000. DOI: `10.1103/PhysRevB.61.11807`.

[3] A. Kozorezov, "Energy Down-Conversion and Thermalization in Metal Absorbers," *J. Low Temp. Phys.*, vol. 167, no. 3, pp. 473–484, May 2012. DOI: `10.1007/s10909-011-0426-1`.

[4] M. Kurakado, "Possibility of high resolution detectors using superconducting tunnel junctions," *Nucl. Instrum. Methods Phys. Res.*, vol. 196, no. 1, pp. 275–277, May 1982. DOI: `10.1016/0029-554X(82)90654-1`.

[5] N. Rando, A. Peacock, A. van Dordrecht, *et al.*, "The properties of niobium superconducting tunneling junctions as X-ray detectors," *Nucl. Instrum. Methods Phys. Res. A*, vol. 313, no. 1, pp. 173–195, Mar. 1992. DOI: `10.1016/0168-9002(92)90095-L`.

[6] T. Guruswamy, D. J. Goldie, and S. Withington, "Quasiparticle generation efficiency in superconducting thin films," *Supercond. Sci. Technol.*, vol. 27, no. 5, p. 055 012, Mar. 2014. DOI: `10.1088/0953-2048/27/5/055012`.

[7] P. J. de Visser, S. J. C. Yates, T. Guruswamy, *et al.*, "The non-equilibrium response of a superconductor to pair-breaking radiation measured over a broad frequency band," *Appl. Phys. Lett.*, vol. 106, no. 25, p. 252 602, Jun. 2015, ISSN: 0003-6951. DOI: `10.1063/1.4923097`.

[8] S. R. Meeker, B. A. Mazin, A. B. Walter, *et al.*, "DARKNESS: A Microwave Kinetic Inductance Detector Integral Field Spectrograph for High-contrast Astronomy," *PASP*, vol. 130, no. 988, p. 065 001, Apr. 2018. DOI: `10.1088/1538-3873/aab5e7`.

[9] B. A. Mazin, B. Bumble, S. R. Meeker, K. O'Brien, S. McHugh, and E. Langman, "A superconducting focal plane array for ultraviolet, optical, and near-infrared astrophysics," *Opt. Express*, vol. 20, no. 2, pp. 1503–1511, Jan. 2012. DOI: `10.1364/OE.20.001503`.

[10] B. A. Mazin, S. R. Meeker, M. J. Strader, *et al.*, "ARCONS: A 2024 Pixel Optical through Near-IR Cryogenic Imaging Spectrophotometer," *PASP*, vol. 125, no. 933, p. 1348, Nov. 2013. DOI: `10.1086/674013`.

[11] P. Szypryt, S. R. Meeker, G. Coiffard, *et al.*, "Large-format platinum silicide microwave kinetic inductance detectors for optical to near-IR astronomy," *Opt. Express*, vol. 25, no. 21, p. 25 894, Oct. 2017. DOI: `10.1364/OE.25.025894`.

[12] N. Zobrist, G. Coiffard, B. Bumble, *et al.*, "Design and performance of hafnium optical and near-IR kinetic inductance detectors," *Appl. Phys. Lett.*, vol. 115, no. 21, p. 213 503, Nov. 2019. DOI: `10.1063/1.5127768`.

[13] K. Kouwenhoven, I. Elwakil, J. v. Wingerden, *et al.*, "Model and Measurements of an Optical Stack for Broadband Visible to Near-Infrared Absorption in TiN MKIDs," *J. Low Temp. Phys*, Jul. 2022. DOI: `10.1007/s10909-022-02774-0`.

[14] B. A. Mazin, "Superconducting Materials for Microwave Kinetic Inductance Detectors," pp. 756–765, Apr. 2020. DOI: `10.48550/arxiv.2004.14576`. arXiv: `2004.14576 [astro-ph,physics:cond-mat]`.

[15] D. W. Face and D. E. Prober, "Nucleation of body-centered-cubic tantalum films with a thin niobium underlayer," *J. Vac. Sci. Technol. A*, vol. 5, no. 6, pp. 3408–3411, 1987. DOI: `10.1116/1.574203`.

[16] R. M. J. Janssen, J. J. A. Baselmans, A. Endo, *et al.*, "High optical efficiency and photon noise limited sensitivity of microwave kinetic inductance detectors using phase readout," *Appl. Phys. Lett.*, vol. 103, no. 20, p. 203 503, Nov. 2013. DOI: `10.1063/1.4829657`.

[17] S. J. C. Yates, J. J. A. Baselmans, A. Endo, *et al.*, "Photon noise limited radiation detection with lens-antenna coupled microwave kinetic inductance detectors," *Appl. Phys. Lett.*, vol. 99, no. 7, p. 073 505, Aug. 2011. DOI: `10.1063/1.3624846`.

[18] N. Zobrist, N. Klimovich, B. Eom, *et al.*, "Improving the dynamic range of single photon counting kinetic inductance detectors," *J. Astron. Telesc. Instrum. Syst.*, vol. 7, no. 1, p. 010 501, Feb. 2021, ISSN: 2329-4124. DOI: `10.1117/1.JATIS.7.1.010501`.

[19] D. J. Thoen, B. G. C. Bos, E. A. F. Haalebos, T. M. Klapwijk, J. J. A. Baselmans, and A. Endo, "Superconducting NbTin Thin Films With Highly Uniform Properties Over a 100 mm Wafer," *IEEE Trans. Appl. Supercond.*, vol. 27, no. 4, pp. 1–5, Jun. 2017. DOI: `10.1109/TASC.2016.2631948`.

[20] B. G. C. Bos, D. J. Thoen, E. A. F. Haalebos, *et al.*, "Reactive Magnetron Sputter Deposition of Superconducting Niobium Titanium Nitride Thin Films With Different Target Sizes," *IEEE Trans. Appl. Supercond.*, vol. 27, no. 4, pp. 1–5, Jun. 2017. DOI: `10.1109/TASC.2016.2631939`.

[21] P. J. De Visser, "Quasiparticle dynamics in aluminium superconducting microwave resonators," Ph.D. dissertation, Delft University of Technology, 2014. DOI: `10.4233/uuid:eae4c9fc-f90d-4c12-a878-8428ee4adb4c`. [Online]. Available: `http://resolver.tudelft.nl/uuid:eae4c9fc-f90d-4c12-a878-8428ee4adb4c`.

[22] J. Baselmans, S. Yates, P. Diener, and P. de Visser, "Ultra Low Background Cryogenic Test Facility for Far-Infrared Radiation Detectors," *J. Low Temp. Phys.*, vol. 167, no. 3-4, pp. 360–366, May 2012. DOI: `10.1007/s10909-012-0511-0`.

[23] M. S. Khalil, M. J. A. Stoutimore, F. C. Wellstood, and K. D. Osborn, "An analysis method for asymmetric resonator transmission applied to superconducting devices," *J. Appl. Phys.*, vol. 111, no. 5, p. 054 510, Mar. 2012, ISSN: 0021-8979. DOI: `10.1063/1.3692073`.

[24] P. J. de Visser, S. Withington, and D. J. Goldie, "Readout-power heating and hysteretic switching between thermal quasiparticle states in kinetic inductance detectors," *J. Appl. Phys.*, vol. 108, no. 11, p. 114 504, Dec. 2010. DOI: `10.1063/1.3517152`.

[25] L. J. Swenson, P. K. Day, B. H. Eom, *et al.*, "Operation of a titanium nitride superconducting microresonator detector in the nonlinear regime," *J. Appl. Phys.*, vol. 113, no. 10, p. 104 501, Mar. 2013, ISSN: 0021-8979. DOI: `10.1063/1.4794808`.

[26] K. D. Irwin, "Phonon-mediated particle detection using superconducting tungsten transition-edge sensors," en, Ph.D. dissertation, Stanford University, Feb. 1995. DOI: `10.2172/1423679`.

[27] P. J. de Visser, S. A. de Rooij, V. Murugesan, D. J. Thoen, and J. J. Baselmans, "Phonon-Trapping-Enhanced Energy Resolution in Superconducting Single-Photon Detectors," *Phys. Rev. Applied*, vol. 16, no. 3, p. 034 051, Sep. 2021. DOI: `10.1103/PhysRevApplied.16.034051`.

[28] M. E. Eckart, "Measurements of X-Ray Selected AGN and Novel Superconducting X-Ray Detectors," phd, California Institute of Technology, 2007. DOI: `10.7907/SZAB-0Y07`.

[29] J. R. Clem and K. K. Berggren, "Geometry-dependent critical currents in superconducting nanocircuits," *Phys. Rev. B*, vol. 84, no. 17, p. 174 510, 17 Nov. 2011. DOI: `10.1103/PhysRevB.84.174510`.

[30] N. Zobrist, W. H. Clay, G. Coiffard, *et al.*, "Membraneless Phonon Trapping and Resolution Enhancement in Optical Microwave Kinetic Inductance Detectors," *Phys. Rev. Lett.*, vol. 129, no. 1, p. 017 701, Jul. 2022. DOI: `10.1103/PhysRevLett.129.017701`.

[31] S. van Haver, J. J. M. Braat, and S. F. Pereira, "Enabling aberration retrieval of microlenses with the Extended Nijboer-Zernike (ENZ) diffraction theory," in *Optical Modelling and Design*, International Society for Optics and Photonics, vol. 7717, SPIE, 2010, 77170U. DOI: `10.1117/12.854412`.

[32] D. C. Mattis and J. Bardeen, "Theory of the anomalous skin effect in normal and superconducting metals," *Phys. Rev.*, vol. 111, no. 2, pp. 412–417, 2 Jul. 1958. DOI: `10.1103/PhysRev.111.412`.

[33] S. de Rooij, "Quasiparticle Dynamics in Optical MKIDs: Single Photon Response and Temperture Dependent Generation-Recombination Noise," Ph.D. dissertation, 2020. [Online]. Available: `https://repository.tudelft.nl/islandora/object/uuid:1d935dc8-58d1-438f-995b-872e9d5f077e`.

[34] A. Rothwarf and B. N. Taylor, "Measurement of recombination lifetimes in superconductors," *Phys. Rev. Lett.*, vol. 19, pp. 27–30, 1 Jul. 1967. DOI: `10.1103/PhysRevLett.19.27`.

Chapter 5

Model and Measurements of an Optical Stack for Broadband Visible to Near-Infrared Absorption in TiN MKIDs

Typical materials for optical Microwave Kinetic Inductance Detetectors (MKIDs) are metals with a natural absorption of ∼30-50% in the visible and near-infrared. To reach high absorption efficiencies (90-100%) the KID must be embedded in an optical stack. We show an optical stack design for a 60 nm TiN film. The optical stack is modeled as sections of transmission lines, where the parameters for each section are related to the optical properties of each layer. We derive the complex permittivity of the TiN film from a spectral ellipsometry measurement. The designed optical stack is optimised for broadband absorption and consists of, from top (illumination side) to bottom: 85 nm SiO_2, 60 nm TiN, 23 nm of SiO_2, and a 100 nm thick Al mirror. We show the modeled absorption and reflection of this stack, which has >80% absorption from 400 nm to 1550 nm and near-unity absorption for 500 nm to 800 nm. We measure transmission and reflection of this stack with a commercial spectrophotometer. The results are in good agreement with the model.

This chapter was published as K. Kouwenhoven, I. Elwakil, J. van Wingerden, V. Murugesan, D. J. Thoen, J. J. A. Baselmans and P. J. de Visser *J Low Temp Phys* **209**, 1249-1257 (2022).

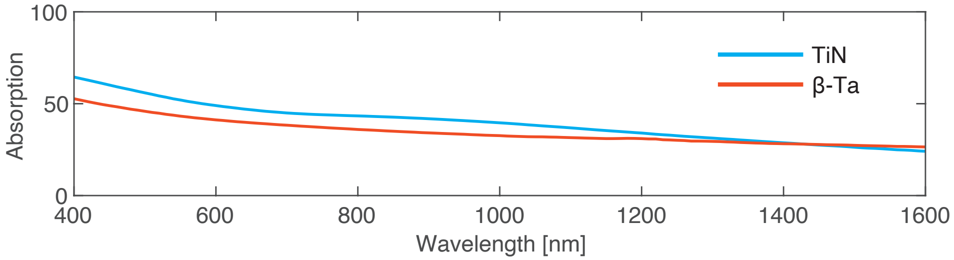

Figure 5.1: Absorbed power under normal incidence for two high resistivity superconductors, TiN (*blue*) and beta phase tantalum (β-Ta) (*red*). The plotted absorption is calculated from the measured optical constants of both films. Both films are 60 nm thick and deposited on a 350 μm polished c-plane sapphire substrate. TiN: T_c = 3.45 K, R_s = 237.2 Ω. β-Ta: T_c = 0.99 K, R_s = 38.8 Ω. (Color figure online.)

5.1. Introduction

There is a wide variation in the superconductors used for Microwave Kinetic Inductance Detectors (MKIDs) [1]. Some common materials are Hafnium (Hf), Titanium nitride (TiN), Platinum Silicide (PtSi), and alpha- or beta-phase Tantalum (Ta). Although the properties of these metals differ, they have one thing in common. They suffer from low absorption efficiency in the visible to near-IR wavelength range. For β-Ta, TiN, PtSi, and Hf absorption is limited to around 50% in the visible and 30% in the IR range, as illustrated by Fig. 5.1 and presented in [2]. To increase the power absorbed in the MKID, we embed it in an optical stack consisting of a mirror (cavity) and one or multiple matching layers. With this approach, unity absorption can be achieved [3]–[5]. However, the bandwidth over which high absorption is achieved is usually limited. Here we show the design of an optical stack for a 60 nm thick TiN layer, based on a transmission line model, that achieves absorption $> 80\%$ over a band from 400 nm to 1550 nm, with near-unity transmission from 500 nm to 800 nm. We verify the model with a reflection and transmission measurement using a commercial spectrophotometer.

5.2. Model

The optical stack consists of the superconducting MKID layer (TiN), a superconducting Al mirror, and two dielectric layers, as illustrated in Fig. 5.2. The 100 nm thick mirror is deposited on top of the sapphire substrate and has to be made from a superconducting material to maintain the high quality factor of the MKIDs [5]. The

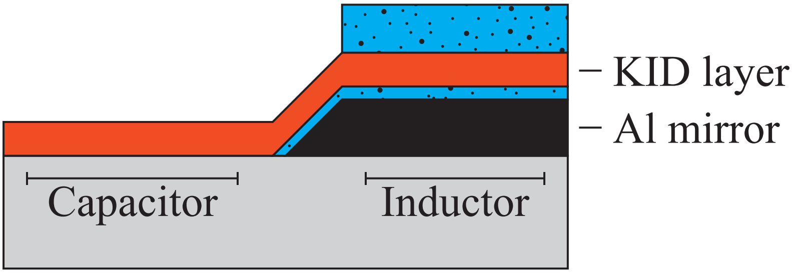

Figure 5.2: Illustration of the proposed optical stack. The MKID layer (*red*) is backed by a 100 nm thick superconducting Al mirror (*black*). The stack contains two dielectric layers (*blue*), one to create the back-short spacing between the MKID and the superconducting mirror and a second to reduce reflection from the MKID layer. The number of dielectric layers deposited on top of the MKID can be increased to improve the stacks performance when necessary. To limit the added dielectric loss and Two Level System (TLS) noise from the deposited dielectrics, the capacitor should not be embedded in the stack. In this case the MKID is front-side (top) illuminated. (Color figure online.)

basic version contains two dielectric layers. One layer realizes the spacing between the MKID layer and the mirror. The other layer, deposited on top of the MKID layer, is used to match the impedance of the MKID plus mirror to the impedance of free-space η_0. The number of layers on top of the MKID can be increased to realize either multi-layer interference or tapered impedance matching structures.

The deposited dielectrics will increase the dielectric loss and Two-Level System (TLS) noise levels in the MKID, especially in regions with a high E-field density. For this reason, the optical stack should be limited to the inductor area.

5.2.1. Transmission Line Representation

To model the expected absorption of the optical stack based on the optical properties of each layer, we represent each layer with a section of transmission line as illustrated in Fig. 5.3. The length l of the transmission line is the thickness of the respective layer, and the complex impedance η_c and propagation constant k_c are a function of the layer's optical properties. We characterize each layer by its relative permittivity $\tilde{\epsilon_r}(\omega) = \epsilon_r'(\omega) - i\epsilon_r''(\omega)$, where ω indicates the frequency dependency of the relative permittivity. For ease of readability, we will omit the frequency dependency of $\tilde{\epsilon_r}(\omega)$ in the following equations. The transmission line parameters are given by [6]

$$k_c = \beta_d \sqrt{1 - i\tau}, \tag{5.1}$$

$$\eta_c = \eta_d \frac{1}{\sqrt{1 - i\tau}}, \tag{5.2}$$

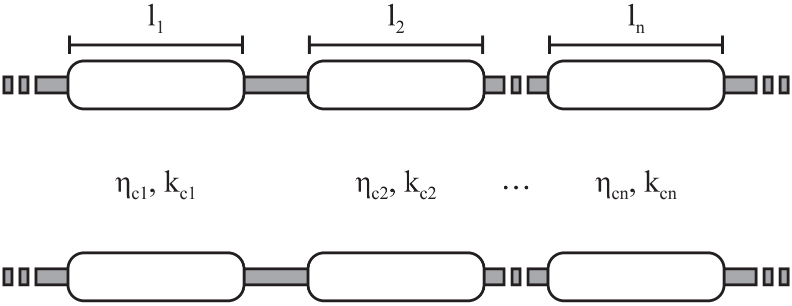

Figure 5.3: Transmission line representation of the optical stack. Each of the layers, either dielectric or metal, is represented by a section of transmission line with length equal to the height of the layer. The transmission lines are characterized by a complex impedance η_c and a complex propagation constant k_c. (Color figure online.)

where β_d and η_d are the phase constant and impedance for a plane-wave in a lossless dielectric $\beta_d = \frac{2\pi}{\lambda_0}\sqrt{\epsilon_r'}$ and $\eta_d = \frac{\eta_0}{\sqrt{\epsilon_r'}}$ with η_0 the free space impedance and λ_0 the wavelength in free space. The electric loss tangent $\tan\delta_e$ is given by

$$\tau = \tan\delta_e = \frac{\epsilon_r''}{\epsilon_r'}. \tag{5.3}$$

For a perfect conductor $\tau = \infty$ and for a lossless dielectric $\tau = 0$. The ABCD matrix is a useful tool for the analysis of the full optical stack. The ABCD matrix of a transmission line section is [6]

$$\begin{bmatrix} A & B \\ C & D \end{bmatrix} = \begin{bmatrix} \cos(k_c l) & \eta_c i \sin(k_c l) \\ \eta_c^{-1} i \sin(k_c l) & \cos(k_c l) \end{bmatrix} \tag{5.4}$$

and the matrix of the full stack is then given by the cascade of the ABCD matrices corresponding to the different layers [6]

$$\begin{bmatrix} A & B \\ C & D \end{bmatrix} = \begin{bmatrix} A_1 & B_1 \\ C_1 & D_1 \end{bmatrix} \begin{bmatrix} A_2 & B_2 \\ C_2 & D_2 \end{bmatrix} \cdots \begin{bmatrix} A_n & B_n \\ C_n & D_n \end{bmatrix}. \tag{5.5}$$

The reflection (Γ) and transmission (T) coefficients of the stack are obtained as [7]

$$\Gamma = \frac{AZ_{02} + B - CZ_{01}^* Z_{02} - DZ_{01}^*}{AZ_{02} + B + CZ_{01}Z_{02} + DZ_{01}} \tag{5.6}$$

$$T = \frac{2\sqrt{\mathrm{Re}(Z_{01})\,\mathrm{Re}(Z_{02})}}{AZ_{02} + B + CZ_{01}Z_{02} + DZ_{01}}, \tag{5.7}$$

where Z_{01} and Z_{02} are the terminations of the transmission line [7] as given in Fig. 5.3. For the structure in Fig. 5.2, Z_{01} is the wave impedance of free space ($\eta_0 \approx 120\pi\ \Omega$) and Z_{02} the wave impedance of the substrate ($\eta_0/\sqrt{\epsilon_{r,sub}}$). The absorbed power fraction of the complete stack is then given by $A = 1 - |\Gamma|^2 - |T|^2$.

5.2.2. Spectroscopic Ellipsometry

We characterize the superconducting films with a room temperature spectroscopic ellipsometry measurement. We measure the amplitude component ψ and phase difference Δ at multiple angles Θ ranging from 55° to 80° in steps of 5° (typically centered around the Brewster's angle). We assume that the films are isotropic, homogeneous and that the measured reflection is dominated by the first reflection at the air-TiN interface. In this case, the film can be considered infinitely thick. Under these assumptions, the complex permittivity of the film is retrieved as

$$\tilde{\epsilon}(\omega) = \sin^2(\Theta)\left[1 + \tan^2(\Theta)\left(\frac{1-\rho}{1+\rho}\right)^2\right] \tag{5.8}$$

with $\rho = \tan(\psi)\exp(i\Delta)$ and $\tilde{\epsilon_r} = \epsilon_r' - i\epsilon_r''$. The complex permittivity $\tilde{\epsilon_r}$ is related to the complex refractive index as

$$\tilde{\epsilon_r} = (n + ik)^2. \tag{5.9}$$

The derived complex permittivity for a 60 nm thick TiN film, deposited on a sapphire substrate, is given in Fig. 5.4. The TiN film has a critical temperature (T_c) of 3.45 K and a sheet resistance (R_s) of 237.2 Ω.

5.2.3. Optimization for Broadband Absorption

For high absorption at single wavelengths, the optimization is easy. The thicknesses of both dielectrics, see Fig. 5.2, should be chosen as $\lambda_d/4$ (quarter wavelength) with λ_d the wavelength in the dielectric. For absorption over a large wavelength range, however, the optimal thicknesses can no longer be calculated analytically since the optical constants of the metal layer vary strongly with wavelength, as indicated by Fig. 5.4. Therefore we parameterize the optical stack with respect to the layer thicknesses and calculate the achieved absorption for multiple thickness combinations. We optimize for maximum average absorption over a defined wavelength range, in this case, 400 nm to 1550 nm. The optimal layer combination for a 60 nm TiN film consists of, from top (illumination side) to bottom: 85 nm SiO_2, 60 nm of unpatterned TiN, 23 nm of SiO_2, and a 100 nm thick Al mirror. SiO_2 is chosen since it is transparent (lossless)

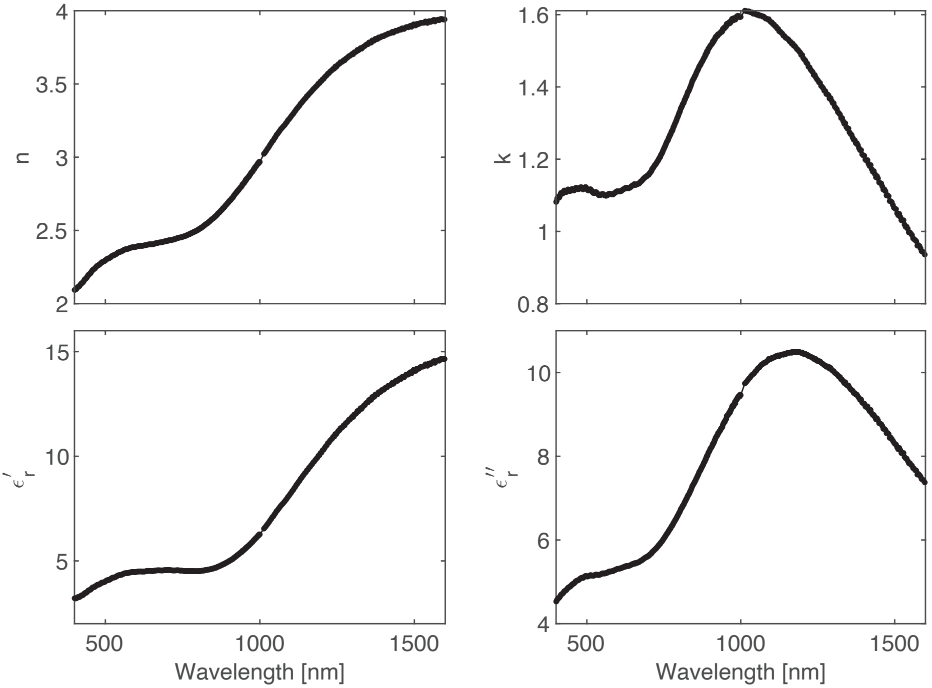

Figure 5.4: Optical constants (n,k) and relative permittivity for TiN. These values are derived from a multi-angle spectroscopic ellipsometry measurement of a 60 nm thick TiN film deposited on a 350 μm polished c-plane sapphire substrate. Individual measurements points are plotted, showing a gap around 1000 nm where the set-up switches between two different detectors. Measured from 191.35 nm to 1688.0 nm in 710 non-equidistant measurement points.

for visible light and has a relative permittivity close to the desired value for a $\lambda/4$ matching layer, $\epsilon_{r,\lambda/4} = \sqrt{\epsilon_{r,1}\epsilon_{r,2}}$ with $\epsilon_{r,1}$ and $\epsilon_{r,2}$ the relative permittivity of the two media surrounding the matching layer. The material properties for SiO_2 and Al are taken from [8] and [9].

The calculated absorbed and reflected power fractions for this stack are given in Fig. 5.5. The given absorption is for the entire structure and contains the power absorbed by the Al mirror in addition to the power absorbed in the TiN MKID. The transmission line model presented here can be used to extract the power absorbed per layer, separating the power absorbed in the TiN layer from the power lost in the dielectric and Al layers. The model shows that of the power absorbed by the stack, 1-5% is absorbed in the Al mirror with a ∼1% absorption in the two dielectric layers for shorter wavelengths, see Fig. 5.5. The authors of [10] quote an absorption of 3% in the metallic mirror at 1550 nm, similar to the results presented here. For a single wavelength application an optimal stack can be analytically designed for 100% absorption. However, the power absorbed in the actual detector is limited to ∼95-98% by absorption in the dielectric and Al layers.

5.3. Measurement

We measure the reflectance and transmittance from 400 nm to 1550 nm with a commercial spectrophotometer (PerkinElmer Lambda 1050+) equipped with an integrating sphere (IS), with the sample mounted at the front (transmission) or back (reflection) port of the IS. The measurement is self-calibrating through spectralon (white disk) reference measurements. At around 900 nm, the spectrophotometer switches gratings, which causes a calibration error resulting in fluctuations around the 900 nm point. The measured reflection and derived absorption are given in Fig. 5.5, which shows a good agreement between the model and measurement. The transmitted power is omitted from this figure since it is 0% over the entire wavelength range for both the model and measurement due to the 100 nm thick Al mirror. The SiO_2 layers are sputter deposited from a quartz target.

The disagreement between model and measurement can be explained by a relatively small change in optical properties or a deviation in the layer thicknesses. We did not measure the layer thicknesses of the fabricated sample. These changes can explain the larger deviation at shorter wavelengths in Fig. 5.5 as they can create destructive interference close to the wavelength range of interest.

The reflection and transmission measurement is performed at room temperature while the operating temperature of MKIDs is around 100 mK. The change in temperature can have an effect on the optical constants of the metallic layers. To study the temperature dependence of these films, the optical constants of metallic layers can

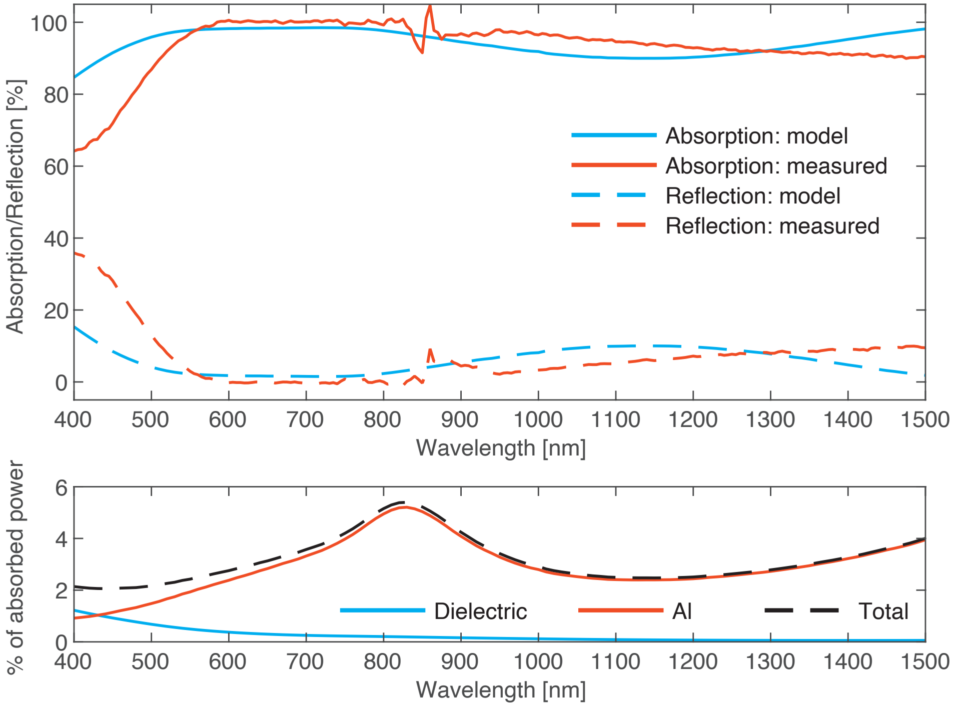

Figure 5.5: **Top:** Model (*blue*) and measurement (*red*) of the absorption (*solid*) and reflection (*dashed*), of a stack consisting of, from top (illumination side) to bottom: 85 nm layer of SiO_2, a 60 nm thick unpatterned TiN film, a 23 nm SiO_2 layer and a 100 nm thick Al mirror deposited on a 350 μm polished c-plane sapphire substrate.The absorbed power is derived from the measured reflection and transmission. The measurement is performed with a PerkinElmer Lambda 1050+ spectrophotometer equipped with an integrating sphere. **Bottom:** Power lost per material defined as the fraction of total absorbed power. The material properties for SiO_2 and Al are taken from [8] and [9]. (Color figure online.)

be modelled as a combination of a Drude term and a set of Lorentz oscillators, as is done for TiN in [11] and for Al in [8]. The Drude term scales with the conductivity of the sample σ and is thus temperature dependent. We assume the interband transitions, modelled with the Lorentz oscillator model, are temperature independent. We measure the temperature dependency of σ with a four-probe DC structure during a cool-down as the Residual-Resistance Ratio (RRR). For TiN, RRR is $\sim$1 and for Al it is $\sim$3, indicating that the optical constants of TiN should be temperature independent. Furthermore, the analysis in [8] and [11] show that the optical constants of both the Al and TiN films are dominated by the temperature independent interband transitions.

5.4. Conclusion and Outlook

We have designed an optical stack consisting of, from top (illumination side) to bottom: 85 nm SiO_2, 60 nm TiN (MKID inductor), 23 nm SiO_2 and a 100 nm thick Al mirror optimized for broadband absorption in the visible to near-infrared. As presented in Fig. 5.5, the initial results are promising, showing near-unity absorption from 600 nm to 800 nm and overall high absorption in the 400 nm to 1550 nm band. For the next iteration, we will measure both the layer thickness and optical constants of each deposited layer, to get a better agreement between model and measurement. The final goal is to measure the absorption efficiency of a MKID with its inductor embedded in an optical stack. In addition to the analysis in this paper, this requires an understanding of the effect of temperature on the optical properties of each layer, as well as the effect of a patterned MKID layer (inductor lines).

5.5. acknowledgements

We acknowledge Martijn Tijssen and Olindo Isabella for their support with the ellipsometry and reflection/transmission measurements. This work is financially supported by the Netherlands Organisation for Scientific Research NWO (Projectruimte 680-91-127 and Veni Grant No. 639.041.750). JJAB was supported by the European Research Council ERC (Consolidator Grant No. 648135 MOSAIC). The datasets generated during and/or analysed during the current study are available in the ZENODO repository, `https://doi.org/10.5281/zenodo.5549994`.

Bibliography

[1] B. A. Mazin, "Superconducting Materials for Microwave Kinetic Inductance Detectors," pp. 756–765, Apr. 2020. DOI: `10.48550/arxiv.2004.14576`. arXiv: `2004.14576 [astro-ph,physics:cond-mat]`.

[2] G. Coiffard, M. Daal, N. Zobrist, *et al.*, "Characterization of sputtered hafnium thin films for high quality factor microwave kinetic inductance detectors," en, *Supercond. Sci. Technol.*, vol. 33, no. 7, 07LT02, May 2020, Publisher: IOP Publishing, ISSN: 0953-2048. DOI: `10.1088/1361-6668/ab8d99`.

[3] D. Rosenberg, S. W. Nam, A. J. Miller, *et al.*, "Near-unity absorption of near-infrared light in tungsten films," *Nucl. Instrum. Methods Phys. Res., Sect. A*, Proceedings of the 10th International Workshop on Low Temperature Detectors, vol. 520, no. 1, pp. 537–540, Mar. 2004, ISSN: 0168-9002. DOI: `10.1016/j.nima.2003.11.308`.

[4] A. E. Lita, A. J. Miller, and S. W. Nam, "Counting near-infrared single-photons with 95% efficiency," EN, *Optics Express*, vol. 16, no. 5, pp. 3032–3040, Mar. 2008, Publisher: Optica Publishing Group, ISSN: 1094-4087. DOI: `10.1364/OE.16.003032`.

[5] M. Dai, W. Guo, X. Liu, *et al.*, "Measurement of Optical Constants of TiN and TiN/Ti/TiN Multilayer Films for Microwave Kinetic Inductance Photon-Number-Resolving Detectors," en, *J. Low Temp. Phys.*, vol. 194, no. 5, pp. 361–369, Mar. 2019, ISSN: 1573-7357. DOI: `10.1007/s10909-018-2095-9`.

[6] D. M. Pozar, *Microwave Engineering.* Wiley, 2012, ISBN: 9781118213636.

[7] D. A. Frickey, "Conversions between S, Z, Y, H, ABCD, and T parameters which are valid for complex source and load impedances," *IEEE Trans. Microw. Theory Techn.*, vol. 42, no. 2, pp. 205–211, Feb. 1994, Conference Name: IEEE Transactions on Microwave Theory and Techniques, ISSN: 1557-9670. DOI: `10.1109/22.275248`.

[8] A. D. Rakić, "Algorithm for the determination of intrinsic optical constants of metal films: Application to aluminum," EN, *Applied Optics*, vol. 34, no. 22, pp. 4755–4767, Aug. 1995, Publisher: Optica Publishing Group, ISSN: 2155-3165. DOI: `10.1364/AO.34.004755`.

[9] L. V. R. de Marcos, J. I. Larruquert, J. A. Méndez, and J. A. Aznárez, "Self-consistent optical constants of SiO_2 and Ta_2O_5 films," EN, *Optical Materials Express*, vol. 6, no. 11, pp. 3622–3637, Nov. 2016, Publisher: Optica Publishing Group, ISSN: 2159-3930. DOI: `10.1364/OME.6.003622`.

[10] D. V. Reddy, R. R. Nerem, S. W. Nam, R. P. Mirin, and V. B. Verma, "Superconducting nanowire single-photon detectors with 98% system detection efficiency at 1550 nm," EN, *Optica*, vol. 7, no. 12, pp. 1649–1653, Dec. 2020, Publisher: Optica Publishing Group, ISSN: 2334-2536. DOI: `10.1364/OPTICA.400751`.

[11] P. Patsalas and S. Logothetidis, "Optical, electronic, and transport properties of nanocrystalline titanium nitride thin films," *J. Appl. Phys.*, vol. 90, no. 9, pp. 4725–4734, Nov. 2001, ISSN: 0021-8979. DOI: `10.1063/1.1403677`.

Chapter 6

61% Detector Efficiency in Kinetic Inductance Detectors Using a SiN Anti-Reflection Layer

A model based on the optical properties of superconductors predicts nearly perfect absorption efficiency in the VIS-NIR range for kinetic inductance detectors (KIDs) integrated into an optical stack of anti-reflection (AR) layers and a backing reflector. However, efficiency measurements for KIDs with AR-layers remain scarce. We present detector efficiency measurements of lens-coupled KIDs with a 54-nm thick SiN AR layer that improves the absorption efficiency predominantly between 400 and 800 nm. At 500 nm, these KIDs demonstrate an enhanced detector efficiency of 61%, nearly double the efficiency that we expect without the AR layer. The measured detector efficiency includes the reflections of the AR-coated microlens array. The wavelength dependency of the detector efficiency matches with the predicted absorption efficiency.

6.1. Introduction

The absorption efficiency, which quantifies the ratio of absorbed photons to photons incident on the absorbing structure, is an important parameter for any detector. For superconducting detectors, this efficiency is typically limited to around 50% at 400 nm by the low absorption efficiency of bare high-resistivity superconductors used for the absorbing structure [1]–[3]. However, this absorption efficiency can be improved to near-unity by embedding the absorber in a multi-layer optical stack [2]–[6].

The absorbing structure varies between different types of superconducting detectors. For a Transition Edge Sensor (TES), radiation is absorbed in a square, unpatterned patch, e.g., of 25×25 μm^2 [5]. On the other hand, Superconducting Nanowire Single-Photon Detectors (SNSPDs) absorb radiation in narrow, meandering lines. The width of the wires and the spacing between them are typically much smaller ($\sim$100 nm) than the wavelength. Because the dimensions of the wires are subwavelength, they need to be taken into account to calculate the absorption efficiency of the superconducting absorber structure [7].

An improved absorption efficiency has been measured by embedding the absorber of these devices in a multi-layer optical stack [4]–[6]. For a TES with a 25×25 μm^2 tungsten absorber, the efficiency is increased to greater than 97% at 1550 nm by embedding the tungsten layer in a stack of Au:SiO_2:W:SiN [6]. For a SNSPD with molybdenum silicide wires, the absorption efficiency is increased to 98% at 1550 nm by patterning the wires (80 nm width with 60 nm gaps) on a SiO_2 and amorphous silicon (α-Si) distributed Bragg reflector (DBR), and depositing a three-layer anti-reflection (AR) coating of α-Si, SiO_2, and α-Si atop the devices [4].

For kinetic inductance detectors (KIDs) in the visible to near-infrared, radiation is absorbed by the inductor. For KIDs, the width and spacing of the inductor lines are typically larger, in the order of a few microns, than the wavelengths of interest (400-1550 nm). In this case, we can separate the absorption efficiency into the absorption efficiency of the unpatterned superconducting layer and the filling ratio of the absorber (inductor) wires.

Although designs that improve the absorption efficiency of KIDs to near-unity are available [3], [8], and proof-of-concept reflection-transmission measurements on unpatterned films show the feasibility of such designs, measurements of the improved absorption efficiency of an actual KID remain sparse. In Ref. [9] the authors show measurements of a two-layer AR-coating of SiO_2 and Ta_2O_5 on a platinum silicide (PtSi) KID. They expected a factor two improvement in absorption efficiency based on reflection and transmission measurements of an unpatterned PtSi film plus AR-coating. The authors did, however, not achieve the expected increase in detector efficiency.

In this work, we demonstrate KIDs with a thin SiN AR-coating. Based on the transmission line model introduced in Ref. [3], the 54-nm thick SiN AR-layer should improve the absorption efficiency from ∼40% to ∼80% at a wavelength of 600 nm. With this AR-coating, we reach a maximum detector efficiency of 61% at 500 nm. This detector efficiency relates the power incident on each pixel to the detected number of photons and is the combined efficiency of the following contributions:

- **Absorption efficiency:** For a KID, we separate the efficiency of the absorber into the absorption efficiency of an unpatterned film and the effective filling-fraction of the inductor wires. This efficiency is then the power absorbed by an unpatterned superconducting film, including the optical stack, with respect to the power incident on that film.
- **Effective filling-fraction:** For a uniformly illuminated absorber, this is given by the fill factor of the inductor based on the line width and spacing. However, for a lens-coupled device, where the focussed spot falls within the total area of the inductor, we have an effective filling-fraction that depends on both the spot size and location, i.e., the effective filling-fraction is one if the spot falls entirely on a single wire. This effective filling-fraction can be smaller or bigger than the fill factor calculated from the line width and spacing.
- **Lens efficiency**: Defined as the power in the focused lens spot compared to the power intersecting the physical aperture of the lens. This efficiency includes the surface reflections on both sides of the lens array. In addition, it includes the decrease in efficiency at the edges of the lens due to geometrical effects, where the beam has an off-normal angle of incidence with respect to the lens surface. For shallow lenses, like the ones in this work, this efficiency is dominated by the surface reflections.
- **Detection efficiency:** The ratio between absorbed and detected photons. For an SNSPD [4], the energy deposited by the absorbed photon needs to surpass a certain threshold to lead to a detection event. Due to fluctuations in the energy downconversion process, some absorbed photons might not trigger the detector [4]. For KIDs, which are energy-resolving detectors, every absorbed photon will lead to a photon pulse where the fluctuations during the downconversion process lead to pulse-height fluctuations, and we expect the detection efficiency to be 100% as long as we have enough signal-to-noise to identify the pulses in the measured readout timestreams.

6.2. Design

We use a 400-pixel (20×20) chip with hybrid lumped element β-Ta/NbTiN KIDs similar in design to those presented in Ref. [10]. A microscope image of a section of the array is given in Fig. 6.1. The KIDs consist of a NbTiN interdigitated capacitor (IDC) and a β-Ta meandered inductor and are coupled to a NbTiN coplanar waveguide (CPW) readout line with a NbTiN coupling bar that runs alongside the IDC. This coupling bar galvanically connects to the central line of the CPW. At regular intervals, β-Ta on polyimide bridges galvanically connect the two ground planes of the CPW.

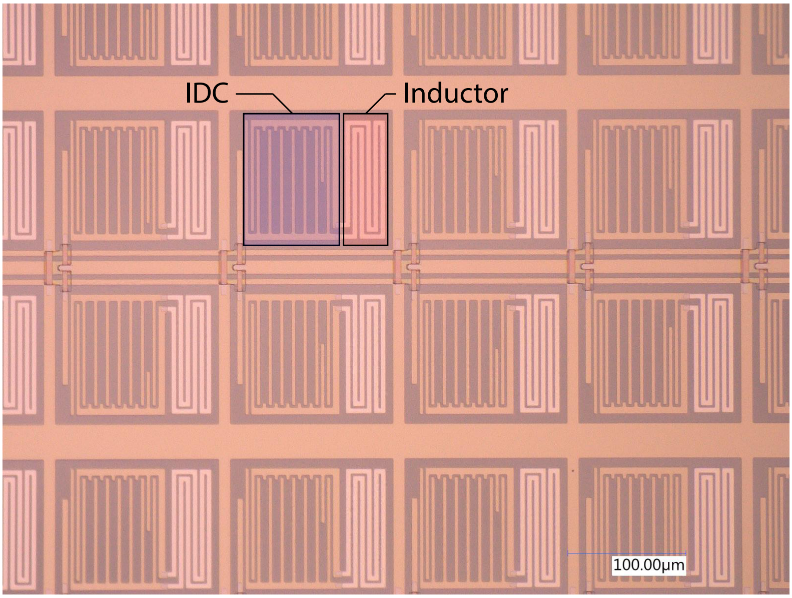

Figure 6.1: Microscope image of a section of the array of hybrid β-Ta/NbTiN LEKIDs before the SiN layer that covers the entire chip was deposited. Each KID is connected to the coplanar waveguide (CPW) readout line with a double-sided coupling bridge. Pixels have a 150 µm pitch. Microlenses ($\sim f/4$) are mounted above the array on Perminex pillars (not in this picture) and focus light on the center of the meandering inductors.

There are a few modifications compared to Ref. [10]; the inductor lines are now 4-µm wide, with 2-µm spacing limited by optical lithography. The β-Ta layer is 40 nm thick, and the total volume of the inductor is increased such that pulses do not saturate for 400 nm photons as discussed in Chapter 4. Additionally, we have reduced the number of fabrication steps by making the bridges crossing the readout line from the same β-Ta layer as the inductor.

We fabricate the resonators on a 350-μm c-plane sapphire substrate using optical contact lithography and reactive-ion etching to pattern the structures. The IDC and readout-line, which are deposited first, are patterned in 150 nm of reactive magnetron sputter-deposited NbTiN [11], [12]. The inductor is patterned in a 40-nm thick film of sputter-deposited β-Ta.

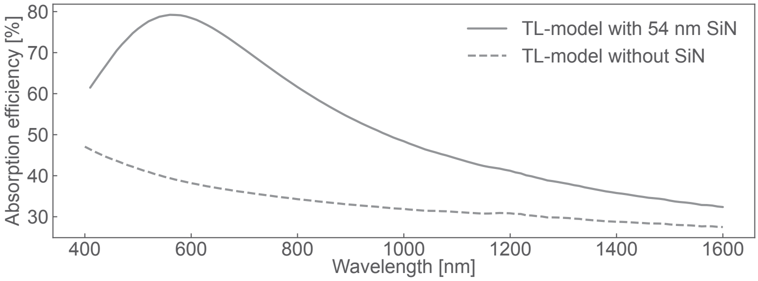

Figure 6.2: Modelled absorption efficiencies of a bare, 40-nm thick, $\beta - \mathrm{Ta}$ film (dashed) and an AR-coated β-Ta film (solid). Difference between the lines is the expected increase in absorption efficiency from a 54-nm thick layer of SiN deposited on top of a 40-nm thick β-Ta layer. Absorption efficiency is calculated with the transmission line model discussed in Chapter 5.

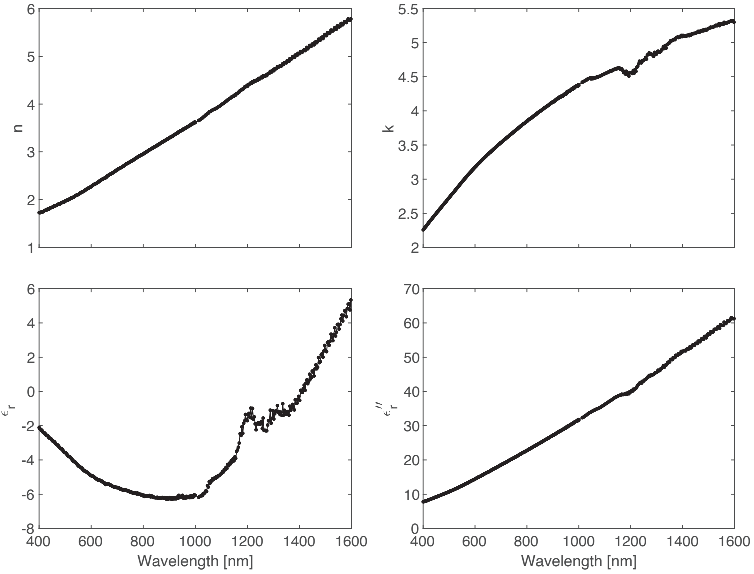

Figure 6.3: Optical constants (n,k) and relative permittivity for β-Ta. These values are derived from a multi-angle spectroscopic ellipsometry measurement of a 60 nm thick β-Ta film on a 350 μm polished c-plane sapphire substrate. Individual measurement points are plotted, showing a gap around 1000 nm where the set-up switches between two detectors. Measured from 191.35 nm to 1688.0 nm in 710 non-equidistant measurement points.

To improve the absorption efficiency, the entire chip is coated with a 54-nm thick layer of SiN. We use the transmission line model discussed in Chapter 5 to model the absorption efficiency of 40-nm thick β-Ta film with and without a SiN coating, see Fig. 6.2. At 600 nm, the AR-coated absorber has an absorption efficiency of 78%, while the bare β-Ta layer has an absorption efficiency of 38%. The modeled absorption efficiencies are based on the optical constants of the β-Ta layer in Fig. 6.3, retrieved from spectroscopic ellipsometry measurements [Woollam M-2000] of a film deposited with the same recipe as used for the inductors [10]. For the SiN layer, we use a constant value of n = 2.0 and assume the losses to be negligible, which is appropriate for dielectric layers at these wavelengths.

The SiN layer is deposited using a plasma-enhanced chemical vapor deposition (PECVD) at a temperature of 300 °C, with SiH_4 and N_2, in an Oxford Instruments PlasmaPro800.

Before the deposition of the SiN layer, the 40-nm thick β-Ta film had a T_c of 1.0 K and a sheet resistance (R_s) of 47.2 $\Omega/\Box$. After SiN deposition, we no longer see a superconducting transition in the DC structures, so we cannot perform representative DC-measurements for the β-Ta + SiN layer. However, based on VNA measurements, we see that the KIDs shifted down in frequency after the SiN deposition, with the lowest frequency KID now resonating at 4.41 GHz instead of 4.63 GHz. Simulating the KID in Sonnet, we expect a downward frequency shift of ~0.02 GHz due to the increased capacitance from the SiN layer for this KID. Since the measured frequency shift is much larger, we assume that the β-Ta has a lower T_c or a higher R_s, or both, after the SiN deposition. The KIDs show similar photon pulse heights for the same wavelength with and without the SiN layer.

6.2.1. Lens array

We focus incoming light onto the inductors with a 100×100 microlens array [Advanced microoptic systems GmbH APO-Q-P150-R0.19]. The fused silica microlenses have a pitch of 150 um and a radius of 0.19 mm. The fused silica block in which the lenses are patterned is 0.6 mm thick. The lenses are AR-coated on both sides, with a single surface reflection $R < 1.5\%$ across the 400 to 1000 nm wavelength range. We use the lens array for front illumination of the devices, where the incoming light does not pass through the chip's substrate.

The lens array is bonded to the chip with pillars of PermiNex 1010, a spin-on photo-sensitive glue, which creates a vacuum gap between the chip and lens array as illustrated in Fig. 6.4. The thickness of the spin-on Perminex layer, and thus the height of the pillars varies between fabrication within 10-15 µm. We align the lenses to the center of the KID inductor using a microscope and two separate manipulation stages. Once we achieve rotational alignment between the lens array and the KID

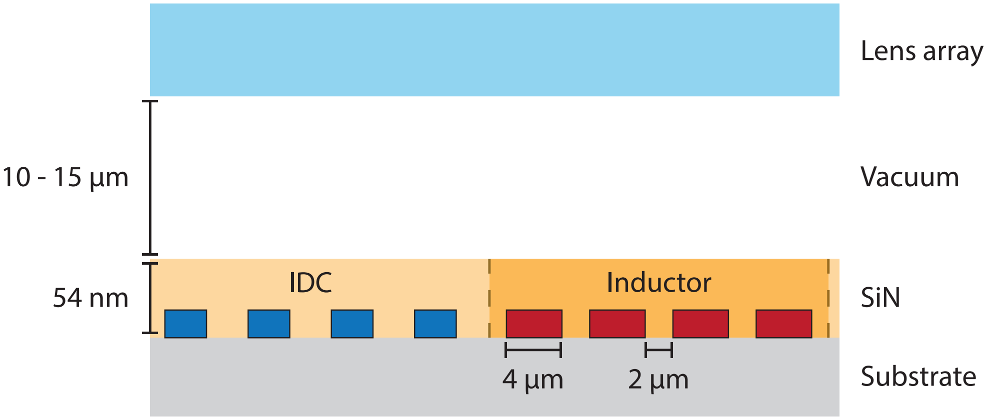

Figure 6.4: Cross-sectional view of the chip. A lens array is spaced 10-15 µm from the chip on Perminex pillars. The entire chip is coated with a 54-nm thick SiN AR-layer, which means that both the inductor (absorber) and the interdigitated capacitor (IDC) are capped by SiN. Ideally, the AR layer would be restricted to the inductor where power is absorbed, as indicated by the dashed lines, to limit the additional TLS noise caused by electric fields of the IDC interacting with defects in the SiN layer, see Ref. [3].

chip and align the lens's center with the inductor's center, we press the lens array onto the Perminex pillars and glue it to the chip. Using this method, we measured the alignment accuracy of the lenses to typically be within 4 µm of the center of the inductor [13].

6.3. Measurements

As discussed in Section 3.3, we use a grating monochromator to illuminate the KID array at different wavelengths. Using standard Thorlabs components, we create a 25-mm diameter beam using a single lens focused on the output of an integrating sphere. A graphical representation of this setup is given in Fig. 3.6. The beam that travels to the KID array passes through the 10% transmission side of a beamsplitter cube and a neutral density filter with an optical density of 2.0. This beam is then coupled into the cryostat, where it passes through a set of filters before falling on the KID lens array, uniformly illuminating all 400 pixels. For this experiment, the total size of the KID array (3×3 mm^2) is smaller than the incoming beam diameter (25 mm). The sample holder contains a 3.7×3.7 mm^2 square aperture that limits the total power falling on the chip but does not limit the power falling on each KID.

To obtain the detector efficiency, we first measure the power in the full 25-mm diameter beam. We then use the transmission curve of the cryostat filters to estimate the power incident on the KID array. The incident power gives us the expected photon countrate of a 100% efficient detector, which we compare to the measured photon countrates of five KIDs.

6.3.1. Power at sample

We use the photodiode in the secondary arm of Fig. 3.6, behind a 90:10 beamsplitter, to monitor the power and stability of the source during each measurement. As explained in Section 3.3, the power falling on the chip was independently calibrated with respect to this photodiode, as explained in Section 3.3. The measured total power of the 25-mm diameter beam falling on the chip, without the cryostat filters, for the two different beamsplitters we use is given in Fig. 6.5a. The power per KID is a factor $A_{KID}/A_{beam} = 4.6 \times 10^{-5}$ lower, where A_{KID} is the aperture of the lens (150×150 µm^2).

The cryostat contains a set of filters with transmission curves as shown in Fig. 6.5 to create a passband between roughly 400 and 1100 nm. This combination of filters is a specific configuration of the setup described in Section 3.2. The vacuum window is a 6-mm thick CaF2 window that blocks radiation above ~ 10 μm. The window at the 30-K stage is an Asahi super cold filter [YSC1100] with a cut-off wavelength of 1.1 μm that blocks the blackbody radiation from the 300 K stage at wavelengths where the BK-7 windows are still transparent (< 3 µm). The 3-K, 100-mK, and sample stage have 5-mm thick BK7 windows, which are AR-coated for the VIS-NIR [WG11050-AB], which reject thermal radiation at wavelengths longer than 3 µm. Figs. 3.2 and 3.3 are cut views of the cryostat and sample stage.

6.3.2. Photon countrate

We measured KID response timestreams with and without illumination from the monochromator source at different wavelengths between 400 and 1100 nm. We measure 100 one-second-long timestreams at each wavelength, sampled at 1 Msample/s, and apply a peak-finding algorithm to the raw timestreams to identify individual photon events. We do not filter the timestreams before we apply the peak-finding algorithm since we measure very short, ~7 µs, pulses for β-Ta KIDs as discussed Chapter 4 for which a filter does not improve the SNR. Peaks exceeding a threshold of 4σ, with σ the standard deviation of the timestream, and with a minimum peak prominence of 0.6 are marked as photon hits, as demonstrated in Fig. 6.6. The prominence of a peak is the vertical difference between a peak's height and its lowest contour line or base [14].

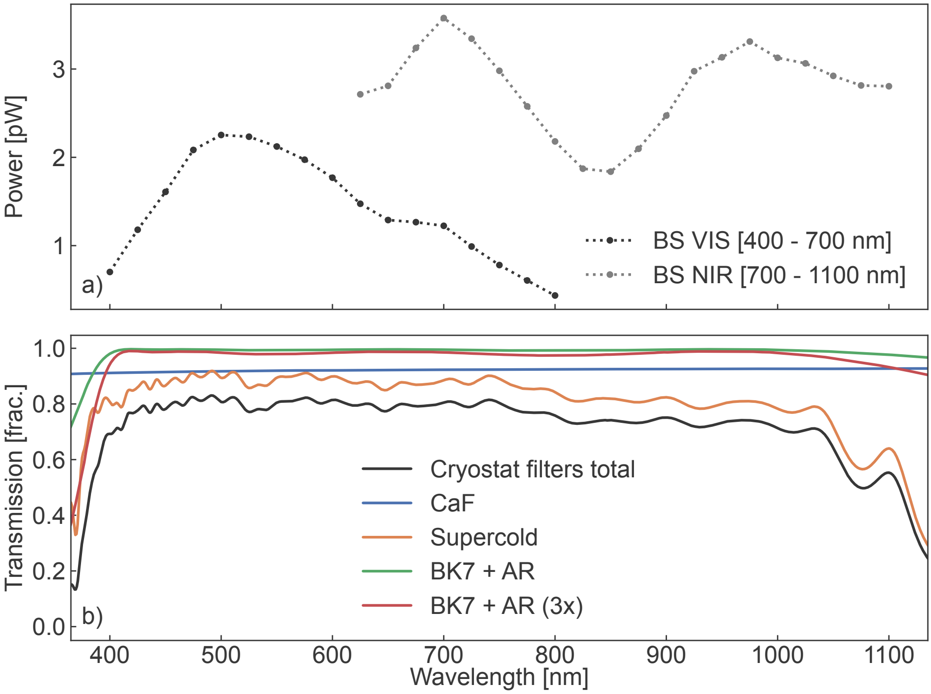

Figure 6.5: **a)** Total power in the 25-mm diameter beam incident on the lens array without the cryostat shields. Power is measured for both beamsplitters since the provided transmission curves are inaccurate; see Section 3.3. We use the VIS-beamsplitter up to 700 nm. Measurements are described in Section 3.3. Of this power, only A_{KID}/A_{beam} falls onto each KID. **b)** Filters in the cryostat shields, from input (room temperature) to sample: a 6-mm thick CaF2 vacuum window, an Asahi super cold filter [YSC1100] at 30 K, and three AR-coated BK7 windows [WG11050-AB] at the 3 K shield, the 100 mK stage and on the sample holder. The power per KID is obtained by multiplying the power in panel a with the total filter transmission and the factor $A_{KID}/A_{beam} = 4.6 \times 10^{-5}$

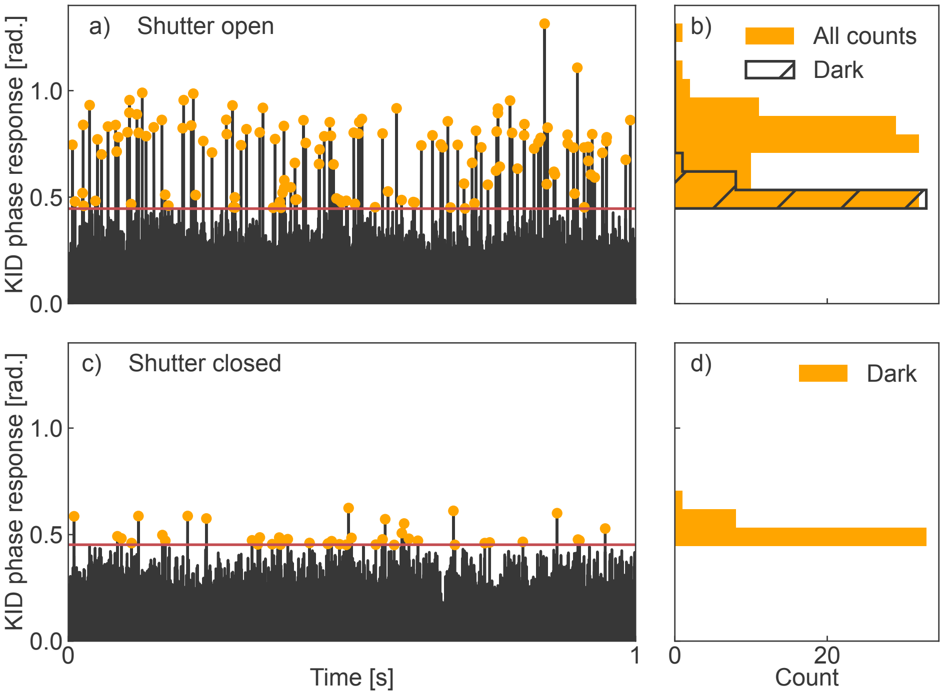

Figure 6.6: Raw KID readout timestreams of one second out of a total of 100 seconds of data. A peak-finding algorithm identifies all pulses above a 4σ threshold given in red with a peak prominence of at least 0.6. Histograms give the number of detected pulses of a given height. The top row is measured with the monochromator on (900 nm), while the bottom row is with the monochromator shutter closed. The dark count rate during the monochromator on measurements in panels a) and b) is estimated from the measurements in panels c) and d) where the shutter of the monochromator is closed. In reality, we use 100 seconds of data to get an accurate estimate of the photon count rate. The histograms in panels b and d show that, for this wavelength, some of the photon pulses have a similar height as the background counts, and their distributions overlap. For shorter wavelengths, the distributions of photon and dark counts are clearly separated.

With the shutter closed, there will still be a residual "dark" count rate, as visible in Fig. 6.6c, This count rate consists of background hits, where quasiparticles are created by photons originating from sources other than the monochromator, and of counts from noise fluctuations that pass the threshold. To measure each KID's dark count rate, we use the same selection criteria for identifying photon events to determine the number of counts in 100 seconds of data with the monochromator shutter closed, see Fig. 6.6c. We then estimate the photon count rate for each wavelength by subtracting the number of dark counts in the 100-second "off" interval (Fig. 6.6d) from the total number of photon events recorded in the 100-second "on" interval (Fig. 6.6b).

The measured photon count rate of 5 KIDs is given in Fig. 6.7b. For the shorter wavelengths, the photon hits are clearly separated from the background noise, and "dark" counts do not pass the threshold. Around 900 nm, photon hits start to become indistinguishable from some of the "dark" counts, and we need to set a threshold low enough to still pass the photon hits that are on the same level as some of the dark counts, see Fig. 6.6. We don't have enough signal-to-noise to measure the photon count rate for wavelengths longer than 1000 nm, where we cannot separate the pulses from the background noise.

6.3.3. Analysis

Since the illumination is radially uniform, see Section 3.3, each KID will capture a fraction of the beam given by $f_{cap} = A_{lens}/A_{beam} = 4.58 \times 10^{-5}$, with A_{lens} the area of the 150 × 150 μm^2 microlenses and A_{beam} the area of the 25-mm diameter beam. The expected power incident on the lens of one pixel is then given by $P_{pixel} = P_{in} \cdot T_{filters} \cdot f_{cap}$, with P_{in} the power in Fig. 6.5a and $T_{filters}$ the total filter transmission of Fig. 6.5b. Dividing this power by the photon energy at each wavelength gives the expected photon count rate for a 100% efficient detector, given in Fig. 6.7b. The detector efficiency in Fig. 6.7c is the ratio between the measured photon count rates and the expected count rate. This efficiency includes the lens efficiency, the KID's absorption efficiency, and the effective filling-fraction of the inductor lines.

The beam in our current optical setup diverges so the power measured by the diode during the photon counting measurements is different than the power falling on the KID array. In Section 3.3, we discuss how we calculate a calibration curve that gives the power incident on the KID array based on the power readings from the photodiode. We obtained this calibration by comparing the measured power at the position of the diode in the secondary arm of Fig. 3.6 and at the location of the KID lens array. However, any uncertainty in the placement of the focussing lens with respect to the actual location of the KID lens array in the closed setup will translate to an uncertainty in power. To get an estimate of this uncertainty, we record the power at ± 2.5 cm offsets to where we predict the KID-plane to be based on the

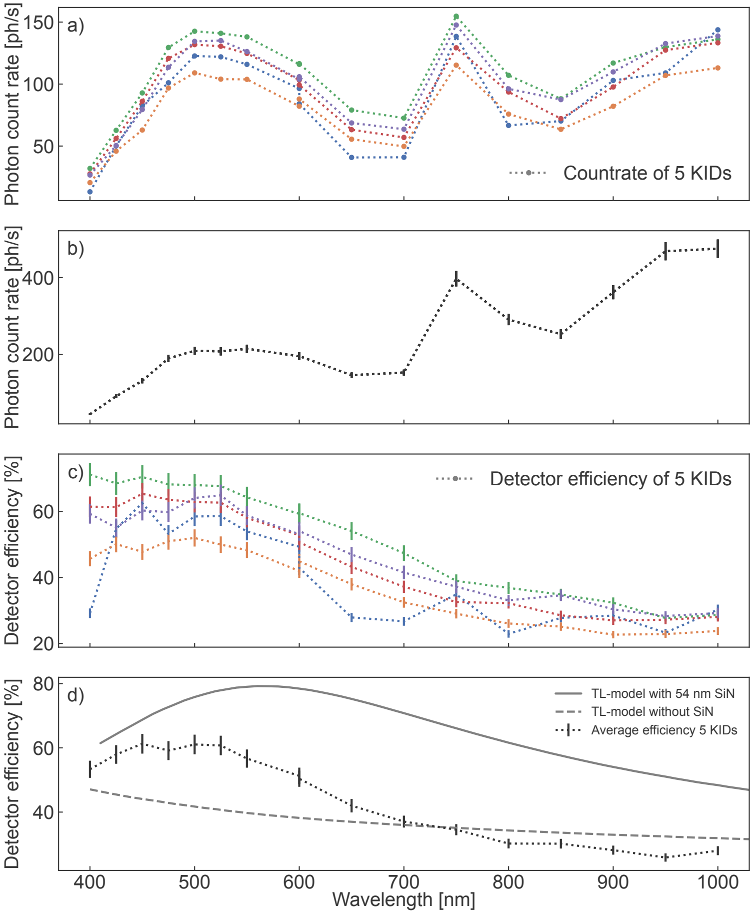

Figure 6.7: **a)** Photon count rates of five KIDs are measured by counting the number of photon hits in 100 seconds of data when the array is illuminated at a single wavelength by the monochromator and subtracting the number of dark counts in 100 seconds of data with the monochromator shutter closed, see Fig. 6.6. **b)** Expected photon count rate for a 100% efficient detector based on the total power in the beam at the sample location (Fig. 6.5a) and the transmission of cryostat filters (Fig. 6.5b). Each KID captures only a fraction of the total power in the beam, given by $A_{KID}/A_{beam} = 4.58 \times 10^{-5}$. There is a jump between 700 nm and 750 nm because we switch between two different beamsplitters, see Fig. 6.5a. Each point has a relative error of 5% due to uncertainty in power at the sample location; refer to the main text for details. **c)** Detector efficiency based on panels a) and b). This efficiency includes reflection from the microlens array, the absorption efficiency, and the fill fraction of the inductor. Error bars are a relative 5% error from the uncertainty in the expected photon count rate; see panel b. **d)** Measured average detector efficiency of the 5 KIDs from panel c) plotted together with the expected absorption efficiencies of a bare 40-nm thick β-Ta film (dashed) and a 40-nm thick β-Ta layer with a 54-nm thick SiN AR-coating (solid). Error bars are the 5% relative error from panel c.

geometry of the set-up. The difference in power recorded at these points gives an uncertainty of roughly 5% on the power plotted in Fig. 6.5, and a 5% relative error on the measured efficiencies in Figs. 6.7c and 6.7d.

6.4. Results and Discussion

The main result is the measured averaged detector efficiency of 5 KIDs in Fig. 6.7d, where we achieve a 61% detector efficiency at 500 nm. Based on the modeled absorption curves, this detector efficiency would be roughly a factor two lower without the SiN AR-layer. Since we can recognize the expected absorption efficiency profile in the average efficiency in Fig. 6.7d, we conclude that the SiN AR-coating works and has improved the detector efficiency by roughly a factor of two. However, since the measured detector efficiency "peak" in Fig. 6.7d is shifted to shorter wavelengths, the SiN layer is either thinner than expected, has a higher refractive index than expected, or both.

The measured detector efficiency includes the effective filling-fraction of the inductors. The patterned inductors have a fill factor of 66% (measured 4 µm lines with 2 µm gaps). It is difficult to predict the effective filling-fraction for a given inductor design since it depends on the size of the lens focal spot, which is wavelength-dependent. In addition, it depends on the alignment of the lens to the inductor and any tip/tilt of the lens array with respect to the KID chip. We can roughly estimate the effective filling-fraction by comparing the maximum measured detector efficiency and the maximum of the modeled absorption in Fig. 6.7d, which gives an effective filling ratio of 75%.

There are differences in count rates between the 5 KIDs in Fig. 6.7c, which are consistent with wavelength. These differences could result from source instabilities, given that the KIDs are measured sequentially for each wavelength. This is unlikely since the stability of the source is continuously monitored by the photodiode in the secondary arm, confirming that the source remains stable throughout the measurement. In section 3.3, we verified that the beam is radially uniform with an iris, but we did not measure if the beam is laterally uniform. if the beam is not laterally uniform, this could explain the variations in count rates between KIDs. Alternatively, the difference in count rates between KIDs can indicate that the beam falling on the array is spatially non-uniform or that the lens array is either be rotated or tilted with respect to the KID array such that each KID has a different effective filling faction. Additional measurements are required to measure the beam's spatial uniformity and check the lens's rotation and tip-tilt with respect to the chip.

The entire chip was coated with the SiN AR-layer for this experiment. The presence of SiN on the interdigitated capacitor in Figs. 6.1 and 6.4 will increase the noise level of the KID as two-level system (TLS) defects in the dielectric can couple to the electric field of the resonator which introduced excess frequency noise [15]. Comparing AR-coated and bare resonators from different chips, the AR-coated KIDs have a roughly 8 dB higher phase noise level at 10 Hz and an order of magnitude lower Qi ($\sim 1\times10^4$ instead of $\sim 1\times10^5$). In the future, we plan to constrain the SiN to patches on the inductor as in Fig. 6.4 to limit the amount of electric field in the dielectric which should prevent the increase in TLS-frequency noise, thus improving the SNR of the detector. In addition, we plan to measure chips with and without AR coating to study whether the variation in absorption efficiency is inherent to the detectors or if the SiN coating introduces it. Finally, we will measure the absorption efficiency of more pixels and identify the location of each pixel on the chip to see if there are any spatial dependencies in the absorption efficiency that could point to inhomogeneities in the beam or effects of the lens mounting process, such as rotation or tip-tilt with respect to the chip.

We plan to improve the setup by reducing the divergence in the beam so that we can use the photodiode in the reference arm without relying on the extra calibration from Section 3.3 to calculate the power incident on the cryostat window. In the future, we plan to demonstrate near-unity absorption with the multi-layer designs similar to Chapter 5, which contain, in addition to the SiN AR-layer, a Al backing reflector spaced behind the inductor with a thin SiN layer.

Bibliography

[1] P. Szypryt, B. A. Mazin, G. Ulbricht, *et al.*, “High quality factor platinum silicide microwave kinetic inductance detectors,” *Appl. Phys. Lett.*, vol. 109, no. 15, p. 151 102, Oct. 2016, ISSN: 0003-6951. DOI: `10.1063/1.4964665`.

[2] G. Coiffard, M. Daal, N. Zobrist, *et al.*, “Characterization of sputtered hafnium thin films for high quality factor microwave kinetic inductance detectors,” en, *Supercond. Sci. Technol.*, vol. 33, no. 7, 07LT02, May 2020, Publisher: IOP Publishing, ISSN: 0953-2048. DOI: `10.1088/1361-6668/ab8d99`.

[3] K. Kouwenhoven, I. Elwakil, J. v. Wingerden, *et al.*, “Model and Measurements of an Optical Stack for Broadband Visible to Near-Infrared Absorption in TiN MKIDs,” *J. Low Temp. Phys*, Jul. 2022. DOI: `10.1007/s10909-022-02774-0`.

[4] D. V. Reddy, R. R. Nerem, S. W. Nam, R. P. Mirin, and V. B. Verma, “Superconducting nanowire single-photon detectors with 98% system detection efficiency at 1550 nm,” EN, *Optica*, vol. 7, no. 12, pp. 1649–1653, Dec. 2020, Publisher: Optica Publishing Group, ISSN: 2334-2536. DOI: `10.1364/OPTICA.400751`.

[5] A. E. Lita, A. J. Miller, and S. W. Nam, “Counting near-infrared single-photons with 95% efficiency,” EN, *Optics Express*, vol. 16, no. 5, pp. 3032–3040, Mar. 2008, Publisher: Optica Publishing Group, ISSN: 1094-4087. DOI: `10.1364/OE.16.003032`.

[6] D. Rosenberg, S. W. Nam, A. J. Miller, *et al.*, “Near-unity absorption of near-infrared light in tungsten films,” *Nucl. Instrum. Methods Phys. Res., Sect. A*, Proceedings of the 10th International Workshop on Low Temperature Detectors, vol. 520, no. 1, pp. 537–540, Mar. 2004, ISSN: 0168-9002. DOI: `10.1016/j.nima.2003.11.308`.

[7] M. G. Moharam and T. K. Gaylord, “Rigorous coupled-wave analysis of planar-grating diffraction,” *J. Opt. Soc. Am.*, vol. 71, no. 7, pp. 811–818, Jul. 1981. DOI: `10.1364/JOSA.71.000811`.

[8] M. Dai, W. Guo, X. Liu, *et al.*, “Measurement of Optical Constants of TiN and TiN/Ti/TiN Multilayer Films for Microwave Kinetic Inductance Photon-Number-Resolving Detectors,” en, *J. Low Temp. Phys.*, vol. 194, no. 5, pp. 361–369, Mar. 2019, ISSN: 1573-7357. DOI: `10.1007/s10909-018-2095-9`.

[9] G. Coiffard, B. Mazin, N. Zobrist, M. Daal, and S. Steiger, "Anti-reflection coating to improve the optical quantum efficiency of PtSi MKIDs arrays," in *18th International Workshop on Low Temperature Detectors (LTD-18)*, 2019. [Online]. Available: `https://agenda.infn.it/event/15448/contributions/95577/`.

[10] K. Kouwenhoven, D. Fan, E. Biancalani, *et al.*, "Resolving Power of Visible-To-Near-Infrared Hybrid β-Ta/Nb-Ti-N Kinetic Inductance Detectors," *Phys. Rev. Applied*, vol. 19, no. 3, p. 034 007, Mar. 2023, ISSN: 2331-7019. DOI: `10.1103/physrevapplied.19.034007`.

[11] D. J. Thoen, B. G. C. Bos, E. A. F. Haalebos, T. M. Klapwijk, J. J. A. Baselmans, and A. Endo, "Superconducting NbTin Thin Films With Highly Uniform Properties Over a 100 mm Wafer," *IEEE Trans. Appl. Supercond.*, vol. 27, no. 4, pp. 1–5, Jun. 2017. DOI: `10.1109/TASC.2016.2631948`.

[12] B. G. C. Bos, D. J. Thoen, E. A. F. Haalebos, *et al.*, "Reactive Magnetron Sputter Deposition of Superconducting Niobium Titanium Nitride Thin Films With Different Target Sizes," *IEEE Trans. Appl. Supercond.*, vol. 27, no. 4, pp. 1–5, Jun. 2017. DOI: `10.1109/TASC.2016.2631939`.

[13] I. Elfferich, "Accurate alignment of microlens arrays to superconducting detectors," Internship report, The Hague University of Applied Sciences, 2022.

[14] SciPy documentation. "Peak_prominences." (n.d.), [Online]. Available: `https://docs.scipy.org/doc/scipy/reference/generated/scipy.signal.peak_prominences.html#scipy.signal.peak_prominences`.

[15] C. Müller, J. H. Cole, and J. Lisenfeld, "Towards understanding two-level-systems in amorphous solids: Insights from quantum circuits," *Rep. Progr. Phys.*, vol. 82, no. 12, p. 124 501, Oct. 2019. DOI: `10.1088/1361-6633/ab3a7e`.

Chapter 7

Geometry dependence of TLS noise and loss in *a*-SiC:H parallel plate capacitors for superconducting microwave resonators

Parallel plate capacitors (PPC) significantly reduce the size of superconducting microwave resonators, reducing the pixel pitch for arrays of single photon energy-resolving kinetic inductance detectors (KIDs). The frequency noise of KIDs is typically limited by tunneling Two-Level Systems (TLS), which originate from lattice defects in the dielectric materials required for PPCs. How the frequency noise level depends on the PPC's dimensions has not been experimentally addressed. We measure the frequency noise of 56 resonators with *a*-SiC:H PPCs, which cover a factor 44 in PPC area and a factor 4 in dielectric thickness. To support the noise analysis, we measure the resonators' TLS-induced, power-dependent, intrinsic loss and temperature-dependent resonance frequency shift. From the TLS models, we expect a geometry-independent microwave loss and resonance frequency shift, set by the TLS properties of the dielectric. However, we observe a thickness-dependent microwave loss and resonance frequency shift, explained by surface layers that limit the performance of PPC-based resonators. For a uniform dielectric, the frequency noise level should scale directly inversely with the PPC area and thickness. We observe that an increase in PPC size reduces the frequency noise, but the exact scaling is, in some cases, weaker than expected. Finally, we derive engineering guidelines for the design of KIDs based on PPC-based resonators.

This chapter was published as K. Kouwenhoven, G.P.J. van Doorn, B.T. Buijtendorp, S.A.H. de Rooij, D. Lamers, D.J. Thoen, V. Murugesan, J.J.A. Baselmans and P.J. de Visser, *Phys. Rev. Applied* **21**, 044036 (2024)

7.1. Introduction

Superconducting microwave resonators are one of the key elements of kinetic inductance detectors (KIDs) [1]–[3] and superconducting qubits [4]–[6]. The current resonators are typically based on planar structures such as coplanar waveguides (CPWs) and interdigitated capacitors (IDCs). These planar structures provide little capacitance per unit area since the fields are spread between the substrate and air, which limits the packing density or pixel pitch of these resonators [7], [8]. An alternative is the parallel-plate capacitor (PPC) [9]–[12], for which the entire field is in a dense ($\epsilon_r \sim 10$) and/or thin dielectric layer. Such a PPC can drastically shrink the resonator's size, but the deposited dielectric required to fabricate a PPC will likely increase the resonator's microwave loss and frequency noise level due to tunneling states in the dielectric.

The microscopic nature of these two-level tunneling states (TLSs) is still unknown, but they are typically assumed to arise from disorder in the crystalline lattice. Due to the disordered lattice, one or multiple atoms can tunnel between two energetically similar states modeled by the standard tunneling model (STM) [13]–[15]. The TLSs can couple to the electric field of the resonator through their electric dipole moment and modify the material's dielectric constant based on their individual states. Averaging over all TLSs that are resonant with the resonator gives the TLS contribution to the dielectric constant, ϵ_{TLS} [14], [15].

The real part of ϵ_{TLS} introduces a resonance frequency shift, while the imaginary part introduces microwave loss. In addition, TLSs can randomly switch states, which gives rise to a time-fluctuating dielectric constant. This, in turn, causes the resonator's resonance frequency to fluctuate in time, introducing excess frequency noise.

Recent studies have focused on developing and characterizing low-loss and low-noise dielectrics [16], [17]. However, how the microwave loss and frequency noise level scale with a PPC's dimensions has not been experimentally addressed.

Here, we experimentally study the TLS noise of PPC resonators based on hydrogenated amorphous silicon carbide (a-SiC:H). Recent work showed that a-SiC:H, depending on the exact deposition details, can be a low-loss, low-stress, deposited dielectric [17]. The exact deposition details for a-SiC:H used in this work are found in Ref. [17]. We vary two geometrical parameters of the PPC: the plate area and the dielectric thickness. We present an extensive dataset, containing 56 devices, with a factor of 44 in area variation and a factor of 4 in dielectric thickness.

In Sec. 7.2 we describe the resonator design, fabrication and the experimental setup. In Sec. 7.3.1 we focus on the TLS-induced microwave loss and frequency shift and show that the dielectric between the PPC plates contains lossy surface layers. Sec. 7.3.2 focuses on the resonator's frequency noise and how it scales with the PPC's dimensions. We first discuss the frequency noise spectrum and the power and temperature dependencies. Then, we show that the noise level decreases when the area or thickness of the PPC increases. In Sec. 7.4 we draw conclusions on the practical applicability of PPC-based resonators and discuss PPC-based KIDs.

7.2. Design, Fabrication and experimental setup

We use a lumped-element resonator design consisting of an *a*-SiC:H PPC and a meandered inductor, as shown in Fig. 7.1. The resonators couple to the CPW readout line with a small separate capacitor with a bottom plate that is galvanically connected to the central line of the CPW. The two ground planes of the CPW are electrically balanced at regular intervals by bridges that galvanically connect the ground planes (not shown). The resonators, coupling lines, readout line, and bridges are made from NbTiN with a critical temperature (T_c) of 14.3 K, sheet resistance of 12.4 $\Omega/\square$, and kinetic inductance of 1.2 pH/$\square$.

We vary the capacitor area by a factor of 44 on each chip with 20 resonators. To keep the resonant frequency within the range of our setup, we reduce the length of the inductor for the larger capacitors, as shown in Fig. 7.1 and Fig. 7.5. We vary the PPC thickness by fabricating the same design with three different dielectric thicknesses of *a*-SiC:H: 100, 200, and 400 nm. The designed resonance frequencies on the 200-nm wafer lie between 4.0 and 8.45 GHz and will shift down or up for the 100- and 400-nm wafers, respectively. For the 400-nm design, four resonators shifted beyond 9 GHz and could not be measured with our current setup.

We fabricate the resonators on a 350-μm *c*-plane sapphire substrate using optical contact lithography and reactive-ion etching to pattern the structures. The bottom PPC plate, inductor, readout lines and the bottom line of the coupling structure are fabricated from a 220-nm-thick reactive-magnetron sputtered layer of NbTiN [18], [19]. The NbTiN layer is etched with O_2-SF_6 (25 and 13.5 sccm, respectively) at 5 mTorr and 50 W for 460 s, with an additional 45-s overetch on the substrate to ensure a "sharp" definition of the structures. We use an O_2 (100 sccm, 100 mTorr, 50 W) etch of 90 s to remove any resist remnants. The next step is a layer of *a*-SiC:H deposited by PECVD using a Novellus Concept One. Details regarding the *a*-SiC:H deposition are discussed in Ref. [17]. The top PPC plate, readout line bridges, and the top line of the coupling structure are fabricated from a second layer of 15-nm NbTiN. To create good galvanic contact between the two NbTiN layers, the wafer is cleaned with HF before the second NbTiN layer is deposited. The use of a sapphire substrate prevents surface erosion due to the 45-s overetch needed for patterning the NbTiN and *a*-SiC:H layers.

In addition to the PPC resonators, we fabricate a set of planar reference devices in the bottom NbTiN layer. These reference devices are used to separate the noise contributions from the capacitor and inductor [20] which we come back to in the

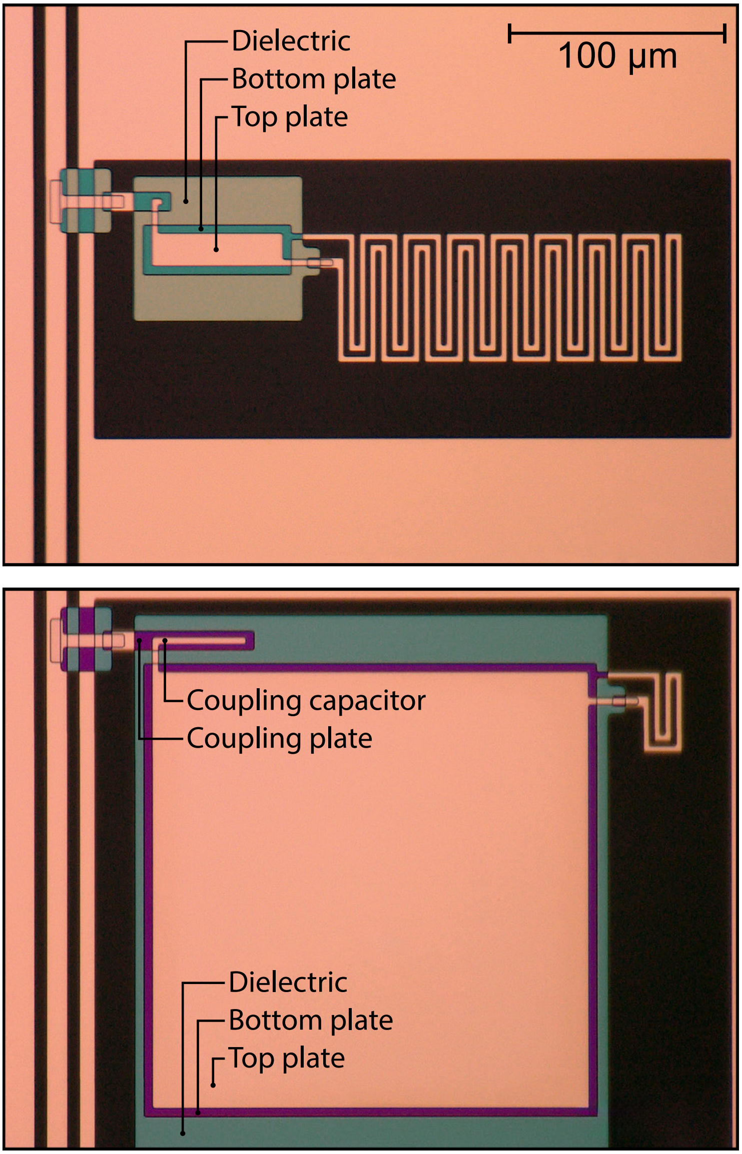

Figure 7.1: Optical micrograph of lumped element resonators with *a*-SiC:H parallel-plate capacitors. All metallic structures (pink) are NbTiN with a T_c of 14.3 K. Perceived colour of *a*-SiC:H is different if *a*-SiC:H is on top of the NbTiN layer (i.e. on top of the bottom plate) and varies due to thickness variations over the wafer. **Top**, smallest (60×16 μm^2) PPC resonator; **bottom**, Biggest (200×200 μm^2) PPC resonator.

Sec. 7.4.

The samples are cooled in a pulse-tube precooled dilution refrigerator. We use a box-in-box sample-stage design [21], [22] to shield the sample from stray light coming from the 3-K stage of the cooler. The sample stage is surrounded by two magnetic shields, a superconducting niobium shield, and a Cryophy shield. A graphical representation of the setup is presented in Ref. [8], but the sample holder is closed with a lid. Microwave measurements are performed with the standard homodyne detection scheme discussed in Appendix 7.6. Unless otherwise specified, all measurements are taken at a base temperature of 100 mK.

7.3. Measurements

7.3.1. Scattering parameter measurements

We measure the complex transmission parameter, S_{21}, with a vector network analyzer (VNA) to characterize the resonators. We perform a frequency sweep to obtain each resonator's resonance circle (S_{21}) at different readout powers and sample-stage temperatures.

Fitting the resonance dip in magnitude space ($|S_{21}|$) to an analytical model [23] provides the resonator's resonance frequency, f_r, and the internal (Q_i) and coupling (Q_c) quality factors as a function of readout power and temperature. At the highest readout powers the resonance dip ($|S_{21}|$) becomes nonlinear [24]. To estimate the Q factors at these powers we include the nonlinear frequency response [24] in the analytical model of Ref. [23]. The maximum readout power we use is set by the point at which the analytical model that combines the resonance dip asymmetry [23] and nonlinearity [24] no longer represents the observed resonance dip ($|S_{21}|$).

The resonator's intrinsic loss is given by Q_i, which is related to the loss tangent of the dielectric,

$$\tan\delta_d = \frac{1}{pQ_i}, \tag{7.1}$$

if the dielectric material dominates the resonator's microwave loss. Here, p is the participation ratio of the dielectric, given by $p = w_d^{\mathrm{e}}/w^{\mathrm{e}}$, where w_e is the total electric energy stored in the resonator and w_d^{e} is the energy stored in the dielectric. For a PPC where the dielectric thickness is small compared to the dimensions of the plates, the fringing fields are negligible, so we can assume that the entire electric field is in the dielectric and $p = 1$.

We measure Q_i over a wide power range, from the bifurcation point of the resonator down to the single-photon level. The measured data points of three resonators, one

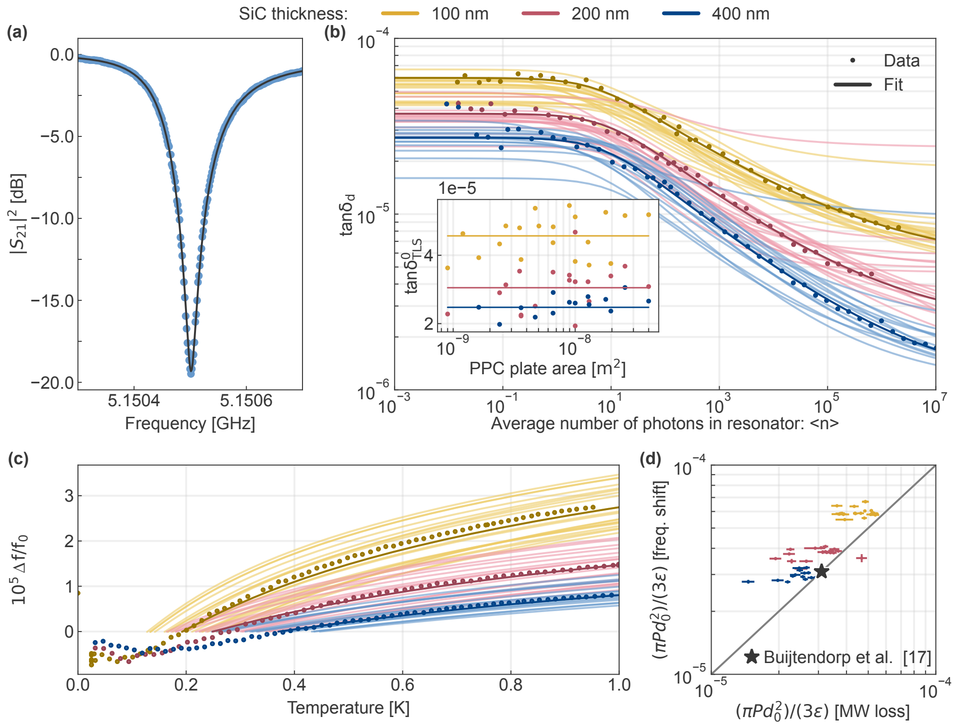

Figure 7.2: **(a)** Example resonance $|S_{21}|^2$ dip fitted in magnitude space with equations from Refs. [23] and [24] for asymmetric nonlinear dips. **(b)** Power-dependent microwave loss $\tan\delta_d$, plotted against the average number of photons in the resonator ($\langle n\rangle \propto |\vec{E}|^2$), with $\vec{E}$ as the electric field in the dielectric. Measured data points and the fit to Eq. 7.2 are highlighted for one KID of each thickness. For all other KIDs, only the fitted lines are presented. Error bars on each data point are small compared to the size of the data points. **Inset** shows that the TLS contribution to the microwave loss, $\tan\delta^0_{\mathrm{TLS}} = (\pi P d_0^2)/(3\epsilon)$, is independent of the parallel-plate area. Solid lines are the average $\tan\delta^0_{\mathrm{TLS}}$ of each thickness, presented as a guide to the eye (not a fit). **(c)** Temperature-induced relative frequency shift. Measured data points for three KIDs, together with the fit to Eq. 7.4, are highlighted for each dielectric thickness. For all other KIDs only the fitted lines are presented. Fitted range is $\hbar\omega/k_B$ - 1K which, for a KID resonating at 4 GHz starts at about 200 mK. At $\hbar\omega = k_B T$, $\delta f/f_0$ crosses zero. Error bars on each data point are small compared to the size of the data points. **d)** Fitted TLS contribution $(\pi P d_0^2)/(3\epsilon)$. ★ aata point from a 295 nm a-SiC:H microstrip resonator with identical a-SiC:H deposition conditions [17]; $(\pi P d_0^2)/(3\epsilon)$ obtained from the loss tangent fit. TLS contribution is thickness dependent, which cannot be explained by a uniform dielectric that assumes a constant TLS density (P) and dipole moment (d_0).

for each PPC thickness, are presented in Fig. 7.2(a). The STM predicts a power-dependent microwave loss:

$$\tan\delta_d = \frac{\pi P d_0^2}{3\epsilon}\tanh\frac{\hbar\omega_r}{2k_BT}\left(1+\frac{|\vec{E}|}{E_c}\right)^{-\beta} + \tan\delta_{\mathrm{HP}}, \tag{7.2}$$

which should be geometry independent. Here, P is the TLS density, d_0 is the TLS dipole moment, ϵ is the dielectric constant of the TLS hosting material, $|\vec{E}|$ is the electric field in the dielectric, ω_r is the resonance frequency, T is the temperature, and E_c is the critical field above which the TLSs start to saturate with $\beta = 0.5$ in the STM. The TLS contribution, $(\pi P d_0^2)/(3\epsilon)$, is often presented as the TLS contribution to the loss tangent at zero temperature: $\tan\delta^0_{\mathrm{TLS}}$. The loss no longer follows the STM at high powers and saturates to $\tan\delta_{\mathrm{HP}}$.

Figure 7.7(b) shows the measured loss tangent $(1/Q_i)$ versus the average number of microwave photons in the resonator,

$$\langle n\rangle = \frac{2Q^2}{Q_c}\frac{P_{\mathrm{read}}}{\hbar\omega_r^2}, \tag{7.3}$$

where $\langle n\rangle \propto |\vec{E}|^2$, ω_r is the resonance frequency, Q is the loaded quality factor, and Q_c is the coupling quality factor. The readout power at the sample, P_{read}, is calibrated by measuring the transmission through two identical input lines, including attenuation, with a short cable instead of the sample, see Appendix 7.6. To extract the TLS contribution to the microwave loss we, fit Eq. 7.2 to the measured internal quality factor, Q_i. Fig. 7.2(b) gives the fits for all resonators. The fitted TLS contribution, $\tan\delta^0_{\mathrm{TLS}}$,of each resonator is plotted against the PPC area in the inset of Fig. 7.2(b), which shows that $\tan\delta^0_{\mathrm{TLS}}$ is independent of the PPC area.

For the wafer with 200 nm of *a*-SiC:H, we observe that some resonators become nonlinear at lower readout powers (< -20dB) compared to the other devices on the same chip [24]. For these devices, there are not enough data points to accurately fit Eq. 7.2, and they are therefore omitted from the analysis. We measured a second chip of the same design and fabrication run to extend the dataset. The full dataset, with all measured devices, is available in the reproduction package [25].

Next, we analyze the KID resonance frequency as a function of temperature by varying the temperature of the sample stage with a PID-controlled heater, from 25.0 mK to 1.0 K. The STM predicts a temperature-dependent shift of the KID resonance frequency ($\Delta f_0/f_0 = -\frac{1}{2}\Delta\epsilon'/\epsilon$):

$$\frac{\Delta f_0}{f_0} = p\frac{P d_0^2}{3\epsilon}\left[\mathrm{Re}\left\{\Psi\left(\frac{1}{2}+\frac{\hbar\omega}{2\pi j k_BT}\right)\right\} - \log\frac{\hbar\omega}{2\pi k_BT}\right], \tag{7.4}$$

which should be geometry independent [26]. Here, $\Delta f_0 = f_r(T) - f_0$, where f_0 is the resonance frequency at $T = 0$; Ψ is the complex digamma function; and p is the participation ratio, as in Eq. 7.1. We fit Eq. 7.4 to the measured resonance frequencies, highlighted for one resonator of each dielectric thickness in Fig. 7.2(c). For all other resonators, only the fitted line is presented.

Equation 7.4 contains two regimes, for $k_B T < \hbar\omega$ the digamma term dominates, while, for $k_B T > \hbar\omega$ the logarithmic term dominates. In the first regime ($k_B T < \hbar\omega$) we have a low signal-to-noise ratio and expect TLS saturation effects [26], so we limit the fit to the range $k_B T > \hbar\omega$. Since the measured temperature range is far below the T_c of NbTiN (14.3 K), there is no quasiparticle contribution to the measured frequency shift [27], [28].

The only TLS parameters that impact the TLS-induced microwave loss and resonance frequency shift are the TLS density (P) and the TLS dipole moment (d_0). The fitted TLS contributions, $(\pi P d_0^2)/(3\epsilon)$, from both Eq. 7.2 and Eq. 7.4, for all devices, are plotted in Fig. 7.2(d). There is a clear close to 1:1 agreement between the obtained TLS contribution, $(\pi P d_0^2)/(3\epsilon)$,from both measurements.

The TLS data in Fig. 7.2 show a clear thickness dependence, where a thicker dielectric has both a lower TLS-induced microwave loss [Fig. 7.2(b)] and a smaller TLS-induced resonance frequency shift [Fig. 7.2(c], as summarized by Fig. 7.2(d). The inset of Fig. 7.2(b) highlights that the TLS-induced microwave loss does not depend on the area of the PPC and is thus only a function of the thickness of the dielectric. The thickness dependence cannot be explained by a uniform dielectric, which assumes a constant TLS density (P) and dipole moment (d_0) in Eq. 7.2 and Eq. 7.4. Instead, the medium between the PPC plates likely contains one or more surface layers with a higher TLS density or a stronger TLS dipole moment (or both) than the bulk dielectric. The TLS contribution we obtain in Fig. 7.2 is then the thickness-weighted average of the bulk dielectric material and surface layers. If the thickness of the dielectric changes, the bulk-to-surface-layer ratio changes, which yields a different effective TLS contribution, $(\pi P d_0^2)/(3\epsilon)$.

7.3.2. Noise measurements

We perform noise measurements at the resonator's resonance frequency with the homodyne detection scheme discussed in Appendix 7.6. The noise measurement consists of two timestreams: one of 40 s sampled at 50 ksample/s and one of 0.5 s sampled at 1 Msample/s. The fluctuations in the IQ coordinates are translated to phase (θ) and amplitude (A) with respect to the resonance circle's center [21]. We estimate the PSD from both timestreams and stitch them at 20 kHz. The resonance circle relates the measured phase noise to frequency noise as

$$S_f/f_r^2 = \frac{S_\theta}{(4Q_l)^2} \tag{7.5}$$

where S_θ is the PSD in the phase coordinate. The resonance frequency, f_r, and

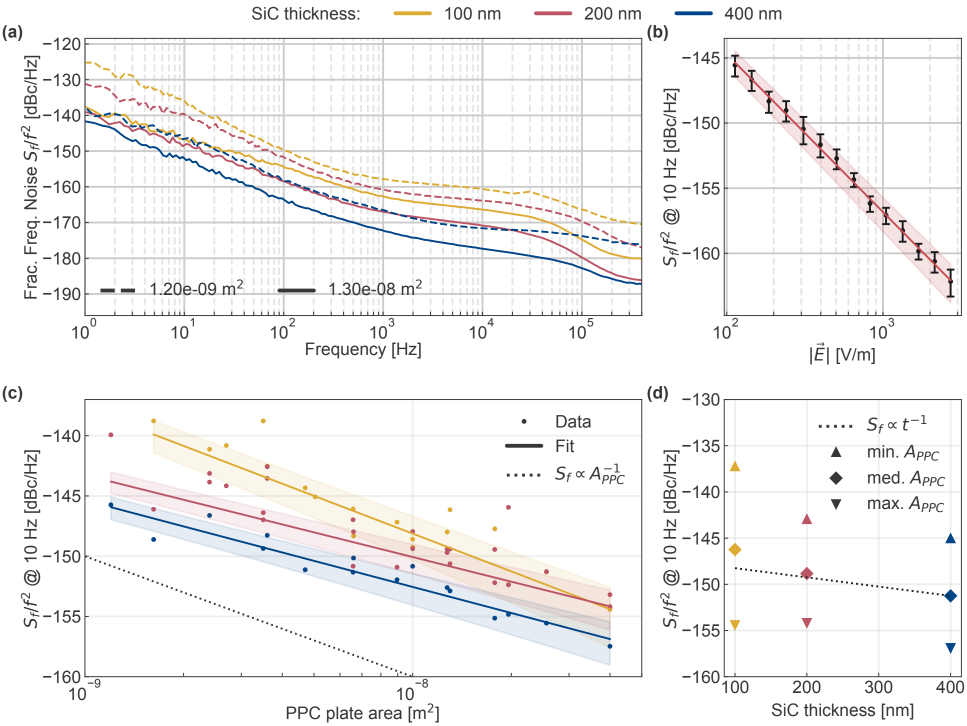

Figure 7.3: **a)** Frequency noise spectra for resonators with different plate sizes and dielectric thickness, at the same internal electric field of $|\vec{E}| = 1.13 \times 10^3$ V/m ($\epsilon_r = 10$). TLS noise level shows a clear area and thickness scaling. Spectra typically show a $1/f$ spectrum up to 0.1-1 kHz. Roll-off in the noise level at the resonator-ring time is visible at higher frequencies ($> 10^4$ Hz). **b)** Frequency noise level of one PPC resonator ($A = 200 \times 200$ µm^2, $t = 400$ nm, $f_r = 5.15$ GHz) as a function of $|\vec{E}|$, which follows the expected $|\vec{E}|^{-1}$ scaling from the tunneling models [15], [29]. **c)** TLS noise level at 10 Hz versus parallel-plate area (A_{PPC}) for all three a-SiC:H thicknesses at the same internal electric field. Solid lines are fits $cA_{\mathrm{PPC}}^{-\alpha}$. From thinnest to thickest dielectric layer, the slopes (α) are 1.04 ± 0.12, 0.73 ± 0.10, and 0.72 ± 0.09. Standard-deviation error on the fit parameters α and c gives the uncertainty range. Dotted line indicates the slope of the expected $S_f \propto A_{\mathrm{PPC}}^{-1}$ scaling. **d)** Observed thickness scaling of the TLS noise level. Points are then obtained from the fitted $S_f(A_{\mathrm{PPC}})/f^2$ relations in (c), at the smallest PPC area (▲), the median area of 6.6×10^{-9} m^2 (◆), and the largest PPC area (▼). Dashed line indicates a t^{-1} scaling with respect to the 400-nm median-area point.

loaded quality factor, $Q_l = (1/Q_c + 1/Q_i)^{-1}$, are obtained from the resonance circle, see sec. 7.3.1. We focus on the frequency noise from the phase coordinate, which has a higher TLS noise level compared to the amplitude coordinate at powers where $|\vec{E}| > E_{\mathrm{c}}$ [30].

The frequency noise spectrum for a microwave resonator, for which the total electric field volume, V, contains a TLS host volume, V_h, is given by [14], [15]

$$\frac{S_f(f)}{f^2} \sim \frac{\int_{V_h} S_\epsilon(f, \vec{E}, T)|\vec{E}|^4 dV}{4\left(\int_V \epsilon|\vec{E}|^2 dV\right)^2} \tag{7.6}$$

where S_ϵ describes the fluctuations in the real part of the dielectric constant (ϵ_{TLS}) due to random switching of TLSs. If we assume a uniform distribution of TLS in the dielectric volume of the PPC V_{PPC}, then $V_h = V = V_{\mathrm{PPC}}$ and the frequency noise level should scale as V_{PPC}^{-1}. The derivation for the interacting tunneling model [29] shows that S_ϵ has a $1/f$ spectrum and in strong electric fields ($|\vec{E}| \gg E_{\mathrm{c}}$) scales with $|\vec{E}|^{-1}$, matching the empirical relations of the STM [14], [15]. The interacting TLSs do, however, result in a temperature-dependent noise level that is not explained by the STM: at low temperatures ($k_B T \ll \hbar\omega$) and strong field ($|\vec{E}| \gg E_{\mathrm{c}}$) $S_f \propto T^{(1-\mu)/2}$, while, at high temperatures ($k_B T \gg \hbar\omega$) $S_f \propto T^{\mu-1}$, where $\mu \approx 0.3$.

The measured frequency spectra ($S_f(f)/f^2$) of six KIDs, with different PPC areas and dielectric thicknesses, are presented in Fig. 7.3(a) at a temperature of 100 mK.

The frequency noise spectra show apparent $1/f$ behavior at lower frequencies, transitioning to something more akin to $f^{-1/2}$, typically between 0.1 and1 kHz. Both behaviors have been observed before in different measurements and device architectures [14], [28], [31], [32], but typically not simultaneously. The transition frequency varies between resonators and geometries, see Appendix. 7.7. To compare the noise levels of different resonators, we fit the $1/f$ spectrum between 5 and 50 Hz, where the spectrum is always fully $1/f$, and use the fitted 10-Hz point as the TLS noise-level reference.

We measure the noise spectra over a range of readout powers with 2-dB steps. In general, the electric field in the TLS medium is proportional to the readout power on the through line as $|\vec{E}| \propto P_{\mathrm{read}}^{-1/2}$. For a PPC, the internal electric field is directly calculated from the readout power and geometry as

$$\left|\vec{E}\right| = 2\sqrt{\frac{\pi P_{\mathrm{int}}}{\omega_r \epsilon} \frac{1}{V_{\mathrm{PPC}}}}, \tag{7.7}$$

where ω_r is the resonance frequency, ϵ is the dielectric constant, and V_{PPC} is the volume of the dielectric in the PPC. The internal power, P_{int}, is given by $P_{\mathrm{int}} = Q^2/(\pi Q_c) P_{\mathrm{read}} = \langle n\rangle \hbar\omega^2/(2\pi)$. The frequency noise level at 10 Hz for one PPC resonator ($A = 200 \times 200$ µm^2, $t = 400$ nm, $f_r = 5.15$ GHz) for different electric fields is given in Fig. 7.3(b) to illustrate that we indeed observe the expected $\propto |\vec{E}|^{-1}$ relationship.

In addition, we have measured the temperature dependence of the frequency noise. The frequency noise spectra and noise levels at 10 Hz for temperatures between 25 and

800 mK, and at different internal powers, are discussed in Appendix 7.9 and plotted in Fig. 7.10. At all measured powers, where $|\vec{E}| \gg E_c$, the frequency noise level follows the temperature dependence predicted by the interacting tunneling model.

Neither the STM nor the interacting tunneling model [29] predict the $f^{-1/2}$ region of the noise spectra we typically observe for superconducting resonators [14], [28], [31]. The $f^{-1/2}$ region roughly follows the expected $|\vec{E}|$ and temperature scalings of the $1/f$ region [29], which suggests that the $f^{-1/2}$ region has a similar field and temperature dependence to the TLSs and is therefore interesting for follow up.

For a uniform dielectric where the TLSs are uniformly distributed over the dielectric volume, we expect a frequency noise level that scales as $S_f \propto V_{\mathrm{PPC}}^{-1}$. Separated in the two geometrical parameters of the PPC, PPC area and thickness, we expect that the frequency noise level scales the same with area, $S_f \propto A_{PPC}^{-1}$, and with thickness, $S_f \propto t^{-1}$.

To see the effect of the PPC dimensions on the TLS noise level, we need to compare the noise levels at equal electric fields in the resonator. For each resonator, we translate the measured read power points to the electric field in the dielectric (Eq. 7.7). We interpolate between these measured electric field points, using the known $S_f \propto |\vec{E}|^{-1}$ relationship, to find the noise level at a desired electric field, see Fig. 7.3(b). Details of the interpolation are discussed in Appendix 7.8. The TLS noise level, at 10 Hz, versus the PPC plate area at $|\vec{E}| = 1.13 \times 10^3$ V/m, assuming $\epsilon_r = 10$ for a-SiC:H, is given in Fig. 7.3(c).

As expected, the frequency noise level in Fig. 7.3(c) scales as a power law with the parallel-plate area. We fit the relation $S_f = \beta A_{\mathrm{PPC}}^{-\alpha}$, where A_{PPC} is the PPC area, and find that α is 1.04 ± 0.12 for 100 nm, 0.73 ± 0.10 for 200 nm, and 0.72 ± 0.09 for 400 nm. The STM predicts $S_f \propto A_{\mathrm{PPC}}^{-1}$, as in Eq. 7.6. The obtained area scalings qualitatively agree with the predicted scaling for a uniform dielectric. However, we expect all three dielectric thicknesses to have the same frequency noise scaling with area. Instead, we observe that the frequency noise scaling is stronger with area for the 100-nm thick film than for the 200- and 400-nm films.

The resonance frequency scaling, $S_f \propto f_0^{\mu}$, from the interacting tunneling model [29], with $\mu \approx 0.3$, would only introduce a scatter on the data points in Fig. 7.3(c), since the resonance frequency is, by design, not correlated with the PPC area.

In Fig. 7.3(d), we compare the fitted noise level for the different dielectric thicknesses. Since the slopes in Fig. 7.3(c) differ, we compare the noise level at different PPC surface areas: the smallest area (▲), the median area (◆), and the largest area (▼). If we compare data from the 200- and 400-nm films, which show a similar area scaling ($\sim A_{\mathrm{PPC}}^{-0.7}$), we see that the frequency noise level scales roughly with the expected t_{PPC}^{-1} scaling for a uniform dielectric.

In Sec. 7.3.1, we concluded that the dielectric contained surface layers based on the thickness-dependent microwave loss and resonance frequency shift. If these surface layers have a similar effect on the frequency noise, we expect a frequency noise scaling with thickness stronger than the scaling for a uniform dielectric ($S_f \propto t^{-1}$). The data in Fig. 7.3d do not show a thickness dependence that is unambiguously stronger than $S_f \propto t^{-1}$, which implies that the surface layers affect the noise differently than the microwave loss and frequency shift discussed in Sec. 7.3.1. The origin of this difference is unknown. Barends et al. [28] made a similar observation: the resonance frequency shift and frequency noise respond differently to thicker and thicker dielectric ($\mathrm{SiO_x}$) layers deposited on top of a CPW resonator.

7.4. Discussion and Conclusions

In addition to the PPC designs, each wafer contains single-layer reference devices: CPW and IDC resonators. The measured microwave loss and frequency noise for these devices are presented in Appendix. 7.7. The frequency noise against internal power is plotted in Fig. 7.4. Calculating the electric field inside the TLS medium for a CPW or IDC is nontrivial due to the degeneracy in $p \tan \delta_d$ (Eq. 7.1). This means we cannot quantitatively compare the TLS properties of the substrate to *a*-SiC:H, but we can show that the PPC resonator is dominated by a different TLS contribution than the CPW and IDC resonators.

The inductor's loss and frequency noise contribution can be analyzed by comparing the IDC and CPW resonators, which have an equal line and gap width, and thus, the same field distribution in the substrate TLS layer [20]. The difference between the CPW and IDC resonators is the inductor in the IDC resonator. Figure 7.4 shows that the CPW and IDC have similar frequency noise levels, which means the contribution of the inductor is negligible. The IDC and PPC resonators have the same inductor but a different lumped-element capacitor. Compared to the IDC designs, the PPC resonators show a 15–20-dB-higher TLS noise level in the $1/f$ region of the spectrum. This means the noise of the PPC resonators is dominated by the *a*-SiC:H capacitor.

In the measured microwave loss and resonance frequencies in Fig. 7.2, we observe a thickness dependency that can be explained by a volume between the PPC plates that is not one uniform dielectric bulk material but contains one or more surface layers. Since these surface layers have a different $\tan \delta_{\mathrm{TLS}}$ than the bulk, they could affect the frequency noise of the PPC as well, where the noise level scales more strongly with the thickness of the dielectric than with the PPC area. The measured frequency noise in Fig. 7.3 does not clearly indicate that we see this effect, see Sec. 7.3.2. This could mean that the surface layers affect the noise differently than the microwave loss and frequency shift.

The location or nature of the surface layer(s) is unknown. They can be surface oxides on the metal capacitor plates or growth effects of *a*-SiC:H. To find $\tan \delta_{\mathrm{TLS}}$ of the bulk dielectric, we would need to extend the dielectric thickness range far enough to reach two extremes: thin enough to be dominated by the surface layers and thick enough to be limited by the properties of the bulk dielectric. A way to mitigate these surface layers might be found by exploring various cleaning steps on the bottom NbTiN plate of the capacitor.

One of the applications of superconducting resonators is the KID. Since the noise level scales with P_{int}, KIDs are always operated at their maximum internal power, $P_{\mathrm{int}}^{\mathrm{max}}$, at the edge of bifurcation [24], [33]. The bifurcation point, and thus, $P_{\mathrm{int,max}}$, typically depends on the critical current in the narrow inductor lines and does not depend on the capacitor geometry. For a set $P_{\mathrm{int,max}}$, the internal electric field inside the capacitor will depend on the capacitor geometry, see Eq. 7.7. This gives us two PPC dimension scalings, one for the internal electric field and one for the dielectric volume (V_{PPC}) in the resonator, as discussed before:

$$S_f \propto \frac{1}{|\vec{E}|}\frac{1}{V_{\mathrm{PPC}}}, \tag{7.8}$$

where $|\vec{E}| \propto 1/\sqrt{\omega_r V_{\mathrm{PPC}}}$. The two dielectric volumes factors, V_{PPC}, partly cancel and a

$$S_f \propto \sqrt{\omega_r/V_{\mathrm{PPC}}} \tag{7.9}$$

scaling remains for a dielectric with uniform TLS density. However, if we look at the measured data in Fig. 7.3, we see that, for the 200- and 400-nm-thick films, we have a geometric scaling

$$S_f \propto A_{\mathrm{PPC}}^{-\alpha} t^{-\beta} < V_{\mathrm{PPC}}^{-1}, \tag{7.10}$$

since $\alpha \approx 0.72 - 0.73$ (see Fig. 7.3(c)) and $\beta \approx 1$ (see Fig. 7.3(d)). The resulting geometric volume scaling, which is weaker than V_{PPC}^{-1}, reduces the combined geometry and electric field scaling in Eq. 7.9.

The practical applicability of PPC resonators for KIDs depends on how their noise level compares to the standard planar structures. Figure 7.4 shows the measured S_f/f^2 of a 200-nm PPC KID and of the planar reference designs fabricated on the same chip. In addition, Fig. 7.4 contains data points from two different MKID designs operated at their maximal internal power. The first is a compact lumped-element KID (LEKID) design for an optical-to-near-IR energy-resolving pixel based on an IDC [8]. The second point is for ultra-sensitive antenna-coupled terahertz KIDs based on planar structures [3].

Compared to the IDC of the LEKIDs in Ref. [8], which have 2-μm fingers and gaps, the 200-nm PPC of Fig. 7.4 with 60×100-μm sides has a capacitance that is 42 times higher. This means we can replace the IDC of Ref. [8] with a 12×12 $\mu\mathrm{m}^2$ PPC to get the same KID resonance frequencies. Assuming the noise scaling from Eq. 7.9, this would add roughly 8 dB of frequency noise to the 200-nm PPC line

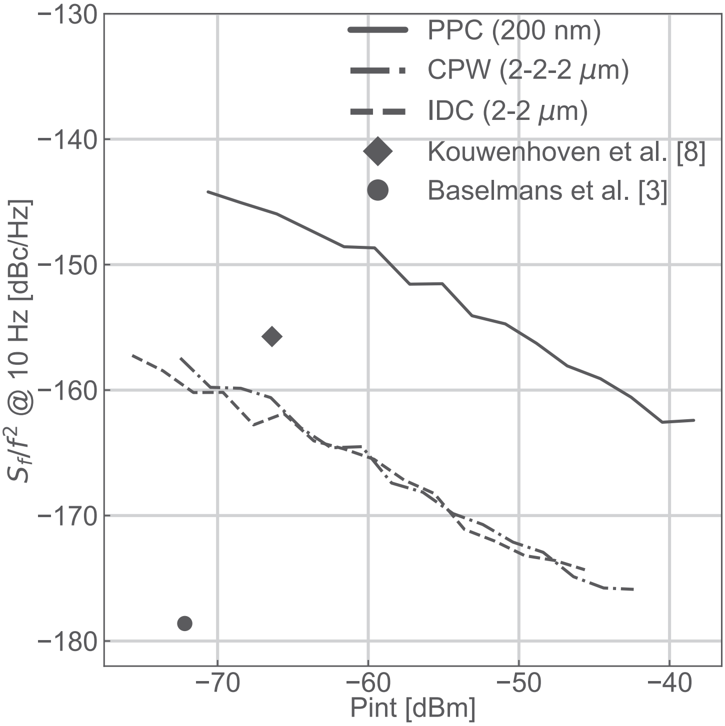

Figure 7.4: TLS noise level at 10 Hz versus internal power for different resonator types. PPC, IDC, and CPW resonators are fabricated on the same chip, where the PPC and IDC share the same inductor design. PPC has a plate area of 6000 µm^2 (60×100 µm^2). There is a strong increase in noise level between the planar devices deposited on the crystalline substrate (CPW, IDC) and the devices based on the *a*-SiC:H parallel-plate capacitor, but no difference between the planar devices themselves. Markers are the frequency noise of an optical-to-near-IR energy-resolving KID (pixel pitch 150 μm) [8] and an ultra-sensitive far-infrared KID (pixel pitch ∼1.5 mm) [3], both operated at their highest internal power.

in Fig. 7.4. Considering the inductor's dimensions, we can use the *a*-SiC:H PPC to reduce the area required for a KID by a factor of 10 at the cost of roughly 20 dB of extra frequency noise.

The second application is in ultra-sensitive KIDs for the far-infrared (FIR), where one of the limiting factors is the frequency noise at low frequencies ($0.1-10$ Hz) [3]. The FIR KIDs [3] have a TLS noise level far below both the PPC and the reference resonators, see Fig. 7.4. The noise level of these KIDs is so low because they are based on wide planar structures (central line of 40 μm with 8-μm gaps) that leverage the $W_{tot}^{-1.6}$ scaling of the frequency noise [14], [34]. Compared to the expected $V_{\mathrm{PPC}}^{-1/2}$ scaling for a PPC resonator with a uniform dielectric, the CPW has a much stronger geometrical scaling. This means that PPC-based resonators are at a disadvantage for FIR KID arrays, which are not limited by the pixel pitch (~ 1.5 mm). A promising route would be to investigate the dielectric material's properties and eliminate any possible TLS surface layers to reduce the frequency noise level of a PPC-based resonator.

Data availability

The full dataset of all measured resonators, and the reproduction package that generates the figures are available on Zenodo: `https://doi.org/10.5281/zenodo.10159731`. The colorblind and grayscale safe color scheme is from Paul Tol's Notes: `https://personal.sron.nl/~pault/`

Acknowledgments

We acknowledge Nick de Keijzer and Robert Huiting for their work on the 100 mK sample stage. This work is financially supported by the Netherlands Organisation for Scientific Research NWO (Projectruimte 680-91-127)

B. T. Buijtendorp is supported by the European Union (ERC Consolidator Grant No. 101043486 TIFUUN). Views and opinions expressed are however those of the authors only and do not necessarily reflect those of the European Union or the European Research Council Executive Agency. Neither the European Union nor the granting authority can be held responsible for them.

7.5. Area variation

The area of each of the 20 PPC resonators with respect to the smallest PPC is plotted against their designed resonance frequency for the 200-nm *a*-SiC:H wafer in Fig. 7.5.

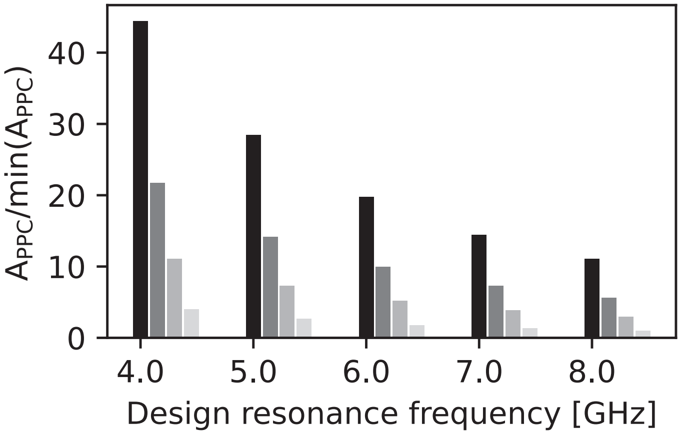

Figure 7.5: The area of each of the 20 PPC resonators with respect to the smallest PPC plotted against their designed resonance frequency for the 200 nm *a*-SiC:H wafer. Bars of the same color correspond to resonators with identical inductor lengths; black corresponds to the shortest inductors. There is no direct correlation between PPC area and resonance frequency.

7.6. Measurement setup

The homodyne readout setup is presented in detail in Section 3.2.1.

7.7. Reference devices (CPW and IDC)

In addition to the parallel-plate capacitor designs, each wafer contains reference designs based on the work in Ref. [20]. In addition to three PPC resonators, this chip contains three IDC resonators and three CPW resonators. A microscope image from one of the IDC resonators is presented in Fig. 7.6. The IDC has fingers and gaps of 2 μm, and the CPW has a center line and gap width of 2 μm (2-2-2) with same

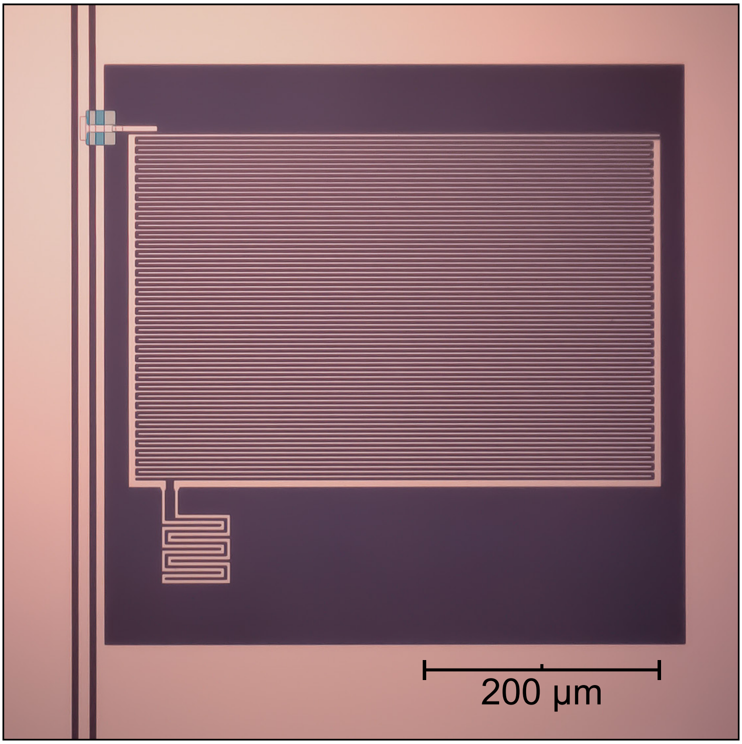

Figure 7.6: Microscope image of one of the IDC reference resonators. IDC has 2 μm defined fingers and gaps. Single-layer planar resonator fabricated in the bottom NbTiN layer which has a T_c of 14.3 K.

electric field distribution. Both resonators should then probe the TLS defects in the substrate the same way, see Eq. 7.1. The difference in loss and frequency noise between the CPW and IDC can then be attributed to the effects of the inductor of the IDC resonator if one takes the stray capacitance in the inductor into account [20].

The microwave losses $[(pQ_i)^{-1}]$ for one of each resonator type are plotted in Fig. 7.7. Since the layer thickness of the substrate TLS layer that gives the TLS-induced loss of the CPW an IDC [15], [35] is unknown, the participation ratio, p, is unknown and we cannot extract $\tan\delta_d$ from the CPW and IDC measurements. The CPW and IDC show similar noise levels, so the loss introduced by the inductor is negligible. The PPC on the other hand has roughly an order of magnitude higher $\tan\delta_{\mathrm{TLS}}$ than the CPW resonator, which shows that the PPC resonator is dominated by $\tan\delta_{\mathrm{TLS}}$ of the PPC and the contribution of the inductor is negligible.

The measured frequency noise spectra (S_f/f^2) for one of each resonator type are

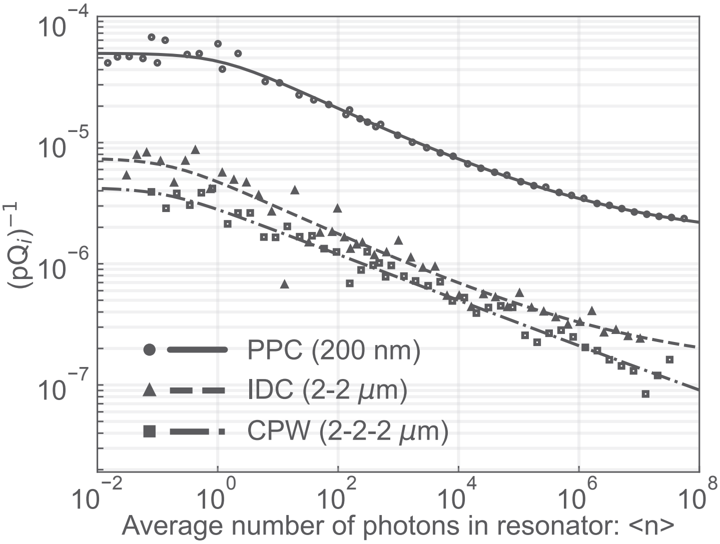

Figure 7.7: Measured loss tangent $\tan\delta_d = (pQ_i)^{-1}$, for a PPC-, IDC-, and CPW-based resonator. Scatter at high Q_i is higher due to the uncertainty in fitting deep S_{21} dips [$\min(S_{21}) = Q/Q_i$]. We fit Eq. 7.2 to the measured data points with powers below the bifurcation point of the resonator.

plotted in Fig. 7.8. The IDC and CPW resonators have near-identical noise spectra, while the PPC resonator has a 15–20-dB-higher noise level. As before, we conclude that the contribution of the inductor is negligible, and the frequency noise of the PPC is dominated by the *a*-SiC:H PPC. Note that the point at which the spectra change to $f^{-1/2}$ is at lower frequencies for the CPW and IDC resonators, around 10 Hz. For the PPC resonators this is transition lies between 10^2 and 10^3 Hz, see Fig. 7.8.

7.8. Frequency noise spectra analysis

Several analysis steps have to be taken to arrive at Fig. 7.3(b) from the measured frequency noise spectra in Fig. 7.3(a). First, the $1/f$ region of the spectrum is fitted to a linear af^{-b} relationship from 5 to 50 Hz. The frequency noise at 10 Hz is then calculated with the fitted parameters (a, b) and has an uncertainty given by the standard-deviation error on those parameters. The result is the frequency noise at 10 Hz at the measured read powers for each KID. The readout power is translated to the internal electric field inside the PPC through Eq. 7.7. This yields the points in Fig. 7.9, which follow the expected $|\vec{E}|^{-1}$ relationship [15], [29].

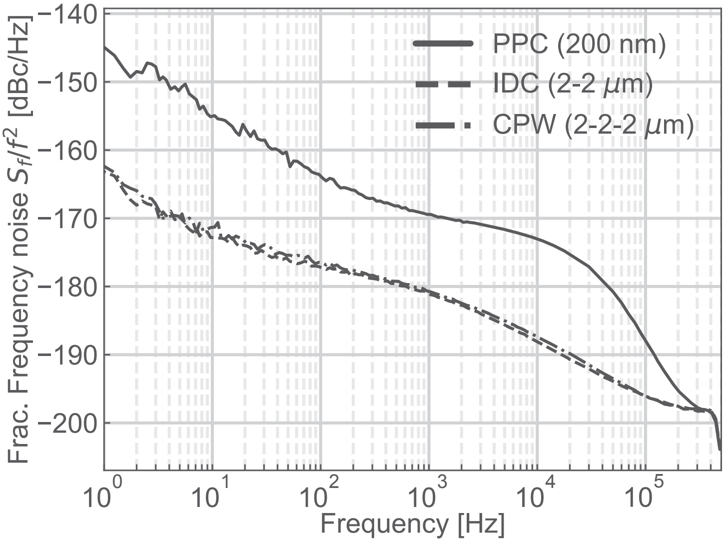

Figure 7.8: Resonator frequency noise, S_f/f^2, from the measured phase noise, S_θ, power spectral density of each resonator at the same internal power, $P_{\text{int}} = -50$ dBm. PPC has a plate area of 6000 μm^2 (60×100 μm^2)

To get the frequency noise at a desired electric field ($|\vec{E}_{des}|$), we fit the expected $a\cdot|\vec{E}|^{-b}$ relation to these data points, with $b \approx 1$. Using the fitted function parameters we obtain the frequency noise level at the desired field strength, with uncertainty given by the standard-deviation error in the fitted parameters (a,b). The total error of the point $S_f(f = 10\text{ Hz}, |\vec{E}| = |\vec{E}_{des}|)$ in Fig. 7.9 is the propagated error of the uncertainties in the $S_f(f)$ and $S_f(f = 10\text{ Hz}, |\vec{E}|)$ fits.

7.9. Temperature dependence

The interacting tunneling model [29] predicts the following temperature-dependent TLS noise level.

$$S_f \propto \begin{cases} T^{-(1+\mu)}, & T \ll \omega_r \text{ in weak field} \\ T^{(1-\mu)/2}, & T \ll \omega_r \text{ in strong field} \\ T^{\mu-1}, & T \gg \omega_r \end{cases} \tag{7.11}$$

We measure the frequency noise at temperatures between 25 mK and 1 K for

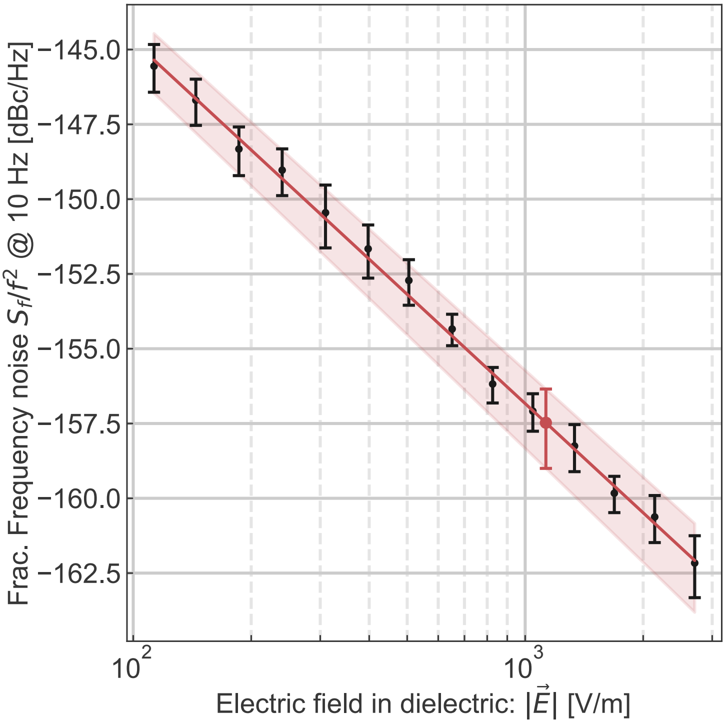

Figure 7.9: Fractional frequency noise at 10 Hz versus the internal electric field of the PPC. Each point is retrieved by fitting the $1/f$ region of the frequency noise spectra and calculating the 10-Hz point from the fitted parameter. Error bar of each point is the calculated uncertainty based on the standard-deviation error of the fit parameter. Red line is a fit with $a|\vec{E}|^{-b}$, with the uncertainty region based on the standard-deviation error of the fit. Red point is the retrieved frequency noise at 10 Hz and the desired electric field.

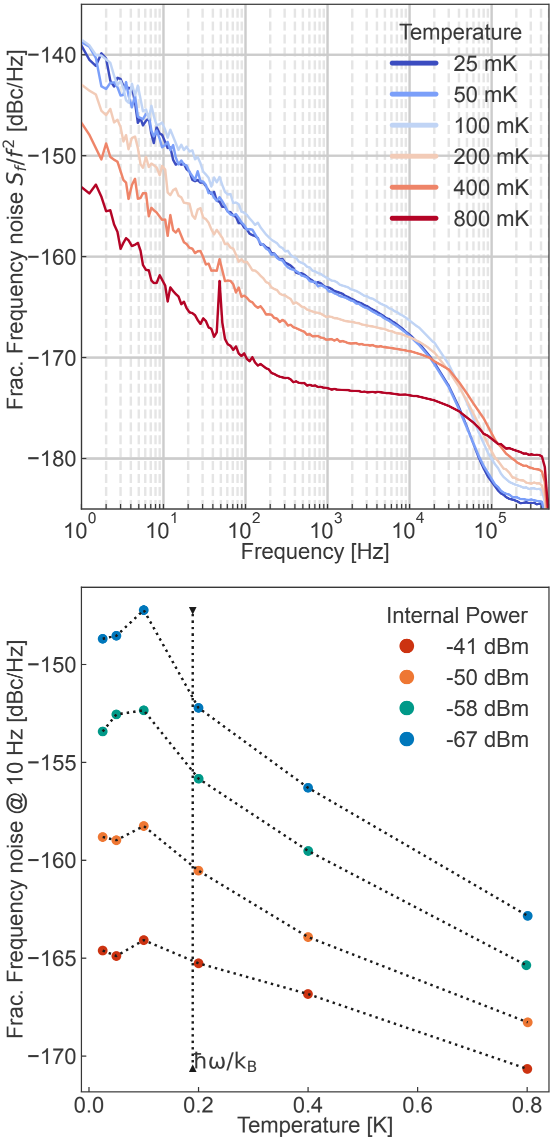

Figure 7.10: Fractional frequency noise of a PPC resonator for different bath temperatures and internal powers at 10 Hz. The internal powers fall within the strong field condition of Eq. 7.11. The vertical line is based on the resonance frequency at 100 mK: $T = \hbar\omega/k_B$. The dotted lines connect measured data points to highlight the backbend below $\hbar\omega = k_B T$.

all three resonator designs (PPC, IDC, CPW). The frequency noise spectra at one internal power and the frequency noise at 10 Hz versus internal power for a PPC resonator are plotted in Fig. 7.10. For all powers, the resonator is operated under the strong-field condition of Eq. 7.11, where one expects a smooth crossover between the limits of Eq. 7.11 around $\hbar\omega = k_B T$. In Fig. 7.10, the frequency noise indeed shows a backbend below $\hbar\omega = k_B T$. This temperature dependence is not explained by the STM [15] but can be explained by the interacting tunneling model presented in Ref. [29].

The spectrum at $f > 100$ Hz follows an $f^{-1/2}$ relationship at the lowest temperatures. The slope of this region changes with temperature, resulting in an almost-white spectrum between 1 kHz and the resonator roll-off at 800 mK. The $f > 100$-Hz region roughly follows the temperature dependence of Eq. 7.11. Neither the STM nor the interacting tunneling model explains the spectrum's $f^{-1/2}$ region nor its temperature dependence.

Bibliography

[1] P. K. Day, H. G. LeDuc, B. A. Mazin, A. Vayonakis, and J. Zmuidzinas, "A broadband superconducting detector suitable for use in large arrays," *Nature*, vol. 425, no. 6960, pp. 817–821, Oct. 2003. DOI: `10.1038/nature02037`.

[2] J. Zmuidzinas, "Superconducting microresonators: Physics and applications," *Annu. Rev. Conden. Ma. P.*, vol. 3, no. Volume 3, 2012, pp. 169–214, Mar. 2012, ISSN: 1947-5462. DOI: `10.1146/annurev-conmatphys-020911-125022`.

[3] J. J. A. Baselmans, F. Facchin, A. P. Laguna, *et al.*, "Ultra-sensitive THz microwave kinetic inductance detectors for future space telescopes," *Astron. Astrophys.*, vol. 665, A17, Sep. 2022. DOI: `10.1051/0004-6361/202243840`.

[4] M. Steffen, M. Sandberg, and S. Srinivasan, "Recent research trends for high coherence quantum circuits," *Supercond. Sci. Technol.*, vol. 30, no. 3, p. 030 301, Jan. 2017. DOI: `10.1088/1361-6668/aa55a2`.

[5] P. Krantz, M. Kjaergaard, F. Yan, T. P. Orlando, S. Gustavsson, and W. D. Oliver, "A quantum engineer's guide to superconducting qubits," *Appl. Phys. Rev.*, vol. 6, no. 2, p. 021 318, Jun. 2019. DOI: `10.1063/1.5089550`.

[6] M. Kjaergaard, M. E. Schwartz, J. Braumüller, *et al.*, "Superconducting Qubits: Current State of Play," *Annu. Rev. Conden. Ma. P.*, vol. 11, no. 1, pp. 369–395, Mar. 2020. DOI: `10.1146/annurev-conmatphys-031119-050605`.

[7] S. R. Meeker, B. A. Mazin, A. B. Walter, *et al.*, "DARKNESS: A Microwave Kinetic Inductance Detector Integral Field Spectrograph for High-contrast Astronomy," *PASP*, vol. 130, no. 988, p. 065 001, Apr. 2018. DOI: `10.1088/1538-3873/aab5e7`.

[8] K. Kouwenhoven, D. Fan, E. Biancalani, *et al.*, "Resolving Power of Visible-To-Near-Infrared Hybrid β-Ta/Nb-Ti-N Kinetic Inductance Detectors," *Phys. Rev. Applied*, vol. 19, no. 3, p. 034 007, Mar. 2023, ISSN: 2331-7019. DOI: `10.1103/physrevapplied.19.034007`.

[9] S. J. Weber, K. W. Murch, D. H. Slichter, R. Vijay, and I. Siddiqi, "Single crystal silicon capacitors with low microwave loss in the single photon regime," *Appl. Phys. Lett.*, vol. 98, no. 17, p. 172 510, Apr. 2011. DOI: `10.1063/1.3583449`.

[10] F. Boussaha, S. Beldi, A. Monfardini, *et al.*, "Development of TiN Vacuum-Gap Capacitor Lumped-Element Kinetic Inductance Detectors," *J. Low Temp. Phys.*, vol. 199, no. 3-4, pp. 994–1003, Dec. 2019. DOI: `10.1007/s10909-019-02309-0`.

[11] S. Beldi, F. Boussaha, J. Hu, *et al.*, "High Q-factor near infrared and visible Al2O3-based parallel-plate capacitor kinetic inductance detectors," *Opt. Express*, vol. 27, no. 9, p. 13 319, Apr. 2019. DOI: `10.1364/oe.27.013319`.

[12] J. Zotova, R. Wang, A. Semenov, *et al.*, "Compact superconducting microwave resonators based on Al-AlO$_x$-Al capacitors," *Phys. Rev. Applied*, vol. 19, no. 4, Apr. 2023. DOI: `10.1103/physrevapplied.19.044067`.

[13] W. A. Phillips, "Tunneling states in amorphous solids," *J. Low Temp. Phys.*, vol. 7, no. 3-4, pp. 351–360, May 1972. DOI: `10.1007/bf00660072`.

[14] J. Gao, M. Daal, J. M. Martinis, *et al.*, "A semiempirical model for two-level system noise in superconducting microresonators," *Appl. Phys. Lett.*, vol. 92, no. 21, p. 212 504, May 2008, ISSN: 0003-6951. DOI: `10.1063/1.2937855`.

[15] J. Gao, "The Physics of Superconducting Microwave Resonators," Ph.D. dissertation, California Institute of Technology, 2008. [Online]. Available: `http://web.physics.ucsb.edu/~bmazin/Papers/2008/Gao/Caltech%20Thesis%202008%20Gao.pdf`.

[16] A. D. O'Connell, M. Ansmann, R. C. Bialczak, *et al.*, "Microwave dielectric loss at single photon energies and millikelvin temperatures," *Appl. Phys. Lett.*, vol. 92, no. 11, p. 112 903, Mar. 2008. DOI: `10.1063/1.2898887`.

[17] B. T. Buijtendorp, S. Vollebregt, K. Karatsu, *et al.*, "Hydrogenated Amorphous Silicon Carbide: A Low-Loss Deposited Dielectric for Microwave to Submillimeter-Wave Superconducting Circuits," *Phys. Rev. Applied*, vol. 18, no. 6, Dec. 2022. DOI: `10.1103/physrevapplied.18.064003`.

[18] D. J. Thoen, B. G. C. Bos, E. A. F. Haalebos, T. M. Klapwijk, J. J. A. Baselmans, and A. Endo, "Superconducting NbTin Thin Films With Highly Uniform Properties Over a 100 mm Wafer," *IEEE Trans. Appl. Supercond.*, vol. 27, no. 4, pp. 1–5, Jun. 2017. DOI: `10.1109/TASC.2016.2631948`.

[19] B. G. C. Bos, D. J. Thoen, E. A. F. Haalebos, *et al.*, "Reactive Magnetron Sputter Deposition of Superconducting Niobium Titanium Nitride Thin Films With Different Target Sizes," *IEEE Trans. Appl. Supercond.*, vol. 27, no. 4, pp. 1–5, Jun. 2017. DOI: `10.1109/TASC.2016.2631939`.

[20] C. R. H. McRae, R. E. Lake, J. L. Long, *et al.*, "Dielectric loss extraction for superconducting microwave resonators," *Appl. Phys. Lett.*, vol. 116, no. 19, p. 194 003, May 2020. DOI: `10.1063/5.0004622`.

[21] P. J. De Visser, "Quasiparticle dynamics in aluminium superconducting microwave resonators," Ph.D. dissertation, Delft University of Technology, 2014. DOI: `10.4233/uuid:eae4c9fc-f90d-4c12-a878-8428ee4adb4c`. [Online]. Available: `http://resolver.tudelft.nl/uuid:eae4c9fc-f90d-4c12-a878-8428ee4adb4c`.

[22] J. Baselmans, S. Yates, P. Diener, and P. de Visser, "Ultra Low Background Cryogenic Test Facility for Far-Infrared Radiation Detectors," *J. Low Temp. Phys.*, vol. 167, no. 3-4, pp. 360–366, May 2012. DOI: `10.1007/s10909-012-0511-0`.

[23] M. S. Khalil, M. J. A. Stoutimore, F. C. Wellstood, and K. D. Osborn, "An analysis method for asymmetric resonator transmission applied to superconducting devices," *J. Appl. Phys.*, vol. 111, no. 5, p. 054 510, Mar. 2012, ISSN: 0021-8979. DOI: `10.1063/1.3692073`.

[24] L. J. Swenson, P. K. Day, B. H. Eom, *et al.*, "Operation of a titanium nitride superconducting microresonator detector in the nonlinear regime," *J. Appl. Phys.*, vol. 113, no. 10, p. 104 501, Mar. 2013, ISSN: 0021-8979. DOI: `10.1063/1.4794808`.

[25] K. Kouwenhoven, G. P. J. van Doorn, B. T. Buijtendorp, *et al.*, "Reproduction Package: Geometry dependence of TLS noise and loss in a-SiC:H parallel plate capacitors for superconducting microwave resonators," *Zenodo*, Nov. 2023. DOI: `10.5281/zenodo.10159731`.

[26] J. Gao, J. Zmuidzinas, A. Vayonakis, P. Day, B. Mazin, and H. Leduc, "Equivalence of the Effects on the Complex Conductivity of Superconductor due to Temperature Change and External Pair Breaking," *J. Low Temp. Phys.*, vol. 151, no. 1, pp. 557–563, 2008. DOI: `10.1007/s10909-007-9688-z`.

[27] D. C. Mattis and J. Bardeen, "Theory of the anomalous skin effect in normal and superconducting metals," *Phys. Rev.*, vol. 111, no. 2, pp. 412–417, 2 Jul. 1958. DOI: `10.1103/PhysRev.111.412`.

[28] R. Barends, H. L. Hortensius, T. Zijlstra, *et al.*, "Contribution of dielectrics to frequency and noise of NbTiN superconducting resonators," *Appl. Phys. Lett.*, vol. 92, no. 22, p. 223 502, Jun. 2008, ISSN: 0003-6951. DOI: `10.1063/1.2937837`.

[29] L. Faoro and L. B. Ioffe, "Interacting tunneling model for two-level systems in amorphous materials and its predictions for their dephasing and noise in superconducting microresonators," *Phys. Rev. B*, vol. 91, no. 1, p. 014 201, 1 Jan. 2015. DOI: `10.1103/PhysRevB.91.014201`.

[30] C. Neill, A. Megrant, R. Barends, *et al.*, "Fluctuations from edge defects in superconducting resonators," *Appl. Phys. Lett.*, vol. 103, no. 7, p. 072 601, Aug. 2013, ISSN: 0003-6951. DOI: `10.1063/1.4818710`.

[31] J. Gao, J. Zmuidzinas, B. A. Mazin, H. G. LeDuc, and P. K. Day, "Noise properties of superconducting coplanar waveguide microwave resonators," *Appl. Phys. Lett.*, vol. 90, no. 10, p. 102 507, Mar. 2007. DOI: `10.1063/1.2711770`.

[32] J. Burnett, L. Faoro, I. Wisby, *et al.*, "Evidence for interacting two-level systems from the 1/f noise of a superconducting resonator," *Nat. Commun.*, vol. 5, no. 1, Jun. 2014. DOI: `10.1038/ncomms5119`.

[33] P. J. de Visser, S. Withington, and D. J. Goldie, “Readout-power heating and hysteretic switching between thermal quasiparticle states in kinetic inductance detectors,” *J. Appl. Phys.*, vol. 108, no. 11, p. 114 504, Dec. 2010. DOI: `10.1063/1.3517152`.

[34] S. A. Hähnle, “Superconducting Integrated Circuits at Sub-millimeter Wavelengths,” Ph.D. dissertation, Delft University of Technology, 2021. DOI: `10.4233/UUID:91047108-E77E-4D3B-956E-1E97EE8F8C47`. [Online]. Available: `http://resolver.tudelft.nl/uuid:91047108-e77e-4d3b-956e-1e97ee8f8c47`.

[35] R. Barends, N. Vercruyssen, A. Endo, *et al.*, “Reduced frequency noise in superconducting resonators,” *Appl. Phys. Lett.*, vol. 97, no. 3, p. 033 507, Jul. 2010. DOI: `10.1063/1.3467052`.

Summary

Kinetic inductance detectors (KIDs) are superconducting resonators whose resonance condition strongly depends on the properties of a thin superconducting film. Below the critical temperature of the superconducting film, most of the electrons have paired up into Cooper pairs, which give rise to a kinetic inductance. The remaining excitations are a mix of electrons and holes, which can be described as quasiparticles and lead to microwave loss. The resonator's resonance frequency then depends on the Cooper pair density, while the resonator's internal loss depends on the quasiparticle density.

When the resonator is exposed to a photon flux of sufficient energy to break Cooper pairs, either by direct absorption or through an antenna, excess quasiparticles are created. Due to the change in Cooper pairs and quasiparticle densities, the resonator shifts to a lower resonance frequency while the internal losses increase. We can measure this change using a homodyne microwave readout scheme.

This thesis describes my work of the past four to five years on hybrid lumped element kinetic inductance detectors based on high resistivity disordered superconductors. The thesis can be divided into four parts: A theoretical and experimental background, the energy resolution of hybrid lumped element KIDs, improving the quantum efficiency of KIDs based on high resistivity superconductors with anti-reflection coatings and optical stacks, and reducing the pixel pitch of KIDs with parallel plate capacitors.

In the first part, we describe a superconducting film in terms of a surface impedance, which can be separated into two channels: a real resistance and an imaginary part, the reactance. Both circuit elements change upon a change in quasiparticle density. Implementing this impedance in an electrical circuit that describes the resonator itself and its connection to the "external" readout line, we can derive the response of a superconducting resonator to a change in quasiparticle density.

The response, a change in the detector's complex scattering parameter recorded at the detector's original resonance frequency, can be mapped onto different coordinate systems. Since the scattering parameter (S_{21}) is complex, the standard approach is to map the change in S_{21} as a change in amplitude and phase. For a small response, these two coordinates are linear; however, for a larger response, the phase and amplitude response saturate. Alternatively, the complex scattering parameter can be mapped to changes in resistance and reactance using a Möbius transform, which electrical engineers are familiar with as the Smith chart. Since the change in resistance and reactance is linear with the change in quasiparticle density, this results in a set of linear response coordinates.

When a single visible or near-infrared (VIS-NIR) photon is absorbed in the induc-

tor, thousands of quasiparticles with an average energy of 1.7Δ are created within just a few nanoseconds. Afterward, these excess quasiparticles recombine into Cooper pairs, and the resonator relaxes into equilibrium over tens to hundreds of microseconds. Since the detector's response is a function of quasiparticle density, and the number of created excess quasiparticles depends on the absorbed photon's energy, the height of the resulting pulse is a direct measure of the photon's energy.

We use an optimal filter to estimate the height of the pulse, which is measured in the presence of noise. There is variation in the obtained pulse heights, which sets the energy resolution of the detector. The fundamental limit in energy resolution is due to the nature of the photon-to-quasiparticle energy down-conversion process. This Fano limit is a function of the superconductor's gap, where a lower gap yields a higher resolving power. In addition, energy can leak out of the detector during the down-conversion process through "hot" phonons, where a high phonon loss leads to a lower energy resolution. The pulse measurement is influenced by various noise sources, of which we discuss two: the white noise level due to the microwave components in the readout scheme and a $1/f$ TLS noise due to rattling defects in amorphous dielectric layers.

Instead of fabricating the entire resonator out of a single superconductor, we use a hybrid design where we use a superconductor with a large gap ($T_c \sim 15$ K) for the insensitive capacitive part of the resonator and a disordered superconductor with a small gap ($T_c < 1$ K) and high resistivity for the sensitive inductor. The high resistivity leads to a high sheet kinetic inductance, which allows us to make a compact resonator with a low volume inductor for a high responsivity.

Chapter 4 focuses on a hybrid NbTiN/β-Ta lumped element KID. Here, we show how we determine the experimental energy resolution of the detector within the optimal filter framework by recording roughly a thousand pulses, which we align in arrival time and average to create a model pulse. Filtering each recorded photon pulse with this model pulse yields the best estimate of each pulse's height and, thus, photon energy.

We show that we can resolve two lines, closely spaced in wavelength, with this method and that the estimated photon energy distribution corresponds with the experimentally determined energy resolution. The energy resolution of the detectors presented in Chapter 4 is not limited by the detector's signal-to-noise ratio (SNR), which would have a linear dependency on photon energy, nor by phonon loss, which would have a square root dependency with energy. Instead, the resolving power saturates for wavelengths shorter than 986 nm.

Another benefit of the disordered superconductors is that it is easier to match the high resistivity superconductor to free space for a high quantum efficiency. These superconductors absorb around 50% of the incoming photons for visible wavelengths. The superconductor must be embedded in an optical stack with an anti-reflection coating and a back short to reach high absorption efficiencies (90-100%). In Chapter

5, we model the absorption efficiency of an optical stack design for a 60 nm TiN film. The model is based on sections of transmission lines, where each section represents the optical properties of one layer in the optical stack. The modeled stack has an absorption efficiency $> 80\%$ from 400 nm to 1550 nm and near-unity absorption from 500 nm to 800 nm. We verify the model with transmission and reflection measurements.

In Chapter 6, we discuss the setup we made to measure the detector efficiency of a KID, which includes, in addition to the absorption efficiency, the filling ratio of the inductor and the efficiency of the lens. We use the setup to measure the detection efficiency of NbTiN/β-Ta lens-coupled KIDs coated with a 54-nm thick SiN AR layer that improves the absorption efficiency between 400 and 800 nm. At 500 nm, these KIDs demonstrate an enhanced detector efficiency of 61%, nearly double the efficiency we expect without the AR layer.

Our current generation of lumped element KIDs rely on interdigitated capacitors as the capacitive element of the resonator. Compared to the 3D alternative, the parallel plate capacitor (PPC), these planar structures offer relatively little capacitance per unit area. This leads to pixels where the insensitive capacitor takes up most of the pixel. Switching to parallel capacitors, however, could increase $1/f$ noise due to the two-level state (TLS) defects in dielectric between the two plates. In Chapter 7, we experimentally test how the TLS-dependent resonator properties, the microwave loss, and the frequency noise depend on the PPC's geometry.

However, we observe that the resonator's microwave loss decreases for thicker dielectric. We do not see a dependency of the microwave loss on the area of the capacitor. This suggests that the dielectric between the plates is not uniform in thickness but contains, for example, surface layers on the metal plates, which have a higher TLS loss contribution than the bulk of the dielectric. A thicker dielectric increases the ratio of bulk to surface layers, reducing the TLS-induced microwave loss.

We measure the expected volume (V) scaling where the TLS-induced frequency noise decreases as capacitor volume increases. Surprisingly, we do not see any indication of the surface layers when it comes to the frequency noise, which agrees with earlier observations by different authors that the TLS-induced loss and frequency noise could be decoupled. In practice, when designing a detector based on a PPC, the volume scaling of the frequency noise is counteracted by the internal field scaling for a given read power. As a result, the expected frequency noise level scales as $1/\sqrt{V}$.

Samenvatting

Kinetische inductantiedetectoren (KIDs) zijn supergeleidende resonatoren waarvan de resonantie sterk afhangt van de eigenschappen van een dunne supergeleidende film. Onder de kritische temperatuur van de supergeleidende film zijn de meeste elektronen gepaard in Cooperparen, die aanleiding geven tot een kinetische inductantie. De resterende excitaties bestaan uit een mengsel van elektronen en gaten, die beschreven kunnen worden als quasideeltjes en leiden tot microgolfverliezen. De resonantiefrequentie van de resonator hangt daarom af van de dichtheid van Cooperparen, terwijl het interne verlies van de resonator afhangt van de dichtheid van quasideeltjes.

Wanneer de resonator wordt blootgesteld aan een fotonflux met voldoende energie om Cooperparen te breken, hetzij door directe absorptie of via een antenne, worden extra quasideeltjes gecreëerd. Door de verandering in de dichtheid van Cooperparen en quasideeltjes verschuift de resonator naar een lagere resonantiefrequentie, terwijl de interne verliezen toenemen. Deze verandering kan worden gemeten met behulp van een homodyne microgolf-uitleessysteem.

Dit proefschrift beschrijft mijn werk van de afgelopen vier à vijf jaar aan hybride lumped-element kinetische inductantiedetectoren gebaseerd op ongeordende supergeleiders met een hoge weerstand. Dit proefschrift kan worden onderverdeeld in vier delen: een theoretische en experimentele achtergrond, de energie-resolutie van hybride lumped-element KIDs, het verbeteren van de kwantumefficiëntie van KIDs op basis van supergeleiders met een hoge weerstand met behulp van antireflectiecoatings, en het verkleinen van de pixelafstand van KIDs met parallelle plaatcondensatoren.

In het eerste deel beschrijven we een supergeleidende film in termen van een oppervlakte-impedantie, die kan worden opgesplitst in twee kanalen: een reële weerstand en een imaginaire reactantie. Beide circuitcomponenten veranderen bij een verandering in de dichtheid van quasideeltjes. Door deze impedantie te implementeren in een elektrisch circuit dat de resonator en de koppeling naar de “externe” uitleeslijn beschrijft, kunnen we de respons van een supergeleidende resonator op een verandering in de dichtheid van quasideeltjes afleiden.

De respons, een verandering in de complexe reflectie en transmissie van de detector ten opzicht van de de oorspronkelijke resonantiefrequentie van de detector, kan worden weergegeven in verschillende coördinatensystemen. Aangezien de transmissie (S_{21}) complex is, is het logisch de verandering in S_{21} weer te geven als een verandering in amplitude en fase. Voor een kleine respons zijn deze twee coördinaten lineair; bij een grotere respons verzadigen de fase- en amplituderespons. Als alternatief kan de complexe transmissie worden omgezet in veranderingen in termen van weerstand en reactantie met behulp van een Möbiustransformatie, bekend bij elektrotechnici als het Smith-diagram. Omdat de verandering in weerstand en reactantie lineair is met de verandering in de dichtheid van quasideeltjes, resulteert dit in een set lineaire responscoördinaten.

Wanneer één enkel zichtbaar of nabij-infrarood foton wordt geabsorbeerd in de inductor, worden duizenden quasideeltjes met een gemiddelde energie van $1,7\Delta$ gecreëerd binnen enkele nanoseconden. Vervolgens recombineren deze overtollige quasideeltjes tot Cooperparen en keert de resonator binnen tientallen tot honderden microseconden terug naar het oorspronkelijke evenwicht. Aangezien de respons van de detector een functie is van de dichtheid van quasideeltjes, en het aantal gecreëerde overtollige quasideeltjes afhankelijk is van de energie van het geabsorbeerde foton, is de hoogte van de resulterende puls een directe maat voor de energie van het foton.

We gebruiken een optimaal filter om de hoogte van de puls te schatten, die gemeten is in de aanwezigheid van ruis. Er is variatie in de verkregen pulshoogten, wat de energie-resolutie van de detector limiteert. De fundamentele limiet in energie-resolutie hangt af van het conversieproces van de hoge energie van één enkel foton naar meerdere 'lage energie quasideeltjes'. Deze Fano-limiet is een functie van de kloof (Δ) van de supergeleider, waarbij een 'kleinere' kloof een hogere energie-resolutie oplevert. Bovendien kan energie weglekken uit de detector tijdens het conversieproces via 'hete' fononen, waarbij een hoog fononenverlies leidt tot een lagere energie-resolutie.

De pulsmeting wordt beïnvloed door verschillende ruisbronnen, waarvan we er twee bespreken: het witte ruisniveau veroorzaakt door de microgolfcomponenten in het uitleessysteem en een $1/f$ TLS-ruis (Two-Level System) als gevolg van trillende defecten in amorfe diëlektrische lagen.

In plaats van de gehele resonator uit een enkele supergeleider te vervaardigen, gebruiken we een hybride ontwerp. Hierbij wordt een supergeleider met een grote kloof ($T_c \sim 15$ K) gebruikt voor het ongevoelige capacitatieve deel van de resonator en een ongeordende supergeleider met een kleine kloof ($T_c < 1$ K) en een hoge weerstand voor de gevoelige inductor. De hoge weerstand leidt tot een hoge bladkinetische inductantie, waardoor we een compacte resonator met een laag-volume-inductor kunnen maken die een hoge gevoeligheid heeft.

Hoofdstuk 4 richt zich op een hybride NbTiN/β-Ta lumped-element KID. Hier laten we zien hoe we de experimentele energie-resolutie van de detector bepalen binnen het kader van een optimaal filter door ongeveer duizend pulsen te meten. Deze pulsen worden op aankomsttijd uitgelijnd en gemiddeld om een modelpuls te creëren. Door elke gemeten fotonpuls te filteren met deze modelpuls verkrijgen we de beste schatting van de hoogte van elke puls en dus van de foton-energie.

We tonen aan dat we met deze methode twee lijnen met een klein verschil in golflengte van elkaar kunnen onderscheiden, en dat de geschatte energiespreiding overeenkomt met de experimenteel bepaalde energie-resolutie. De energie-resolutie van de in hoofdstuk 4 gepresenteerde detectoren wordt niet beperkt door de signaal-ruisverhouding (SNR) van de detector, die een lineaire afhankelijkheid van de foton-energie zou hebben, noch door fononen-verlies, dat een wortelafhankelijkheid met de energie zou vertonen. In plaats daarvan verzadigt het oplossend vermogen voor golflengtes korter dan 986 nm.

Een ander voordeel van de ongeordende supergeleiders is dat het eenvoudiger is om de supergeleider met hoge weerstand af te stemmen op de impedantie van vacuüm voor een hoge kwantumefficiëntie. Deze supergeleiders absorberen van nature ongeveer 50% van de inkomende fotonen in het zichtbare spectrum. Om hoge absorptie-efficiënties (90-100%) te bereiken, moet de supergeleider echter worden ingebed tussen een antireflectielaag en een reflector. In hoofdstuk 5 modelleren we de absorptie-efficiëntie voor een 60 nm dikke TiN-film Het model is gebaseerd op transmissielijnsecties, waarbij elke sectie de optische eigenschappen van één laag vertegenwoordigt. De gemodelleerde stapel van lagen heeft een absorptie-efficiëntie groter dan 80% van 400 nm tot 1550 nm en bijna volledige absorptie tussen 500 nm en 800 nm. We verifiëren het model met transmissie- en reflectiemetingen.

In hoofdstuk 6 bespreken we de opstelling die we hebben gebouwd om de detectie-efficiëntie van een KID te meten. Deze efficiëntie omvat, naast de absorptie-efficiëntie, ook de vulverhouding van de inductor en de efficiëntie van de lens. We gebruiken de opstelling om de detectie-efficiëntie te meten van lensgekoppelde NbTiN/β-Ta KIDs die voorzien zijn van een 54 nm dikke SiN-antireflectielaag. Deze laag verbetert de absorptie-efficiëntie tussen 400 en 800 nm. Bij 500 nm laten deze KIDs een verbeterde detectie-efficiëntie zien van 61%. Dit is bijna het dubbele van wat we zonder de antireflectielaag verwachten.

Onze huidige generatie lumped-element KIDs maakt gebruik van interdigitale condensatoren als capacitatieve element van de resonator. Vergeleken met het 3D-alternatief, de parallelle plaatcondensator (PPC), bieden deze vlakke structuren relatief weinig capaciteit per oppervlakte-eenheid. Hierdoor nemen de ongevoelige condensatoren het grootste deel van de pixel in beslag. Overstappen naar parallelle condensatoren zou echter $1/f$-ruis kunnen verhogen als gevolg van tweetoestandsdefecten (TLS) in het diëlektricum tussen de platen. In hoofdstuk 7 testen we experimenteel hoe de TLS-afhankelijke resonatoreigenschappen, het microgolfverlies en de frequentieruis afhangen van de geometrie van de PPC.

We observeren dat het microgolfverlies van de resonator afneemt bij een dikkere diëlektricumlaag. We zien geen afhankelijkheid van het microgolfverlies van de oppervlakte van de condensator. Dit suggereert dat het diëlektricum tussen de platen niet uniform in dikte is, maar bijvoorbeeld oppervlaktelagen op de metalen platen bevat die een hogere TLS-verliesbijdrage hebben dan de bulk van het diëlektricum. Een dikkere diëlektricumlaag verhoogt de verhouding tussen bulk- en oppervlaktelagen, wat het TLS-geïnduceerde microgolfverlies vermindert.

We meten de verwachte volumeschaalwet, waarbij de TLS-geïnduceerde frequentieruis afneemt naarmate het diëlektrisch volume (V) toeneemt. Verrassend genoeg zien we geen aanwijzingen voor de oppervlaktelagen met betrekking tot de frequentieruis. Dit komt overeen met eerdere observaties van andere auteurs waaruit bleek dat TLS-geïnduceerd verlies en frequentieruis losgekoppeld zouden kunnen zijn.

In de praktijk wordt bij het ontwerpen van een detector op basis van een PPC de volumeschaling van de frequentieruis tegengewerkt door de interne veldschaling voor een gegeven uitleesvermogen. Als gevolg hiervan schaalt het verwachte frequentieruisniveau als $1/\sqrt{V}$.

Curriculum Vitæ

Kevin KOUWENHOVEN

13–10–1993	Born in Leiderdorp, Netherlands.

Education

2012 – 2017	B.Sc. Electrical Engineering Delft University of Technology, Delft, Netherlands
2017 – 2019	M.Sc. Electrical Engineering Delft University of Technology, Delft, Netherlands *Thesis:* Dielectric Loss Tangent Measurements at Sub-K Temperatures and Terahertz Frequencies *Supervisors:* Prof. dr. ir. J. J. A. Baselmans
2019 – 2014	Ph.D. research SRON (Netherlands Institute for Space Research) and Delft University of Technology *Thesis:* Visible to Near-Infrared Kinetic Inductance Detectors *Promotors:* Prof. dr. ir. J. J. A. Baselmans and dr. ir. P. J. de Visser

List of Publications

1. *Recombination of Localized Quasiparticles in Disordered Superconductors*
   S. A. H. de Rooij, R. Fermin, **K. Kouwenhoven** T. Coppens, V. Murugesan,
   D. J. Thoen, J. Aarts, J. A. A. Baselmans and P. J. de Visser
   submitted for publication

2. *Vibrational modes as the origin of dielectric loss at 0.27-100 THz in* α-SiC:H
   B. T. Buijtendorp, A. Endo, W. Jellema, K. Karatsu, **K. Kouwenhoven** D. Lamers,
   A. J. van der Linden, K. Rostem, M. Veen, E. J. Wollack, J. A. A. Baselmans and
   S. Vollebregt
   submitted for publication

3. *Geometry dependence of two-level-system noise and loss in* α-SiC:H *parallel-plate capacitors for superconducting microwave resonators*
   K. Kouwenhoven, G. P. J. van Doorn, B. T. Buijtendorp, S. A. H. de Rooij,
   D. Lamers, D. J. Thoen, V. Murugesan, J. J. A. Baselmans and P. J. de Visser
   Physical Review Applied **21**, 044036 (2024)

4. *Resolving Power of Visible-To-Near-Infrared Hybrid* β-Ta/NbTiN *Kinetic Inductance Detectors*
   K. Kouwenhoven, D. Fan, E. Biancalani, S. A. H. de Rooij, T. Karim, C. S. Smith,
   V. Murugesan, D. J. Thoen, J. J. A. Baselmans and P. J. de Visser
   Physical Review Applied **19**, 034007 (2023)

5. *Hydrogenated Amorphous Silicon Carbide: A Low-Loss Deposited Dielectric for Microwave to Submillimeter-Wave Superconducting Circuits*
   B. T. Buijtendorp, S. Vollebregt, K. Karatsu, D. J. Thoen, V. Murugesan,
   K. Kouwenhoven, S. Hähnle, J. J. A. Baselmans and A. Endo
   Physical Review Applied **18**, 064003 (2022)

6. *Model and Measurements of an Optical Stack for Broadband Visible to Near-Infrared Absorption in* TiN *MKIDs*
   K. Kouwenhoven, I. Elwakil, J. van Wingerden, V. Murugesan, D. J. Thoen,
   J. J. A. Baselmans, P. J. de Visser
   Journal of Low Temperature Physics **209**, 1249–1257 (2022)

7. *Superconducting Microstrip Losses at Microwave and Submillimeter Wavelengths*
   S. Hähnle, **K. Kouwenhoven**, B. Buijtendorp, A. Endo, K. Karatsu, D. J. Thoen,
   V. Murugesan and J. J. A. Baselmans
   Physical Review Applied **16**, 014019 (2021)

Students Supervised

1. Gwen van Doorn, Internship, Applied Physics, The Hague University of Applied Sciences, *"TLS Noise of a Parallel Plate Capacitor in Microwave Kinetic Inductance Detectors"*, won the NNV-hbo Young Talent Award
2. Wilbert Ras, Ms.C. Thesis, Applied Physics, Delft University of Technology, *"Microwave Kinetic Inductance Detectors for the Mid-Infrared"*
3. Laurens Feije, Ms.C. Internship, Applied Physics, Delft University of Technology, *"Improving the Quantum Efficiency and Pixel Density of a LEKID for Visibile/Near-Infrared Photons"*

Propositions Accompanying the Doctoral Thesis

1. To characterize a specific resolving power contribution, you need an "ideal" detector only limited by that contribution. (Chapter 4)
2. Although the end goal is broadband absorption, it is beneficial to have a detector with clear features in the absorption efficiency to verify your quantum efficiency setup. (Chapters 5 and 6)
3. Rules of thumb like "a bigger parallel plate capacitor reduces the noise" are useful for communicating notions but overshadow the intricacies of a real design. (Chapter 7)
4. The characteristics of a KID, like response, noise, and power handling, are not independent. There is no "isolated" dial to turn that improves the KID's performance without negatively impacting another KID property. (This thesis)
5. A species that cannot live in harmony with its environment cannot call itself intelligent.
6. For the health of our planet, it's more beneficial to have ten birds in the sky than one in hand. *Inversion of the Dutch proverb "Beter één vogel in de hand dan tien in de lucht." English version: "A bird in the hand is worth two in the bush."*
7. True happiness is not based on circumstance; it requires intention, dedication, and effort.
8. Workplace diversity cannot be imposed, but it can be nurtured through inclusive practices and supportive environments.
9. Supervision should focus on personal development and mutual growth.
10. Writing propositions to accompany the thesis is useless if it is the only time when PhD students are forced or encouraged to think about societal issues.
11. Baking is a discipline-related skill if you share your creations with your coworkers.

These propositions are regarded as opposable and defendable, and have been approved as such by the promotor prof. dr. ir. J. J. A. Baselmans and co-promotor dr. ir. P. J. de Visser.

Acknowledgements

I, and by extension this thesis, would not be the same without the supervision, support, and mentorship I received from Pieter and Jochem these past years.

Pieter, I am extremely happy that you took the risk of accepting an electrical engineering student as your first PhD candidate. I have learned so much from you over these past years, both professionally and in baking bread and cakes. It was, and still is, such a pleasure to be part of the optical KIDs group you created within SRON—a place where people from different (educational) backgrounds feel welcome, safe, and seen. This inclusivity always seems to come up in the feedback we receive from our students.

Jochem, you have an almost sage-like quality when it comes to guiding people through the ups and downs of a PhD journey. Thank you for all the advice you've given over the years on how to handle the rougher aspects of such a journey. I've always appreciated how you cut straight to the core of any issue or struggle I faced, whether it was personal, related to writing a paper, or conducting experiments. Your ability to quickly grasp the essence of everyone's research, summarize it, and identify the key lessons learned—or the biggest gaps in a paper or presentation—is something I greatly admire.

Henk and Bilim, thank you for all your work behind the scenes to keep things running smoothly. I'm sure I don't even know about half the time and effort you put into keeping this experimental astronomy group on track.

Thanks to Sebastian, Shahab, and Alejandro for being such great role models. My desire to do a PhD came, in part, from the example you set. Sebastian, I was extremely lucky to have you as my MSc thesis supervisor. Thank you for explaining even the smallest details of the setup, KID physics, or your KID design code. Your continued friendship means a lot to me, and I'll always be grateful to you for starting the DnD group that carried us through the pandemic. Shahab, I don't think I know anyone who cares as deeply about their students or who can spend as much time in a museum as you. Thank you for all the small history lessons, jokes, and game and series recommendations over the years. Alejandro, I admire your curiosity and the interest you take in understanding your coworkers' work. I hope you're doing well in Spain, and I'm glad I got to see you again in Japan—I'm sure it won't be our last meeting at a conference.

I was lucky to be part of an amazing group of experimental astronomy PhDs. Bruno, Steven, Wilbert, Louis, Arend, Leon, and Michiel—thank you for the fantastic conference trips these past years. From cups of maple syrup in Montreal to markets and BBQ in South Korea, and finally, ramen and temples in Japan, you were amazing

travel companions. Steven, thank you for being willing to answer all my quasiparticle questions. Wilbert, supervising you was, in the words of my MSc supervisor, “almost too easy at times.” Michiel, thank you for braving rainstorm after rainstorm in Japan with me to visit temple after temple and for being the lab DJ.

Gwen, thank you for letting me supervise your internship. I had such a great time during your project, and it was a pleasure to see how you naturally fit within both the experimental astronomy and terahertz sensing groups. The award you won for your internship was well deserved, and I can’t wait to hear what you’ll do next! P.S. I hope the voices of Pieter and me don’t haunt you whenever you decide to fire up the oven to bake something!

Not a single paper in the list of publications would exist without the craftsmanship of the Nano Development (Litho) Group at SRON: David, Vignesh, Tonny, Dimitry, Daniella, Vishal, and Rianne. David, thank you for cheering us up on cold winter days with glühwein and hot chocolate. I can’t think of anyone who fits the description of “gangmaker” better than you do. I greatly enjoyed all the impromptu, hour-long presentations you gave on whatever nanofabrication concept I wanted to know more about. Tonny and Dimitry, thank you for all the time you spent brainstorming with us while designing new devices and for explaining the limits and advantages of the techniques you use. Tonny, I hope the optical stacks from Chapters 5 and 6 haven’t given you too many nightmares.

I’m also grateful to the THz sensing group for continuing to host our team of “crazy” people who talk about “single” photons. Thanks to all the staff and students who were part of this group over the past five years. Special thanks to Andrea Neto and Nuria Llombart for giving the best lectures I attended during my Bachelor’s and Master’s programs and for creating a close-knit group of PhD students.

Special mentions go to my office mates. Sander, you’ve been a close friend for the past ~7 years, a friendship forged in the fires of the THz master. Thank you for always tearing my posters and graphics apart so I could rebuild them better. Thank you for all the tea breaks and for trying to get me to cycle instead of stopping every few meters to look at birds. Caitlin, thank you for your friendship, the lunch walks, the books you loaned me, and for always sharing your genuine opinions—whether about books, series, politics, or anything else. Alexandros, our junior office member, thank you for your camaraderie these past few months as I wrote this thesis. Our discussions were a welcome distraction, and your artistic critique helped bring this thesis cover together. I’m happy to say Sander and I leave the office in good hands.

To my parents, thank you for raising me to be such a curious person, whether about nature or electronics. Thank you for always being proud of me, even when I chose such an outlandish and alien subject as experimental astronomy. Thank you for supporting my lifelong dream of becoming a “satellietenbouwer.” I think I got pretty close! Ralf, my “little” brother who is so similar yet so different from me, thank you for all the hours we spent playing video games together or sharing one of our other

hobbies. I hope you know how proud I am of you.

Karlijn, thank you for always supporting me during these years. I don't think there's anyone I could spend so much time with, just watching birds—whether it's something special like a "goudplevier" or just a flock of geese. Hans de Winter's haiku (vogelwacht Delft) captures our time together beautifully:

Een paartje buizerd
Rustig zwevend op thermiek
Die komen er wel

Na de volgende bocht...

Wiro Pieterse

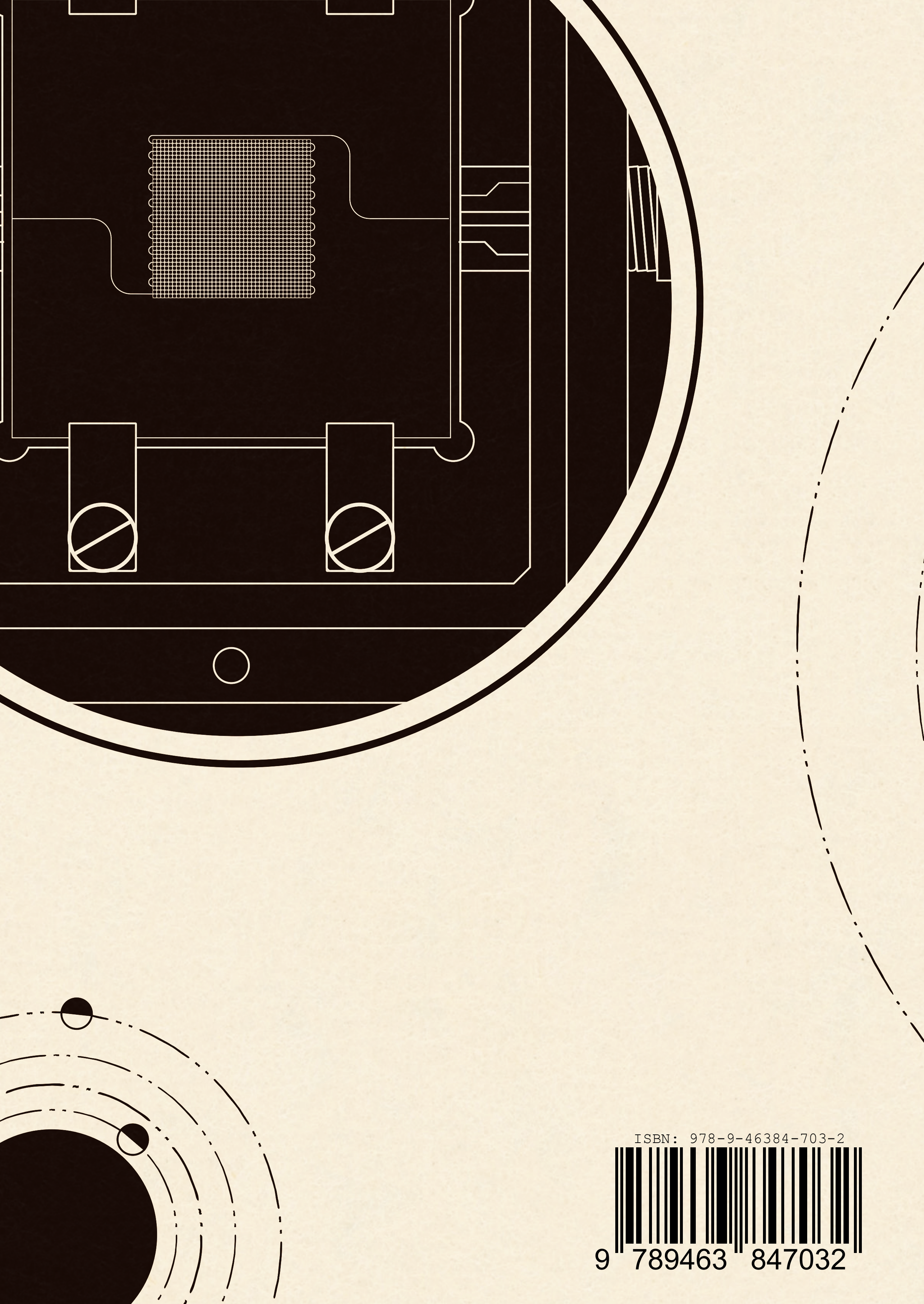

ISBN: 978-9-46384-703-2